Vol. 26, no. 2, 2026 eISSN 2687-1653
PEER-REVIEWED SCIENTIFIC AND PRACTICAL JOURNAL

Advanced Engineering Research (Rostov-on-Don)

Mechanics

Machine Buiding and Machine Science

Information Technology, Computer Science and Management

www.vestnik-donstu.ru
DOI 10.23947/2687-1653

Advanced Engineering Research (Rostov-on-Don)

Peer-reviewed scientific and practical journal

eISSN 2687–1653

Published since 2000

Periodicity – 4 issues per year

DOI: 10.23947/2687–1653

Founder and Publisher — Don State Technical University (DSTU), Rostov-on-Don, Russian Federation

The journal is aimed at informing the readership about the latest achievements and prospects in the field of mechanics, mechanical engineering, computer science and computer technology. The publication is a forum for cooperation between Russian and foreign scientists, it contributes to the convergence of the Russian and world scientific and information space.

The journal is included in the List of the leading peer-reviewed scientific publications (Higher Attestation Commission under the Ministry of Science and Higher Education of the Russian Federation), where basic scientific results of dissertations for the degrees of Doctor and Candidate of Science in scientific specialties and their respective branches of science should be published.

The journal publishes articles in the following fields of science:

– Theoretical Mechanics, Dynamics of Machines (Engineering Sciences)
– Deformable Solid Mechanics (Engineering, Physical and Mathematical Sciences)
– Mechanics of Liquid, Gas and Plasma (Engineering Sciences)
– Mathematical Simulation, Numerical Methods and Program Systems (Engineering Sciences)
– System Analysis, Information Management and Processing, Statistics (Engineering Sciences)
– Automation and Control of Technological Processes and Productions (Engineering Sciences)
– Software and Mathematical Support of Machines, Complexes and Computer Networks (Engineering Sciences)
– Computer Modeling and Design Automation (Engineering, Physical and Mathematical Sciences)
– Computer Science and Information Processes (Engineering Sciences)
– Machine Science (Engineering Sciences)
– Machine Friction and Wear (Engineering Sciences)
– Technology and Equipment of Mechanical and Physicotechnical Processing (Engineering Sciences)
– Engineering Technology (Engineering Sciences)
– Welding, Allied Processes and Technologies (Engineering Sciences)
– Methods and Devices for Monitoring and Diagnostics of Materials, Products, Substances and the Natural Environment (Engineering Sciences)
– Hydraulic Machines, Vacuum, Compressor Equipment, Hydraulic and Pneumatic Systems (Engineering Sciences)

Registration	Extract from the Register of Registered Mass Media ЭЛ № ФС 77 – 78854 dated August 07, 2020, issued by the Federal Service for Supervision of Communications, Information Technology and Mass Media
Indexing and Archiving	Scopus, RSCI, RISC (core), CyberLeninka, CrossRef, Dimensions, DOAJ, EBSCO, Index Copernicus, Internet Archive, Google Scholar
Website	https://vestnik-donstu.ru
Address of the Editorial Office	1, Gagarin sq., Rostov-on-Don, 344003, Russian Federation
E-mail	vestnik@donstu.ru
Telephone	+7 (863) 2–738–372
Date of Publication No.2,2026	30.06.2026

Advanced Engineering Research (Rostov-on-Don)

Рецензируемый научно-практический журнал

eISSN 2687–1653

Издается с 2000 года

Периодичность – 4 выпуска в год

DOI: 10.23947/2687–1653

Учредитель и издатель — Федеральное государственное бюджетное образовательное учреждение высшего образования «Донской государственный технический университет» (ДГТУ), г. Ростов-на-Дону

Создан в целях информирования читательской аудитории о новейших достижениях и перспективах в области механики, машиностроения, информатики и вычислительной техники. Издание является форумом для сотрудничества российских и иностранных ученых, способствует сближению российского и мирового научно-информационного пространства.

Журнал включен в перечень рецензируемых научных изданий (К2), в котором должны быть опубликованы основные научные результаты диссертаций на соискание ученой степени кандидата наук, на соискание ученой степени доктора наук (Перечень ВАК) по следующим научным специальностям:

1.1.7 – Теоретическая механика, динамика машин (технические науки)
1.1.8 – Механика деформируемого твердого тела (технические, физико-математические науки)
1.1.9 – Механика жидкости, газа и плазмы (технические науки)
1.2.2 – Математическое моделирование, численные методы и комплексы программ (технические науки)
2.3.1 – Системный анализ, управление и обработка информации, статистика (технические науки)
2.3.3 – Автоматизация и управление технологическими процессами и производствами (технические науки)
2.3.5 – Математическое и программное обеспечение вычислительных систем, комплексов и компьютерных сетей (технические науки)
2.3.7 – Компьютерное моделирование и автоматизация проектирования (технические, физико-математические науки)
2.3.8 – Информатика и информационные процессы (технические науки)
2.5.2 – Машиноведение (технические науки)
2.5.3 – Трение и износ в машинах (технические науки)
2.5.5 – Технология и оборудование механической и физико-технической обработки (технические науки)
2.5.6 – Технология машиностроения (технические науки)
2.5.8 – Сварка, родственные процессы и технологии (технические науки)
2.5.9 – Методы и приборы контроля и диагностики материалов, изделий, веществ и природной среды (технические науки)
2.5.10 – Гидравлические машины, вакуумная, компрессорная техника, гидро- и пневмосистемы (технические науки)

Регистрация	Выписка из реестра зарегистрированных средств массовой информации ЭЛ № ФС 77 – 78854 от 07 августа 2020 г., выдано Федеральной службой по надзору в сфере связи, информационных технологий и массовых коммуникаций
Индексация и архивация	Scopus, RSCI, РИНЦ (ядро), CyberLeninka, CrossRef, Dimensions, DOAJ, EBSCO, Index Copernicus, Internet Archive, Google Scholar
Сайт	https://vestnik-donstu.ru
Адрес редакции	344003, Российская Федерация, г. Ростов-на-Дону, пл. Гагарина, 1
E-mail	vestnik@donstu.ru
Телефон	+7 (863) 2–738–372
Дата выхода №2,2026 в свет	30.06.2026

Contents

Содержание

MECHANICS
МЕХАНИКА

UDC 537.528
https://doi.org/10.23947/2687-1653-2026-26-2-2245

Original Empirical Research

Electric Discharge between a Jet Electrolytic Cathode and a Metal Anode

Sergey Yu. Petryakov, Eduard R. Belgibaev, Almaz F. Gaisin ✉, Rushan R. Kayumov
Kazan National Research Technical University named after A. N. Tupolev – KAI,
Kazan, Russian Federation
✉ almaz87@mail.ru

EDN: MNOFIY

Abstract

Introduction. Gas discharges with liquid electrodes are considered as a promising tool for improving adhesion properties and preparing surfaces for coating application. Glow and arc discharges with electrolytic electrodes have been investigated in detail in the literature, but most studies focus on configurations with a stationary electrolyte. For "jet electrolytic cathode–metal anode" systems at atmospheric pressure, the discharge combustion modes, their stability limits, and the energy characteristics of the process are insufficiently systematized. This hinders the scalability of localized aluminum processing technologies. The objective of this study is to experimentally classify combustion modes and their stability regions, determine the electrical, spectral, and thermal parameters of the discharge, and substantiate practical modes for localized aluminum surface preparation for adhesion and coating.

Materials and Methods. To achieve this goal, a laboratory setup was built: a 3% NaCl jet served as the cathode, and an AMTs-40 (aluminum-manganese alloy in the RU system, ISO analog: AW-3003) aluminum plate served as the anode. The jet-anode assembly was placed in a temperature-controlled electrolytic cell with closed circulation of the solution. Typical conditions: $U \approx 600$ V, $v_k \approx 0.6$–0.7 m/s, $d \approx 2$ mm, $\sigma \approx 0.10$–0.12 Ω^{-1} cm^{-1}. A power supply of up to 4 kV/10 A provided a wide range of settings. The diagnostics included oscillographic measurements, high-speed video recording (Casio EX-F1, 600–1200 fps), thermal imaging (FLIR A6500sc), and optical emission spectroscopy (OES) on a PLASUS EC 150201 MC spectrometer with electron density n_e estimated from Stark broadening of H_α.

Results. Two plasma localization topologies were detected: a contact zone on the triple gas-liquid-solid line and a jet breakup region. The current was pulsed with an amplitude of 0.8–1.6 A. The spectra were dominated by the Na I doublet (~589 nm), the OH(A–X) bands, and the Hα line; from $\Delta\lambda_L$ (H_α) ≈ 0.64 nm, an estimate of ne ≈ 6.4 × 10^{16} cm^{-3} was obtained. Thermal imaging maps showed a maximum effective temperature of ~47°C at the point of contact, and an energy deposition zone elongated along the jet with a length of ~7 mm (diameter ~2 mm).

Discussion. The pulsed nature of the current with an amplitude of 0.8–1.6 A at 600 V indicates the periodic formation and breakdown of the current channel, which is typical for discharges with a nonstationary geometry of the cathode region and has been previously noted in studies on discharges with flowing jets. The estimate of the electron density $n_e \approx 6.4\times10^{16}$ cm^{-3} based on the Stark broadening of Hα falls within the range of 10^{15}–10^{17} cm^{-3}, characteristic of atmospheric discharges with liquid electrodes, and indicates a relatively dense plasma sufficient for effective surface activation. The dominance of Na I lines in the spectrum confirms the intense transfer of electrolyte components into the discharge gap, which is consistent with the aerosol sputtering mechanism in the near-cathode region. The compactness of the temperature spot on the anode (transverse size ~2 mm, maximum 47°C) confirms the localized nature of the energy deposition without global overheating of the component. However, the true surface temperature may be higher than the measured one due to the uncertainty in the emissivity of the growing oxide film.

Conclusion. A discharge between a jet electrolytic cathode and an aluminum anode at atmospheric pressure has been experimentally characterized. Two stable combustion topologies, the pulsed nature of the current, spectral markers, and a thermal energy deposition pattern are demonstrated. The results form the basis for constructing operational maps for local aluminum processing and expanding technology applications. The data obtained form the basis for constructing a map of aluminum processing modes and can be expanded through varying the flow rate, nozzle diameter, electrolyte composition, and using faster diagnostics. Future work includes standardizing the energy metrics, quantitatively decomposing the radiation sources, and scaling the methodology.

Keywords: jet electrode, aluminum anode, gas discharge, pulsed currents, emission spectroscopy, Balmer lines, electron concentration, thermal imaging diagnostics, surface modification

Acknowledgements. The team of authors appreciates the Department of Laser and Additive Technologies, KNITU-KAI, for the provided diagnostic equipment.

Funding Information. The research is done with the support from the Russian Science Foundation (grant no. 25–29–20147), https://rscf.ru/project/25-29-20147/»

For Citation. Petryakov SYu, Belgibaev ER, Gaisin AF, Kayumov RR. Electric Discharge between a Jet Electrolytic Cathode and a Metal Anode. *Advanced Engineering Research (Rostov-on-Don).* 2026;26(2):2245. https://doi.org/10.23947/2687-1653-2026-26-2-2245

Оригинальное эмпирическое исследование

Электрический разряд между струйным электролитическим катодом и металлическим анодом

С.Ю. Петряков, Э.Р. Бельгибаев, А.Ф. Гайсин ✉, Р.Р. Каюмов

Казанский национальный исследовательский технический университет им. А.Н. Туполева – КАИ, г. Казань, Российская Федерация

✉ almaz87@mail.ru

Аннотация.

Введение. Газовые разряды с жидкими электродами рассматриваются как перспективный инструмент для улучшения адгезионных свойств и подготовки поверхностей под нанесение покрытий. В литературе подробно изучены тлеющие и дуговые разряды с электролитическими электродами, однако большинство работ сосредоточено на конфигурациях с неподвижным электролитом. Для систем «струйный электролитический катод — металлический анод» при атмосферном давлении формы горения разряда, границы их устойчивости и энергетические характеристики процесса систематизированы недостаточно. Это препятствует масштабированию технологий локальной обработки алюминия. Цель настоящей работы — экспериментально классифицировать формы горения и области их устойчивости, определить электрические, спектральные и тепловые параметры разряда, а также обосновать практические режимы локальной подготовки алюминиевой поверхности под адгезию и покрытия.

Материалы и методы. Для реализации поставленной цели была создана лабораторная установка: струя 3 % NaCl выполняла роль катода, алюминиевая пластина АМЦ-40 — анода; узел «струя-анод» размещён в термостатируемой электролитической ячейке с замкнутой циркуляцией раствора. Типичные условия: $U \approx 600$ В, $v_k \approx 0{,}6–0{,}7$ м/с, $d \approx 2$ мм, $\sigma \approx 0{,}10–0{,}12$ $\Omega^{-1}\cdot$см$^{-1}$; источник питания до 4 кВ/10 А обеспечивал широкий диапазон настроек. Диагностика включала осциллографические измерения, высокоскоростную видеосъёмку (Casio EX-F1, 600–1200 к/с), тепловизионную съёмку (FLIR A6500sc) и ОЭС на спектрометре PLASUS EC 150201 MC с оценкой n_e по штарковскому уширению H_α.

Результаты исследования. Обнаружены две топологии локализации плазмы: контактная зона на тройной линии «газ-жидкость-твёрдое тело» и область распада струи. Ток носит импульсный характер с амплитудой 0,8–1,6 А. В спектрах доминируют дублет Na I (~589 нм), полосы OH(A–X) и линия Hα; по $\Delta\lambda_L$ (H_α) ≈ 0,64 нм получена оценка $n_e \approx 6{,}4 \times 10^{16}$ см$^{-3}$. Термовизионные карты показали максимум эффективной температуры ~47 °C в точке контакта и вытянутую вдоль струи зону энерговклада длиной ~7 мм (поперечник ~2 мм).

Обсуждение. Импульсный характер тока с амплитудой 0,8–1,6 А при 600 В свидетельствует о периодическом формировании и срыве токового канала, что типично для разрядов с нестационарной геометрией катодной области и ранее отмечалось в работах по разрядам со стекающими струями. Оценка электронной концентрации $n_e \approx 6{,}4\times10^{16}$ см$^{-3}$ по штарковскому уширению Hα попадает в диапазон 10^{15}–10^{17} см$^{-3}$, характерный для атмосферных разрядов с жидкими электродами, и указывает на относительно плотную плазму, достаточную для эффективной активации поверхности. Доминирование линий Na I в спектре подтверждает интенсивный перенос компонентов электролита в разрядный промежуток, что согласуется с механизмом аэрозольного распыления в прикатодной области. Компактность температурного пятна на аноде (поперечный размер ~2 мм, максимум 47 °C) подтверждает локальный характер энерговклада без глобального перегрева детали, однако истинная температура поверхности может быть выше измеренной из-за неопределённости эмиссивности растущей оксидной плёнки.

Заключение. Экспериментально охарактеризован разряд между струйным электролитическим катодом и алюминиевым анодом при атмосферном давлении; показаны две устойчивые топологии горения, импульсная природа тока, спектральные маркеры и тепловая картина энерговклада. Результаты формируют базу для построения режимных карт локальной обработки алюминия и расширения технологических приложений. Полученные данные

составляют основу для построения карты режимов обработки алюминиевых изделий и могут быть расширены за счёт варьирования расхода, диаметра сопла, состава электролита и применения более скоростной диагностики. Направления дальнейших работ: стандартизация энергетических метрик, количественная декомпозиция источников излучения и масштабирование методики.

Ключевые слова: струйный электрод, алюминиевый анод, газовый разряд, импульсные токи, эмиссионная спектроскопия, линии Бальмера, концентрация электронов, тепловизионная диагностика, модификация поверхности

Благодарности. Коллектив авторов выражает благодарность кафедре лазерных и аддитивных технологий при ФГБОУ ВО «КНИТУ-КАИ» за предоставленное диагностическое оборудование.

Финансирование. Исследование выполнено за счет гранта Российского научного фонда № 25–29–20147, https://rscf.ru/project/25-29-20147/»

Для цитирования. Петряков С.Ю., Бельгибаев Э.Р., Гайсин А.Ф., Каюмов Р.Р. Электрический разряд между струйным электролитическим катодом и металлическим анодом. *Advanced Engineering Research (Rostov-on-Don).* 2026;26(2):2245. https://doi.org/10.23947/2687-1653-2026-26-2-2245

Introduction. Gas-discharge plasma, formed in the interelectrode gap where one or both electrodes are liquid, is a promising area of research in the fluid, gas, and plasma mechanics, as well as modern materials processing technologies [1]. One popular configuration is a system with a jet electrolytic cathode and a metal anode, in which the cathode function is performed by a flowing jet of electrolyte [2]. This design allows for the formation of a local cathode region with gas-discharge plasma and provides flexible adjustment of process parameters [3]. Local energy deposition in the cathode spot zone, effective heat removal through liquid electrodes, and rapid removal of reaction products provide the high efficiency of this configuration for local surface treatment of small-sized metal products [4], cleaning [5], burr removal, and the application of functional coatings [6].

The discharge mechanism with a jet electrolytic cathode is determined by complex interphase interactions in a three-phase “gas – liquid – solid” unit [7]. The nature of combustion and the stability of the process are significantly affected by electrical parameters (voltage, current, power, type of power supply – direct or high-frequency current) [8], jet hydrodynamics (flow rate, flow velocity, nozzle diameter, turbulence level) [9], thermal and mass transfer phenomena (evaporation, degassing) [10], chemical composition and specific electrical conductivity of the electrolyte [11], as well as the pressure and composition of the surrounding gas environment [12]. Such systems are characterized by a change in combustion modes, the occurrence of self-excited oscillations and breakdowns, as well as a pronounced nonlinearity of the volt-ampere characteristics [13]. In comparison with the discharge on a solid cathode, the structure of the near-electrode layer of a liquid cathode is specific: a key role is played by ion bombardment of the jet surface, secondary electron emission at the interface between the media, micro-splashes and microdischarges on gas inclusions, as well as electrodynamic stabilization or destabilization of the meniscus [14].

The practical significance of such discharges is due to the possibility of controlled modification of the microrelief and condition of the near-surface layer of the metal anode without critical thermal impact on the component. This allows for the formation of active functional groups, regulation of surface wettability, removal of oxide films and organic contaminants, initiation of nucleation sites for subsequent coating deposition, and improvement of microhardness and corrosion resistance. The localized nature of the impact is particularly relevant for small components with complex geometries, where traditional mechanical and electrochemical methods are inapplicable. For industrial production, the determination of optimal processing conditions that link discharge characteristics and electrolyte jet parameters is the critical task.

However, this area of research remains understudied. The conditions for the transition between different discharge modes, depending on electrodynamic and hydrodynamic factors, is not fully described. Mathematical models of the layer in the liquid cathode region need to be developed, taking into account the processes of vapor-gas shell generation. Systematization of the modes in the form of maps is required, where electrical characteristics (specific energy deposition per unit surface area, voltampere curves) would be compared with the final functional properties of the material. From a diagnostic perspective, the following are in demand: high-speed visualization of interelectrode processes; precision recording of voltampere characteristics and current oscillations; optical emission spectroscopy for identifying plasma composition, determination of the concentration and temperature of electrons, as well as the temperature of the heavy component.

The objective of this study is to establish the combustion modes of an electric discharge between a jet electrolytic cathode and an aluminum anode, identify the regions of their stable existence, and comprehensively determine the electrophysical, spectral, and thermal characteristics. The results obtained are aimed at developing scientifically sound recommendations for the finishing and modification of aluminum and its alloy products.

Materials and Methods. Ignition and stable combustion of a jet electric discharge with a liquid plasma-forming medium under localized action on a metal anode were implemented using a laboratory setup in which a flowing electrolyte jet served as the cathode and a metal plate — as the anode (Fig. 1 *a*). The jet – anode assembly was housed within an electrolytic cell (Fig. 2 *b*), equipped with systems for supplying and removing the solution, temperature control, and standard exhaust ventilation for the work area.

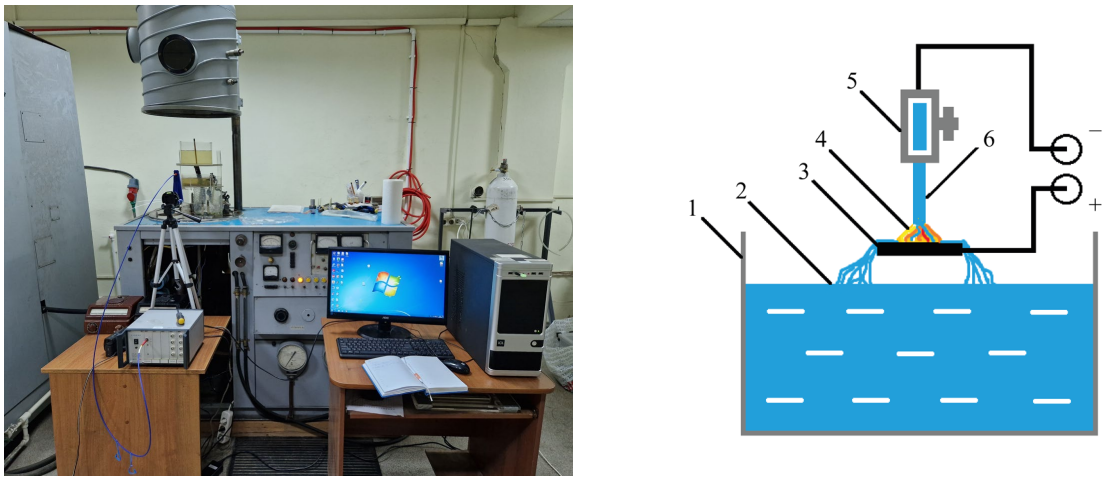

a) *b)*

Fig. 1. Experimental setup for igniting gas-discharge plasma:
a — photograph of the experimental setup; *b* — functional diagram of the gas-discharge chamber for maintaining a jet discharge with a liquid cathode interacting with the surface of a metal anode, where: 1 — electrolytic cell; 2 — electrolyte; 3 — metal anode (aluminum plate); 4 — discharge combustion zone; 5 — jet feed/adjustment nozzle; 6 — electrolyte jet (cathode)

An aluminum plate from AMts-40 (ISO: AW-3003 or AlMn1Cu), secured in a cell, served as the anode. The cathode was formed by a continuous jet of a 3% aqueous NaCl solution prepared with purified tap water. Before starting, a negative potential was applied to the nozzle and the jet, and a positive potential — to the aluminum plate. The jet was generated through a replaceable nozzle; the flow rate was set using a control valve monitored by a flow gage. To ensure the stability of the solution properties, temperature control was provided: a refrigerated circulation cooler maintained the temperature within specified limits, and electrolyte was renewed in a closed loop with a coarse filter to remove mechanical impurities. Vapors and aerosols were removed from the work area by a stationary exhaust system. All current-carrying components and housing were protected by grounding.

The discharge was powered by a high-voltage source up to 4 kV with a nominal current up to 10 A and stepless control, including high-voltage and low-voltage channels. This allowed for flexible setting of voltage and current ranges, as well as powering auxiliary sensors. Current values of U and I were displayed on panel indicators and duplicated on the control PC for operational monitoring. In standard series of experiments, the parameters were: voltage $U = 0.1–1.1$ kV; pressure $p \approx 10^5$ Pa (atmospheric); jet velocity $v_к = 0.5–0.7$ m/s; jet diameter $d = 2$ mm; jet length $l = 15$ mm; v $\sigma = 0.10–0.12$ Ohm^{-1}·cm^{-1}; temperature $T = 12–64$ °C. The polarity of the electrodes was maintained in all modes: jet – cathode, plate – anode.

The diagnostic complex included mutually complementary methods of visualization, thermal and electrical control, as well as optical emission spectroscopy.

1. High-speed video recording of the torch and near-electrode structure dynamics was performed using a Casio EX-F1 camera at 600 and 1200 fps. The camera was mounted on a tripod approximately 300 mm from the discharge zone. Data transfer and initial processing were performed on a PC using HX Link and Movavi Video Editor 14 Plus software. The recording made it possible to capture the shape and oscillations of the cathode jet, as well as the evolution of the anode spot.

2. A FLIR A6500sc thermal imaging camera (640×512 pixels; 3.6–4.9 μm) calibrated with a multi-wavelength pyrometer was used to map the temperature field on the anode surface and in the vicinity of the cathode jet. This compensated for changes in effective emissivity associated with the formation and growth of an oxide film on the aluminum. Thermogram analysis was performed using the ALTAIR v5.91.010 software package.

3. Current and voltage pulsations were recorded using GDS-806S and GOS-6030 digital oscilloscopes. A photodiode discharge radiation sensor connected to the oscilloscope was used to synchronize electrical signals with optical events. This approach ensured that ignition timing, transitions between combustion modes, and surges were correlated with visually observable changes in the flame.

4. Optical emission spectroscopy was performed on a PLASUS EC 150201 MC fiber-optic spectrometer in the range of 195–1105 nm. The radiation was collected by a collimator brought to the combustion zone at a distance of 100–200 mm. The instrumental function was calibrated using a SIRSH 6–100 source; the instrumental width was $\Delta\lambda_g \approx 1$ nm. The spectra were compared with the NIST database. The electron concentration (based on the broadening of H_α) was estimated from the profiles of the Balmer series hydrogen lines.

A set of tools and modes provided representative, reproducible measurements and comparison of electrical, spectral, thermal and visual characteristics of a jet discharge with a liquid cathode and local impact on the surface of a metal anode.

Research Results. The photographs (Fig. 2) show that with the polarity "jet electrolytic cathode —- aluminum anode", the discharge at $U = 600$ V, $p = 10^5$ Pa and jet velocity $v_k = 0.6$ m/s, is localized in two characteristic areas: 1 — in the zone of direct contact of the jet with the surface of the anode (Fig. 2 *a*), and 2 — in the region of jet breakdown (Fig. 2 *b*).

In the first case, a near-electrode light-emitting region is formed, tied to the "contact spot" and the "gas-liquid-solid" triple cross-section line. In the second case, glow and microdischarge events occur at the necks and droplets of the disintegrating jet, where the surface curvature and localized gas inclusions enhance the field and reduce the effective gap length.

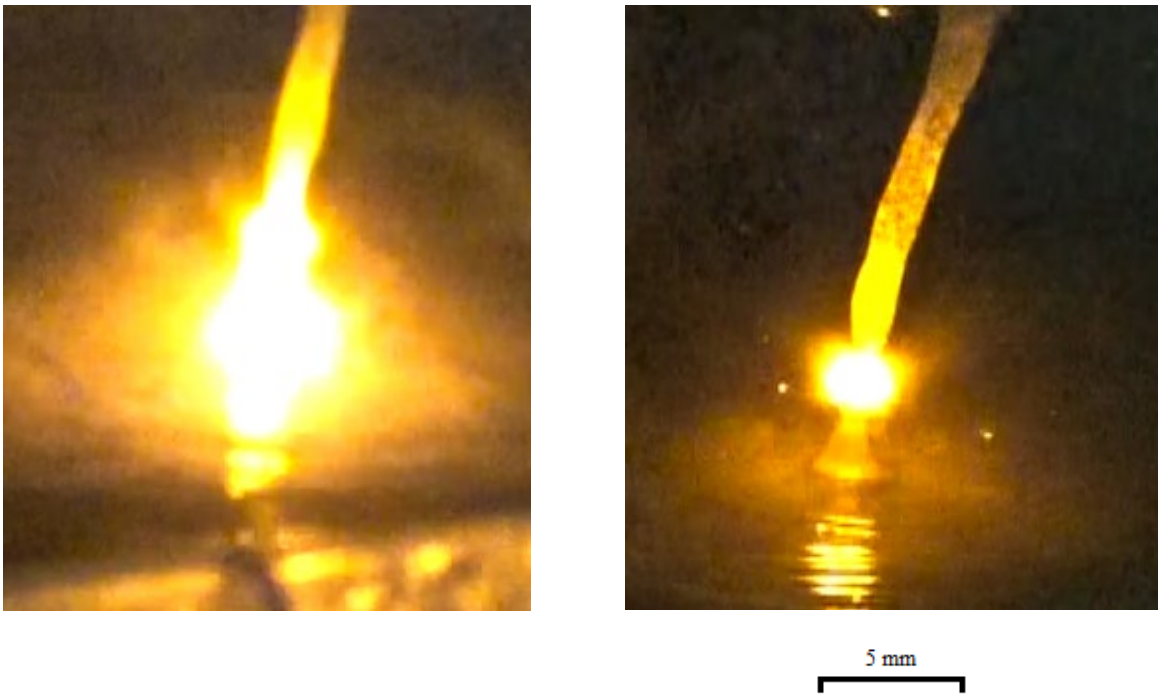

Fig. 2. Jet electric discharge between a jet anode and an aluminum cathode at $U = 600$ V, $I = 1.6$ A, $p = 10^5$ Pa, $v_к = 0.6$ m/s: *a* — at the interface between jet and metal surface; *b* — in the jet breakup zone

The characteristic yellow color of the torch in both cases is primarily due to the intense emission of the sodium resonant doublet (≈ 589 nm), which arises from the evaporation/aerosol emission of Na-containing components from the jet of 3% NaCl solution in the near-cathode zone and their subsequent dissociation-excitation in the discharge volume. The contribution of continuous radiation from heated aerosol particles and local oxide inclusions can impart an orange-yellow hue at moments of peak energy deposition, but remains secondary to the Na lines.

The current oscillograms (Fig. 3) at a fixed voltage of $U = 600$ V demonstrate the pulsed nature of the conductivity: the current is realized in series of pulses with an amplitude of about 0.8–1.6 A. This intermittent structure corresponds to the alternation of stages of amplification and attenuation of electron emission at the gas-liquid interface and the periodic "switching" of the conductivity channel between two geometries — "a spot on the surface of the metal electrode" and "in the jet breakup zone".

a) *b)*

Fig. 3. Oscillograms of discharge current and voltage oscillations between the jet cathode and aluminum anode:
a — at $p = 10^5$ Pa, ΔU – 500 V, $\Delta I = 2$ A, $\Delta t = 25$ ms;
b — at $p = 10^5$ Pa, ΔU – 500 V, $\Delta I = 2$ A, $\Delta t = 5$ ms

Hydrogasdynamic processes, including the formation of gas bubbles, the emergence of convective currents, as well as the specific flow characteristics and jet velocity — along with accompanying variations in the interelectrode distance and cathode spot geometry — cause fluctuations in current density and electromagnetic field strength. These phenomena are recorded on the oscillogram as characteristic pulsed regions (Fig. 3).

Electrical signals obtained using an oscilloscope are compared with optical recordings of the discharge glow. It is found that current pulses correlate temporally with the occurrence of intense radiation in the combustion zone. This indicates that rapid microevents in the near-cathode region are crucial in initiating the pulses, transforming the conditions for the formation of the cathode layer and triggering microdischarges toward the anode.

In this electrode configuration, the following mechanisms of charged particle formation can act as sources of primary electrons for avalanche ionization and subsequent ionization in the volume: (1) secondary electron emission from the surface of the liquid cathode under the impact of bombardment by positive ions and fast neutral particles; (2) field emission from highly curved areas where the field strength increases locally; (3) photoelectron emission from the surface of the jet under the action of radiation from the discharge volume; (4) emission from gas bubbles adjacent to the cathode, where the reduced effective work function and field concentration facilitate the injection of electrons; (5) detachment of electrons from negative ions in the near-electrode layer.

Figure 4 shows the plasma emission spectrum of a discharge between a jet electrolytic cathode and an aluminum anode, with identified bands and lines.

Bands OH (A→X), are recorded, as well as the atomic lines H I, Na I, N I and K I. The presence of an intense resonance doublet Na I (≈ 589.0/589.6 nm) is consistent with the visually observed yellow color of the flame: sodium enters the discharge zone from a 3% NaCl solution via evaporation from the near-cathode region, after which it is excited in the plasma volume.

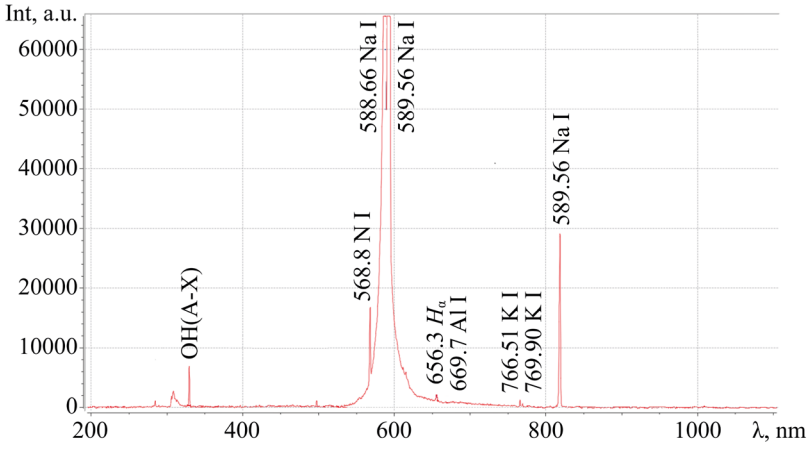

Fig. 4. Emission spectrum of the discharge plasma between the jet cathode and the aluminum anode with identified spectral lines

The instrumental broadening was estimated using the optically thin line K I (769.9 nm); the minimum half-width of the narrow lines was $\Delta\lambda_G \approx 1.0$ nm and was then taken as the Gaussian component of the instrumental function. The observed line profiles were approximated by a Voigt contour; the Voigt ($\Delta\lambda_F$), Lorentzian ($\Delta\lambda_L$ and Gaussian ($\Delta\lambda_G$) half-widths were related using approximation [15]:

$$\Delta\lambda_F \approx 0.5346 \cdot \Delta\lambda_L + \sqrt{0.2166 \cdot \Delta\lambda_L^2 + \Delta\lambda_G^2}.$$

From it, $\Delta\lambda_L$ was found with known $\Delta\lambda_F$ and $\Delta\lambda_G$, thereby eliminating the contribution of instrumental broadening.

For line H_α (656.28 nm), the measured half-width of the Voigt profile was $\Delta\lambda_F(H_\alpha) = 1.38$ nm. Taking into account the instrumental component, the Lorentz half-width was obtained as $\Delta\lambda_L(H_\alpha) \approx 0.64$ nm. The electron concentration $n_e \approx 6.4\times10^{16}$ cm^{-3} was calculated using temperature-dependent coefficients.

This electron density is typical for atmospheric pressure, where the linear Stark broadening of hydrogen lines dominates.

In this series, H_β (486.13 nm) was not detected due to the low signal-to-noise ratio in the channel and exposure adjustment for the bright yellow lines Na I, which does not prevent n_e from H_α.

Table 1

Summary Spectral Parameters for Estimating n_e from Line H_α

Parameter	Value	Note
$\Delta\lambda_F(H_\alpha)$	1.38 nm	Voigt contour half-width
$\Delta\lambda_L(H_\alpha)$	≈ 0.64 nm	Lorentz component (without instrument broadening)
n_e	≈ 6.4×10^{16} cm^{-3}	Stark broadening estimation of H_α

The combination of observed bands and lines confirms the mixed nature of plasma formation (air + electrolyte sputtering products). The yellow color of the flame is due to the dominance of Na I lines, and an estimate based on the broadening of H_α yields an electron concentration of approximately 10^{16} cm^{-3} under the conditions studied.

Thermographic analysis of the discharge zone. In the thermograms (Fig. 5), the origin of coordinates is the position corresponding to the contact area of the jet electrolytic cathode with the aluminum anode ("gas-liquid-solid" line).

At this point, the maximum effective temperature is recorded at $T = 47$°C. As the electrode moves toward the source of the electrolyte jet, that is, along the jet, the temperature decreases within the first 7 mm, indicating a plasma region elongated along the jet, approximately 7 mm in length and with an effective transverse dimension of 2 mm. Outside the plasma region, the temperature profile declines exponentially to the ambient temperature. As the electrode moves toward the aluminum anode, the temperature also drops sharply to 22°C. This profile asymmetry is explained by the high thermal conductivity of aluminum and its effective heat dissipation into the component volume, as well as by intensive convective cooling by the adjacent electrolyte. The temperature "spot" on the anode surface is compact and confined to the contact zone. This corresponds to the pattern of directed energy deposition from the discharge elongated along the cathode jet.

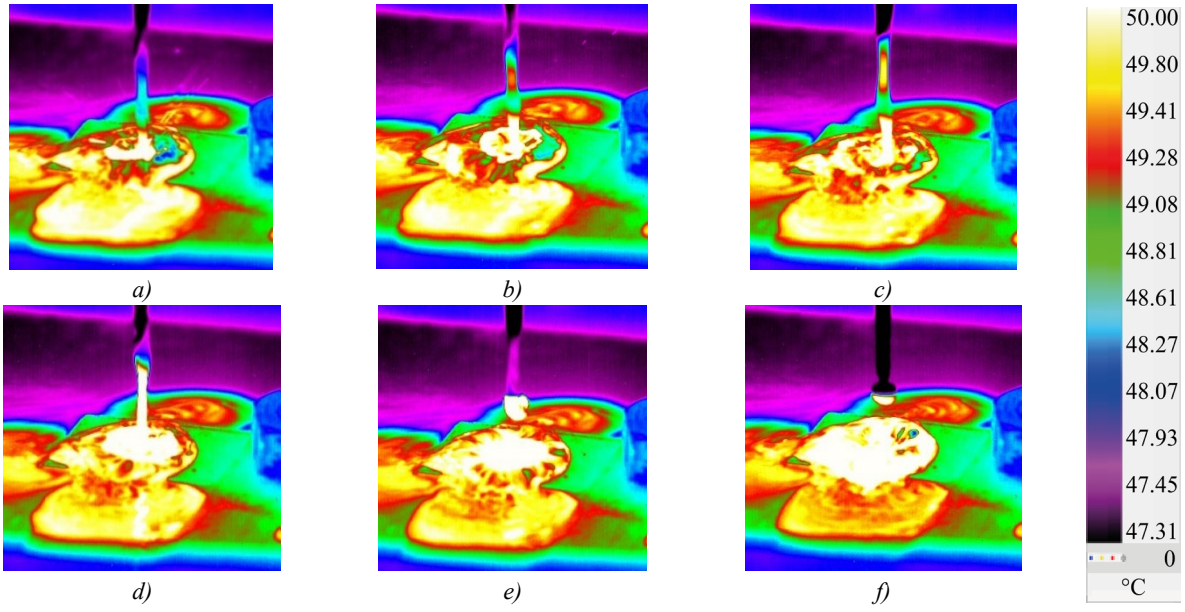

Fig. 5. Dynamics of temperature distribution of the jet electrolytic cathode (thermograms, t = 0–5 s, Δt = 1 s): *a* — 0 s; *b* — 1 s; *c* — 2 s; *d* — 3 s; *e* — 4 s; *f* — 5 s

Discussion. Based on the data obtained, it follows that plasma structures are localized in two areas of the system: (1) — in the area of contact of the jet electrode with the surface of the workpiece, and (2) — in the zone of thinning and disintegration of the jet electrode.

In the first case, the maximum energy deposition from the discharge is localized in the area of the cathode spot on the surface of the metal anode. In the second case, it shifts toward the constriction and disintegration region of the jet electrode, where the surface geometry and the vapor-gas gap enhance the electromagnetic field. This behavior of the jet electrode explains the changes in conductivity and, consequently, current fluctuations in the range of 0.8–1.6 A at a voltage of approximately 600 V.

The pulsed nature of the discharge combustion is due to the interrelationship between the electrical parameters of the discharge, the cathode layer, and the jet hydrodynamics. The dynamics of the jet flow, accompanied by the formation of localized areas of constriction and jet breakup, causes a non-stationary change in the geometry of the cathode region and a change in the electric field strength. Under these conditions, short-term microdischarges are formed in the vapor-gas region between the anode and cathode which show themselves as successive current pulses that correlate with the discharge plasma glow. The initiation of these pulses is determined by the combined contribution of various electron emission mechanisms, including secondary emission under ion bombardment, field emission, and electron injection into the plasma volume from the surface of the near-cathode layer.

Analysis of the emission spectra indicates the combined nature of the gas-discharge plasma, formed by both ambient air components and elements dislocated from the electrolyte. Intense radiation is recorded at the Na I line in the region of approximately 589 nm, which determines the predominance of the yellow color of the discharge combustion. The detection of the bands OH (A–X) and line H_α indicates the occurrence of gas-phase processes involving hydrogen and hydroxyl radicals. The electron concentration, estimated from the Stark broadening of line H_α ($\Delta\lambda_L \approx 0.64$ nm), is $n_e \approx 6.4\times10^{16}$ cm^{-3}.

Thermographic measurements show the formation of a localized heating zone on the surface of the metal anode with a maximum temperature of approximately 47°C. The spatial asymmetry of the temperature field is due to the high thermal conductivity of aluminum, which provides intense heat transfer into the bulk of the material and convective cooling from the electrolyte. The recorded temperature values do not determine the mechanism of aluminum surface activation. The change in the properties of the surface layer is realized due to the nonequilibrium effect of gas discharge plasma, including a flow of charged particles, active chemical components, and local electric fields in the anode region, and not as a result of thermal destruction of oxide film Al_2O_3.

From the point of view of practical implementation, the process is characterized by the presence of stable regime regions determined by a set of electrical parameters (voltage, current), hydrodynamic characteristics of the jet (speed, diameter, length of the gap) and the electrical conductivity of the solution.

Limitations of the study include the finite spectral resolution of the equipment used (~1 nm), which imposes restrictions on the interpretation of narrow lines and makes line H_α preferable for estimating electron concentration. An additional factor is the fixed electrolyte composition (3% NaCl), while changes in ionic composition and pH can significantly affect excitation kinetics and the thermal balance of the system. These circumstances determine the directions of further research.

Inspection of the treated aluminum anode surface reveals the formation of a localized impact zone with no signs of melting. This indicates the gentle nature of the plasma-liquid action, ensuring surface cleaning while maintaining the component geometry. Quantitative assessment of changes in roughness, wettability, and micromechanical properties requires further experimental analysis.

From an applied perspective, the established pulsed reactions and the presence of two stable electric discharge combustion modes create the prerequisites for controlled changes in energy deposition through varying the jet parameters and electrical characteristics. This enables a transition from gentle surface cleaning modes to controlled modification of surface morphology without significant thermal impact on the material, which is important for the development of compact technological solutions for the preparation of aluminum surfaces for coating deposition and ensuring adhesion.

Conclusion. An experimental study on an electric discharge in a jet electrolytic cathode–aluminum anode system at atmospheric pressure was performed. Two plasma localization topologies were established: a contact zone on the triple line and a jet breakup region. In both cases, the current was pulsed with an amplitude of approximately 0.8–1.6 A. Optical emission spectroscopy confirmed the mixed nature of the plasma (air + electrolyte sputtering products), and the dominance of the Na I doublet, while an estimate based on the broadening of H_α yielded the electron concentration

$n_e \approx 10^{16}$ cm^{-3}. Thermal imaging data indicated a maximum effective temperature of approximately 47°C on the contact side, and an energy deposition zone approximately 7 mm long, elongated along the jet. It was shown that the pulse triggering mechanism was due to electromechanical feedback between the cathode layer and the jet hydrodynamics. Possible sources of primary electrons included secondary, auto-, and photoemission, as well as emission from gas microcavities. In practice, this allowed for targeted selection of modes (jet velocity/diameter, electrical conductivity, voltage) for delicate activation, cleaning, and microtexturing of aluminum surfaces. Prospects for further research include standardization of energy metrics, quantitative decomposition of the contributions of radiating components, and expansion for constructing process maps.

The presented results form the physical basis for subsequent quantitative analysis of surface quality and construction of operational maps for plasma-liquid processing of aluminum products.

References

1. Haixia Wu, Wei Ye, Wang Shen, Quanfa Zhao. Tetracycline Degradation in the System of Peracetic Acid Activation by Liquid Discharge Plasma. *Separation and Purification Technology.* 2025;354(2):128783. https://doi.org/10.1016/j.seppur.2024.128783

2. Kovačević VV, Sretenović GB, Obradović BM, Kuraica MM. Low-Temperature Plasmas in Contact with Liquids—A Review of Recent Progress and Challenges. *Journal of Physics D: Applied Physics.* 2022;55(47):473002. https://doi.org/10.1088/1361-6463/ac8a56

3. Vasilev M, Conlon P, Bohl D, Thagard SM. The Effect of Discharge Frequency of a Gas–Liquid Plasma Reactor on Bulk Liquid Transport and Removal of Organic Contaminants. *Plasma Chemistry and Plasma Processing.* 2022;42(4):759–783. https://doi.org/10.1007/s11090-022-10246-2

4. Srivastava T, Simeni MS, Nayak G Bruggeman PJ. Self-organized Patterns at the Plasma–Liquid Anode Interface in a Helium Glow Discharge: Temporal Development and Mechanisms. *Plasma Sources Science and Technology.* 2022;31(8):085010. https://doi.org/10.1088/1361-6595/ac83ed

5. Bruggeman P, Garrick SC, Kushner MJ, Locke BR, Gardeniers JGE, Graham WG, et al. Plasma–Liquid Interactions: A Review and Roadmap. *Plasma Sources Science and Technology*. 2016;25(5):053002. https://doi.org/10.1088/0963-0252/25/5/053002

6. Kashapov N, Kashapov R, Kashapov L. Influence of the Electrolytic Cathode Temperature on the Self-Sustaining Mechanism of Plasma-Electrolyte Discharge. *Journal of Physics D: Applied Physics.* 2018;51(49):494003. https://doi.org/10.1088/1361-6463/aae334

7. Yutong Yang, Bing Sun, Shaohua Sun, Xiaomei Zhu, Jinglin Liu. Heterogeneous Liquid Discharge Cracking of n-hexadecane as a Heavy Oil Model Compound: A Way to Generate Plasma in Liquid Hydrocarbons at Low Voltage. *Journal of Analytical and Applied Pyrolysis.* 2024;177:106348. https://doi.org/10.1016/j.jaap.2024.106348

8. Akishev YuS, Grushin ME, Karalnik VB, Monich AE, Pan'kin MV, Trushkin NI, et al. Generation of Nonequilibrium Plasma in Heterogeneous Atmospheric-Pressure Gas–Liquid Media and Demonstration of Its Sterilization Ability. *Plasma Physics Reports*. 2006;32(12):1142–1152. https://doi.org/10.1134/S1063780X06120087

9. Barinov YuA, Shkolnik SM. Discharge with a Liquid Non-metallic Cathode (Tap Water) in Atmospheric-Pressure Air Flow. *Technical Physics*. 2016;86(11):155–158. https://doi.org/10.21883/jtf.2016.11.43833.1833

10. Sirotkin NA, Titov VA. Experimental Study of the Liquid Cathode Heating and Transfer of Its Components to a Gas Phase under Action of a Direct Current Discharge. *Applied Physics*. 2016;(6):25–31.

11. Averin KA, Lebedev YuA, Shakhatov VA. Some Results of Studies of a Microwave Discharge in Liquid Heavy Hydrocarbons. *Applied Physics.* 2016;(2):41–45.

12. Gaisin AlF, Gaisin FM, Zheltukhin VS, Son EE. High-Frequency Discharge with a Jet Electrolytic Electrode. *Plasma Physics Reports*. 2022;48(1):48–54. https://doi.org/10.1134/S1063780X22010068

13. Gaisin Al, Kayumov R, Kuputdinova A, Mardanov R. Plasma–Liquid Recycling of Metal Powder for 3D Printing. *Physics and Chemistry of Material Treatment.* 2023;(1):37–44. https://doi.org/10.30791/0015-3214-2023-1-37-44

14. Petryakov SYu, Mirkhanov DN, Gaisin AF, Basyrov RSh, Kashapov NF. DC Discharge between a Metal Anode and a Liquid Non-metallic Cathode. *Journal of Applied Mechanics and Technical Physics.* 2022;63(5):20–32. https://doi.org/10.15372/PMTF20220502

15. Ochkin VN. *Low-Temperature Plasma Spectroscopy*. Moscow: Fizmatlit; 2006. 472 p. (In Russ).

About the Authors:

Sergey Yu. Petryakov, Assistant Professor of the Technical Physics Department, Kazan National Research Technical University named after A.N. Tupolev – KAI (10, K.Marx Str., Kazan 420111, Russian Federation), SPIN-code, serioga_com@mail.ru

Eduard R. Belgibaev, Assistant Professor of the Technical Physics Department, Kazan National Research Technical University named after A.N. Tupolev – KAI (10, K.Marx Str., Kazan 420111, Russian Federation), SPIN-code, erbelgibaev@kai.ru

Almaz F. Gaisin, Dr.Sci. (Eng.), Associate Professor, Head of the Technical Physics Department, Kazan National Research Technical University named after A.N. Tupolev – KAI (10, K.Marx Str., Kazan 420111, Russian Federation), SPIN-code, ORCID, ScopusID, ResearcherID, almaz87@mail.ru

Rushan R. Kayumov, Cand.Sci. (Eng.), Associate Professor of the Technical Physics Department, Kazan National Research Technical University named after A.N. Tupolev – KAI (10, K.Marx Str., Kazan 420111, Russian Federation), SPIN-code, ORCID, ScopusID, ResearcherID, rushan_250189033@mail.ru

***Claimed Contributorship*:**
SYu Petryakov: writing – review & editing.
ER Belgibaev: investigation.
RR Kayumov: investigation.
AF Gaisin: supervision.

***Conflict of Interest Statement*: the authors declare no conflict of interest.**

All authors have read and approved the final version of manuscript.

Об авторах:

Сергей Юрьевич Петряков, ассистент кафедры «Техническая физика» Казанского национального исследовательского технического университета им. А.Н. Туполева – КАИ» (420111, Российская Федерация, г. Казань, ул. К. Маркса, 10), SPIN-код, serioga_com@mail.ru

Эдуард Рустемович Бельгибаев, ассистент кафедры «Техническая физика» Казанского национального исследовательского технического университета им. А.Н. Туполева – КАИ» (420111, Российская Федерация, г. Казань, ул. К. Маркса, 10), SPIN-код, erbelgibaev@kai.ru

Алмаз Фивзатович Гайсин, доктор технических наук, доцент, заведующий кафедрой «Техническая физика» Казанского национального исследовательского технического университета им. А.Н. Туполева – КАИ» (420111, Российская Федерация, г. Казань, ул. К. Маркса, 10), SPIN-код, ORCID, ScopusID, ResearcherID, almaz87@mail.ru

Рушан Рашитович Каюмов, кандидат технических наук, доцент кафедры «Техническая физика» Казанского национального исследовательского технического университета им. А.Н. Туполева – КАИ» (420111, Российская Федерация, г. Казань, ул. К. Маркса, 10), SPIN-код, ORCID, ScopusID, ResearcherID, rushan_250189033@mail.ru

Заявленный вклад авторов:
С.Ю. Петряков: написание рукописи — внесение замечаний и исправлений.
Э.Р. Бельгибаев: проведение исследования.
Р.Р. Каюмов: проведение исследования.
А.Ф. Гайсин: научное руководство.

***Конфликт интересов:* авторы заявляют об отсутствии конфликта интересов.**

Все авторы прочитали и одобрили окончательный вариант рукописи.

Received / Поступила в редакцию 26.02.2026
Reviewed / Поступила после рецензирования 25.03.2026
Accepted / Принята к публикации 01.04.2026

MECHANICS
МЕХАНИКА

UDC 624.012.45:004.8
https://doi.org/10.23947/2687-1653-2026-26-2-2285

Original Empirical Research

Machine Learning Model for Determining the 28-day Limit of Concrete Heat Release in Massive Monolithic Foundation Slabs

Tatiana N. Kondratieva, Vasilina S. Tyurina, Anton S. Chepurnenko ✉
Don State Technical University, Rostov-on-Don, Russian Federation
✉ anton_chepurnenk@mail.ru

EDN: KRLFMB

Abstract

Introduction. Thermal cracking is a significant challenge for massive monolithic structures. The primary approach to mitigating this risk is to control the overall heat release during cement hydration. Published scientific papers address the direct problem of assessing thermal stresses under given conditions, including the exothermic properties of concrete mixtures. The objective of the study is to solve the inverse problem, that is, to create a reliable machine learning model to predict the 28-day maximum allowable total heat release (Q_{max}). Implementation of the proposed approach will enable monitoring the crack resistance of massive foundation slabs.

Materials and Methods. To build the machine learning model, a training dataset of 9375 samples was created using finite element parametric modeling. The model takes into account six input parameters: foundation slab thickness, upper surface heat transfer coefficient, ambient temperature, concrete compressive strength class, initial temperature, and concrete hardening rate. To improve forecast accuracy, the CatBoost (categorical boosting) algorithm was used with hyperparameters tuned by Bayesian optimization. Forecast quality was assessed using the mean absolute error, mean absolute percentage error, mean square error, root mean square error, and the coefficient of determination. The value of the parameters for forecasting was determined by a method based on the Shapley theory.

Results. The trained model demonstrated high accuracy. The mean absolute percentage error (MAPE) on the training set was 0.52%. The coefficient of determination was 0.99 on the training dataset, and 0.98 — on the independent test dataset. This indicated good agreement within the considered ranges of input parameters. Shap (Shapley additive explanations) analysis identified two key factors for Q_{max}: heat transfer coefficient and slab thickness (with significance values of 0.57 and 0.48, respectively). The parameters ranked by significance were as follows: surface heat transfer — 96%, slab thickness — 75%, ambient temperature — 61%, hardening rate — 35%, concrete grade — 17%, and initial temperature of the mix — 14%.

Discussion. The feature correlation was dictated by both the physical processes involved and the modeling methodology. The relatively high correlation between ambient temperature and initial mix temperature ($\rho = 0.63$) is explained by the conditions under which the model was trained. During dataset construction, the maximum initial concrete temperature was constrained by the ambient temperature. The weak positive correlation between concrete grade and Q_{max} is explained by the ability of high-strength concrete structures to withstand higher temperature gradients. Shap analysis allowed us to clarify: fast hardening at high temperatures reduced Q_{max}, while slow hardening at low temperatures increased it.

Conclusion. The machine learning model developed in this study provides an auxiliary computational framework for optimizing concrete composition selection during the design process. Bayesian optimization of hyperparameters provided high quality of algorithm performance in terms of metrics: MAE = 0.67; MSE = 1.78; RMSE = 1.33; MAPE = 0.52%. Three limitations of the model are unaccounted for fast-onset concrete creep, external deformation limitations, and cases of using slabs for transfer structures.

Keywords: heat release of concrete, crack formation in concrete slabs, guaranteed prediction of crack resistance, crack resistance criterion, selection of concrete composition in design

Acknowledgements. The authors would like to thank the editors and reviewers for their attentive attitude towards the article and the valuable recommendations for its improvement.

Funding Information. The study was supported by the grant of the Russian Science Foundation no. 25-19-00164, https://rscf.ru/project/25-19-00164/

For Citation. Kondratieva TN, Tyurina VS, Chepurnenko AS. Machine Learning Model for Determining the 28-day Limit of Concrete Heat Release in Massive Monolithic Foundation Slabs. *Advanced Engineering Research (Rostov-on-Don)*. 2026;26(2):2285. https://doi.org/10.23947/2687-1653-2026-26-2-2285

Оригинальное эмпирическое исследование

Модель машинного обучения для определения предельно допустимого тепловыделения бетона к 28-м суткам в массивных монолитных фундаментных плитах

Т.Н. Кондратьева, В.С. Тюрина, А.С. Чепурненко ✉

Донской государственный технический университет, г. Ростов-на-Дону, Российская Федерация

✉ anton_chepurnenk@mail.ru

Аннотация

Введение. Температурное трещинообразование представляет собой серьезную проблему для массивных монолитных конструкций. Главный метод снижения этого риска — контроль общего тепловыделения в процессе гидратации цемента. Опубликованные научные работы посвящены решению прямой задачи оценки температурных напряжений при заданных условиях, включая экзотермию бетонных смесей. Цель исследования — решение обратной задачи, т. е. создание надежной модели машинного обучения, способной прогнозировать максимально допустимое общее тепловыделение к возрасту 28 дней (Q_{max}). Реализация предложенного подхода позволит контролировать трещиностойкость массивных фундаментных плит.

Материалы и методы. Для построения модели машинного обучения сформировали обучающий датасет из 9375 образцов путем конечноэлементного параметрического моделирования. Модель учитывает шесть входных параметров: толщину фундаментной плиты, коэффициент теплоотдачи верхней поверхности, температуру окружающей среды, класс бетона по прочности на сжатие, начальную температуру и темп твердения бетона. Для повышения точности прогнозирования использовался алгоритм CatBoost[1] с гиперпараметрами, настроенными по байесовской оптимизации. Качество прогнозирования оценивали по средней абсолютной, средней абсолютной процентной, среднеквадратичной ошибке, корню из нее и коэффициенту детерминации. Ценность параметров для прогноза определили методом, основанным на теории Шепли.

Результаты исследования. Обученная модель продемонстрировала высокую точность. Средняя абсолютная процентная ошибка (MAPE)[2] на обучающем наборе — 0,52 %. Коэффициент детерминации — 0,99 на обучающем наборе данных и 0,98 — на независимом тестовом. Это указывает на хорошее соответствие в пределах рассмотренных диапазонов входных параметров. Анализ Shap[3] выявил два главных фактора Q_{max}: коэффициент теплоотдачи и толщина плиты (значимость 0,57 и 0,48 соответственно). По значимости параметры распределились так: теплоотдача поверхности — 96 %, толщина плиты — 75 %, температура среды — 61 %, темп твердения — 35 %, класс бетона — 17 %, начальная температура смеси — 14 %.

Обсуждение. Корреляция признаков обусловлена особенностями физических процессов и моделирования. Значимый показатель для температуры окружающей среды и начальной температуры смеси ($\rho = 0,63$) объясняется условием обучения модели. При формировании датасета максимальная начальная температура бетона ограничивалась температурой окружающей среды. Слабая положительная связь класса бетона с Q_{max} объясняется способностью конструкций из высокопрочного бетона выдерживать более высокие температурные градиенты. Shap-анализ позволил уточнить: быстрое твердение при высокой температуре сокращает Q_{max}, а медленное при низкой температуре — увеличивает.

Заключение. Разработанная модель машинного обучения как вспомогательный вычислительный инструмент оптимизирует выбор состава бетона при проектировании. Байесовская оптимизация гиперпараметров обеспечила высокое качество работы алгоритма по метрикам: MAE = 0,67; MSE = 1,78; RMSE = 1,33; MAPE = 0,52 %. Три ограничения модели: неучтенные быстронатекающая ползучесть бетона, внешние ограничения деформации и случаи использования плит для трансферных конструкций.

Ключевые слова: тепловыделение бетона, трещинообразование в бетонных плитах, гарантированное прогнозирование трещиностойкости, критерий трещиностойкости, выбор состава бетона при проектировании

[1] От англ. categorical boosting — категориальное повышение.
[2] От англ. mean absolute percentage error — средняя абсолютная процентная ошибка.
[3] От англ. Shapley additive explanations — аддитивное объяснение на основе теории игр Шепли.

Благодарности. Авторы выражают благодарность редакции и рецензентам за внимательное отношение к статье и замечания, которые позволили повысить ее качество.

Финансирование. Исследование выполнено за счет гранта Российского научного фонда № 25-19-00164, https://rscf.ru/project/25-19-00164/

Для цитирования. Кондратьева Т.Н., Тюрина В.С., Чепурненко А.С. Модель машинного обучения для определения предельно допустимого тепловыделения бетона к 28-м суткам в массивных монолитных фундаментных плитах. *Advanced Engineering Research* (*Rostov-on-Don*). 2026;26(2):2285. https://doi.org/10.23947/2687-1653-2026-26-2-2285

Introduction. Crack resistance in massive monolithic reinforced concrete structures remains one of the most critical challenges in modern construction. The solution to this problem directly affects the durability and operational reliability of buildings and civil structures. Uneven temperature distribution and shrinkage deformations during concrete hardening are the key factors contributing to crack formation in early-age concrete [1]. To prevent defects, timely risk assessment is essential, and this issue is actively discussed in the literature. Thus, the algorithm from [2] allows concrete properties to be linked to the temperature field variation during hardening. The authors [3] investigate the temperature gradient in a massive monolithic slab based on field measurements, and demonstrate how the difference between the core and surface structures generates internal tensile stresses. In [4], with an emphasis on finite element modeling (FEM), the temperature gradients between the core and surface zones of the masses are analyzed. The results of three-dimensional calculations make it possible to formulate requirements for the mechanical properties of concrete and the temperature difference between the core and surface of a structure when modeling thermal stresses in the core — surface system [5]. In [6], a modern numerical phase field method is considered, which allows modeling the process of temperature crack formation and the dynamics of their development in massive concrete structures. The authors of this work introduce a criterion for comparing the calculated stresses and tensile strength of concrete.

In [7], methods for calculating the temperature field are considered. They take into account changes in the properties of concrete over time and such control measures as thermal insulation, modification of the mixture, and limitations of the temperature regime of concrete during placement. The authors [8] introduce strength criteria under thermal stress. In [9], the risk of early cracking is assessed based on temperature stresses.

The authors of the above publications address the direct problem of assessing the risk of early cracking in massive monolithic structures during construction, using parameters such as structural geometry, concrete heat release, mechanical properties, and heat transfer parameters. These approaches, based on FEM, allow for highly accurate assessment of cracking risk, but require significant computational resources, time, and detailed model tuning. This makes them unsuitable for rapid use during the preliminary selection of concrete mix design, when it is necessary to quickly evaluate numerous cement and additive options.

One of the highly efficient approach to minimizing the risk of early cracking in massive monolithic elements involves decreasing the specific heat release per 1 m^3 of concrete mix. This value is determined by the cement content in 1 m^3 of concrete mix and its mineralogical composition. To prevent early cracking in massive structures, low-exothermic cements are used, as well as additives that allow for a reduction in cement content while maintaining strength. A number of foreign researchers are focusing specifically on optimizing the composition of concrete mixtures for massive structures, paying particular attention to managing heat release during hydration through the use of supplementary cementitious materials (SCM) such as granulated blast furnace slag (GBFS), fly ash (FA), microsilica, and metakaolin [10].

Although supplementary cementitious materials significantly affect heat generation, the recommendations available in the literature on these processes remain primarily qualitative or only partially quantitative (for example, “replacing cement with 30% slag reduces heat generation by 15–20%”). Based on such approaches, it is difficult to obtain a specific numerical value for the maximum permissible heat generation Q_{max} for given geometric and climatic conditions. This difficulty is explained by the fact that the final permissible value depends on the complex interaction of a large number of parameters (slab geometry, environmental conditions, heat generation kinetics, initial mixture temperature, concrete strength class, etc.).

In [11], approaches to selecting the compositions of low-thermal mixtures with different proportions of GBFS and FA are considered. In [12], it is shown how heat generation and hardening kinetics depend on the degree of cement substitution. In [13], the effect of these factors on the development of thermal stresses is studied. The authors [14] offer a generalized review of the effect of different types of SCM on the heat of hydration. In [15], their impact on the microstructure of cement stone is considered. In [16], the formation of concrete strength at the early stages of hardening using SCM is analyzed.

Technical studies devoted to modeling the temperature field and stress development at an early age are discussed in detail in [17]. In [18], numerical methods for assessing the thermomechanical behavior of massive concrete structures are proposed. Study [19] develops this approach taking into account real heat generation parameters and mixture composition. The authors [20] write about the development of stable low-thermal compositions, including modern systems such as LC3 (Limestone Calcined Clay Cement), which demonstrate the potential for reducing the carbon footprint and hydration temperature while maintaining performance characteristics.

Practical recommendations for optimizing component proportions, including the use of ternary mixtures and low-carbon binder systems, are presented in [21]. Specific cement substitution ranges, laboratory testing methods, and examples of formulations that provide an optimal balance between reducing heat generation and maintaining strength characteristics are proposed in [22].

Despite the undeniable merits of these studies, they are typically focused on specific materials and conditions, and their results are not summarized in a compact predictive model suitable for engineering practice. Thus, a gap remains between:

– composition selection task (it is required to quickly estimate the permissible heat release);

– existing tools (labor-intensive FEM or experimental mixture preparation).

Thus, published studies offer:

– direct modeling of thermal stresses for given concrete properties (which requires considerable time and specialized software);

– prescription-based reduction of heat generation without reference to a specific permissible threshold determined by the structure geometry and heat exchange conditions.

At the composition selection stage, there is no tool available that would immediately answer the question: “What is the maximum allowable heat release by 28 days for a foundation slab with specified parameters to guarantee crack resistance?” This study aims to fill this gap. The research objective is to develop a predictive model for determining the acceptable heat release level that provides crack resistance for massive monolithic foundation slabs. Solving this problem is crucial when selecting the concrete mix for concreting massive monolithic structures. The maximum stress level (ratio of maximum tensile stress to tensile strength) is used as the crack resistance criterion. It should not exceed unity.

To achieve this goal, two sets of tasks were sequentially solved. The first was the development of an initial physicomechanical design model. Its three components are presented below:

– a one-dimensional finite element formulation of the thermal conductivity problem was selected, taking into account layer-by-layer concreting;

– the dependences of the thermophysical and mechanical properties of concrete on time and temperature (heat release function, hardening kinetics, strength, instantaneous modulus of elastic deformation) were specified;

– an algorithm for finding the maximum permissible heat release Q_{max} by the bisection method based on the criterion of a tensile stress level less than unity was implemented.

The second group of tasks involved constructing and testing a machine learning model. It had four components:

– a dataset of 9375 samples was generated through parametric finite element modeling;

– the CatBoost algorithm was selected and trained with hyperparameter optimization;

– accuracy was assessed on the training and test sets;

– shap interpretation of the model was performed.

Materials and Methods. The following physical, technical, and process parameters were selected as input:

– foundation slab thickness, h, m;

– heat transfer coefficient on the upper surface, α, W/(m^2·°C);

– ambient temperature, T_{amb}, °C;

– initial temperature of the concrete mix, T_0, °C;

– concrete compressive strength class, B, MPa (GOST 18105-2018[4]);

– hardening rate, which can take three values (1 — fast-hardening, 2 — normal-hardening, and 3 — slow-hardening).

The output variable was the maximum allowable total heat release of concrete during active cement hydration for 28 days (Q_{max}, MJ/m^3). The dataset size was 9375 samples obtained through numerical modeling and parametric analysis.

[4] GOST 18105-2018 *Concretes. Rules for control and assessment of strength*. Garant. URL: https://base.garant.ru/72932108/ (accessed: 02.03.2026).

When generating the training dataset, the thickness of the foundation slab ranged from 1 to 2 m in steps of 0.25 m. The heat transfer coefficient ranged from 3 to 23 W/(m^2·°C) with a step of 5 W/(m^2·°C). The ambient temperature ranged from 5 to 35°C with a step of 7.5°C. Concrete grades were B25, B30, B35, B40, B45. The heat release function was determined by equation [23]:

$$Q(t) = Q_{28}\, exp\left(k\left(1 - \left(\frac{28}{t-b} \right)^{x} \right) \right), \tag{1}$$

where Q_{28} — heat release in MJ/m^3 by the 28th day; t — time in days; k and x — parameters determining the heat release rate; b = 4 h — induction period.

The calculation of the thermal stress state was performed in a simplified formulation using the method given in [24]. It had previously been tested repeatedly using experimental data [25].

To calculate the temperature field, a one-dimensional heat transfer equation was used:

$$\lambda \frac{\partial^2 T}{\partial z^2} + W = \rho c \frac{\partial T}{\partial t}, \tag{2}$$

where λ — thermal conductivity coefficient; T — temperature; $W = \frac{\partial Q}{\partial t}$ — density of internal heat sources; ρ — density; c — specific heat capacity; t — time.

When calculating the temperature fields, the interaction of the slab with the soil mass, whose thickness was assumed to be constant and equal to 3 m, was taken into account. Thermophysical properties of concrete: ρ = 2400 kg/m^3, c = 1000 J/(kg·°C), λ = 2.67 W/(m·°C). Thermophysical properties of the soil: ρ_g = 1800 kg/m^3, c_g = 750 J/(kg·°C), λ_g = 0.9 W/(m·°C).

Boundary conditions for convective heat transfer were assumed on the slab surface:

$$\lambda \frac{\partial T}{\partial z} + \alpha \left(T - T_{amb} \right) = 0, \tag{3}$$

where α — heat transfer coefficient; T_{amb} — ambient temperature.

For simplicity, the temperature on the lower side of the soil mass was assumed to be equal to a constant value T_{amb}:

$$T_g(t) = T_{amb}. \tag{4}$$

The initial temperature of the entire soil mass was also assumed to be T_{amb}, and for concrete — the initial temperature of the concrete mix T_0.

Equation (2) with boundary conditions (3) and (4) was solved by the finite element method. For this, a z- and t-dimensional mesh was introduced (40 finite elements across the slab thickness, 40 finite elements across the soil thickness, with 3000 time steps over the 28-day period). The duration and layering of the structure were taken into account when calculating the temperature fields and stresses. The layer thickness was assumed to be 0.25 m, and the laying time per layer was 2 hours. Before the layer's "birth", it was assigned:

– abnormally high thermal conductivity value — λ = 1000 W/(m·°C);

– zero heat capacity, which is physically equivalent to the absence of the layer.

After "birth", the layer was assigned its actual characteristics.

Before and for 12 hours after concrete placement, the foundation slab surface was assumed to be open, with free heat exchange with the environment and a heat transfer coefficient of 23 W/(m^2·°C). After 12 hours, the heat transfer coefficient was assumed to be equal to the model input variable α. Calculations were performed using a program developed by the authors in the MATLAB environment.

When calculating the stress-strain state, the strength characteristics of concrete were represented as functions of its equivalent age t_{eq}, determined from the formula [26]:

$$t_{eq} = \frac{DM}{20}. \tag{5}$$

Here, DM — degree of maturity of concrete determined by the integral:

$$DM = \int_0^t T(\tau)\, d\tau, \tag{6}$$

where t — current moment in time, τ — integration variable, $T(\tau)$ — temperature at the moment in time τ.

The compressive strength of concrete R was determined by the formula [25]:

$$R = R_{28}\, exp\left(s\left(1 - \sqrt{\frac{28}{t_{eq} - b}} \right) \right), \tag{7}$$

where R_{28} = B + 12 — compressive strength at 28 days; t_{eq} — equivalent age in days; b = 0.167 days = 4 h — induction period; s — coefficient depending on heat release kinetics.

Three concrete hardening rates were adopted: fast, normal, and slow. Table 1 presents the values of the coefficients k and x in formula (1), as well as the coefficient s in formula (7) for the three hardening rates.

Table 1

Heat Release Rate and Kinetics Parameters versus Hardening Rate

Hardening Rate	k	x	s
Fast (1)	0.14	0.40	0.20
Normal (2)	0.19	0.51	0.35
Slow (3)	0.24	0.62	0.50

Instantaneous modulus of elastic deformation of concrete E and its tensile strength R_t were determined through the compressive strength using the formulas [25]:

$$E = 22265 \cdot \left(\frac{R}{10} \right)^{0.28}, \tag{8}$$

$$R_t = 0.29 R^{0.6}. \tag{9}$$

Formula (8) was used to calculate the modulus of elasticity for an equivalent age of concrete of at least 12 hours. For an equivalent age of less than 12 hours, value E was assumed to be zero (it was considered that concrete before the age of 12 hours was not yet a solid body and there were no thermal stresses in it).

Stress increments $\Delta\sigma_x = \Delta\sigma_y = \Delta\sigma$ at each time step at all mesh nodes were calculated using the formula [24]:

$$\Delta\sigma = \frac{E(z,t)}{1-\nu}\left(\Delta\varepsilon - \alpha_T \Delta T\right). \tag{10}$$

Here v = 0.2 — Poisson's ratio of concrete; $\alpha_T = 10^{-5}$ 1/°C — coefficient of linear thermal expansion; ΔT — change in temperature at the design node over time ΔT; $\Delta\varepsilon$ — increment in total deformation, determined by the formula:

$$\Delta\varepsilon = \frac{\alpha_T \int_{-\frac{h}{2}}^{\frac{h}{2}} E(z,t)\Delta T(z)\, dz}{\int_{-\frac{h}{2}}^{\frac{h}{2}} E(z,t)\, dz}. \tag{11}$$

For each data set [h α T_{amb} B *rate*], the maximum permissible heat release value $Q_{max} = Q_{28}$ was determined at various initial concrete mix temperatures — from 5°C to T_{amb}. According to Code Specifications 70.13330.2012 (Load-Bearing and Separating Constructions), a value of 5°C corresponds to the minimum concrete mix temperature at the start of curing. This same regulatory document establishes the maximum concrete mix temperature. It should not exceed 30°C when concreting structures with a surface modulus greater than 3. The limit for massive structures with a surface modulus less than 3 is 25°C. However, in practice, the maximum temperature requirement is rarely met, thus, in the training dataset, the maximum value of T_0 was 35°C at the same ambient temperature. Specifying T_0 higher than T_{amb} (e.g., 35°C at T_{amb} = 5°C) would be physically unreasonable and would contradict regulatory requirements. In this study, we do not consider winter concreting with preheated concrete mix, as evident from the minimum ambient temperature taken into account (5°C).

Using the bisection method, $Q_{max} = f(h, \alpha, T_{amb}, T_0, B, rate)$ was determined for the given values of the input variables from the training set. The search for value Q_{28} in the range from 20 to 520 MJ/m^3, was performed under the condition that the maximum tensile stress ratio σ/R_t was equal to unity. The bisection method was applied with an allowable error of 1% in finding Q_{max}

The range from 20 to 520 MJ/m3 was selected for the following reasons. According to [27], the specific heat release of Portland cement at the age of 28 days can take values from 120 to 513 kJ/kg. The cement content in concrete can vary from 200 to 600 kg/m^3 (SNiP 5.01.23-83[5]). As a result, for the lower limit of Q_{28}, 120 kJ/kg · 200 kg/m^3 = 24 MJ/m^3 was obtained. This value was rounded to 20 MJ/m^3. The upper limit was 513 kJ/kg · 600 kg/m^3 = 308 MJ/m^3. However, some cements, such as prestressed cements, have higher heat release than Portland cement. The difference can be as much as twofold. Therefore, the upper limit was adjusted upward.

Table 2 partially presents the resulting dataset for training the artificial intelligence model.

Table 2

Initial Data for Model Training

No.	h, m	α, W/(m^2·°C)	T_{amb}, °C	T_0, °C	B, MPa	*rate*	Q_{max}, MJ/m^3
1	1	3	5	5	25	1	302.2265625
2	1	3	5	5	25	2	325.6640625
3	1	3	5	5	25	3	298.3203125
4	1	3	5	5	30	1	310.0390625
5	1	3	5	5	30	2	335.4296875
6	1	3	5	5	30	3	310.0390625
7	1	3	5	5	35	1	317.8515625
8	1	3	5	5	35	2	343.2421875
9	1	3	5	5	35	3	321.7578125
10	1	3	5	5	40	1	323.7109375
11	1	3	5	5	40	2	351.0546875
12	1	3	5	5	40	3	333.4765625
13	1	3	5	5	45	1	327.6171875
…	…	…	…	…	…	…	…
2341	1.25	8	12.5	5	45	3	136.6992188
2342	1.25	8	12.5	6.875	25	1	168.9257813
2343	1.25	8	12.5	6.875	25	2	167.9492188
2344	1.25	8	12.5	6.875	25	3	120.0976563
2345	1.25	8	12.5	6.875	30	1	177.7148438
2346	1.25	8	12.5	6.875	30	2	175.7617188
2347	1.25	8	12.5	6.875	30	3	125.9570313
2348	1.25	8	12.5	6.875	35	1	185.5273438
2349	1.25	8	12.5	6.875	35	2	183.5742188
…	…	…	…	…	…	…	…
9366	2	23	35	35	30	3	64.67773438
9367	2	23	35	35	35	1	62.72460938
9368	2	23	35	35	35	2	78.34960938
9369	2	23	35	35	35	3	66.63085938
9370	2	23	35	35	40	1	64.67773438
9371	2	23	35	35	40	2	81.27929688
9372	2	23	35	35	40	3	69.07226563
9373	2	23	35	35	45	1	66.63085938
9374	2	23	35	35	45	2	83.72070313
9375	2	23	35	35	45	3	71.02539063

[5] SNiP 5.01.23-83. *Standard rates of cement consumption for the preparation of precast and monolithic concrete, reinforced concrete products and structures*. Moscow: Stroiizdat, 1985. (In Russ.)

As we can see, the resulting dataset consists of six input features and one target variable. To build and validate the model, the entire dataset was divided into training and test sets. The ratio generation procedure was 80/20, with multiple cross-validation performed using the Repeated k-Fold Cross-Validation system ($k = 5$) with a fixed initial random number generator parameter (random_state = 42).

Before splitting, the values were checked for correctness and the consistency of the variable dimensions. The "rate" feature was converted to an ordinal variable according to Table 1. Thus, with a total sample size of 9375 observations, the quantitative component of the training sample was 7500 records for model training and 1875 records for its validation. The test sample data was used only once to evaluate the generalization ability of the model.

The statistical characteristics of the original dataset are summarized in Table 3. The ranges of variation of the input and output parameters are also presented. Key indicators include sample size, sample mean, dispersion, and extreme values of variables. These indicators, taken together, help conduct statistical analysis of the variables, determine their dispersion relative to the core, demonstrate distribution asymmetry, and derive distribution laws for the data of the variation series.

Table 3

Original Dataset Statistical Characteristics

Parameter	h, m	α, W/(m^2·°C)	T_{amb}, °C	T_0, °C	B, MPa	*rate*	Q_{max}, MJ/m^3
Average	1.50	13.00	20.00	12.50	35.00	2.00	129.00
Standard deviation	0.35	7.07	10.61	8.39	7.07	0.82	51.36
Min	1.00	3.00	5.00	5.00	25.00	1.00	38.68
25 %	1.25	8.00	12.50	5.00	30.00	1.00	92.51
50 %	1.50	13.00	20.00	10.62	35.00	2.00	116.19
75 %	1.75	18.00	27.50	16.25	40.00	3.00	154.28
Max	2.00	23.00	35.00	35.00	45.00	3.00	35.87

Machine learning can be viewed as multidimensional interpolation. Hence, the model dependable operation is guaranteed exclusively within the domain of the input parameters represented in the training dataset. The minimum and maximum input parameter values listed in Table 3 cover the range of the most common characteristics of massive monolithic foundation slabs.

To improve the quality of the models, correlations between variables were analyzed. Gradient Boosting and CatBoostRegressor, implemented via the CatBoost library, were used to analyze data and build a model predicting the maximum permissible concrete heat generation in massive monolithic foundation slab construction. Random search and Bayesian optimization methods were used to optimize the model hyperparameters.

Gradient boosting model parameter values for regression (CatBoostRegressor):

– iterations (number of iterations) — 600–2000;

– depth (depth of learning) — 4–12;

– learning_rate (training speed) — 0.01–0.09;

– L2 reg_lambda (variable regularization coefficient of the L2 loss function) — 0.001–0.009.

The forecast quality was assessed using the metrics MAE (mean absolute error), MSE (mean square error), MAPE (mean absolute percentage error), RMSE (root mean square error), and coefficient of determination R^2.

To interpret the impact of the parameters under consideration on the model predicted value, a visual feature influence method (Shap summary plot), based on the Shapley theory, was used. This method allows evaluating not only the significance of each parameter contribution to the final model prediction but also determining the direction of its influence. Key properties were used in constructing the Shap summary plot: local accuracy, linearity, symmetry, and the absence of a missing feature effect (the contribution of a missing feature is zero). This approach demonstrates how much the prediction results change when changing the values of a specific parameter.

Research Results. Figure 1 shows the correlation between the input and output parameters of the model. With the exception of the initial concrete mix temperature and ambient temperature, there is no correlation between the remaining input parameters, indicating their independence.

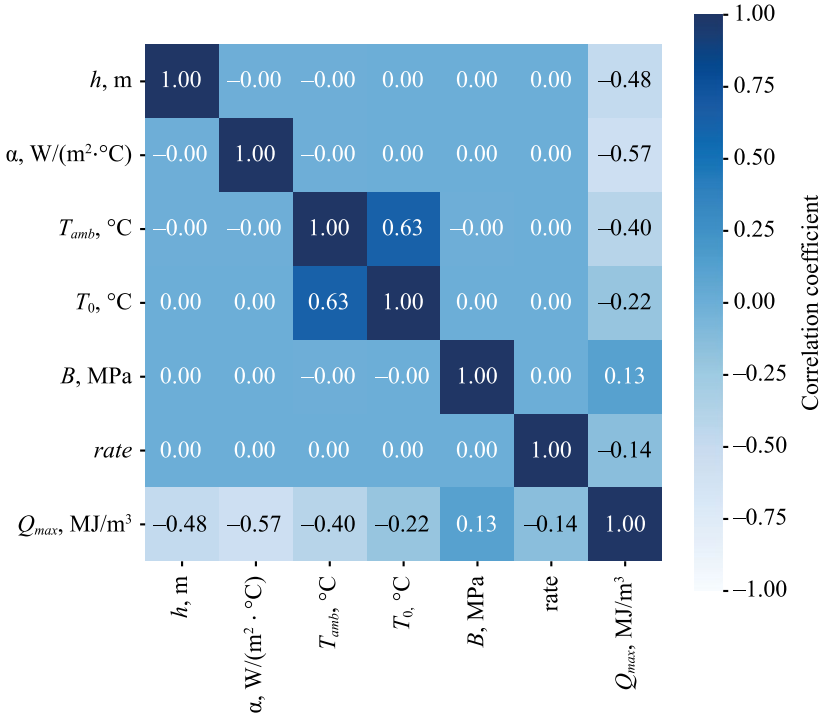

Fig. 1. Correlation matrix

The initial concrete temperature parameter has a significant correlation with the ambient temperature ($\rho = 0.63$). Weak to moderate correlation is observed between the maximum heat release of concrete and the model input parameters:

– foundation slab thickness ($\rho_{h/Q_{max}} = 0.48$);

– heat transfer coefficient on the upper surface ($\rho_{\alpha/Q_{max}} = 0.57$).

The quantitative significance of the model parameters by degree of significance is clearly shown in Figure 2:

– surface heat transfer coefficient — 96%;
– foundation slab thickness — 75%;
– ambient temperature — 61%;
– hardening rate — 35%;
– concrete grade — 17%;
– initial temperature of the concrete mix — 14%.

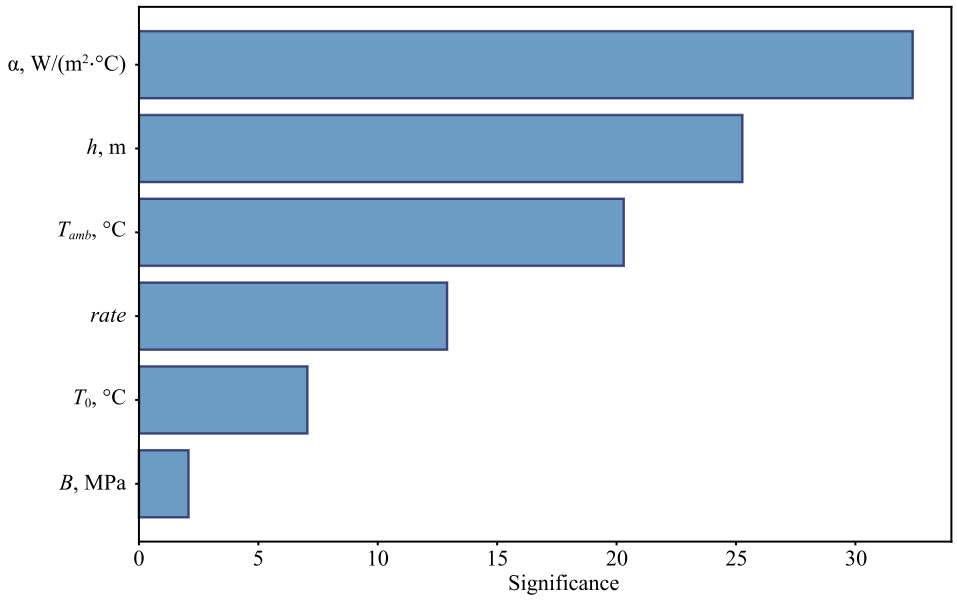

Fig. 2. Average absolute influence of features on the output variable

The optimal values of the parameters obtained during the model training process are presented in Table 4.

Table 4

Optimal Values of Model Parameters

Model	Parameter	Value
CatBoost	Iterations (number of iterations)	1488
	Depth (depth of learning)	8
	Learning rate	0.06
	L2 leaf reg (L2- regularization to prevent overfitting)	0.006

The performance metrics of the algorithm are given in Table 5.

Table 5

Model Quality Metrics

Metric/Model	Value
MAE	0.67
MSE	1.53
RMSE	1.33
MAPE, %	0.52
R^2train (training)	0.99
R^2test (testing)	0.98

Visualization of the predictions for the training and test sets is shown in Figures 3 and 4, respectively. The target values T of the output parameter are plotted on the abscissa axis, and the predicted values P are plotted on the ordinate axis. All points are located very close to the straight line $P = T$, indicating very high prediction quality.

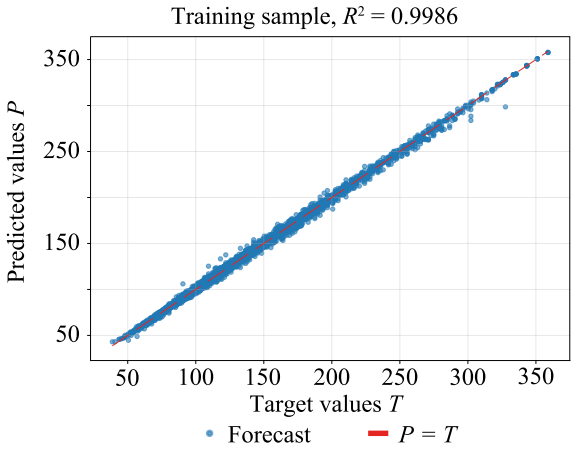

Fig. 3. Forecast error graph for the training sample

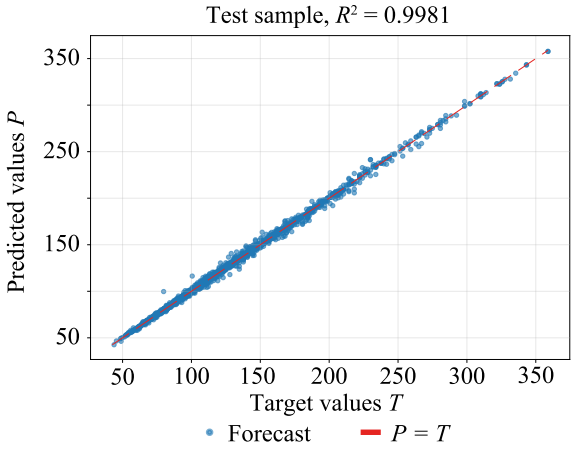

Fig. 4. Forecast error graph for the test sample

Discussion. The significant correlation between ambient temperature and the initial concrete temperature (ρ = 0.63) is explained by the fact that the upper limit of the initial concrete temperature was limited by the ambient temperature when generating the training dataset. The presence of weak or moderate correlation between the input parameters and the maximum heat release of concrete indicates a complex interaction between individual model parameters. The effect of parameters on Q_{max} can be nonlinear or interdependent. For example, slab thickness interacts with the heat transfer coefficient on the surface. With a large slab thickness, heat transfer from the surface is impeded, resulting in heat accumulation within the structure. However, with a higher heat transfer coefficient, heat is dissipated more quickly, reducing the risk of overheating.

All input parameters, with the exception of concrete grade, show a negative correlation with the output parameter Q_{max}. This is consistent with the physics of the process.

A reduction of the ambient temperature and the initial temperature of the concrete mix, while maintaining the heat release, results in a decrease in the maximum stress level. A well-known technique is adding ice to the concrete mix when working in hot climates [28]. Direct injection of liquid nitrogen into the tanks of concrete mixers is becoming an increasingly popular cooling method [29]. Consequently, with the stress level remaining constant, a decrease in the values T_{amb} and T_0 will provide an increase in the permissible value Q_{max}.

The weak positive correlation between concrete grade and maximum permissible heat release arises because the use of higher-grade concretes results in an increase in tensile strength alongside compressive strength, thereby enabling structures to tolerate larger temperature gradients.

To better interpret the forecast results, an alternative approach to analyzing model features — Shap summary plot — was also considered. This method clearly demonstrated the significance of features, the direction of their effect, and the distribution of their contributions to the target variable values (Fig. 5).

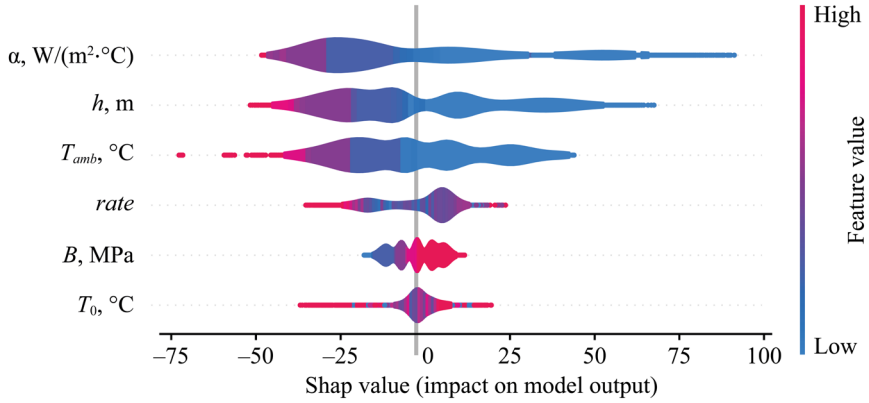

Fig. 5. Assessment of significance of model features

Analysis of the Shap-graph showed that the greatest effect on the maximum permissible total heat release was exerted by the slab thickness and the heat transfer coefficient, which determined the intensity of heat removal and the distribution of the temperature field between the core and surface zones. As the thickness of the structure of massive monolithic slabs increased, the thermal gradient grew, and the stress in the surface layers increased, which resulted in a decrease in the permissible heat release. The ambient temperature parameter demonstrated less significance. Its relationship with the rate of concrete hardening is particularly significant:

– accelerated hardening at high ambient temperatures reduces the maximum allowable heat release of concrete;

– slow hardening at low ambient temperatures increases the maximum allowable heat release of concrete.

Overall, the trend in the effect of the attributes, determined by the analysis of Shap values, coincides with the results of the correlation analysis.

Conclusion. Most input parameters in the tested model for predicting concrete maximum allowable heat release show weak correlation, indicating that each factor independently contributes to thermal stress formation during construction of massive monolithic foundation slabs. This suggests a complex, nonlinear interaction of variables, in which the risk of early cracking in massive monolithic structures is determined not by a single dominant parameter, but by their multifactorial impact.

Hyperparameter tuning via Bayesian search methods resulted in high algorithm quality as measured by the specified metrics: MAE = 0.67; MSE = 1.78; RMSE = 1.33; MAPE = 0.52%.

Shap analysis of the thermal stress state calculations for structures, considering both time-dependent and temperature-dependent strength properties of concrete, enabled the contribution of each input parameter to the final predictions to be determined. The most significant are the foundation slab thickness and the surface heat transfer coefficient. These parameters have the greatest impact on whether heat generation will reach the permissible maximum.

A comprehensive approach to predicting the maximum allowable heat release of concrete during the construction of massive monolithic foundation slabs has been developed, based on a combination of finite element modeling and machine learning methods.

The proposed machine learning model can be used at the preliminary stage of concrete mix design to estimate the maximum permissible cement consumption. However, further validation using experimental data is required for widespread implementation in design practice.

The limitations of the present model must also be acknowledged.

1. When training the model, stress levels were determined without taking into account the fast-onset creep of concrete. The true stress level, when creep is taken into account, will be lower than the calculated value, thus, the developed model predicts the permissible heat release level with some margin. Further research could focus on incorporating creep into predictive models.

2. The developed model is applicable to structures in which thermal stresses are caused solely by so-called internal deformation constraints (cross-sections remain flat despite unequal thermal deformations along the cross-section height). In addition to internal constraints, the structure may also experience external deformation constraints, such as when a slab is erected on a bedrock foundation and is rigidly connected to it, limiting the total deformations. The proposed model is not applicable to structures subject to external deformation constraints. In such structures, the risk of early crack formation can only be assessed through a comprehensive 3D finite element analysis.

3. In addition to foundations, massive slabs are used as transfer structures, providing interaction between misaligned columns in the above- and below-ground parts of a building. In this case, the boundary conditions are different (instead of interaction with the soil mass on the lower surface, heat exchange with the environment occurs). The development of predictive models for such structures can also be noted as a promising area for further research.

References

1. Puzatova AV, Dmitrieva MA, Tovpinets AO, Leitsin VN. Study of Structural Defects Evolution in Fine-Grained Concrete Using Computed Tomography Methods. *Advanced Engineering Research (Rostov-on-Don)*. 2024;24(3):227–237. https://doi.org/10.23947/2687-1653-2024-24-3-227-237

2. Klemczak B, Smolana A. Multi-Step Procedure for Predicting Early-Age Thermal Cracking Risk in Mass Concrete Structures. *Materials*. 2024;17(15):3700. https://doi.org/10.3390/ma17153700

3. Smolana A, Klemczak B, Azenha M, Schlicke D. Early Age Cracking Risk in a Massive Concrete Foundation Slab: Comparison of Analytical and Numerical Prediction Models with On-site Measurements. *Construction and Building Materials*. 2021;301:124135. https://doi.org/10.1016/j.conbuildmat.2021.124135

4. Tyurina V, Chepurnenko A, Akopyan V. Prediction of Thermal Cracking during Construction of Massive Monolithic Structures. *Applied Sciences*. 2025;15(3):1499. https://doi.org/10.3390/app15031499

5. Tzu-Han Wen, Terry TYP Yuen, Victor KS Li, Albert T Yeung. A Case Study on Early-Age Cracking of High-Strength Concrete Construction by Coupled Thermal-Mechanical Analysis and Field Monitoring. *Case Studies in Construction Materials*. 2024;21:e03436. https://doi.org/10.1016/j.cscm.2024.e03436

6. Ghasabeh M, Göktepe S. Phase-Field Modeling of Thermal Cracking in Hardening Mass Concrete. *Engineering Fracture Mechanics*. 2023;289:109398. https://doi.org/10.1016/j.engfracmech.2023.109398

7. Zhiwei Qu, Yingda Zhang, Zihao Liu, Ruizhe Si, Jie Wu. A Review on Early-Age Cracking of concrete: Causes and control. *Case Studies in Construction Materials*. 2024;21:e03848. https://doi.org/10.1016/j.cscm.2024.e03848

8. Golewski GL. The Phenomenon of Cracking in Cement Concretes and Reinforced Concrete Structures: The Mechanism of Cracks Formation, Causes of Their Initiation, Types and Places of Occurrence, and Methods of Detection — A Review. *Buildings*. 2023;13(3):765. https://doi.org/10.3390/buildings13030765

9. Klemczak B, Żmij A. Insight into Thermal Stress Distribution and Required Reinforcement Reducing Early-Age Cracking in Mass Foundation Slabs. *Materials*. 2021;14(3):477. https://doi.org/10.3390/ma14030477

10. Raghav M, Park T, Hyun-Min Yang, Seung-Yeop Lee, Karthick S, Han-Seung Lee. Review of the Effects of Additive Cementitious Materials and Chemical Additives on the Physical, Mechanical and Durability Properties of Hydraulic Concrete. *Materials*. 2021;14(23):7270. https://doi.org/10.3390/ma14237270

11. Ozyildirim HC, Sharifi M, Hossain MS. Mass Concrete Mixtures Optimized for Temperature Control and High Workability. *Transportation Research Record*. 2023;2677(6):827–836. https://doi.org/10.1177/03611981221150400

12. Saeed MK, Rahman MK, Baluch MH. Early Age Thermal Cracking of Mass Concrete Blocks with Portland Cement and Ground Granulated Blast-Furnace Slag. *Magazine of Concrete Research*. 2016;68(13):647–663. https://doi.org/10.1680/jmacr.15.00044

13. Yaseen N, Alcivar-Bastidas S, Irfan-ul-Hassan M, Petroche DM, Qazi AU, Ramirez AD. Concrete Incorporating Supplementary Cementitious Materials: Temporal Evolution of Compressive Strength and Environmental Life Cycle Assessment. *Heliyon*. 2024;10(3):e25056. https://doi.org/10.1016/j.heliyon.2024.e25056

14. Ahmed A. Assessing the Effects of Additive Cementitious Materials on Concrete Properties: A Review. *Discover Civil Engineering*. 2024;1(1):145. https://doi.org/10.1007/s44290-024-00154-z

15. Hoon Moon, Ramanathan S, Suraneni P, Chang-Seon Shon, Chang-Joon Lee, Chul-Woo Chung. Revisiting the Effect of Slag in Reducing Heat of Hydration in Concrete in Comparison to Other Supplementary Cementitious Materials. *Materials*. 2018;11(10):1847. https://doi.org/10.3390/ma11101847

16. Yingda Zhang, Xinyue Liu, Ziyi Xu, Weiguang Yuan, Yong Xu, Zuobang Yao, et al. Early-age cracking of fly ash and GGBFS concrete due to shrinkage, creep, and thermal effects: a review. *Materials*. 2024;17(10):2288. https://doi.org/10.3390/ma17102288

17. Mardmomen S, Hung Liang (Roger) Chen. Modeling the thermal and mechanical properties of early age concrete containing ground granulated blast furnace slag. *Construction and Building Materials*. 2023;401:132902. https://doi.org/10.1016/j.conbuildmat.2023.132902

18. Tahsin Alper Yikici, Hayri Sezer, Hung Liang (Roger) Chen. Modeling Thermal Behavior of Mass Concrete Structures at Early Age. *Transportation Research Record*. 2022;2676(6):536–548. https://doi.org/10.1177/03611981221075626

19. Elmahdy H, Tahwia AM, Elmasoudi I, Youssf O. Mechanical and Thermal Properties of Sustainable Low-Heat High-Performance Concrete. *Sustainability*. 2023;15(23):16139. https://doi.org/10.3390/su152316139

20. Haoyu Zeng, Ming Jin, Wenwei Li, Chang Gao, Yuefeng Ma, Qingfeng Guan, et al. Performance evolution of low heat cement under thermal cycling fatigue: A comparative study with moderate heat cement and ordinary Portland cement. *Construction and Building Materials*. 2024;412:134863. https://doi.org/10.1016/j.conbuildmat.2024.134863

21. Mokal MP, Mandal R, Nayak S, Panda SK. Efficacy of High-Volume Fly Ash and Slag on the Physicomechanical, Durability, and Analytical Characteristics of High-Strength Mass Concrete. *Journal of Building Engineering*. 2023;76:107295. https://doi.org/10.1016/j.jobe.2023.107295

22. Lallas ZN, Gombeda MJ, Mendonca F. Review of Supplementary Cementitious Materials with Implications for Age-Dependent Concrete Properties Affecting Precast Concrete. *PCI Journal*. 2023;68(6):46–64. https://doi.org/10.15554/pcij68.6-01

23. Nesvetaev GV, Koryanova YI, Yazyev BM. Autogenous Shrinkage and Early Cracking of Massive Foundation Slabs. *Magazine of Civil Engineering*. 2024;17(6):13005. https://doi.org/10.34910/MCE.130.5

24. Chepurnenko A, Nesvetaev G, Koryanova Yu, Yazyev B. Simplified Model for Determining the Stress-Strain State in Massive Monolithic Foundation Slabs during Construction. *International Journal for Computational Civil and Structural Engineering*. 2022;18(3):126–136. https://doi.org/10.22337/2587-9618-2022-18-3-126-136

25. Chepurnenko AS, Nesvetaev GV, Koryanova YuI, Shut VV, Tyurina VS. Experience of Concreting a Massive Monolithic Foundation Slab. *Construction Materials and Products*. 2025;8(5):1–15. https://doi.org/10.58224/2618-7183-2025-8-5-2

26. Nesvetaev G. V., Koryanova Yu.I., Shut V. V. Specific heat dissipation of concrete and the risk of early cracking of massive reinforced concrete foundation slabs. *Construction Materials and Products*. 2024;7(3):1–13. https://doi.org/10.58224/2618-7183-2024-7-4-3

27. Nesvetaev GV, Koryanova YuI, Khezhev TA. Heat Dissipation of Cement and Design the Composition of Concrete for Massive Structures. *Construction Materials and Products* 2025;8(1):1–11. https://doi.org/10.58224/2618-7183-2025-8-1-3

28. Sanling Zhang, Peng Liu, Lei Liu, Jingxiang Huang, Xiang Cheng, Ying Chen, et al. Heat of Hydration Analysis and Temperature Field Distribution Study for Super-Long Mass Concrete. *Coatings*. 2024;14(3):369. https://doi.org/10.3390/coatings14030369

29. Kattoof I, Hassan MS, Hasan SS. Effects of Liquid Nitrogen Cooling on the Microstructure Properties of Nano-Modified Concrete under Hot Conditions. *Arabian Journal for Science and Engineering*. 2022;47(10):12569–12583. https://doi.org/10.1007/s13369-021-06496-5

About the Authors:

Tatiana N. Kondratieva, Cand.Sci. (Eng.), Associate Professor of the Mathematics and Informatics Department, Don State Technical University (1, Gagarin Sq., Rostov-on-Don, 344003, Russian Federation), SPIN-code, ORCID, ScopusID, ResearcherID, ResearchGate, ktn618@yandex.ru

Vasilina S. Tyurina, Cand.Sci. (Eng.), Associate Professor of the Structural Mechanics and Theory of Structures Department, Don State Technical University (1, Gagarin Sq., Rostov-on-Don, 344003, Russian Federation), SPIN-code, ORCID, ScopusID, ResearchGate, vasilina.93@mail.ru

Anton S. Chepurnenko, Dr.Sci. (Eng.), Professor of the Structural Mechanics and Theory of Structures Department, Don State Technical University (1, Gagarin Sq., Rostov-on-Don, 344003, Russian Federation), SPIN-code, ORCID, ScopusID, ResearcherID, ResearchGate, anton_chepurnenk@mail.ru

Claimed Contributorship:

TN Kondratieva: investigation, data curation, formal analysis, software, visualization, writing — original draft preparation.

VS Tyurina: conceptualization, methodology, validation, writing — review & editing.

AS Chepurnenko: supervision, funding acquisition, project administration.

Conflict of Interest Statement: **the authors declare no conflict of interest.**

All authors have read and approved the final manuscript.

Об авторах:

Татьяна Николаевна Кондратьева, кандидат технических наук, доцент кафедры «Математика и информатика» Донского государственного технического университета (344003, Российская Федерация, г. Ростов-на-Дону, пл. Гагарина, 1), SPIN-код, ORCID, ScopusID, ResearcherID, ResearchGate, ktn618@yandex.ru

Василина Сергеевна Тюрина, кандидат технических наук, доцент кафедры «Строительная механика и теория сооружений» Донского государственного технического университета (344003, Российская Федерация, г. Ростов-на-Дону, пл. Гагарина, 1), SPIN-код, ORCID, ScopusID, ResearchGate, vasilina.93@mail.ru

Антон Сергеевич Чепурненко, доктор технических наук, профессор кафедры «Строительная механика и теория сооружений» Донского государственного технического университета (344003, Российская Федерация, г. Ростов-на-Дону, пл. Гагарина, 1), SPIN-код, ORCID, ScopusID, ResearcherID, ResearchGate, anton_chepurnenk@mail.ru

Заявленный вклад авторов:

Т.Н. Кондратьева: проведение исследования, курирование данных, формальный анализ, разработка программного обеспечения, визуализация, написание черновика рукописи.

В.С. Тюрина: разработка концепции, разработка методологии, валидация результатов, написание рукописи — внесение замечаний и исправлений.

А.С. Чепурненко: научное руководство, получение финансирования, административное руководство исследовательским проектом.

Конфликт интересов: **авторы заявляют об отсутствии конфликта интересов.**

Все авторы прочитали и одобрили окончательный вариант рукописи.

Received / Поступила в редакцию 14.02.2026
Reviewed / Поступила после рецензирования 06.04.2026
Accepted / Принята к публикации 25.04.2026

MECHANICS
МЕХАНИКА

UDC 620.3:616.314
https://doi.org/10.23947/2687-1653-2026-26-2-2679

Original Empirical Research

Electric-Field-Assisted Formation of a Biomimetic Organomineral Coating on Natural Human Tooth Enamel: Morphology and Surface Mechanical Properties

EDN: BVNNLU

Pavel V. Seredin[1] ✉, **Dmitry L. Goloshchapov**[1], **Tatyana A. Litvinova**[2], **Olga V. Dekhnich**[2], **Yury A. Ippolitov**[3]

[1] Voronezh State University, Voronezh, Russian Federation
[2] Belgorod National Research University, Belgorod, Russian Federation
[3] N.N. Burdenko Voronezh State Medical University, Voronezh, Russian Federation
✉ paul@phys.vsu.ru

Abstract

Introduction. The development of coatings capable of reproducing the structural and functional properties of dental enamel is of considerable interest for dental materials science and biomimetic surface engineering. Despite the progress achieved in biomimetic calcium-phosphate systems, the most common approaches still rely on multistep protocols that are highly sensitive to interfacial-layer formation conditions and do not always ensure simultaneous reduction of deposition time, control of coating morphology, and reproducible surface mechanical response. The objective of this study was to experimentally evaluate the feasibility of one-step formation of a biomimetic hybrid nHAp/PDA coating in an electric field using isolated electrodes, and to determine the effect of the deposition mode on surface morphology and the surface microhardness of the "coating–substrate" system.

Materials and Methods. Segments of native human permanent tooth enamel were used as a model of a natural apatite-containing substrate. Four surface conditions were compared: native enamel, an nHAp/AA layer formed after acid conditioning, a PDA/nHAp coating obtained by sequential deposition, and a hybrid coating formed via simultaneous electric-field-assisted mineralization and accelerated dopamine polymerization. Deposition was performed in a potentiostatic cell with isolated copper electrodes. Surface morphology was evaluated using scanning electron microscopy and atomic force microscopy (AFM). Surface mechanical response was assessed by Vickers microhardness testing at a 50 g load, AFM mapping of indentation imprints, and local nanoindentation.

Results. The one-step electric-field-assisted mode was found to produce the densest and most uniform surface layer, approximately 1 μm thick, with a minimum roughness of about 20 nm. Sample D demonstrated the highest surface microhardness values, reaching approximately 310 VHN, whereas native enamel showed values of approximately 280 VHN, sample B — about 120 VHN, and sample C — about 190 VHN. One-way ANOVA confirmed a statistically significant effect of sample type on microhardness ($p < 0.001$). AFM mapping of the indentation imprints confirmed the accuracy of optical diagonal measurements on the textured surface.

Discussion. The increased surface microhardness of the electric-field-assisted sample appears to be associated with more organized interfacial interactions involving polydopamine and a denser packing of the mineral component of the coating. At the same time, Vickers microhardness testing and AFM nanoindentation characterize different scale levels of the mechanical response and should therefore be interpreted as complementary methods.

Conclusion. It is shown that one-step formation of a hybrid nHAp/PDA coating in an electric field using isolated electrodes makes it possible to obtain a morphologically organized layer with a surface mechanical response comparable to that of intact enamel. The proposed approach appears promising for the accelerated formation of functional organomineral coatings on apatite-containing substrates.

Keywords: electric field, organomineral coating, native enamel, microhardness atomic force microscopy

Acknowledgements. The authors would like to thank the Brazilian Synchrotron Light Laboratory (LNLS), Brazilian Center for Research in Energy and Materials (CNPEM), for providing access to equipment and related experimental infrastructure for SINS and s-SNOM experiments at the Imbuia beamline of Sirius (Proposal 20252761).

Funding Information. The study was supported by the Russian Science Foundation, project No. 26-15-20057, https://rscf.ru/project/26-15-20057

For Citation. Seredin PV, Goloshchapov DL, Litvinova TA, Dekhnich OV, Ippolitov YuA. Electric-Field-Assisted Formation of a Biomimetic Organomineral Coating on Natural Human Tooth Enamel: Morphology and Surface Mechanical Properties. *Advanced Engineering Research (Rostov-on-Don)*. 2026;26(2):2679. https://doi.org/10.23947/2687-1653-2026-26-2-2679

Оригинальное эмпирическое исследование

Электрополевое формирование биомиметического органоминерального покрытия на природной эмали человеческого зуба: морфология и поверхностные механические свойства

П.В. Середин[1] ✉, Д.Л. Голощапов[1], Т.А. Литвинова[2], О.В. Дехнич[2], Ю.А. Ипполитов[3]

[1] Воронежский государственный университет, г. Воронеж, Российская Федерация

[2] Белгородский государственный национальный исследовательский университет, г. Белгород, Российская Федерация

[3] Воронежский государственный медицинский университет имени Н.Н. Бурденко, г. Воронеж, Российская Федерация

✉ paul@phys.vsu.ru

Аннотация

Введение. Разработка покрытий, способных воспроизводить структурно-функциональные свойства зубной эмали, представляет значительный интерес для стоматологического материаловедения и биомиметической инженерии поверхностей. Несмотря на развитие биомиметических кальций-фосфатных систем, наиболее распространённые подходы по-прежнему основаны на многостадийных протоколах, чувствительных к условиям формирования межфазного слоя, и не обеспечивают в полной мере одновременного сокращения времени осаждения, контроля морфологии покрытия и воспроизводимого механического отклика поверхности. Цель данной работы состояла в экспериментальной оценке возможности одностадийного формирования биомиметического гибридного nHAp/PDA-покрытия в электрическом поле с использованием изолированных электродов, а также в установлении влияния режима осаждения на морфологию поверхности и микротвёрдость системы «покрытие–подложка».

Материалы и методы. В качестве модели природной апатитовой подложки использовали сегменты нативной эмали постоянных зубов человека. Сравнивали четыре состояния поверхности: нативную эмаль; слой nHAp/AA, сформированный после кислотного кондиционирования; покрытие PDA/nHAp, полученное в последовательном режиме; гибридное покрытие, сформированное при одновременной электрополевой минерализации и ускоренной полимеризации дофамина. Осаждение выполняли в потенциостатической ячейке с изолированными медными электродами. Морфологию поверхности оценивали методами сканирующей электронной и атомно-силовой микроскопии. Поверхностный механический отклик исследовали по микротвёрдости Виккерса при нагрузке 50 г, AFM-картированию отпечатков и локальной наноиндентации.

Результаты исследования. Установлено, что одностадийный электрополевой режим обеспечивает формирование наиболее плотного и равномерного поверхностного слоя толщиной порядка 1 мкм с минимальной шероховатостью около 20 нм. Для образца D зарегистрированы наибольшие значения поверхностной микротвёрдости — около 310 VHN; для нативной эмали они составили около 280 VHN, для образца B — около 120 VHN, для образца C — около 190 VHN. Однофакторный дисперсионный анализ подтвердил статистически значимое влияние типа образца на микротвёрдость ($p < 0{,}001$). AFM-картирование отпечатков подтвердило корректность оптической оценки диагоналей на текстурированной поверхности.

Обсуждение. Повышение поверхностной микротвёрдости образца, сформированного в электрополевом режиме, связано, по-видимому, с более организованным межфазным взаимодействием при участии полидофамина и более плотной упаковкой минеральной составляющей покрытия. При этом микротвёрдость Виккерса и AFM-наноиндентация характеризуют различные масштабные уровни механического отклика и должны интерпретироваться как взаимодополняющие методы.

Заключение. Показано, что одностадийное формирование гибридного nHAp/PDA-покрытия в электрическом поле с использованием изолированных электродов позволяет получить морфологически организованный слой с поверхностным механическим откликом, сопоставимым с интактной эмалью. Предложенный подход представляет интерес для ускоренного формирования функциональных органоминеральных покрытий на апатитсодержащих подложках.

Ключевые слова: электрическое поле, органоминеральное покрытие, природная эмаль, микротвёрдость, атомно-силовая микроскопия

Благодарности. Авторы выражают благодарность «Бразильской лаборатории синхротронного излучения (LNLS)» Бразильского центра исследований в области энергетики и материалов (CNPEM) за предоставленное оборудование в рамках проекта №20252761 и возможность проведения сопутствующих исследований.

Финансирование. Работа выполнена при поддержке Российского научного фонда, проект №26-15-20057, https://rscf.ru/project/26-15-20057

Для цитирования. Середин П.В., Голощапов Д.Л., Литвинова Т.А., Дехнич О.В., Ипполитов Ю.А. Электрополевое формирование биомиметического органоминерального покрытия на природной эмали человеческого зуба: морфология и поверхностные механические свойства. *Advanced Engineering Research (Rostov-on-Don).* 2026;26(2):2679. https://doi.org/10.23947/2687-1653-2026-26-2-2679

Introduction. Enamel is a highly mineralized, hierarchically organized tissue, whose mechanical characteristics are determined by the orientation of apatite crystallites, compositional gradient, and structural anisotropy [1]. The scientific and applied significance of developing coatings capable of partially reproducing or restoring the specified characteristics is associated not only with the tasks of local regeneration of hard dental tissues, but also with the creation of controlled biomimetic systems in which the interphase organization and mechanical response are regulated by the composition and mode of formation of the coating [2].

Modern approaches to remineralization and the production of enamel-like coatings include systems based on functional inorganic materials, organic matrices, and polymer carriers [3]. A separate direction is represented by hydrogel systems that make it possible to simulate a gel-like mineralization environment and control the local delivery of ions [4]. Hydroxyapatite (nHAp) is of significant interest as a functional material with high bioactivity and structural similarity to the mineral phase of hard tissues [5]. Clinical and materials science reviews confirm the high potential of hydroxyapatite-containing systems for the prevention of damage and restoration of enamel [6]. However, the use of predominantly mineral systems does not always provide stable adhesion of the coating to the enamel surface and controlled interphase organization at the coating – substrate interface, which limits the reproducibility of the morphology and mechanical properties of the formed layer.

At the same time, polydopamine (PDA) is considered as one of the most universal interfacial components due to its pronounced adhesive properties and the ability to initiate the binding of the inorganic phase to the substrate [7]. Modern reviews devoted to the chemistry of polydopamine show that such films not only stabilize the surface, but also form a functional interphase capable of directing mineral formation [8]. Although accelerated deposition schemes involving the $CuSO_4/H_2O_2$ system can significantly reduce the time to obtain a more uniform layer [9], the problem of reproducible control of the morphology and interphase organization of hybrid coatings remains challenging. For dental applications, it is important that PDA is able to initiate mineral formation on demineralized enamel [10] and enhance the remineralization effect in one-step coatings combining polydopamine and fluoride ion [11]. It is also shown that polydopamine coatings affect the nature of nucleation of the calcium phosphate phase on the surface of mineralized substrates [12].

At the same time, alternative biomimetic matrices, including amelogenin-like systems, are capable of directing the oriented formation of an enamel-like mineral structure, but, as a rule, require more complex multistage protocols [13]. Electrokinetic approaches, on the contrary, improve the transport of ions into the thickness of the enamel, but by themselves do not solve the problem of controlled interfacial organization of a hybrid coating [14]. Previous work by the authors shows the possibility of rapid deposition of hybrid hydroxyapatite-polydopamine layers on natural enamel [15]. However, the question of whether one-step coating formation in an electric field with isolated electrodes can simultaneously ensure reduced deposition time, controlled morphology, and a reproducible surface mechanical response, remains insufficiently studied. The possibility of more localized control of deposition processes and interphase interaction under conditions of spatial separation of electrode processes, which potentially makes it possible to increase the homogeneity and structural organization of the formed hybrid layer**,** is of particular interest.

The objective of this work is to experimentally evaluate the possibility of one-step formation of a hybrid nHAp/PDA coating in an electric field using isolated electrodes, as well as to establish the effect of the deposition mode on the surface morphology and surface microhardness of the coating – substrate system.

This study answers the following questions.

1. Does a one-step electric-field-assisted mode provide a more uniform and structurally organized coating compared to sequential deposition schemes?

2. Are morphological changes in the surface accompanied by an increase in surface microhardness?

3. Are the results of Vickers microhardness and local AFM nanoindentation consistent in assessing the mechanical response of the formed hybrid layer?

Materials and Methods. The study included the following main phases.

Phase 1: Preparation of dental enamel samples. Enamel segments from permanent human teeth without visible carious lesions, cracks, or restorations were used as substrates. The enamel samples were prepared, processed, and the test series were formed according to a protocol previously described in detail for a related deposition system [15]. At the selection phase, the teeth were subjected to a cursory clinical examination to confirm the absence of carious lesions, defects, including erosions and wedge-shaped lesions, as well as visually detectable changes in the enamel structure.

Dental enamel segments measuring 5x5 mm^2 and approximately 2 mm thick were obtained using a low-speed diamond saw with water cooling. After segmentation, the sections were placed in sealed containers with constant humidity, where they were stored until the start of experimental studies.

Phase 2: Formation of series A and B. Sample A represented native enamel and served as a control group. To obtain Sample B, the native enamel surface was conditioned with 37% phosphoric acid for 30 seconds, followed by deposition of an nHAp/AA layer.

Phase 3: Formation of series C. After surface conditioning with 37% orthophosphoric acid for 30 s and subsequent alkaline activation, a hybrid layer was sequentially formed: first, dopamine was polymerized for 2 h, then nHAp was deposited. This resulted in a PDA/nHAp coating, which allowed evaluating the contribution of polydopamine to the sequential organization of the interfacial layer and mineral phase.

Phase 4: Formation of series D. Sample D was obtained in one step by combined electric field mineralization and dopamine polymerization. The coating was formed in a potentiostatic cell with insulated copper electrodes that were not in contact with the working solution. The basic one-step deposition mode included a TRIS buffer with pH = 8.5, dopamine hydrochloride — 2 mg/ml, 5 mM $CuSO_4$ $6H_2O$, 20 mmol H_2O_2, suspension with a mean particle size of 20–30 nm and a final concentration of 1 mg/ml. Aspartic acid was used as the amino acid component at a concentration of 0.1 mg/ml. The voltage was approximately 45 V, the distance between the electrodes was approximately 4 mm, and the process duration was 4 h. The use of the Cu^{2+}/H_2O_2 system was consistent with published data on the accelerated deposition of more homogeneous PDA films [8]. This design allowed for a sequential evaluation of the contributions of pretreatment, mineral phase, polydopamine, and the electric field. A separate control series without an electric field or without an accelerating system was not included in this study, which was taken into account when interpreting the results obtained.

Phase 5**:** Morphological analysis of the samples obtained. The surface morphology was examined using scanning electron microscopy (SEM) on a JEOL JSM-6700F instrument (JEOL, Japan) and atomic force microscopy using the IMBUIA-nano ultramicroscopy setup at the Brazilian Synchrotron Radiation Laboratory (LNLS), which combined scanning near-field optical microscopy (s-SNOM) with infrared radiation from the synchrotron. SEM was used to assess layer continuity, substrate overlap, and determine coating thickness on transverse cleavages. IMBUIA-nano equipment was applied to analyze nanorelief, surface profiles, and indentation geometry. Roughness was quantified using parameter Ra on 10 × 10 μm scans. The selection of these techniques and their application parameters followed the previously used protocol for studying hybrid coatings on enamel [15, 16].

Phase 6**:** Assessment of mechanical properties and statistical processing. Surface mechanical properties were assessed by Vickers microhardness using an HVS-1000 device (TIME Group Inc., China) at a load of 50 g and a holding time of 15 s; 10 measurements were performed for each sample. Since the thickness of the coating was finite, the measured value was interpreted as the surface microhardness of the composite coating-enamel system, and not as the intrinsic hardness of the isolated layer [16]. For sample D, AFM mapping of Vickers fingerprints and local analysis of DvZ/DFL curves were additionally performed.

This sequence of phases made it possible to compare the effect of pretreatment, the method of forming the hybrid layer, and the deposition mode on the morphological and mechanical characteristics of the coating-enamel system.

Statistical processing of the results was performed using one-way ANOVA analysis of variance followed by multiple pairwise comparison of groups using the Tukey test; differences were considered statistically significant at $p < 0.05$.

Research Results. In accordance with the objective of the work, the morphology of coatings formed in different modes was first analyzed, and then their surface mechanical response was assessed. A comparison of the coating formation modes showed that the type of interphase interaction affects significantly the final surface morphology (Table 1). For sample B, in which an nHAp/AA layer was deposited after pretreatment, a developed, but thin and poorly integrated layer with a thickness of about 0.4 μm was formed. According to morphometric analysis, the surface roughness in this series reached 47.8 ± 5.6 nm, while for native enamel, it was 22.1±3.4 nm. With the sequential introduction of polydopamine in sample C, the coating thickness increased to approximately 0.9 μm, and parameter Ra decreased to 25.4 ± 3.2 nm. The most pronounced effect was recorded for sample D: the one-step electric-field-assisted mode provided a more uniform substrate coverage and the formation of a dense layer 1.0–1.2 μm thick with a minimum roughness of 18.3 ± 2.6 nm, which may indicate a higher degree of morphological ordering of the coating.

According to AFM data, sample D is characterized by the presence of ordered nanoaggregates of approximately 50–80 nm in size, forming a distinct relief and denser surface packing. The presence of denser packing and ordered nanoaggregates is consistent with the assumption of a more organized interfacial structure of the coating [13, 18].

Table 1

Vickers Surface Microhardness at a Load of 50 g

Indicator	A, native enamel	B, nHAp/AA	C, PDA/nHAp	D, (electric-field-assisted)
VHN, M±SD	280±20	120±10	190±13	310±22

Microhardness measurements showed that the minimum value was found for sample B — approximately 120 VHN. For sample C, an increase in hardness to approximately 190 VHN was recorded. The maximum values were obtained for sample D — approximately 310 VHN, which is slightly higher than the average value for native enamel — approximately 280 VHN. One-way analysis of variance showed a statistically significant effect of sample type on microhardness ($p < 0.001$). According to post-hoc analysis using Tukey test, significant differences were found between all pairs of samples, with the exception of pair A–D, which indicated the absence of statistically significant differences between sample D and intact enamel under the conditions of the experiment.

To verify the mechanical properties of sample D, optical images of the Vickers indenter marks on native enamel and in the electric field series were first analyzed (Fig. 1 *a*, *b*). To more accurately determine the geometry of the marks on the textured surface, they were then further examined using AFM mapping (Fig. 1 *c, d*). According to this analysis, for sample D, values of about 320 VHN were obtained at a load of 50 g and about 290 VHN at a load of 10 g. The obtained values are consistent with the results of the optical microhardness tester and confirm that the high level of surface microhardness is not an artifact of measuring the diagonals of the indentation on the textured surface (Fig. 1 *a–d*).

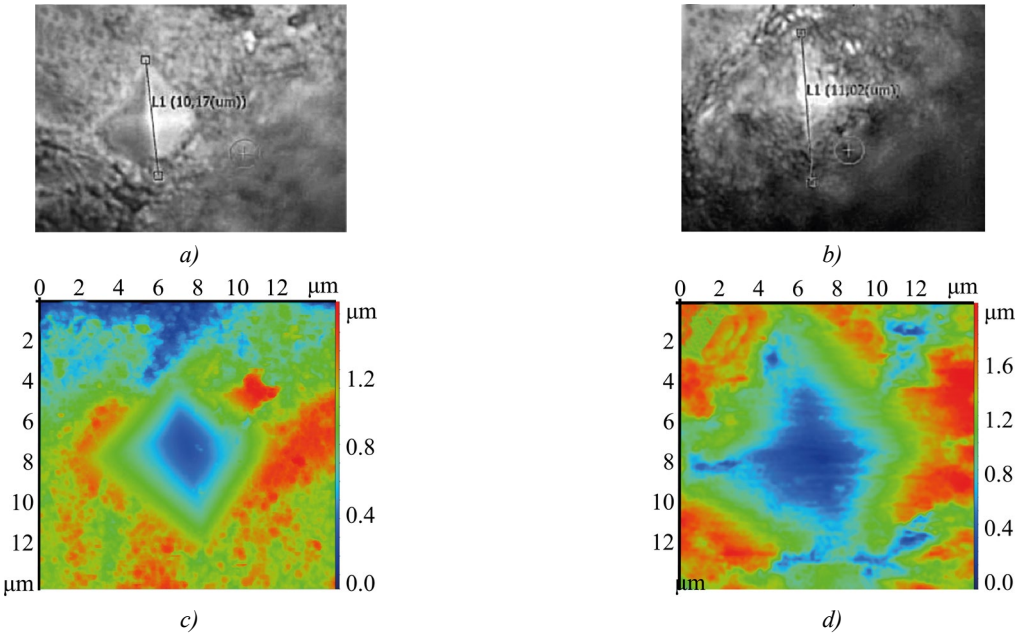

a) *b)* *c)* *d)*

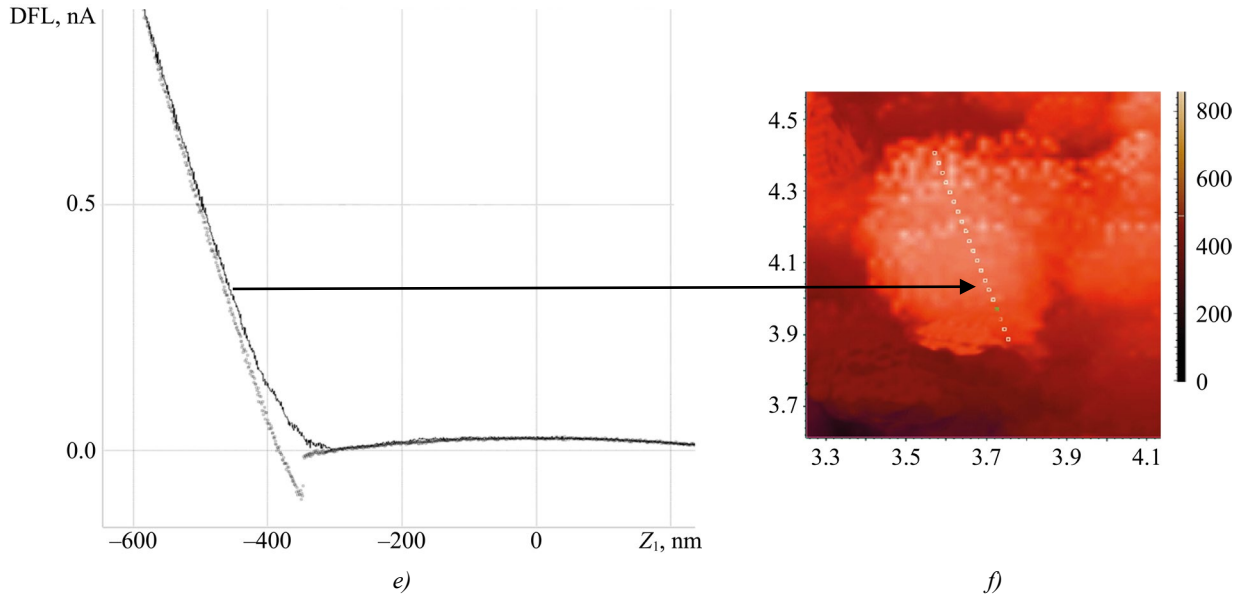

e) *f)*

Fig. 1. Mechanical characterization of native enamel and sample D: *a, b* — optical images of Vickers indenter prints; *c, d* — AFM topography of prints; *e* — typical force curve of local AFM nanoindentation; *f* — AFM image of the surface area where the force response was recorded

To further evaluate the local mechanical response of the near-surface layer, AFM nanoindentation was performed.

During local AFM nanoindentation at depths less than 50 nm, the response of the near-surface PDA-rich shell with a Young's modulus of approximately 1 GPa was recorded. A typical force curve is shown in Figure 1 *d*, and the surface region where the force response was recorded is shown in Figure 1 *f*.

Discussion. The results obtained show that the higher surface microhardness of sample D is associated not only with the presence of the mineral component, but also with the nature of the interfacial organization of the hybrid layer. This is consistent with existing data indicating that polydopamine can act as an adhesive interphase and simultaneously affect the early stages of mineral formation [8, 10, 12].

Compared to sample B, which formed a thin and poorly integrated layer after acid conditioning, and sample C, where the morphology improvement was achieved mainly due to the sequential introduction of PDA, the electric-field-assisted mode provided a denser coating packing and a more uniform substrate overlap. Probably, a more organized interphase structure and reduced localized coating heterogeneity contributed to a stable distribution of mechanical load under indentation. However, the presented data do not allow us to definitively link the increase in hardness solely to the effect of the electric field, as chemical acceleration of polymerization could also have made a significant contribution.

Crucially, the recorded microhardness characterizes not the isolated coating, but the composite coating – substrate system. Comparison of the layer thickness of approximately 1.0–1.2 μm with the strain scale under a 50 g load shows that the substrate contribution to the measured mechanical response remains significant. Therefore, the obtained values are more accurately interpreted as the surface microhardness of the system as a whole. In this sense, Vickers indentation and AFM nanoindentation data are complementary: the former reflects the integrated response of the hybrid layer and the substrate, while the latter characterizes the local properties of the near-surface PDA-rich shell [16].

The obtained data confirm that the combination of an organic interphase and a mineral component can play an important role in the formation of mechanically stable enamel-like coatings. The results are consistent with modern approaches, according to which the most promising biomimetic materials for hard tissues combine a controlled organic interphase and a mineral component [2, 17, 18]. In this context, a one-step scheme with isolated electrodes is of interest not only as a remineralization option, but also as an engineering strategy for the accelerated formation of an organized surface layer. A limitation of the study remains the lack of a dedicated control series that would allow for a complete separation of the contributions of the electric field and chemical polymerization accelerator. This makes it impossible to fully separate the contributions of the electric field and chemical accelerator to the observed changes in the morphology and mechanical properties of the coating. Further research should include dedicated control modes and an assessment of the long-term stability of the resulting coatings, including the use of a combination of machine learning methods and algorithms [19].

Conclusion. A method has been developed for the one-step formation of a hybrid nHAp/PDA coating in an electric field using insulated electrodes.

It is shown that the electric field mode provides the formation of a denser and morphologically organized layer compared to sequential deposition schemes and is accompanied by the highest values of surface microhardness — up to 310 VHN at a load of 50 g.

The results of AFM analysis of the indentations and local nanomechanical testing confirm the consistency of the mechanical response assessment at different scale levels.

The data obtained allow us to consider the proposed approach as a promising method for accelerating the formation of functional organomineral coatings on apatite-containing substrates. Further research should be focused on varying the electric field parameters, controlling the layer thickness, and assessing the long-term stability of the coating under combined chemical-mechanical effects.

References

1. Ya-Rong Zhang, Wen Du, Xue-Dong Zhou, Hai-Yang Yu. Review of Research on the Mechanical Properties of the Human Tooth. *International Journal of Oral Science*. 2014;6(2):61–69. https://doi.org/10.1038/ijos.2014.21

2. Shuxian Tang, Zhiyun Dong, Xiang Ke, Jun Luo, Jianshu Li. Advances in Biomineralization-Inspired Materials for Hard Tissue Repair. *International Journal of Oral Science*. 2021;13:42. https://doi.org/10.1038/s41368-021-00147-z

3. Jiarong Xu, Hui Shi, Jun Luo, Haiyan Yao, Pei Wang, Zhinhua Li, et al. Advanced Materials for Enamel Remineralization. *Frontiers in Bioengineering and Biotechnology*. 2022;10:985881. https://doi.org/10.3389/fbioe.2022.985881

4. Jiayi Liao, Junhong Qiu, Yarfang Lin, Zhihua Li Z. The Application of Hydrogels for Enamel Remineralization. *Heliyon*. 2024;10(13):e33574. https://doi.org/10.1016/j.heliyon.2024.e33574

5. Sudip Mondal, Sumin Park, Jaeyeop Choi, Thi Thu Ha Vu, Vu Hoang Minh Doan, Truong Tien Vo, et al. Hydroxyapatite: A Journey from Biomaterials to Advanced Functional Materials. *Advances in Colloid and Interface Science*. 2023;321:103013. https://doi.org/10.1016/j.cis.2023.103013

6. Pawinska M, Paszynska E, Amaechi BT, Meyer F, Enax J, Limeback H. Clinical Evidence of Caries Prevention by Hydroxyapatite: An Updated Systematic Review and Meta-Analysis. *Journal of Dentistry*. 2024;151:105429. https://doi.org/10.1016/j.jdent.2024.105429

7. Haeshin Lee, Dellatore SM, Miller WM, Messersmith PB. Mussel-Inspired Surface Chemistry for Multifunctional Coatings. *Science*. 2007;318(5849):426–430. https://doi.org/10.1126/science.1147241

8. Ji Hyun Ryu, Messersmith PB, Haeshin Lee. Polydopamine Surface Chemistry: A Decade of Discovery. *ACS Applied Materials and Interfaces*. 2018;10(9):7523–7540. https://doi.org/10.1021/acsami.7b19865

9. Chao Zhang, Yang Ou, Wen-Xi Lei, Ling-Shu Wan, Jian Ji, Zhi-Kang Xu. $CuSO_4/H_2O_2$-Induced Rapid Deposition of Polydopamine Coatings with High Uniformity and Enhanced Stability. *Angewandte Chemie International Edition*. 2016;55(9):3054–3057. https://doi.org/10.1002/anie.201510724

10. Yun-Zhi Zhou, Ying Cao, Wei Liu, Chun Hung Chu, Quan-Li Li. Polydopamine-Induced Tooth Remineralization. *ACS Applied Materials and Interfaces*. 2012;4(12):6901–6910. https://doi.org/10.1021/am302041b

11. Seok-Min Choi, Hee-Won Jung, Ji Hyun Ryu, Hyung-Keun You. Effect of Polydopamine and Fluoride Ion Coating on Dental Enamel Remineralization: An in vitro Study. *BMC Oral Health*. 2023;23:526. https://doi.org/10.1186/s12903-023-03221-6

12. Murari G, Bock N, Huan Zhou, Lei Yang, Liew T, Fox K, et al. Effects of Polydopamine Coatings on Nucleation Modes of Surface Mineralization from Simulated Body Fluid. *Scientific Reports*. 2020;10:14982. https://doi.org/10.1038/s41598-020-71900-3

13. Dong Wang, Jingjing Deng, Xuliang Deng, Changqing Fang, Xu Zhang, Peng Yang. Controlling Enamel Remineralization by Amyloid-Like Amelogenin Mimics. *Advanced Materials*. 2020;32(31):e2002080. https://doi.org/10.1002/adma.202002080

14. NamBeng Tay, HiongYapGan, Frederico Barbosa de Sousa, Lu Shen, Diego Figueiredo Nóbrega, Chenhui Peng, et al. Improved Mineralization of Dental Enamel by Electrokinetic Delivery of F− and Ca2+ Ions. *Scientific Reports*. 2023;13:516. https://doi.org/10.1038/s41598-022-26423-4

15. Seredin P, Goloshchapov D, Emelyanova A, Eremeev K, Peshkov Y, Shikhaliev K, et al. Rapid deposition of the biomimetic hydroxyapatite-polydopamine-amino acid composite layers onto the natural enamel. *ACS Omega*. 2024;9(15):17012–17027. https://doi.org/10.1021/acsomega.3c08491

16. Chi-Dat Lam, Soyeun Park. Nanomechanical Characterization of Soft Nanomaterial Using Atomic Force Microscopy. *Materials Today Bio*. 2025;31:101506. https://doi.org/10.1016/j.mtbio.2025.101506

17. Xinyu Luo, Jiayue Niu, Guanyu Su, Linxi Zhou, Xue Zhang, Ying Liu, et al. Research Progress of Biomimetic materials in oral medicine. *Journal of Biological Engineering*. 2023;17:72. https://doi.org/10.1186/s13036-023-00382-4

18. Seredin P, Goloshchapov D, Peshkov Ya, Potapov A, Gribanova Ya, Shikhaliev K, et al. Biomimetic Organomineral Layers with Antibacterial Properties Based on Di/Tetrahydroquinolinediol and Nanocrystalline Hydroxyapatite Deposited on Enamel Surface. *Biomaterials Science.* 2025;13(9):2444–2461. https://doi.org/10.1039/D5BM00070J

19. Kondratieva T.N., Chepurnenko A.S. Prediction of Rheological Parameters of Polymers by Machine Learning Methods. *Advanced Engineering Research (Rostov-on-Don).* 2024;24(1):36–47. https://doi.org/10.23947/2687-1653-2024-24-1-36-47

About the Authors:

Pavel V. Seredin, Dr.Sci. (Phys.-Math.), Professor, Head of the Department of Solid State Physics and Nanostructures, Voronezh State University (1, University Sq., Voronezh, 394018, Russian Federation), SPIN-code, ORCID, ScopusID, ResearcherID, ResearchGate, paul@phys.vsu.ru

Dmitry L. Goloshchapov, Cand.Sci. (Phys.-Math.), Associate Professor of the Solid-State Physics and Nanostructures Department, Voronezh State University (1, University Sq., Voronezh, 394018, Russian Federation), SPIN-code, ORCID, ScopusID, ResearcherID, ResearchGate, goloshchapov@phys.vsu.ru

Tatyana A. Litvinova, Dr.Sci. (Philol.), Professor of the Developmental and Social Psychology Department, Belgorod State National Research University (85, Pobeda Str., Belgorod, 308015, Russian Federation), SPIN-code, ORCID, ScopusID, ResearcherID, ResearchGate, centr_rus_yaz@mail.ru

Olga V. Dekhnich, Cand.Sci. (Philol.), Associate Professor of the Department of English Philology and Intercultural Communication, Institute of Intercultural Communication and International Relations, Belgorod National Research University (85, Pobeda Str., Belgorod, 308015, Russian Federation), SPIN-code, ORCID, ScopusID, ResearcherID, ResearchGate, dekhnich@bsu.edu.ru

Yury A. Ippolitov, Dr.Sci. (Med.), Professor of the Department of Pediatric Dentistry with Orthodontics, N.N. Burdenko Voronezh State Medical University (10, Studencheskaya Str., Voronezh, 394036, Russian Federation), SPIN-code, ORCID, ScopusID, ResearcherID, ResearchGate, dsvgma@mail.ru

Claimed Contributorship:

PV Seredin: conceptualization, data curation, formal analysis, investigation, methodology, project administration, validation, writing original draft preparation.

DL Goloshchapov: funding acquisition, formal analysis, investigation.

TA Litvinova: data curation, formal analysis, validation.

OV Dekhnich: writing review & editing**.**

YA Ippolitov: investigation.

Conflict of Interest Statement: **the authors declare no conflict of interest.**

All authors have read and approved the final version of manuscript.

Об авторах:

Павел Владимирович Середин, доктор физико-математических наук, профессор, заведующий кафедрой «Физика твёрдого тела и наноструктур» Воронежского государственного университета (394018, Российская Федерация, г. Воронеж, Университетская площадь, 1), SPIN-код, ORCID, ScopusID, ResearcherID, ResearchGate, paul@phys.vsu.ru

Дмитрий Львович Голощапов, кандидат физико-математических наук, доцент кафедры «Физика твёрдого тела и наноструктур» Воронежского государственного университета (394018, Российская Федерация, г. Воронеж, Университетская площадь, 1), SPIN-код, ORCID, ScopusID, ResearcherID, ResearchGate, goloshchapov@phys.vsu.ru

Татьяна Александровна Литвинова, доктор филологических наук, профессор кафедры «Возрастная и социальная психология» Белгородского государственного национального исследовательского университета (308015, Российская Федерация, г. Белгород, ул. Победы, 85), SPIN-код, ORCID, ScopusID, ResearcherID, ResearchGate, centr_rus_yaz@mail.ru

Ольга Витальевна Дехнич, кандидат филологических наук, доцент кафедры «Английская филология и межкультурная коммуникация» института межкультурной коммуникации и международных отношений Белгородского государственного национального исследовательского университета (308015, Российская Федерация, г. Белгород, ул. Победы, 85), SPIN-код, ORCID, ScopusID, ResearcherID, ResearchGate, dekhnich@bsu.edu.ru

Юрий Алексеевич Ипполитов, доктор медицинских наук, профессор кафедры «Детская стоматология с ортодонтией» Воронежского государственного медицинского университета имени Н.Н. Бурденко (394036, Российская Федерация, г. Воронеж, ул. Студенческая, 10), SPIN-код, ORCID, ScopusID, ResearcherID, ResearchGate, dsvgma@mail.ru

Заявленный вклад авторов:

П.В. Середин: разработка концепции, курирование данных, формальный анализ, проведение исследования, разработка методологии, административное руководство исследовательским проектом, валидация результатов, написание черновика рукописи.

Д.Л. Голощапов: получение финансирования, формальный анализ, проведение исследования.

Т.А. Литвинова: курирование данных, формальный анализ, валидация результатов.

О.В. Дехнич: написание рукописи внесение замечаний и исправлений.

Ю.А. Ипполитов: проведение исследования.

Конфликт интересов: **авторы заявляют об отсутствии конфликта интересов.**

Все авторы прочитали и одобрили окончательный вариант рукописи.

Received / **Поступила в редакцию** 26.05.2026
Reviewed / Поступила после рецензирования 08.06.2026
Accepted / **Принята к публикации** 15.06.2026

INFORMATION TECHNOLOGY, COMPUTER SCIENCE AND MANAGEMENT
ИНФОРМАТИКА, ВЫЧИСЛИТЕЛЬНАЯ ТЕХНИКА И УПРАВЛЕНИЕ

UDC 004.738.5
https://doi.org/10.23947/2687-1653-2026-26-2-2228

Original Empirical Research

Efficiency and Prospects of the Experimental QUIC Protocol

Jahed Rahmani, Serafim P. Sukharev ✉
Moscow Technical University of Communication and Informatics, Moscow, Russian Federation
✉ s.p.suharev@mtuci.ru

EDN: CNWWGW

Abstract

Introduction. Ensuring and improving the availability of web resources on the Internet is a crucial task for developers of information systems. A critical role in the page accessibility via the Hypertext Transfer Protocol (HTTP) is played by the protocol version and its transport-level implementation. The QUIC (Quick User Datagram Protocol Internet Connections) protocol, developed by Google, provides an increase in resource loading speed through the use of User Datagram Protocol (UDP) in HTTP/3. However, QUIC has an experimental status, and existing research primarily focuses on theoretical aspects or general performance metrics in the global network. At the same time, the following aspects remain insufficiently studied: simultaneous comparison of three protocol versions under unified controlled conditions, practical complexities of configuration and the effect of congestion control algorithms on application-level metrics, labor costs for implementation and configuration, tuning efforts, and quantifying gains under controlled condition.

These gaps create a disconnect between theoretical expectations and practical implementation. Therefore, the objective of this study is to experimentally evaluate the applied performance of HTTP/3 (QUIC) under controlled conditions on a unified testbed, including a comparison of HTTP/1.1, HTTP/2, and HTTP/3, an analysis of the impact of the CUBIC and BBR congestion control algorithms, and documentation of the HTTP/3 server configuration procedure.

Materials and Methods. A testbed was deployed based on a virtual server running the Linux operating system (OS) and the nginx web server supporting HTTP/1.1, HTTP/3 (QUIC), and congestion control algorithms CUBIC and Bottleneck Bandwidth and Round-trip propagation time (BBR). The Google Chrome browser over a 4G network was used as the client. Performance was evaluated using the Time to First Byte (TTFB) metric, file download speed, and total web page load time. Measurements were performed multiple times using Chrome DevTools and client-side scripts. The paper provides a detailed description of the server configuration process for enabling HTTP/3.

Results. The experiments showed that using HTTP/3 (QUIC) reduced the time to first byte by 23.06% and accelerated full page load by 9.5% compared to HTTP/1.1. The theoretical model predicted a TTFB reduction of 71.43% due to the combined QUIC and TLS 1.3 handshake. The observed discrepancy was attributed to the specifics of UDP traffic processing by internet service providers, the experimental status of the implementation, and mobile channel instability. When downloading large files, the CUBIC and BBR algorithms provided comparable average speeds (≈13.12 MB/s and 12.75 MB/s, respectively). However, BBR transmitted 18.2% more data within the first three seconds, demonstrating faster ramp-up to operational speed and a more stable transfer profile.

Discussion. Practical results partially differed from theoretical estimates: the observed latency reduction was lower than expected due to Transport Layer Security (TLS) implementation features, UDP traffic processing by Internet providers, and hardware characteristics. It is shown that the advantages of QUIC/HTTP/3 are most noticeable under conditions of multiple short requests and high latency. The advantage of BBR over CUBIC is realized not in long-duration transfers, but when loading numerous small page resources — a typical web interaction scenario. To improve the reliability of performance evaluation, further experiments are planned under various network conditions, protocol implementations, and geographically distributed clients.

Conclusion. The study confirmed the advantages of HTTP/3 (QUIC): TTFB decreased by 23.06%, and page load time by 9.5%. However, the theoretical model predicted a greater reduction, indicating the influence of implementation and

network environment factors. The comparison of CUBIC and BBR revealed the advantage of BBR when transferring small-sized files. Despite the complexity of HTTP/3 configuration, the transition is justified for services with a significant number of resources. The experimental limitations indicate the need for further studies under different network scenarios.

Keywords: QUIC, HTTP/3, transport layer protocols, congestion control algorithms, BBR, CUBIC, TTFB, web performance

Acknowledgments. The authors sincerely acknowledge the Department of Network Information Technologies and Services, Moscow Technical University of Communications and Informatics, for their support in conducting this research. Special thanks are expressed to the journal editorial team for their attentive attitude to the manuscript, prompt support in the preparation of the publication, and organization of the peer-review process.

For Citation. Rahmani J, Sukharev SP. Efficiency and Prospects of the Experimental QUIC Protocol. *Advanced Engineering Research* (*Rostov-on-Don*). 2026;26(2):2228. https://doi.org/10.23947/2687-1653-2026-26-2-2228

Оригинальное эмпирическое исследование

Эффективность и перспективы экспериментального протокола Quick User Datagram Protocol Internet Connections

Д. Рахмани ✉, С.П. Сухарев ✉
Московский технический университет связи и информатики, г. Москва, Российская Федерация
✉ s.p.suharev@mtuci.ru

Аннотация

Введение. Обеспечение и повышение доступности веб-ресурсов в сети Интернет представляет собой актуальную задачу для разработчиков информационных систем. Критическую роль в доступности страниц по протоколу Hypertext Transfer Protocol (HTTP) играет версия протокола и его реализация на транспортном уровне. Протокол Quick User Datagram Protocol Internet Connections (QUIC), разработанный компанией Google, позволяет добиться прироста скорости загрузки ресурсов за счёт применения протокола User Datagram Protocol (UDP) в HTTP/3. Однако QUIC имеет статус экспериментального, а в существующих исследованиях основное внимание уделяется теоретическим аспектам или общим показателям в глобальной сети. При этом остаются недостаточно изученными: одновременное сопоставление трёх версий протокола в единых контролируемых условиях, практические сложности конфигурирования и влияние алгоритмов контроля перегрузок на прикладные метрики; трудозатраты на внедрение и настройку; усилия по настройке и количественная оценка выигрыша в контролируемых условиях. Указанные пробелы формируют разрыв между теоретическими ожиданиями и практической реализацией. Поэтому целью данного исследования явилась экспериментальная оценка прикладной эффективности HTTP/3 (QUIC) в контролируемых условиях на едином тестовом стенде, включающая сопоставление HTTP/1.1, HTTP/2, HTTP/3, анализ влияния алгоритмов контроля перегрузок CUBIC и BBR и документирование процедуры конфигурирования HTTP/3-сервера.

Материалы и методы. Для исследования был развёрнут тестовый стенд на основе виртуального сервера под управлением операционной системы (ОС) Linux и веб-сервера nginx с поддержкой HTTP/1.1, HTTP/3 (QUIC), а также алгоритмов контроля перегрузок CUBIC и Bottleneck Bandwidth and Round-trip propagation time (BBR). В качестве клиента использовался браузер Google Chrome в сети 4G. Производительность оценивалась по метрике Time to First Byte (TTFB), скорости загрузки файлов и времени полной загрузки веб-страницы. Замеры выполнялись многократно с использованием Chrome DevTools и клиентских скриптов. В статье подробно описан процесс настройки сервера для работы с HTTP/3.

Результаты исследований. Эксперименты показали, что применение HTTP/3 (QUIC) сокращает время до первого байта на 23,06 % и ускоряет полную загрузку страницы на 9,5 % по сравнению с HTTP/1.1. Теоретическая модель прогнозировала снижение TTFB на 71,43 % за счёт объединённого рукопожатия QUIC и TLS 1.3. Выявленное расхождение обусловлено особенностями обработки UDP-трафика операторами, экспериментальным статусом реализации и нестабильностью мобильного канала. При скачивании крупных файлов алгоритмы CUBIC и BBR обеспечили сопоставимую среднюю скорость (≈13,12 и 12,75 МБ/с соответственно). Однако BBR за первые три секунды передал на 18,2 % больше данных, демонстрируя более быстрый выход на рабочую скорость и стабильный профиль передачи.

Обсуждение. Практические результаты частично расходятся с теоретическими оценками: снижение задержки оказалось меньше прогнозируемого из-за особенностей реализации Transport Layer Security (TLS), обработки UDP-трафика провайдерами и характеристик оборудования. Показано, что преимущества QUIC/HTTP/3 наиболее заметны при множественных коротких запросах и высоких задержках. Преимущество BBR перед CUBIC

реализуется не на длительных передачах, а при загрузке множества небольших ресурсов страницы — типичного сценария веб-взаимодействий. Для повышения достоверности оценки производительности планируется расширение экспериментов с различными сетевыми условиями, реализациями протокола и географически распределёнными клиентами.

Заключение. Исследование подтвердило преимущество HTTP/3 (QUIC): TTFB снизился на 23,06 %, время загрузки страницы — на 9,5 %. При этом теоретическая модель прогнозировала более существенное сокращение, что указывает на влияние особенностей реализации и сетевой среды. Сравнение CUBIC и BBR выявило преимущество BBR при передаче файлов малого объёма. Несмотря на сложность конфигурирования HTTP/3, переход оправдан для сервисов со значительным количеством ресурсов. Ограничения эксперимента требуют расширения исследований в различных сетевых сценариях.

Ключевые слова: QUIC, HTTP/3, протоколы транспортного уровня, алгоритмы контроля перегрузок, BBR, CUBIC, TTFB, производительность веб-приложений

Благодарности. Авторы выражают искреннюю признательность сотрудникам кафедры «Сетевые информационные технологии и сервисы» Московского технического университета связи и информатики за поддержку в проведении исследования. Особая благодарность выражается редакционной команде журнала за внимательное отношение к рукописи, оперативное сопровождение подготовки публикации и организацию процесса рецензирования.

Для цитирования. Рахмани Д., Сухарев С.П. Эффективность и перспективы экспериментального протокола Quick User Datagram Protocol Internet Connections. *Advanced Engineering Research* (*Rostov-on-Don*). 2026;26(2):2228. https://doi.org/10.23947/2687-1653-2026-26-2-2228

Introduction. Today, available web resources constitute a valuable knowledge base and are an integral part of the operations of organizations across different sectors. The development of the online advertising market is a key factor in the growth of the entire advertising industry in the Russian Federation [1]. Providing comfortable interaction of the end user with information systems on the Internet is a priority task for companies of any scale. The research shows that even a slight increase in web page performance can have a significant positive impact on the financial performance of a business [2, 3].

Data is transmitted to the World Wide Web (WWW) via the HTTP protocol, which has three main versions [4]. Web server support for modern protocols can favorably affect the user experience when browsing websites [5]. HTTP/3 is based on the Quick User Datagram Protocol Internet Connections (QUIC) protocol [6], which was developed as an alternative to the Transmission Control Protocol (TCP) used in previous versions of HTTP [7], in order to increase the speed and security of Internet connections.

Analysis of the current literature identifies both the progress made and major discrepancies within the findings. In [8], the results of the large-scale deployment of QUIC in the Google infrastructure are presented: the delay in search service responses decreased by 8.0% for desktop platforms and 3.6% for mobile users, the frequency of video playback interruptions decreased by 18.0% and 15.3 %, respectively. The authors note that the gain grows with an increase in the Round-Trip Time (RTT) metric and packet loss, but it turns out to be lower than theoretically expected, including due to implementation limitations and the specifics of operators' network equipment. This means that transferring conclusions to moderate-scale deployments requires independent experimental verification.

The authors [9] compared QUIC and TCP in a laboratory environment with a locally installed server and found minimal differences between HTTP/2 and HTTP/3 in multithreaded transmission. In another article, [10], on the contrary, in a similar scenario with a loss rate of 12%, a five-fold advantage of HTTP/3 over HTTP/2 was recorded. This contradiction is due to the difference in network conditions. It remains unresolved in relation to regular deployment without simulated network disruptions. At the same time, the works do not include HTTP/1.1 as a starting point for comparisons and do not contain data on the TTFB metric.

In [11], client-server protocols were investigated from the standpoint of fault tolerance and security under real network conditions. It was found that when switching to QUIC, the actual performance gain varied depending on the configuration of the intermediate network equipment. This conclusion is consistent with the observation of the authors [8] about the discrepancy between the theoretically expected and practically achieved gains from the protocol.

Review paper on the prospects of HTTP/3 and QUIC [12] shows that the combined QUIC handshake and built-in TLS 1.3 encryption form the theoretical basis for significantly reducing latency. However, the researchers point to difficulties in practical deployment due to the immaturity of protocol support in server software. Moreover, the paper does not provide a specific configuration procedure.

Paper [13] has documented that 19.38% of requests in a large mobile web service fall into the slow-start phase, where the statically set initial congestion window size does not correspond to the actual bandwidth. This study thus confirms that the slow start mechanism of the CUBIC algorithm creates measurable delays when transferring small files, which are typically used to make up web pages, which serves as a basis for studying BBR as an alternative solution.

Paper [14] substantiated a BBR algorithm that used channel capacity and propagation delay estimation instead of packet loss as a congestion signal. Deployment of BBR in Google B4 backbone network resulted in throughput increases of 2–25 times compared to CUBIC. However, the paper analyzed aggregated throughput metrics, while the dynamics of the transmission rate over time (the sawtooth profile characteristic of CUBIC compared to the more stable BBR profile) were not experimentally visualized.

Study [15] documented that in QUIC implementations, the CUBIC algorithm remained the default, while BBR was provided as an option. Experiments conducted by the authors in the ns-3 simulator showed that BBR provided higher throughput compared to CUBIC at high channel delays, but at low bandwidth it was inferior to it in terms of the number of lost packets. However, the paper does not analyze the dynamics of the transmission rate over time, which leaves open the question of the stability of the speed profile of each of the algorithms.

This review highlights three interrelated gaps. Existing papers do not compare HTTP/1.1, HTTP/2, and HTTP/3 simultaneously under consistent, controlled conditions: most studies are limited to comparing HTTP/2 and HTTP/3. Protocol performance data varies significantly depending on testing conditions, and benchmarking under normal conditions without proxy servers or artificially introduced packet loss in an emulated network environment is underrepresented. Furthermore, the practical procedure for configuring a standard web server for HTTP/3 is not documented in the scientific literature. Thus, the research gap lies in the lack of studies that, within a unified methodological framework, simultaneously: compare HTTP/1.1, HTTP/2, and HTTP/3 under controlled conditions; document the procedure for configuring a standard web server to support HTTP/3; evaluate the impact of the CUBIC and BBR congestion control algorithms on applied web access metrics. Addressing this gap determines the objective and tasks of this study.

The research objective was to experimentally evaluate the application performance of HTTP/3 (QUIC) under controlled conditions on a single testbed through comparing HTTP/1.1, HTTP/2 and HTTP/3, analyze the impact of the CUBIC and BBR congestion control algorithms, and document the HTTP/3 server configuration procedure.

To achieve this objective, the following tasks were completed:

– deploy a testbed supporting HTTP/1.1, HTTP/2, and HTTP/3;

– document the web server configuration sequence for HTTP/3;

– measure and compare TTFB and full page load time for different HTTP versions;

– compare the behavior of the CUBIC and BBR algorithms when transferring a large file;

– interpret the results obtained taking into account theoretical expectations and published research.

Materials and Methods

Equipment. To conduct the experiments, a testbed was prepared consisting of a virtual machine rented from the IXcellerate data center in Moscow. The following specifications were used: one 2.4 GHz Virtual Central Processing Unit (vCPU), 2 GB of RAM, and a personal workstation running Ubuntu 22.04.5 Long-Term Support (LTS). Both devices had internet access. The virtual machine had a static Internet Protocol (IP) address with the domain name serafimdev.com.

Research Plan. Three experiments were planned for this study: comparison of connection establishment speed using HTTP/1.1, HTTP/2, and HTTP/3; comparison of test page loading speed using HTTP/1.1, HTTP/2, and HTTP/3; and comparison of data transfer speed using the CUBIC and BBR congestion control protocols.

The experiments were performed in the following sequence. On a virtual machine, a web server (nginx) was installed and configured with three subdomains, each responsible for serving traffic over one protocol version: HTTP/1.1, HTTP/2, and HTTP/3. To assess connection speed, the TTFB metric was measured on each subdomain. A web page template consisting of 32 files was then uploaded to the server, and the time it took to fully load was measured. For an experiment

comparing congestion control algorithms, a 3 GB file was uploaded to the server. Downloads were performed sequentially with the CUBIC algorithm active (default configuration) and after switching to BBR, in both cases recording the transfer rate profile. Subsequent analysis of the research findings included a comparison of the experimental data with theoretical values obtained from the model presented below.

When using HTTP/1.1 with TLS 1.2 encryption, the total time to send the first byte of data consisted of several connection initialization stages (Table 1), each of which took a certain number of round trips between network nodes. Thus, the expected initialization time for a secure connection via HTTP/1.1 was obtained using formula (1).

Table 1

HTTP/1.1 Connection Initialization Steps

Step	Assignment	Contribution to initialization time
1	Three-way Handshake of TCP protocol	1.5 RTT
2	ClientHello/ServerHello message exchange with protocol cipher negotiation TLS [16]	1 RTT
3	Transferring certificate and session keys for TLS protocol [16]	1 RTT

$$T_{TCP} = 1.5\,RTT + 1\,RTT + 1\,RTT = 3.5\,RTT. \quad (1)$$

The QUIC protocol combined the transport and cryptographic handshake based on TLS 1.3, reducing the total cost to 1 RTT. From formula (2), we obtained the theoretical gain in terms of the TTFB metric.

$$\mu = \frac{T_{TCP} - T_{QUIC}}{T_{TCP}} \cdot 100\% = \frac{3.5\,RTT - 1\,RTT}{3.5\,RTT} \approx 71.43\%. \quad (2)$$

Tooling. All measurements were performed using a 4G mobile internet connection. Nginx version 1.27.4 was installed on the virtual machine, as support for HTTP/3 connections was added to the Nginx web server starting with version 1.25.0[1].

For the experiments, three subdomains were configured: http1.serafimdev.com, http2.serafimdev.com, and http3.serafimdev.com, with Let's Encrypt certificates for the HTTP/1.1, HTTP/2, and HTTP/3 protocols, respectively. Certbot, a software tool for automating certificate management, was used for the configuration.

The server settings were verified using Google Chrome developer tools. When exchanging data over HTTP/3, the protocol column should display h3 values (Fig. 1). These tools also provided information for assessing web page performance and component loading speeds. They were used to measure full page load times.

Resource	Status	Protocol
images.html	200	h3
1.jpg	200	h3
2.jpg	200	h3
3.jpg	200	h3
4.jpg	200	h3
5.jpg	200	h3

Fig. 1. HTTP/3 protocol in developer tools

The TTFB metric was obtained using a JavaScript script that performed server requests and recorded the metric values. A similar approach was applied to collect the data needed to visualize graphs of resource utilization rates by various overload control algorithms. When making measurements, it was important to disable query caching in the developer's tools to eliminate the impact of the local cache on the results. The collected data was processed using the numpy and matplotlib libraries for Python. To integrate the non-standard BBR overload control algorithm into the operating system kernel — Ubuntu 22.04.5 LTS was used in this study — it was necessary to download the corresponding module — sudo modprobe tcp_bbr and change the value of the variable — sudo sysctl -w net.ipv4.tcp_congestion_control=bbr.

[1] Mukhin S. *How to Enable HTTP/3 in NGINX.* SergeyMukhin.com. URL: https://sergeymukhin.com/blog/kak-vklyuchit-http3-v-nginx (accessed: 11.10.2025). (In Russ.)

Procedures. The Internet connection is often unstable; therefore, a statistical analysis of the results was applied to avoid the impact of outliers on the results of the study. In experiments to measure the connection initialization time and page loading speed, measurements for each protocol were performed 20 times. Then, the interquartile range method was applied to identify outliers, and the arithmetic mean — to aggregate the remaining measurements into the final result. The upper and lower limits of emissions were determined from formulas (3) and (4).

$$\text{Lower limit} = Q1 - 1.5 \times IQR; \quad (3)$$

$$\text{Lower limit} = Q3 + 1.5 \times IQR, \quad (4)$$

where $Q1$ — 25th percentile, $Q3$ — 75th percentile, $IQR = Q3 - Q1$.

When analyzing the transfer rate, the JavaScript XMLHttpRequest module was used for measurements, which provided the number of bytes downloaded every unequal number of milliseconds. Due to the small gap between measurements and the instability of the network, the raw data contained a large number of outliers. To obtain more visual graphs, the results were smoothed using a moving mean with a window of 31 dimensions.

Research Results

HTTP/3 Server Setup Procedure. Documentation of the testbed configuration process was an independent research task. To organize access to web content via HTTP/3, a server with an operating system and access to it was required. The study used a server with the Ubuntu 22.04.5 LTS operating system with remote SSH access. During the setup process, a key difficulty was identified when organizing an HTTP/3 web server — the need to use the nginx mainline repository instead of the standard one.

The default Ubuntu 22.04.5 LTS repository contains nginx version 1.18, while HTTP/3 support has been available since version 1.25.0. To install the latest version, it was necessary to add the main repository with the latest software versions to the system using the commands shown in Figure 2.

```
curl https://nginx.org/keys/nginx_signing.key | gpg --dearmor \
  | sudo tee /usr/share/keyrings/nginx-archive-keyring.gpg >/dev/null

echo "deb [signed-by=/usr/share/keyrings/nginx-archive-keyring.gpg] \
http://nginx.org/packages/mainline/ubuntu `lsb_release -cs` nginx" \
  | sudo tee /etc/apt/sources.list.d/nginx.list
```

Fig. 2. Adding the nginx mainline repository to the operating system's package sources list

These instructions write the key used to sign packages from the new repository to the system's trusted keystore: /usr/share/keyrings and add the address of the nginx mainline repository to the package sources list /etc/apt/sources.list.d, specifying the path to the package signing location. After completing these steps, installing nginx via the apt package manager will use the repository that contains all the latest versions of the service.

Since encryption is built into the QUIC protocol, a certificate and domain name are mandatory requirements when using HTTP/3. In previous versions of the HTTP protocol, TLS encryption is a separate layer, which adds latency when establishing a connection but allows for unsecured data exchange. Unencrypted HTTP is suitable for networks where encryption is already provided via a Virtual Private Network (VPN). Therefore, using HTTP/3 in such networks necessitates the configuration of certificates. The testbed used issued certificates from Let's Encrypt using certbot, a certificate automation software.

Additionally, changes must be made to the site configuration file (Fig. 3). The key lines in the configuration are lines 3, 10, 12, and 16. Line 12 contains an instruction enabling the use of the HTTP/3 protocol. Line 16 specifies the Alt-Svc header. If this header is present in the server's response, the client switches to using HTTP/3 (if supported). Therefore, lines 2 and 3 specify support for standard TCP connections and UDP over QUIC. Subsequently, the header value is cached, and no header exchange occurs over TCP. Since QUIC operates on TLS version 1.3, this version is explicitly specified on line 10.

```
server {
    listen 443 ssl;
    listen 443 quic reuseport;

    server_name http3.serafimdev.com;

    ssl_certificate     /etc/letsencrypt/live/http3.serafimdev.com/fullchain.pem;
    ssl_certificate_key /etc/letsencrypt/live/http3.serafimdev.com/privkey.pem;

    ssl_protocols TLSv1.3;

    http3 on;
    quic_gso on;
    quic_retry on;

    add_header Alt-Svc 'h3=":443"; ma=86400';

    root /var/www/http3.serafimdev.com;
    index index.html;

    location / {
        try_files $uri $uri/ =404;
    }
}

server {
    listen 80;
    server_name http3.serafimdev.com;
    return 301 https://$host$request_uri;
}
```

Fig. 3. Nginx configuration file for HTTP/3 site

TTFB. TTFB is a metric that shows how long it takes from sending a request to the start of resource transfer. A JavaScript script was used to conduct the measurements. The resulting values are presented in Table 2.

Table 2

TTFB Measurements for Different HTTP Protocol Versions

HTTP/1,1, ms	HTTP/2, ms	HTTP/3, ms
20.5	80.3	69.4
28.3	28.4	26.8
38.3	24.4	29.1
27.0	30.4	16.3
41.3	29.1	21.1
24.8	25.7	17.5
30.1	33.2	18.4
26.7	30.4	23.2
30.9	46.0	22.4
24.7	15.6	23.1
29.2	26.0	24.1
33.3	23.6	19.7
25.9	26.1	24.3
34.7	26.3	23.7
33.3	25.1	23.5
33.3	32.5	25.4
25.9	26.5	26.4
29.4	19.7	22.6
25.0	26.9	24.5
22.7	28.6	15.8

The following values were obtained:

– HTTP/1.1: no outliers, mean 29.27 ms;

– HTTP/2: three outliers, mean 27.23 ms;

– HTTP/3: one outlier, mean 22.52 ms.

$$\mu = \frac{29.27 - 22.52}{29.27} \cdot 100\% \approx 23.06\%. \quad (5)$$

According to calculations from formula (5), the experiment showed that the transition from HTTP/1.1 to HTTP/3 with the QUIC protocol provided a reduction in time to first byte (TTFB) by 23.06%.

Page Load Time. To study the impact of using the QUIC protocol on the loading speed of a typical web page, a page template consisting of 32 files, totaling 728 kilobytes, was found in open sources. The values obtained are presented in Table 3**.**

Table 3

Page Load Time for Different Versions of HTTP Protocol

HTTP/1,1, ms	HTTP/2, ms	HTTP/3, ms
1140	1060	781
826	794	699
1160	953	630
726	851	733
731	940	622
757	814	652
746	846	669
815	908	978
791	747	764
834	832	917
709	1060	725
830	868	601
951	744	890
1020	785	643
677	725	906
806	711	739
1100	695	647
743	922	687
775	750	652
739	658	678

The following values were obtained:

– HTTP/1.1: 3 outliers, mean 792.7 ms;

– HTTP/2: no outliers, mean 833.15 ms;

– HTTP/3: 1 outlier, mean 717.63 ms.

$$\mu = \frac{792.7 - 717.63}{792.7} \cdot 100\% \approx 9.5\%. \quad (6)$$

Calculation from formula (6) shows a reduction in page load time of 9.5% when using HTTP/3 and QUIC compared to HTTP/1.1 and TCP.

Transfer Speed. A 3 GB file was used for the experiment, transmitted via the HTTP/2 protocol. The choice of HTTP/2 for this experiment was driven by methodological considerations: the comparison aimed to isolate the effect of the congestion control algorithm on the throughput profile, without additional effects from the transport protocol. The HTTP/3 (QUIC) protocol implements its own congestion control stack on top of UDP, while HTTP/2 uses the standard TCP stack of the operating system kernel, in which switching between CUBIC and BBR algorithms was performed directly through Linux kernel parameters without changing the application-layer protocol logic. A file was downloaded using the CUBIC and BBR congestion control algorithms. Figures 4 and 5 show the initial fragments of the download speed graphs using CUBIC and BBR, respectively.

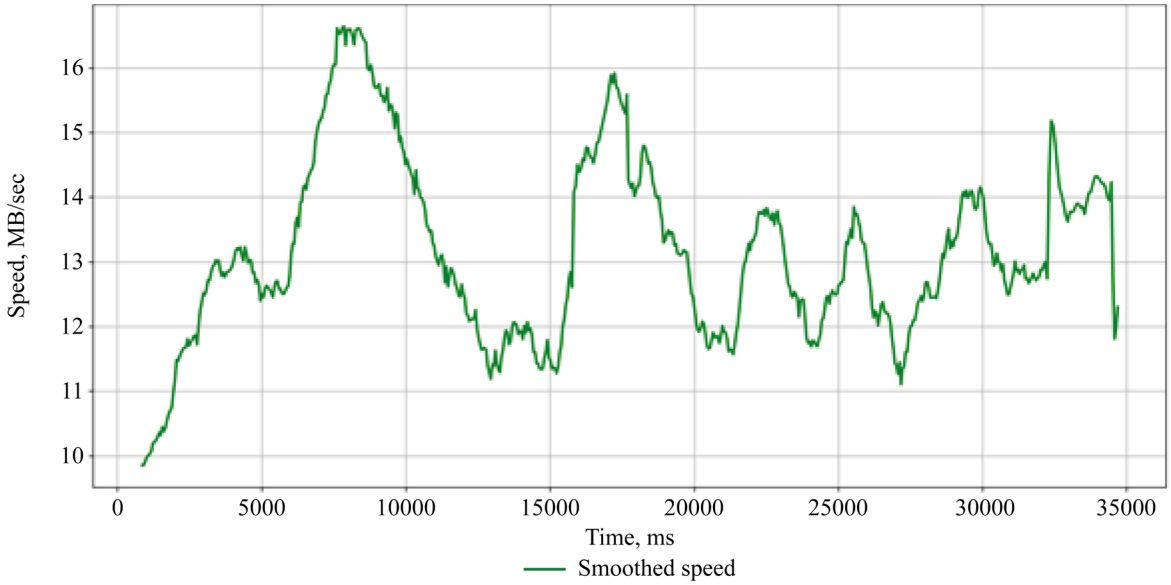

Fig. 4. Download speed when using CUBIC

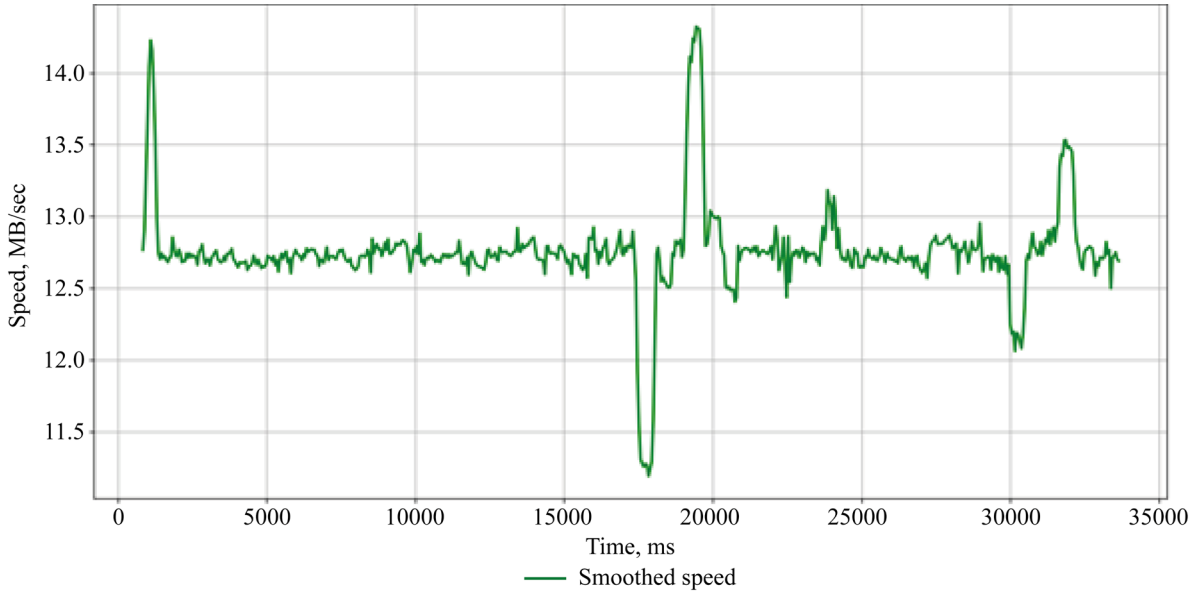

Fig. 5. Download speed when using BBR

When using the BBR algorithm, speed remained constant most of the time. Average download speed was 13.12 MB/s for CUBIC, and 12.75 MB/s for BBR.

The area under the graph curve reflects the amount of information transmitted. It was calculated from formula (7). In the first 3 seconds of transmission, 23.1568 MB of data were transmitted using CUBIC, and 27.3622 MB using BBR.

$$S = \int_0^{3000} v(t)\,dt \approx \sum_{i=0}^{3000} \frac{v_i + v_{i+1}}{2}\left(t_{i+1} - t_i\right). \quad (7)$$

Discussion. The results obtained show that the practical gain from the implementation of HTTP/3 (QUIC) is confirmed experimentally, but its value turns out to be significantly lower than theoretically expected. This requires interpretation taking into account the characteristics of the network environment, software implementation, and measurement methodology.

Configuration Complexities and Operational Risks. The described configuration procedure presents a number of practical challenges that must be considered when planning a production HTTP/3 deployment.

The first challenge is the inability to use standard virtual machine and container images for automated deployment. Most official Ubuntu images and popular Nginx container images based on Alpine Linux or Debian include a version of Nginx from the distribution repository that does not support HTTP/3. When using such images in orchestration systems (Kubernetes, Docker Compose), each node requires either manually adding the mainline repository and reinstalling nginx, or building a custom image with the required version. This complicates automation and increases operational costs for infrastructure maintenance [17].

The second complication stems from the protocol negotiation mechanism via the Alt-Svc header. The first connection between the client and the server is always established over TCP (HTTP/1.1 or HTTP/2), and only after receiving the Alt-Svc header in the response does the browser switch to QUIC for subsequent requests. If there is an intermediary node between the client and the server — a load balancer, reverse proxy, or CDN node — that does not support QUIC or blocks UDP traffic on port 443, the Alt-Svc header either does not reach the client, or the client is unable to establish a UDP connection. This behavior complicates diagnostics and creates the risk of a hidden lack of effect from protocol implementation. According to the QUIC core specification [18], if UDP transport is unavailable, the client should fall back to a TCP connection without explicitly signaling an error. That makes the absence of HTTP/3 in real traffic difficult to diagnose without explicit instrumental verification. To verify the use of HTTP/3, explicit verification via browser developer tools or server logs with protocol version information are required.

A prerequisite for establishing an HTTP/3 connection on the client side is a browser with QUIC support enabled. In Google Chrome, support for the protocol has been enabled by default since version 87, but in corporate environments, it can be disabled via group policies. With QUIC disabled, the browser will not establish HTTP/3 connections, regardless of the correct server configuration and the presence of the Alt-Svc header.

Interpretation of TTFB Results. The combined QUIC and TLS 1.3 handshake, specified in RFC 9001 [19] and based on the TLS 1.3 specification [20], theoretically reduces initialization to 1 RTT, but the practical efficiency of this mechanism is sensitive to the implementation details of the cryptographic stack on specific hardware and in a specific software version. A 23.06% reduction in TTFB when switching from HTTP/1.1 to HTTP/3 experimentally confirms the advantage of the unified QUIC handshake, which eliminates the additional RTT, typical of separate TCP and TLS initialization. However, the measured gain is significantly lower than the theoretically expected value of 71.43%, which is explained by a combination of factors.

Processing of UDP packets on the provider's intermediate network equipment is often less optimized compared to TCP traffic: routers and firewalls are traditionally configured for the TCP load profile, and some operators apply additional inspection or throttling of UDP flows [8, 11]. QUIC implementations in nginx and Google Chrome remained experimental at the time of the experiment, which manifested itself in suboptimal stack parameter values and additional overhead at the application level. The 4G mobile channel introduces an unstable variable component of latency, which offsets some of the gain from the reduced RTT during connection establishment. A similar discrepancy between theory and practice was recorded in Google large-scale deployment of QUIC, where the actual search latency reduction was 8.0% for desktop users and 3.6% for mobile users, instead of the theoretically expected values [8], and was also confirmed in domestic studies of real-world network conditions [11]. This finding also aligns with the data from ITSumma[2], which observed a 12.4% decrease in TTFB. Collectively, this points to a systemic discrepancy between the theoretical and practical performance of the protocol at its current stage of evolution.

Page Load Time Interpretation. The 9.5% speedup in full test page load time using HTTP/3 compared to HTTP/1.1 is primarily due to multiplexing requests within a single QUIC connection and eliminating Head-of-Line blocking at the transport layer. When loading a test page consisting of 32 files, HTTP/3 processes all requests in parallel without deadlocking, whereas HTTP/1.1 is limited by the number of parallel TCP connections.

A notable anomaly in the HTTP/2 results is its average load time (833.15 ms) exceeding that of HTTP/1.1 (792.7 ms). This effect is an artifact of the statistical methodology used, rather than an indicator of any actual protocol inefficiency. In the HTTP/1.1 sample, the interquartile range method excluded three values exceeding the upper bound, significantly lowering the resulting mean. The average load times for HTTP/1.1 and HTTP/2 across all twenty measurements without removing outliers are 843.8 ms and 833.15 ms, respectively. This confirms HTTP/2's superior load performance compared to HTTP/1.1. The HTTP/2 data had no upper-bound outliers, indicating that the protocol achieved a more even distribution of response times by multiplexing requests and prioritizing streams within a single TCP connection. Thus, the comparison of cleaned means does not correctly reflect the real relationship between protocols: HTTP/2 shows higher stability and less variability, while the final mean value after removing outliers turned out to be statistically lower for HTTP/1.1.

[2] ITsumma. *HTTP/3 and QUIC: Future of Fast Internet*. Habr. URL: https://habr.com/ru/companies/itsumma/articles/497520 (accessed: 11.03.2026). (In Russ.)

Interpretation of CUBIC and BBR. Average transfer rates for a 3 GB file using CUBIC (13.12 MB/s) and BBR (12.75 MB/s) are comparable: the 3% difference is within the measurement error for an unstable mobile channel. This result is predictable for long-term transfers of a single file: over hundreds of seconds, both algorithms reach a steady-state channel load, and differences in initialization strategies no longer determine the final average speed.

The fundamental difference between the algorithms is evident in the transmission profile. CUBIC exhibits a characteristic sawtooth speed profile (Fig. 4): it increases monotonically from starting values of less than 10 MB/s to the operating level in approximately four seconds. After that, it cyclically decreases during periods of packet loss. BBR, which uses Bandwidth-Delay Product (BDP) throughput estimation, maintains a stable speed from the first seconds.

When working with the Web, most requested files are small. Assume that the size of a single resource file for a web page is 63 KB, the initial slow-start window size is 10 kilobytes (the default setting on Linux systems), and the maximum window size is 64 KB. With slow-start, the CUBIC algorithm uses an exponential function to increase the congestion window [21].

$$A = \left[log_2 \frac{cwnd_{max}}{cwnd_0} \right] = \left[log_2 \frac{64}{10} \right] = 3. \quad (8)$$

The calculation result obtained from formula (8) shows that transferring the file requires tripling the congestion window size, which takes 3 RTT. Had the transmission started with a congestion window of 64, the transfer could have been accomplished in just 1 RTT.

It is this initial period that determines the practical significance of BBR for web services. A typical page resource — a script, stylesheet, font — is transferred in one or two RTT and fits within CUBIC slow-start phase, during which the algorithm has not yet reached its congestion window. In this scenario, BBR ensures immediate access to optimal speed, which ultimately reduces the time it takes to download multiple small resources in parallel. Thus, BBR advantage over CUBIC is realized not during long transfers, but during page resource downloads, accompanied by multiple short requests immediately after establishing a connection.

Quantitative confirmation of the advantage of BBR in the initial phase of transmission is provided by a comparison of the areas under the curves of the speed graphs calculated from formula (7) by the trapezoidal method. In the first three seconds of transmission, the CUBIC algorithm ensured the transfer of 23.16 MB of data, while BBR provided the transfer of 27.36 MB, which is 18.2% more. This result is consistent with the experimental results in [15], where higher BBR throughput was recorded at high RTT values, which are typical for intercontinental connections.

A promising direction for further research is to experimentally test the benefits of BBR directly in a web scenario: measuring the full page load time of a page consisting of multiple small resources using the CUBIC and BBR algorithms in combination with each version of the HTTP protocol. Such an experiment will allow us to quantify the extent to which the accelerated speed of BBR translates into reduced page load time in a real web scenario, as well as determine which combinations of protocol version and congestion management algorithm produce the most pronounced practical effect.

Study Limitations and Practical Recommendations. While the results obtained are practically valuable for evaluating the gains of switching to HTTP/3, several limitations of the experimental testbed restrict the applicability of the conclusions.

The setup included a single virtual machine with one vCPU and a single client connected via a 4G mobile network. The mobile network introduces unstable, variable latency and inconsistent bandwidth, increasing measurement variability and making it difficult to isolate protocol effects from channel effects. Transport protocol performance is significantly dependent on network topology, RTT values, packet loss rates, and intermediate equipment policies; therefore, transferring the results to other network scenarios requires independent experimental verification [22, 23].

The limited sample size (20 measurements per protocol) provides sufficient accuracy for an initial assessment, but is insufficient for constructing statistically robust confidence intervals. The lack of geographically distributed clients precludes assessing the impact of high RTT — the conditions under which QUIC advantage is theoretically most pronounced.

Based on the data obtained, the following practical recommendations can be formulated. Switching to HTTP/3 is primarily advisable for services with a large number of small resources per page, high-latency audiences (mobile users, remote regions), and requirements for minimizing TTFB. For services that predominantly transfer large files over stable wired connections, the practical gain from switching will be minimal. BBR is recommended for use alongside HTTP/3: although it achieves a comparable average throughput on long-lived transfers, it offers a stable rate profile and shortens the time to reach full operating speed — a critical advantage precisely in the web scenario of numerous short requests.

To improve the reliability of performance assessment in subsequent studies, a comparison of alternative QUIC server implementations (in addition to nginx) is justified, as well as an analysis of the impact of proxy servers on performance metrics when using QUIC [10].

Conclusion. The study has confirmed that implementing the QUIC protocol provides practical gain in terms of web interaction speed. This resulted in a 23.06% reduction in TTFB and a 9.5% reduction in test web page load time. The model presented in the article predicts a 71.43% reduction in TTFB, not 23.06%. This discrepancy reveals the significant impact of the protocol's experimental status on its availability on network infrastructure, as well as the critical role of other factors discussed in the article for the protocol full-scale implementation.

The paper compares the CUBIC (standard) and BBR (most common in HTTP/3) congestion control algorithms, and presents a theoretical justification for the advantage of BBR when transferring small files, due to its higher initial speed and the absence of a slow-start mechanism. Similar advantages of BBR were documented in foreign studies. In particular, article [15] noted the efficiency of this algorithm in channels with high RTT (intercontinental connections) due to the modeling of the communication channel throughput.

The QUIC protocol in combination with HTTP/3 at the current stage of development is associated with certain implementation difficulties, but it has significant potential for building high-performance information systems, which is confirmed by the results of other studies [24], including in relation to systems with requirements for reliable delivery of real-time traffic [25].

Setting up an HTTP/3 server requires loading additional modules into the operating system kernel. This negatively impacts the adoption of the protocol, but if an organization has sufficient qualified personnel to support such an infrastructure, switching to HTTP/3 can provide significant gains. The improved TTFB and the elimination of Head-of-Line blocking can theoretically significantly speed up page resource loading. The performance gains can be particularly noticeable on pages containing numerous small resources.

In addition to performance issues, the transition to QUIC and HTTP/3 poses specific challenges for the information security infrastructure: built-in encryption complicates deep packet inspection (DPI) and the functioning of intrusion detection systems, which is discussed in detail in [26] and requires separate consideration when planning production implementation.

Limitations of the study include a simplified testbed configuration (one virtual machine and a 4G mobile channel) and a small sample size. The results obtained have practical value for assessing the feasibility of switching to HTTP/3, but require confirmation across a wider range of scenarios, as the performance of transport protocols is significantly dependent on network topology, latency, and loss. The subject of congestion control algorithms can be addressed in more depth in subsequent publications, in particular, it seems appropriate to compare various algorithms in combination with different versions of the HTTP protocol. In modern information systems, proxy servers are widely used for traffic management. A promising direction is to study the impact of such intermediate nodes on performance metrics when using QUIC [10].

References

1. Gorokhova PA. Russian Advertising Market: State, Structure, Trends and Development Prospects. *State and Municipal Management. Scholar Notes.* 2020;(1):297–302. https://doi.org/10.22394/2079-1690-2020-1-1-297-302

2. Arapakis I, Park S, Pielot M. Impact of Response Latency on User Behaviour in Mobile Web Search. In: *Proc. ACM SIGIR Conference on Human Information Interaction and Retrieval (CHIIR '21).* Canberra, Australia: ACM; 2021. P. 279–283. https://doi.org/10.1145/3406522.3446038

3. Rahmani J, Baranov MD, Kuzmin DA. Development of a Web Application Optimization Method to Improve Performance. *International Journal of Humanities and Natural Sciences.* 2025;102(3–1):237–241. https://doi.org/10.24412/2500-1000-2025-3-1-237-241

4. Wendroth J, Jaeger B. A Brief Overview on HTTP. In: *Proc. Seminar on Innovative Internet Technologies and Mobile Communications (IITM).* Munich: Technical University of Munich; 2022. P. 59–69. https://doi.org/10.2313/NET-2022-11-1_11

5. Rahmani J, Rogov ID. Trends in the Development of Network Technologies in 2022. In: *Proc. XVI International Industry Scientific and Technical Conference*. Moscow: Izdatel'skii dom Media pablisher; 2022. P. 30–31. (In Russ).

6. Bishop M (ed). *HTTP/3. RFC 9114.* AMS LLC: RFC Editor; 2022. https://doi.org/10.17487/RFC9114

7. Amet M, Thomas L, Ye-Qiong Song. A Performance Evaluation of QUIC in Real-Time Networks. In: *Proc. 32nd International Conference on Real-Time Networks and Systems (RTNS 2024).* New York, NY: ACM; 2024. P. 255–265. https://doi.org/10.1145/3696355.3699698

8. Langley A, Riddoch A, Wilk A, Vicente A, Krasic C, Zhang D, et al. The QUIC Transport Protocol: Design and Internet-Scale Deployment. In: *Proc. ACM SIGCOMM Conference.* New York, NY: ACM; 2017. P. 183–196. https://doi.org/10.1145/3098822.3098842

9. Fan Liu, Crowley P. Security and Performance Characteristics of QUIC and HTTP/3. In: *Proc. 10th ACM Conference on Information-Centric*. New York, NY: ACM; 2023. p. 124–126. https://doi.org/10.1145/3623565.3623757

10. Fan Liu, Farkiani B, Dehart J, Parwatikar J, Crowley P. Performance Comparison of HTTP/3 and HTTP/2 with Proxy Integration. *arXiv preprint*. 2024. https://doi.org/10.48550/arXiv.2409.16267

11. Andreyanov NS, Ryabikov AY. Research on Client-Server Protocols to Improve Fault Tolerance and Connection Security. *International Journal of Humanities and Natural Sciences.* 2024;97(10–1):128–132. https://doi.org/10.24412/2500-1000-2024-10-1-128-132

12. Smirnov IA, Mikhailov MYu, Lapteva MG. HTTP/3 and the QUIC Protocol: Future of High-Performance Web Services. *Vestnik Nauki.* 2025;2(6):1780–1788.

13. Jia Zhang, Haixuan Tong, Enhuan Dong, Xin Qian, Mingwei Xu, Xiaotian Li, et al. Cold Start or Hot Start? Robust Slow Start in Congestion Control with A Priori Knowledge for Mobile Web Services. In: *Proc. ACM Web Conference*. New York, NY: ACM; 2024. P. 2870–2878. https://doi.org/10.1145/3589334.3645393

14. Cardwell N, Yuchung Cheng, Gunn CS, Hassas Yeganeh S, Jacobson V. BBR: Congestion-Based Congestion Control. *Communications of the ACM*. 2017;60(2):58–66. https://doi.org/10.1145/3009824

15. Yi Han, Mengjie Zuo, Huijun Yuan, Yi Zhong, Zhenhui Yuan, Ting Bi. A QoS-Based Fairness-Aware BBR Congestion Control Algorithm Using QUIC. *Mathematical Problems in Engineering.* 2022;2022:7222030. https://doi.org/10.1155/2022/7222030

16. Dierks T, Rescorla E. The Transport Layer Security (TLS) Protocol Version 1.2. *RFC 5246.* New York: IETF; 2008. 101 p. https://doi.org/10.17487/RFC5246

17. Voronova AG. Typification of Projects for the Transition to Cloud Services. *Advanced Engineering Research (Rostov-on-Don)*. 2024;24(3):274–282. https://doi.org/10.23947/2687-1653-2024-24-3-274-282

18. Iyengar J, Thomson M (eds). *QUIC: A UDP-Based Multiplexed and Secure Transport. RFC 9000*. AMS LLC: RFC Editor; 2021. https://doi.org/10.17487/RFC9000

19. Thomson M, Turner S (eds). *Using TLS to Secure QUIC. RFC 9001*. AMS LLC: RFC Editor; 2021. https://doi.org/10.17487/RFC9001

20. Rescorla E. *The Transport Layer Security (TLS) Protocol Version 1.3. RFC 8446.* New York, NY: IETF; 2018. https://doi.org/10.17487/RFC8446

21. Rhee I, Xu L, Ha S, Zimmermann A, Eggert L, Scheffenegger R. *CUBIC for Fast and Long-Distance Networks. RFC 8312.* AMS LLC: RFC Editor; 2018. https://doi.org/10.17487/RFC8312

22. Linets G.I., Voronkin R.A., Slyusarev G.V., Govorova S.V. Optimization Problem for Probabilistic Time Intervals of Quasi-Deterministic Output and Self-Similar Input Data Packet Flow in Telecommunication Networks. Advanced Engineering Research (Rostov-on-Don). 2024;24(4):424-432. https://doi.org/10.23947/2687-1653-2024-24-4-424-432

23. Samoylenko V.V. Concept of a Multilevel Network Infrastructure for Monitoring Agricultural Facilities Based on Wireless Sensor Networks. *Advanced Engineering Research (Rostov-on-Don)*. 2025;25(4):371–382. https://doi.org/10.23947/2687-1653-2025-25-4-2238

24. Gupta A, Bartos R. Improving Web Content Delivery with HTTP/3 and Non-Incremental EPS. In: *Proc. Conference on Networking and Internet Architecture*. Durham, NH: University of New Hampshire; 2024. P. 1–10. https://doi.org/10.48550/arXiv.2404.13460

25. Antonova VM, Buzhin IG, Grechishkina NA, Korochkin ED, Kuznetsov NA. QUIC Transport Protocol as Reliable Transmission Method for Real-Time Traffic. *Information Processes*. 2025;25(3):490–500. https://doi.org/10.53921/18195822_2025_25_3_490

26. Selivanov MA. New Generation Network Protocols and Their Analysis from the Point of View of Information Security. *Young Researcher of the Don.* 2022;(1(34):56–62.

About the Authors:

Jahed Rahmani, Senior Lecturer of the Department of Network Information Technologies and Services, Moscow Technical University of Communications and Informatics (8a, Aviamotornaya Str., Moscow, 111024, Russian Federation), SPIN-code, ORCID, j.rahmani@mtuci.ru

Serafim P. Sukharev, Technician of the Research and Innovation Department "Center for Artificial Intelligence and Advanced Projects", Moscow Technical University of Communications and Informatics (8a, Aviamotornaya Str., Moscow, 111024, Russian Federation), SPIN-code, ORCID, ResearchGate, ResearcherID, s.p.suharev@mtuci.ru

Claimed Contributorship:

J Rahmani: conceptualization, methodology, supervision, writing & editing.

SP Sukharev: data curation, formal analysis, investigation, software, visualization, writing – original draft preparation.

Conflict of Interest Statement: **the authors declare no conflict of interest.**

All authors have read and approved the final version of manuscript.

Об авторах:

Джахед Рахмани, старший преподаватель кафедры «Сетевые информационные технологии и сервисы» Московского технического университета связи и информатики (111024, Российская Федерация, г. Москва, ул. Авиамоторная, 8 а), SPIN-код, ORCID, j.rahmani@mtuci.ru

Серафим Павлович Сухарев, техник НИО «Центр искусственного интеллекта и перспективных проектов» Московского технического университета связи и информатики (111024, Российская Федерация, г. Москва, ул. Авиамоторная, 8 а), SPIN-код, ORCID, ResearchGate, ResearcherID, s.p.suharev@mtuci.ru

Заявленный вклад авторов:

Д. Рахмани: разработка концепции и методологии, научное руководство, написание рукописи, редактирование**.**

С.П. Сухарев: курирование данных, формальный анализ, проведение исследования, разработка программного обеспечения, визуализация, написание черновика рукописи.

Конфликт интересов: **авторы заявляют об отсутствии конфликта интересов.**

Все авторы прочитали и одобрили окончательный вариант рукописи.

Received / **Поступила в редакцию** 02.03.2026
Reviewed / Поступила после рецензирования 02.04.2026
Accepted / **Принята к публикации** 09.04.2026

INFORMATION TECHNOLOGY, COMPUTER SCIENCE AND MANAGEMENT
ИНФОРМАТИКА, ВЫЧИСЛИТЕЛЬНАЯ ТЕХНИКА И УПРАВЛЕНИЕ

UDC 681.5:004.942
https://doi.org/10.23947/2687-1653-2026-26-2-2237

Original Empirical Research

Machine Learning-Based Condition Assessment Method for Shell-and-Tube Heat Exchangers to Improve Energy Efficiency

Larisa G. Tugashova[1] ✉, **Andrey V. Zatonskiy**[2]
[1] State Technological University "Higher School of Petroleum", Almetyevsk, Russian Federation
[2] Perm National Research Polytechnic University, Perm, Russian Federation
✉ tugashova@yandex.ru

EDN: JTIHTA

Abstract

Introduction. Shell-and-tube heat exchangers are widely used in oil treatment and refining plants, as well as in heating systems, where their reliable operation is largely determined by the intensity of thermal fouling on the tube surface. Therefore, it is crucial to promptly determine when heat exchange equipment requires maintenance, as deposit accumulation can result in the reduced heat transfer efficiency and increased operating costs. A review of the literature shows that the problem of predicting heat exchanger fouling is being actively researched. However, existing approaches, which focus on process parameters and the physicochemical properties of heat transfer fluids, are not always applicable to the specific conditions of oil refining, where feedstock composition, operating conditions, and deposit nature differ significantly from typical industrial processes. Thus, there remains a gap in scientific knowledge associated with the insufficient development of models that allow for the reliable description of changes in the thermal resistance of contaminants, and the heat transfer coefficient specifically for shell-and-tube heat exchangers of oil refineries. The objective of this study is to determine the dependence of the coefficients of thermal resistance of contaminants and heat transfer on operating parameters, in particular, on the output temperatures of coolants and oil density. For this, it is planned to use machine learning methods to build more adequate predictive models and thereby increase the validity of decisions on the maintenance of heat exchange equipment.

Materials and Methods. A shell-and-tube heat exchanger in a small refinery unit was investigated. Here, circulating diesel reflux (210–235 °C) was the hot medium on the shell side, and oil was the cold medium in the tube bundle. For the calculation, the cross-sectional areas of the tube and annular spaces, linear flow rates, Reynolds, Prandtl, and Nusselt criteria, as well as the heat transfer coefficients of the hot and cold coolants were determined. The heat transfer coefficient was calculated taking into account the thermal resistance of the wall and contaminants, while heat transfer was calculated from heat balance and heat transfer equations. Machine learning and symbolic regression methods, including PySR, SISSO, FROLS, and CatBoostRegressor, were used to estimate the thermal resistance of contaminants and the heat transfer coefficient, based on oil density and coolant temperature data. The verification calculation of the heat exchanger was performed by the method of successive approximations with the solution to a system of nonlinear equations in Matlab.

Results. A verification calculation of a shell-and-tube heat exchanger for oil from three fields showed that with an increase in the thermal resistance of contaminants from 0 to 0.002 $(m^2 \cdot °C)/W$, the heat transfer coefficient decreased from approximately 93–95 to 81–83 $W/(m^2 \cdot °C)$. It was established that changes in the outlet temperatures of the coolants was an information basis for identifying contaminants. Using the SISSO and PySR symbolic regression methods, analytical dependences of thermal resistance on oil density and outlet temperatures were obtained with RMSE $1.25 \cdot 10^{-8}$ and $2.34 \cdot 10^{-8} (m^2 \cdot °C)/W$, respectively. To predict the dynamics of heat transfer, NARX models based on FROLS and CatBoostRegressor were built, validated on industrial data. Ex-post forecast error for the algorithm CatBoostRegressor RMSE = 0.03573 $W/(m^2 \cdot °C)$, for the algorithm FROLS RMSE = 0.01296 $W/(m^2 \cdot °C)$.

Discussion. A 13% reduction in heat transfer coefficient with an increase in contaminant thermal resistance to 0.002 ($m^2 \cdot °C$)/W was consistent with theoretical models and experimental data from other researchers. The use of SISSO and PySR methods provided significantly higher accuracy compared to neural network approaches with small training sets. The FROLS algorithm outperformed CatBoostRegressor in the accuracy of ex-post forecast of heat transfer coefficient dynamics, which is explained by the compactness of the polynomial model and the smooth nature of the process under study. The established threshold for reducing the heat transfer coefficient by 25% complies with industry standards and provides the transition to equipment maintenance based on actual condition.

Conclusions. A method for determining the thermal resistance of heat exchanger fouling based on the outlet temperature of the coolant and the oil density was developed. Analytical relationships with RMSE $1.25 \cdot 10^{-8}$ ($m^2 \cdot °C$)/W and $2.34 \cdot 10^{-8}$ ($m^2 \cdot °C$)/W were obtained using the SISSO and PySR symbolic regression methods. NARX models for predicting heat transfer coefficients (RMSE 0.01296 and 0.03573 W/($m^2 \cdot °C$) were built and validated using industrial data. A 25.2% reduction in heat transfer coefficient was adopted as the criterion for the need for cleaning the unit, which provided a transition to condition-based maintenance and increased energy efficiency in oil refining.

Keywords: shell-and-tube heat exchanger, thermal resistance, heat transfer coefficient, symbolic regression

Acknowledgements. The authors would like to thank the editors and reviewers for their time and valuable comments.

For Citation. Tugashova LG, Zatonskiy AV. Machine Learning-Based Condition Assessment Method for Shell-and-Tube Heat Exchangers to Improve Energy Efficiency. *Advanced Engineering Research (Rostov-on-Don)*. 2026;26(2):2237. https://doi.org/10.23947/2687-1653-2026-26-2-2237

Оригинальное эмпирическое исследование

Способ оценки состояния кожухотрубчатых теплообменников с применением машинного обучения для повышения энергоэффективности

Л.Г. Тугашова[1] ✉, **А.В. Затонский**[2]

[1] Альметьевский государственный технологический университет «Высшая школа нефти», г. Альметьевск, Российская Федерация

[2] Пермский национальный исследовательский политехнический университет, г. Пермь, Российская Федерация

✉ tugashova@yandex.ru

Аннотация

Введение. Кожухотрубчатые теплообменники широко применяются на установках подготовки и переработки нефти, а также в системах теплоснабжения, где их надежная работа во многом определяется интенсивностью термического загрязнения поверхности труб. В связи с этим актуальной задачей является своевременное определение момента, когда теплообменному оборудованию требуется техническое обслуживание, поскольку накопление отложений приводит к снижению эффективности теплопередачи и росту эксплуатационных затрат. Анализ литературных источников показывает, что проблема прогнозирования загрязнения теплообменных аппаратов достаточно активно исследуется. Однако существующие подходы, ориентированные на учет режимных параметров и физико-химических свойств теплоносителей, не всегда применимы к специфическим условиям нефтепереработки, где состав сырья, режимы эксплуатации и характер отложений существенно отличаются от типовых промышленных процессов. Таким образом, сохраняется пробел в научных знаниях, связанный с недостаточной разработанностью моделей, позволяющих надежно описывать изменение термического сопротивления загрязнений и коэффициента теплопередачи именно для кожухотрубчатых теплообменников нефтеперерабатывающих установок. Целью настоящего исследования является определение зависимости коэффициентов термического сопротивления загрязнений и теплопередачи от режимных параметров — в частности, от выходных температур теплоносителей и плотности нефти. Для достижения поставленной цели предполагается применение методов машинного обучения, позволяющих построить более адекватные прогностические модели и тем самым повысить обоснованность решений по техническому обслуживанию теплообменного оборудования.

Материалы и методы. В качестве объекта исследования рассмотрен кожухотрубчатый теплообменник установки переработки нефти малой мощности, в котором циркуляционное орошение дизельного топлива (210– 235 °C) выступает горячим теплоносителем в межтрубном пространстве, а нефть — холодным теплоносителем в трубном пучке. Для расчета определялись площади сечений трубного и межтрубного пространств, линейные скорости потоков, критерии Рейнольдса, Прандтля и Нуссельта, а также коэффициенты теплоотдачи со

стороны горячего и холодного теплоносителей. Коэффициент теплопередачи рассчитывался с учетом термического сопротивления стенки и загрязнений, теплообмен — по уравнениям теплового баланса и теплопередачи. Для оценки термического сопротивления загрязнений и коэффициента теплопередачи использовались методы машинного обучения и символьной регрессии, в том числе PySR, SISSO, FROLS и CatBoostRegressor, на основе данных о плотности нефти и температуре теплоносителей. Поверочный расчет теплообменника выполнен методом последовательных приближений с решением системы нелинейных уравнений в Matlab.

Результаты исследования. Поверочный расчёт кожухотрубчатого теплообменника для нефти трёх месторождений показал, что при росте термического сопротивления загрязнений от 0 до 0,002 ($м^2 \cdot °C$)/Вт коэффициент теплопередачи снижается примерно с 93–95 до 81–83 Вт/($м^2 \cdot °C$). Установлено, что изменение выходных температур теплоносителей служит информационной основой для идентификации загрязнений. Методами символьной регрессии SISSO и PySR получены аналитические зависимости термического сопротивления от плотности нефти и выходных температур с RMSE $1{,}25 \cdot 10^{-8}$ и $2{,}34 \cdot 10^{-8}$ ($м^2 \cdot °C$)/Вт соответственно. Для прогнозирования динамики теплопередачи построены NARX-модели на базе FROLS и CatBoostRegressor, валидированные на промышленных данных. Ошибка постпрогноза для алгоритма CatBoostRegressor RMSE = 0,03573 Вт/($м^2 \cdot °C$), для алгоритма FROLS RMSE = 0,01296 Вт/($м^2 \cdot °C$).

Обсуждение. Снижение коэффициента теплопередачи на 13 % при росте термического сопротивления загрязнений до 0,002 ($м^2 \cdot °C$)/Вт согласуется с теоретическими моделями и экспериментальными данными других исследователей. Применение методов SISSO и PySR обеспечило существенно более высокую точность по сравнению с нейросетевыми подходами при малых обучающих выборках. Алгоритм FROLS превзошёл CatBoostRegressor по точности постпрогноза динамики коэффициента теплопередачи, что объясняется компактностью полиномиальной модели и гладким характером исследуемого процесса. Установленный порог снижения коэффициента теплопередачи на 25 % соответствует отраслевым нормам и обеспечивает переход к обслуживанию оборудования по фактическому состоянию.

Заключение. Разработана методика определения термического сопротивления загрязнений теплообменника по выходной температуре теплоносителей и плотности нефти. Методами символьной регрессии SISSO и PySR получены аналитические зависимости с RMSE $1{,}25 \cdot 10^{-8}$ ($м^2 \cdot °C$)/Вт и $2{,}34 \cdot 10^{-8}$ ($м^2 \cdot °C$)/Вт. Построены NARX-модели прогнозирования коэффициента теплопередачи (RMSE 0,01296 и 0,03573 Вт/($м^2 \cdot °C$), валидированные на промышленных данных. Снижение коэффициента теплопередачи на 25,2 % принято критерием необходимости очистки аппарата, что обеспечивает переход к обслуживанию по фактическому состоянию и повышение энергоэффективности нефтепереработки.

Ключевые слова: кожухотрубчатый теплообменник, термическое сопротивление, коэффициент теплопередачи, символьная регрессия

Благодарности. Авторы выражают благодарность редакции и рецензентам за уделенное время и ценные комментарии.

Для цитирования. Тугашова Л.Г., Затонский А.В. Способ оценки состояния кожухотрубчатых теплообменников с применением машинного обучения для повышения энергоэффективности. *Advanced Engineering Research (Rostov-on-Don).* 2026;26(2):2237. https://doi.org/10.23947/2687-1653-2026-26-2-2237

Introduction. Improvement of the energy efficiency of oil processing and pretreatment is a pressing practical challenge, particularly given tighter energy regulations, rising cost pressures, and recent export restrictions on oil and petroleum products. Oil producers have no influence over these restrictions, but they can improve internal processes at their facilities to reduce production costs. Specific opportunities include reducing heat loss, thermal energy consumption, and increasing the efficiency of installations. This can be accomplished through controlled process temperatures and equipment diagnostics aimed at reducing unscheduled downtime. These approaches are closely related to heat exchange processes, which are crucial in the petrochemical industry. A 1÷3 mm layer of contaminant deposits on tube surfaces can significantly reduce heat transfer efficiency. Heat losses are estimated at 20–40 %. To compensate for the decrease in heat transfer and maintain the required process parameters, the coolant flow rate must be raised, which in turn increases fuel and electricity consumption. According to experts, a 1 mm fouling of the heat exchanger can result in a 10-15% increase in fuel consumption.

Assessing the condition of shell-and-tube heat exchangers for petroleum products is difficult because of their operating temperatures and the impossibility of directly inspecting internal fouling, corrosion, or deformation. Therefore, the key parameters for monitoring tube wall fouling are the heat transfer coefficient, pressure drop, and outlet coolant temperature.

The cause of deposits on the surfaces of the walls of apparatus is the presence of asphalt-resinous substances, paraffins, water, and salts in the raw materials. To get rid of deposits and scale in the cavities of oil pipelines and heat exchangers, mechanical, thermal and chemical cleaning methods are used. The heat exchanger is cleaned by washing it with a paraffin

solvent. Ultrasonic cleaning of paraffin deposits is used at oil preparation and refining facilities.

Deposits on tube walls impair heat transfer and reduce the heat transfer coefficient. Various methods exist for diagnosing and assessing the fouling layer on the surface of heat exchanger tubes. For example, the characteristics of a clean and fouled heat exchanger can be determined experimentally using monitoring systems. Another approach involves constructing mathematical models. An example is the Ebert-Panchal model and its improved versions.

Article [1] provides an overview of models and examples of quantitative assessment of scale deposit thickness in plate heat exchangers of heating systems. The authors [2] performed an analytical accounting of the impact of fouling on the technical and economic indicators of industrial oil treatment units. In the work, the coefficients of heat transfer, heat emission, and thermal resistance of deposits in heat exchangers were obtained by an experimental method. In [1, 2], the proposed models concern specific types of heat exchangers and deposits; they do not predict the dynamics of fouling.

Software tools, particularly process modeling programs, are widely used to solve heat exchange equipment diagnostic problems. For example, in [3], the authors examine the problem of fouling heat exchangers in diesel fuel hydrotreating units. The problem is solved using the Hysys modeling program. In [4], a numerical solution is obtained by constructing a thermal model based on the finite element method in the Ansys program. In [5], the authors propose simplified formulas for calculating the effective thermal conductivity of porous structures by Mathcad and Ansys. Currently, the use of the above programs is not possible within the framework of import substitution.

The authors [6] use the software package “MiR PiA” to model the quality indicators of oil preparation for transportation. A license is required for use.

A number of studies are aimed at improving the design parameters of equipment used in the industry. Improved design and aerodynamics of tube bundles should provide enhanced heat transfer with high reliability. In [7], this is linked to pressure drops in the heat exchanger, which can cause equipment malfunctions. The implementation of algorithms for automatic adjustment of operating modes is also proposed. The authors [8] propose a neural network model for predicting the thermal-hydraulic efficiency of surface heat exchange intensifiers. Neural network models require large volumes of training data on heat exchanger fouling, which is difficult to collect. Furthermore, such solutions, which require changes to the device design, may not be applicable to the equipment in operation.

The authors [9] use simulation methods to obtain a model of a shell-and-tube heat exchanger and propose techniques for improving the control system of the heat exchanger. The mathematical model of the shell-and-tube evaporator is presented as an object with lumped parameters. A heat balance is compiled in differential form taking into account transport delays.

In [10], a mathematical model of a shell-and-tube heat exchanger is presented in the form of an ARMAX model for participation in a control system. These models do not take into account nonlinearities.

In the operation of heat exchange equipment, the colloidal state of raw materials and products, specifically heavy fractions and residues, plays a major role in increasing the efficiency of heat and mass transfer [11]. This solution is relevant for heavy fractions and also requires the installation of additional equipment.

The literature review shows that predicting thermal fouling and heat transfer coefficients based on feedstock properties, as well as applying small-data methods that handle nonlinearities, remains insufficiently investigated. For approximation and forecasting, a combination of approaches appears to be an interesting approach, such as combining physicochemical (balance) methods with machine learning.

The objective of this research is to create a methodology for calculating the fouling thermal resistance and heat transfer coefficient of a heat exchanger in relation to the outlet temperatures of crude oil and diesel fuel and the density of the oil, as well as to enable prediction of the heat transfer coefficient.

To achieve this goal, the following tasks must be completed:

– perform a verification thermal calculation of a shell-and-tube heat exchanger for a small-capacity oil refining unit, that is, obtain a mathematical model of the heat exchanger in balance form;

– using the shell-and-tube heat exchanger model obtained above, study the effect of the physicochemical properties of the heat transfer fluids and the thermal fouling coefficient on the heat transfer coefficient and output parameters (using oil samples from various fields as an example);

– obtain the dependence of the coefficient of thermal resistance of contaminants and the heat transfer coefficient on the output temperatures of oil and diesel fuel in heat exchangers, as well as on the density of oil, that is, construct approximating dependences through symbolic regression;

– build a nonlinear dynamic model suitable for predicting the heat transfer coefficient using the obtained approximating dependences, experimental data of the operating installation, as well as a description of the object in the form of previously derived ordinary differential equations.

Materials and Methods. To determine the thermal resistance coefficient of fouling and the heat transfer coefficient in shell-and-tube heat exchangers, it is proposed to apply machine learning methods using small sample sizes, such as symbolic regression, since it is difficult to obtain large volumes of information on heat exchanger fouling under real plant operating conditions. A NARX model is proposed for predicting the heat transfer coefficient.

The object of this study is a shell-and-tube heat exchanger for a low-capacity processing unit. The initial design parameters of the heat exchanger were used for the shell-and-tube heat exchanger calculation: heat transfer surface area — 68 m^2, heat exchanger body length — 7.2 m, and tube length — 6 m.

The total thermal contamination of the tube surface was taken in the range from 0 (clean heat exchanger) to 0.002 (m^2·°C)/W (contaminated heat exchanger).

For such units, the circulation reflux (CR) is organized as follows. Diesel fuel from the main column outlet is divided into two streams: product and circulating. The CR, passing through a shell-and-tube heat exchanger, returns to the main column. The CR temperature is 210–235 °C. Diesel fuel (annular space) is the hot coolant, while oil (tube bundle) is the cold coolant.

The first calculation step is to obtain the cross-sectional areas of the tubular and annular space. The second step is to find the linear velocities of the oil and diesel streams.

The flow modes of the coolant and the heat transfer rates are determined by the Reynolds, Prandtl, and Nusselt criteria. The next step is to calculate the heat transfer coefficient from the hot flow (diesel fuel) to the tube wall α_1 and the heat transfer coefficient from the tube surface to the heated feedstock (oil) α_2. The heat exchanger calculation is performed by standard methods. Therefore, well-known formulas and heat exchanger calculation details are not provided.

The heat transfer coefficient is determined by the formula:

$$K = \frac{1}{\frac{1}{\alpha_1} + \frac{\delta_t}{\lambda_t} + \frac{1}{\alpha_2}}, \quad (1)$$

where δ_t — heat exchange tube wall thickness, m; λ_t — thermal conductivity coefficient, W/(m·°C); α_1, α_2 — heat transfer coefficients, W/(m^2·°C).

The heat transfer coefficient depends on the heat transfer coefficients in the heat exchange tubes and the thermal resistance and thermal conductivity of the tube wall.

If there is contamination inside and outside the heat exchange tubes, the heat transfer coefficient is determined by the following formula:

$$K_z = \frac{1}{\frac{1}{\alpha_1} + \frac{\delta_t}{\lambda_t} + \sum r + \frac{1}{\alpha_2}}, \quad (2)$$

where Σr — total thermal resistance of the contamination layer, (m^2·°C)/W.

The heat transfer equation is as follows:

$$Q = K \cdot F \cdot \Delta T, \quad (3)$$

where K — heat transfer coefficient, W/(m^2·°C); F — heat exchange surface, m^2; ΔT — mean temperature difference, °C.

Heat balance equation for a shell-and-tube heat exchanger:

$$G_{LC} \cdot c_{LC} \cdot \left(T_{13} - T_{LC}\right) = G_n \cdot c_n \cdot \left(T_{n2} - T_{n1}\right), \quad (4)$$

where c_{LC} — heat capacity of CR diesel fuel, kJ/(kg ·°C); c_n — heat capacity of oil, kJ/(kg ·°C); G_{LC} — consumption of CR diesel fuel; G_n — oil consumption rate, kg/s; T_{13} — temperature on tray #13 of the diesel fuel outlet, °C; T_{LC} — CR return temperature, °C; T_{n1} — oil temperature at the inlet to the heat exchanger, °C; T_{n2} — oil temperature at the outlet of the heat exchanger, °C.

Using the initial design data, a verification calculation of the shell-and-tube heat exchanger was performed. The heat transfer coefficients and heat transfer coefficient were determined, and the system of equations (3) and (4) was solved.

Figure 1 shows a flowchart of the algorithm for solving equations (3) and (4) for the shell-and-tube heat exchanger.

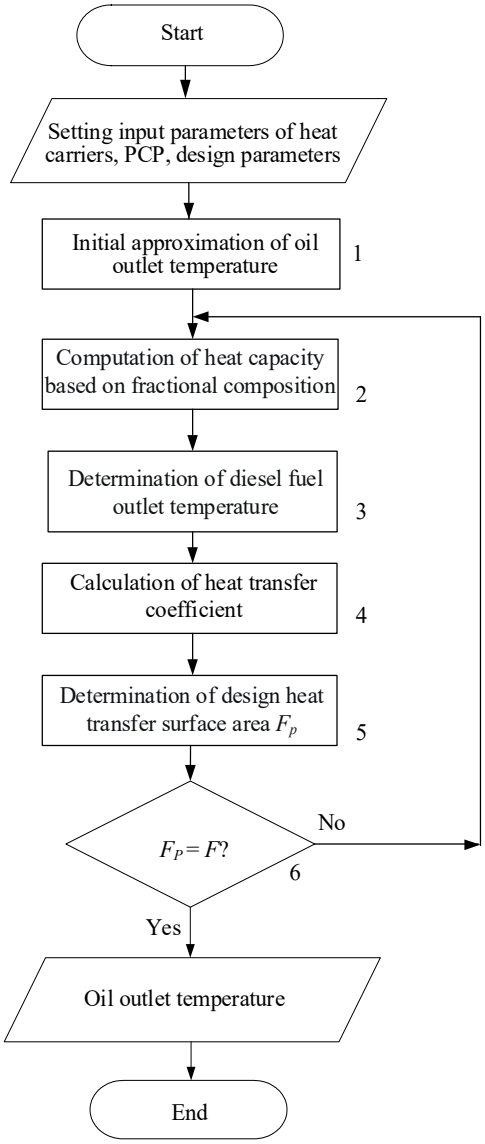

Fig. 1. Flowchart of the heat exchanger equation system solution algorithm

The diesel fuel and oil outlet temperatures are calculated using a method of successive approximations. After entering the initial data in block 1, the first approximation of the hot fluid outlet temperature (diesel fuel) is selected.

Block 2 calculates the heat capacity of oil and diesel fuel, taking into account the fractional composition of the oil. Block 3 calculates the outlet temperature of the diesel fuel through solving the heat balance equation for heat exchanger (4). Block 4 calculates the following parameters: mean temperature difference, heat transfer coefficient of clean heat exchanger (1), and heat transfer coefficient taking into account the thermal resistance coefficient of contaminant layer (2).

In the next block, block 5, the calculated heat transfer area is determined from heat transfer equation (3). In block 6, the obtained calculated area value is verified. A significant discrepancy between the obtained and specified values indicates an incorrect selection of oil and diesel fuel temperature. The iterative calculation continues until the discrepancy between the calculated and specified heat transfer areas is no more than 5%. The solution to the system of nonlinear equations (3) and (4) is implemented by numerical methods in the Matlab environment.

The calculation results are determined for given values of oil and diesel fuel inlet temperatures and oil and diesel fuel flow rates. The oil properties (density, viscosity), its fractional composition at true boiling temperature (TBT), heat exchanger design parameters, thermal load, and thermal resistance of the contaminant layer on the pipe surface are specified.

The efficiency of the heat exchange process is affected by the thermal resistance of the tube surface fouling. Furthermore, the composition and physicochemical properties (PCP) of the feedstock also influence the output parameters, particularly the outlet temperature of the coolant. This study used the PCP of oil from three fields (Table 1).

Table 1

Physicochemical Properties of Oil from Three Fields [12]

Oil field	Density ρ, kg/m^3	Output of fractions up to 350 °C, %	Viscosity η, mPa·s	Asphaltene content, %
Arlanskiy	891	42.8	35.37	5.80
Tuimazinskiy	856	53.4	10.18	3.40
Kuleshovskiy	819	63.6	3.29	0.70

Table 1 lists the physicochemical properties of crude oil from various fields. Density and viscosity are related to asphaltene content. Density and viscosity increase with increasing molecular weight and fraction boiling point. Lower-density oils yield higher light fractions at temperatures up to 350°C. The density and viscosity of oil, based on the PCP listed in Table 1, can be measured in the field and in the laboratory. The data in Table 1 are also used to establish the relationship between the thermal coefficient of contaminant resistance, the heat transfer coefficient, and the density and viscosity of oil.

The following method is proposed for determining the thermal resistance of contaminants. Using the mathematical model of a heat exchanger given in [13] and formulas (1–4), the input and output parameters of the object are determined. These formulas form a training sample. To identify the thermal resistance of contaminants and the heat transfer coefficient in shell-and-tube heat exchangers, it is proposed to use artificial neural networks [14] and machine learning methods associated with symbolic regression and system identification. Examples of symbolic regression methods include SISSO [15], TorchSISSO [16], PySR [17], SyMANTIC, and RGP. To obtain relationships between heat exchanger parameters, the PySR (High-Performance Symbolic Regression) and SISSO (Sure Independence Screening and Sparsifying Operator) methods are selected. They allow finding mathematical expressions that relate the original data. These methods are selected because they are suitable for working with small data sets. Key hyperparameters of the PySR method: binary_operators — list of binary operators ['+', '-', '*', '/', '^'], unary_operators — list of unary operators ['sin', 'cos', 'exp', 'log', 'sqrt', etc.], maxsize — maximum expression size, niterations —— number of iterations, loss_function — loss function, population_size — size of population. Key hyperparameters of the SISSO method: n_expansion — number of feature expansions, n_term — number of terms in the final formula, k — number of features for L0-regularization, initial_screening — initial feature selection, operators — a set of mathematical operations for generating features.

For identification and forecasting tasks over a given period, the NARX (Nonlinear Autoregressive with Exogenous Inputs) model is selected. FROLS (Forward Regression Orthogonal Least Squares) and CatBoostRegressor algorithms are used to determine its structure.

In the presented work, the oil density and the outlet temperature of the hot and cold coolants are used as factors. The output parameter of the relationship is the thermal resistance of the contaminants, or the heat transfer coefficient. The target parameter is calculated from the mathematical expression obtained by the PySR or SISSO, CatBoostRegressor or FROLS methods and measured process parameter values. It allows for determining the heat transfer coefficient and maintenance intervals for heat exchangers.

Research Results. Table 2 presents the values of heat transfer coefficients for different values of thermal fouling, density and viscosity of oil from different sources (data from Table 1).

Table 2

Heat Transfer Coefficient Values

Thermal resistance, (m^2·°C)/W	Heat transfer coefficient of clean and contaminated heat exchangers, W/(m^2 °C)		
	Arlanskiy oil field	Tuymazinskiy oil field	Kuleshovskiy oil field
0.00000	95.27486	94.24999	93.19691
0.00018	93.97257	92.97539	91.95044
0.00036	92.70541	91.73479	90.73687
0.00055	91.47196	90.52687	89.55492
0.00073	90.27091	89.35035	88.40336
0.00091	89.10098	88.20401	87.28104

0.00109	87.96099	87.08672	86.18686
0.00127	86.84981	85.99737	85.11978
0.00145	85.76635	84.93495	84.07879
0.00164	84.70959	83.89845	83.06296
0.00182	83.67855	82.88695	82.07138
0.00200	82.67231	81.89954	81.1032

In the next step, the output temperatures of the coolants (oil and diesel fuel) are calculated depending on the thermal resistance of the contaminant layer and the physicochemical properties of the oil (density and viscosity). Figures 2 and 3 show the results obtained.

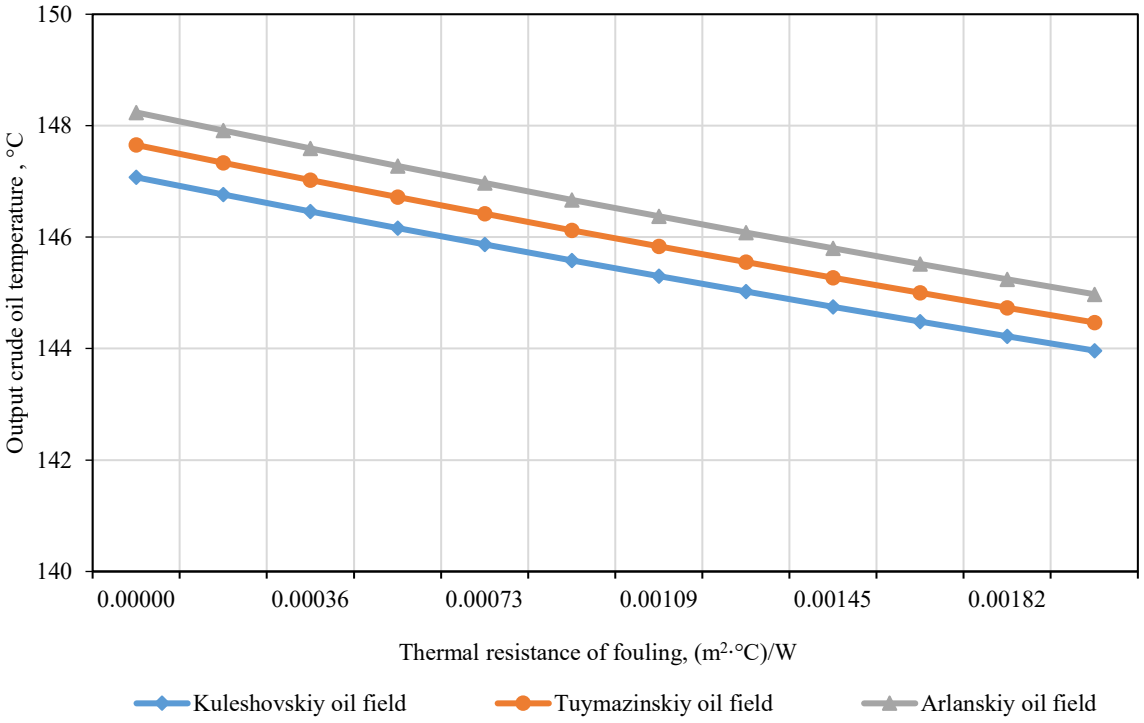

Fig. 2. Oil outlet temperature

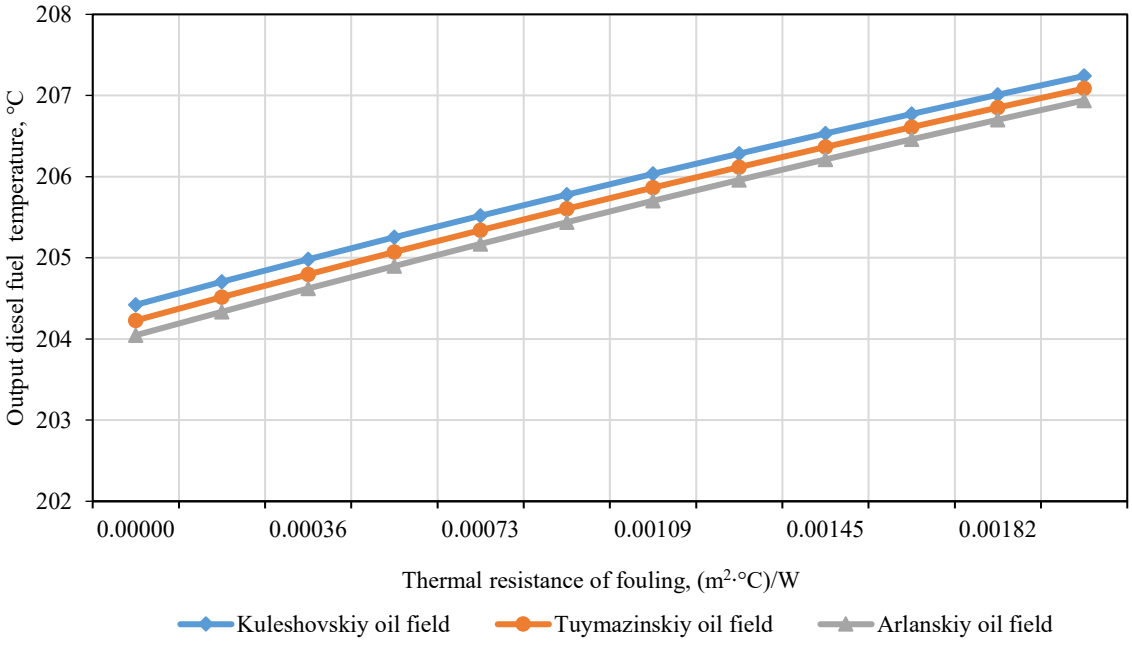

Fig. 3. Diesel fuel outlet temperature

The graphs in Figures 2 and 3 show that thermal fouling of the tube surface reduces heat transfer efficiency. The outlet temperature of the heated oil does not reach the required value, which corresponds to a clean heat exchanger. To maintain the heat flow at the specified level, it is required to increase the flow rate or temperature of the hot coolant.

It can be seen that as the thermal fouling coefficient increases, the difference and ratio between the outlet temperatures of oil and diesel fuel increase. This pattern is taken into account when deriving the thermal fouling coefficient by the SISSO method. The ratio of the outlet temperatures of the fouled heat exchanger to those of the clean heat exchanger also changes. This pattern is taken into account when applying the PySR method.

For training, PySR and SISSO are fed with the oil density and temperature at the outlet, and the diesel fuel temperature at the outlet. The target parameter is the thermal resistance of the contaminants. The Python software package is selected as the implementation tool.

Examples of mathematical relationships for determining the thermal resistance of contaminants obtained using SISSO:

$$y = k_1 \cdot \left(\left(x_2 - x_3 \right) - \left(x_2 / x_1 \right) \right) - k_2 \cdot \frac{ln\left(x_1 \right)}{x_2 - x_3} + k_3 \cdot \frac{x_2 / x_3}{x_2 - x_3} + k_4, \quad (5)$$

where x_1 — oil density, kg/m^3; x_2 — diesel fuel outlet temperature, °C; x_3 — oil outlet temperature, °C; y — thermal resistance, (m^2·°C)/W; k_1–k_4 — coefficients.

Using PySR, a mathematical relationship is obtained for determining the thermal resistance of contaminants:

$$y = x_0 \times log\left(x_1 + k_1 \right) \cdot k_2 - \frac{k_3}{x_2}, \quad (6)$$

where x_0 — oil density, kg/m^3; x_1 — ratio of the outlet temperature of diesel fuel in the contaminated heat exchanger to the outlet temperature of diesel fuel in the clean heat exchanger; x_2 — ratio of the outlet temperature of oil in the contaminated heat exchanger to the outlet temperature of oil in the clean heat exchanger; y — thermal resistance, (m^2·°C)/W; k_1–k_3 — coefficients.

To compare the accuracy of the dependences obtained, the root mean square error (RMSE) is used, which determines the average difference between the predicted and original data. The RMSE for expression (5) is $1.250371 \cdot e^{-08}$ (m^2·°C)/W. For expression (6), RMSE = $2.336612 \cdot e^{-08}$ (m^2·°C)/W.

Mathematical expressions (5, 6) are used to find the thermal resistance values of contaminants based on the measured parameters of the operating unit.

For practical applications, it is also necessary to know the values of the contaminant thermal resistance and heat transfer coefficient, determined not only at a given moment but also over a certain period. To obtain a consistent set of contaminant thermal resistance and heat transfer coefficient values, historical data is required.

The training and test samples are formed using the dynamic model of the heat exchanger given in [18], with dependences (5) or (6) added to the model. After training and testing the models, it is possible to predict the target parameter.

The Python SysIdentPy library is used to model and forecast multiple target parameter values over a given period. The NARX model is suitable for modeling dynamic systems that use both current and previous input and output values.

The FROLS and CatBoostRegressor algorithms are used to select the model structure. Lags of input (xlag) and output (ylag) variables are selected. Lag values are determined by search method.

The parameters selected for the FROLS algorithm are:

method for estimating model parameters — LeastSquares and TotalLeastSquares;

– order_selection=True — automatic selection of the model order (number of significant terms);

– n_terms=12 — maximum number of terms in the final model;

– model_type="NARMAX" — type of model;

– xlag=[1,1,1] — lags for input variables;

– ylag=12 — lags for the target variable;

– Polynomial — base class for generating polynomial functions with a selection of polynomial degree (degree=2);

– information criterion — AIC (Akaike Information Criterion).

For the CatBoostRegressor algorithm (a gradient boosting regressor), the following hyperparameters are defined:

– iterations=500 — number of trees in the ensemble;

– learning_rate=0.1 — learning rate (gradient descent step);

– depth=6 — maximum tree depth;

– xlag=[1,1,1];

– ylag=12.

In this case, a parameter prediction problem is solved, producing results that have not been previously reported. Thus, the ex-post forecast method is the most appropriate. The data are split 80/20 for model building and ex-post forecast.

After training the model, its quality is assessed using ex-post forecast. The post- prediction error for the CatBoostRegressor algorithm is RMSE = 0.03573 W/(m^2·°C), for the FROLS algorithm, RMSE = 0.01296 W/(m^2·°C). When forming the training and test samples, the range of variation of the thermal resistance of contaminants from 0 to 0.0022 (m^2·°C)/W, and the oil density — from 810 to 910 kg/m^3 are used. The results obtained for an oil density of 900 kg/m^3 are shown in Figure 4.

Industrial data for 12 readings is used to validate the models. Time series of measured oil and diesel fuel temperatures are processed by a median filter. Expert assessments by process engineers (regarding the dates of scheduled heat exchanger cleanings) are taken as additional information.

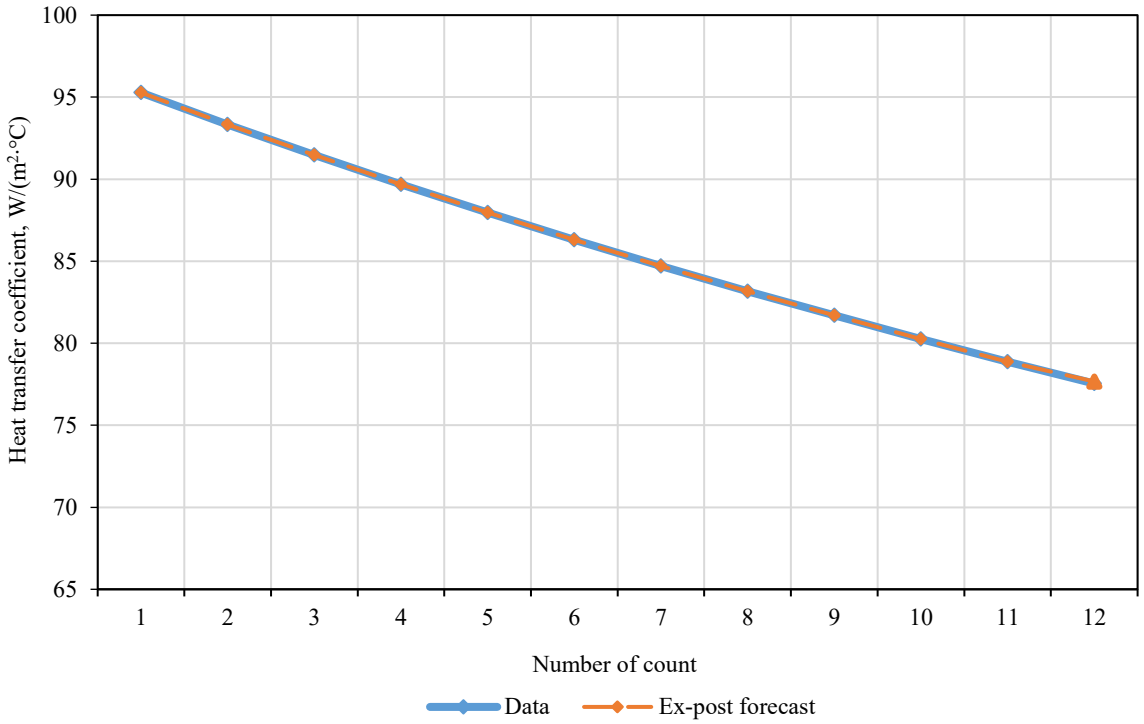

Fig. 4. Actual and predicted values of heat transfer coefficient

For a clean heat exchanger, the heat transfer coefficient is 95 W/(m^2·°C), and after 12 readings, it is 77 W/(m^2·°C). During this time, the heat transfer coefficient has decreased by 18.61%. After 18 readings (not shown in Fig. 4), the heat transfer coefficient has decreased by 25.2%, indicating the need for equipment cleaning to maintain operating efficiency. In this way, the target parameter can be predicted in the event of a change in oil density.

A comparative analysis of the heat transfer coefficient for a clean versus a fouled heat exchanger over a specified time interval indicates a loss of thermal efficiency. If the parameter falls by 25–30%, this serves as a signal that cleaning of the heat exchange unit is required.

Discussion. The results of a calibration thermal calculation of a shell-and-tube heat exchanger for a low-power oil refinery confirm the correctness of the constructed mathematical model. When the total thermal resistance of contaminants increases from 0 to 0.002 (m^2·°C)/W, the heat transfer coefficient decreases by approximately 13 – 14% for all three studies of oil from different sources.

A relationship between heat transfer efficiency and the physicochemical properties of oil is established. As density increases, the heat transfer coefficient increases slightly due to higher heat capacity and thermal conductivity. However, heavier oils contain more asphaltenes, which accelerate the buildup of contaminants. Thus, the effect of density is twofold and requires further study.

The PySR and SISSO symbolic regression methods demonstrated high accuracy in reconstructing analytical relationships: RMSE were $1.25 \cdot 10^{-8}$ and $2.34 \cdot 10^{-8}$ (m^2·°C)/W, respectively. The expression obtained by the SISSO method appeared to be more practically applicable, since it did not require reference values for the clean heat exchanger temperatures.

In the forecasting task, the FROLS algorithm as part of the NARX model outperformed CatBoostRegressor in accuracy (RMSE = 0.013 versus 0.036 W/(m^2·°C), which is explained by the better adaptability of orthogonal regression to small samples with smooth dynamic dependences. The established cleaning criterion (a reduction in the heat transfer coefficient by 25–30%) allows for a transition from a reactive to a proactive maintenance strategy.

Conclusion. This paper presents a method for determining the thermal resistance coefficient of fouling and the heat transfer coefficient of a shell-and-tube heat exchanger for a small-capacity oil refinery by machine learning methods. In the course of the study, a verification thermal calculation of the shell-and-tube heat exchanger was performed using an iterative algorithm for solving a system of heat transfer and heat balance equations. It was shown that as the thermal fouling coefficient of the tube surface increased, the heat transfer coefficient decreased, and the outlet temperatures of the coolants deviated from the values corresponding to a clean unit. The effect of the physical and chemical properties of oil — density and viscosity — on the output parameters of the heat exchanger was also established.

Using the PySR and SISSO symbolic regression methods, analytical dependences of the thermal resistance coefficient of contaminants on the outlet temperatures of oil and diesel fuel, as well as on the oil density, were obtained. The root-mean-square error of the obtained expressions did not exceed $1.25 \cdot 10^{-8}$ and $2.34 \cdot 10^{-8}$ (m^2·°C)/W, respectively, demonstrating their high accuracy.

To predict the heat transfer coefficient over time, the FROLS and CatBoostRegressor algorithms were used within the NARX model. According to the ex-post forecast results, the error for the FROLS algorithm was RMSE = 0.013 W/(m^2·°C), and for CatBoostRegressor — RMSE = 0.036 W/(m^2·°C). Based on the dynamics of the predicted heat transfer coefficient, it was shown that a decrease in this parameter by 25–30% relative to the value of a clean heat exchanger was a justified criterion for scheduling maintenance.

Validation of the developed models was performed using industrial data and expert assessments of technologists, which confirmed the applicability of the proposed methodology under real operating conditions.

The practical significance of this work is that the developed method uses readily available operational data (outlet temperatures and oil density) to evaluate heat exchanger fouling and predict cleaning schedules, thereby improving energy efficiency and reducing unplanned downtime in oil refining.

In the future, it is expected that the application of the method will be expanded to other types of heat exchange equipment, as well as its integration into automated process control systems.

References

1. Elistratova Y, Seminenko A, Minko V. Relevance of Contamination Models for Diagnostics of Plate Heat Exchangers. *Bulletin of Belgorod State Technological University named after V.G. Shukhov*. 2020;5(10):33–40. https://doi.org/10.34031/2071-7318-2020-5-10-33-40

2. Antipov AI, Golubev LG, Mukhtarov YaS. The Effect of Deposits of Solids in Heat Exchange Equipment on Thermal Resistances and Power Supply Costs in the Oil Fields Dealing with Oil Preparation. *Power Engineering: Research, Equipment, Technology*. 2003;5–6:28–35.

3. Demin AM, Naumenko AP. Diagnostics of Heat Exchange Equipment on Basis of Operating Parameters of Diesel Fuel Hydrotreating Unit. *Omsk Scientific Bulletin.* 2019;166(4):84–88. https://doi.org/10.25206/1813-8225-2019-166-84-88

4. Pozevalkin VV, Polyakov AN. Implementation of a Digital Model of Thermal Characteristics Based on the Temperature Field. *Advanced Engineering Research (Rostov-on-Don).* 2024;24(2):178–189. https://doi.org/10.23947/2687-1653-2024-24-2-178-189

5. Gubareva KV, Eremin AV. Numerical Solution to the Problem of Thermal Conductivity in a Porous Plate with a Topology of Triply Periodic Minimal Surfaces. *Advanced Engineering Research (Rostov-on-Don).* 2025;25(1):23–31. https://doi.org/10.23947/2687-1653-2025-25-1-23-31

6. Konygin SB, Konovalenko DV, Kryuchkov DA. Estimating the Effect of Instrument Accuracy on the Accuracy of Mathematical Modeling of Quality Indicators of Oil Treatment for Transportation. *IOP Conference Series: Materials Science and Engineering*. 2020;862(3):032068. https://doi.org/10.1088/1757-899X/862/3/032068

7. Martins T, Spengler AW, Oliveira JLG, de Paiva KV, Seman LO. Active Control System to Prevent Malfunctioning Caused by the Pressure Difference in Gasket Plate Heat Exchangers Applied in the Oil and Gas Industry. *Sensors*. 2022;22(12):4422. https://doi.org/10.3390/s22124422

8. Gil'fanov KK, Shakirov RA. Neural Network Modeling of Thermal Hydraulic Efficiency of Promising Surface Heat Transfer Intensifiers. *Russian Aeronautics*. 2021;64(1):61–70. https://doi.org/10.3103/S1068799821010086

9. Tugashova LG, Zatonskiy AV. Comparison of Methods for Heat Exchanger Control. *Theoretical Foundations of Chemical Engineering*. 2021;55(1):53–61. https://doi.org/10.1134/S0040579520060226

10. Sahoo A, Radhakrishnan TK, Sankar Rao C. Modeling and Control of a Real Time Shell and Tube Heat Exchanger. *Resource-Efficient Technologies*. 2017;3(1):124–132. https://doi.org/10.1016/j.reffit.2016.12.001

11. Glagoleva OF, Kapustin VM, Piskunov IV, Usmanov MR. Controlling the Aggregative Stability of Feedstock Blends and Petroleum Products. *Petroleum Chemistry*. 2020;60(5):971–978. https://doi.org/10.1134/S0965544120090108

12. Kapustin VM, Rudin MG, Kukes SG. *Handbook of Oil Refiner*. Moscow: Khimiya; 2018. 416 p. (In Russ.)

13. Tugashova LG. *Increasing Energy Efficiency and Productivity at Fuel and Energy Complex Facilities Using Modeling and Optimization Methods*. Monograph. Almetyevsk: ASTU "HSO"; 2025. 101 p. (In Russ.)

14. Deryabin IA, Korolev VV, Sorokin GS. Using a Recurrent Neural Network for Solving Inverse Heat Conduction Problem with Application to Calculating the Temperature of Equipment of VVER-Based NPPs. *Nuclear Power Engineering*. 2024;(4):144–154. https://doi.org/10.26583/npe.2024.4.12

15. Xiaolin Jiang, Guanqi Liu, Jiaying Xie, Zhenpeng Hu. *Boosting SISSO Performance on Small Sample Datasets by Using Random Forests Prescreening for Complex Feature Selection*. arXiv:2409.19209

16. Muthyala M, Sorourifar F, Paulson JA. TorchSISSO: A PyTorch-Based Implementation of the Sure Independence Screening and Sparsifying Operator for Efficient and Interpretable Model Discovery. *Digital Chemical Engineering*. 2024;13:100198. https://doi.org/10.1016/j.dche.2024.100198

17. Tonda A. Review of PySR: High-Performance Symbolic Regression in Python and Julia. *Genetic Programming and Evolvable Machines*. 2025;26:7. https://doi.org/10.1007/s10710-024-09503-4

18. Zatonskiy AV, Tugashova LG. Identification of Parameters of a Dynamic Model of a Heat Exchange Apparatus. *Perm National Research Polytechnic University Bulletin. Electrotechnics, Information Technologies, Control Systems.* 2020;33:99–114. https://doi.org/10.15593/2224-9397/2020.1.06

About the Authors:

Larisa G. Tugashova, Cand.Sci. (Eng.), Associate Professor of the Department of Automation and Information Technologies, Almetyevsk State Technological University "Higher School of Petroleum" (186 a, Sovetskaya Str., Almetyevsk, 423462, Russian Federation), SPIN-код, ORCID, ScopusID, ResearcherID, tugashova@yandex.ru

Andrey V. Zatonskiy, Dr.Sci. (Eng.), Professor, Head of the Department of Automation and Information Technologies, Perm National Research Polytechnic University, Berezniki Branch (29, Komsomolsky Pr, Perm, 614990, Russian Federation), SPIN-код, ORCID, ScopusID, ResearchGate, zxenon@narod.ru

Claimed Contributorship:

LG Tugashova: formal analysis, investigation, methodology, writing – original draft preparation, writing – review & editing.

AV Zatonskiy: formal analysis, writing – original draft preparation, writing – review & editing.

Conflict of Interest Statement: **the authors declare no conflict of interest.**

The authors have read and approved the final version of the manuscript.

Об авторах:

Лариса Геннадьевна Тугашова, кандидат технических наук, доцент кафедры «Автоматизация и информационные технологии» Альметьевского государственного технологического университета «Высшая школа нефти» (423462, Российская Федерация, г. Альметьевск, ул. Советская, 186 а), SPIN-код, ORCID, ScopusID, ResearcherID, tugashova@yandex.ru

Андрей Владимирович Затонский, доктор технических наук, профессор, заведующий кафедрой «Автоматизация и информационные технологии» Березниковского филиала Пермского национального исследовательского политехнического университета (614990, Российская Федерация, г. Пермь, пр. Комсомольский, 29), SPIN-код, ORCID, ScopusID, ResearchGate, zxenon@narod.ru

Заявленный вклад авторов:

Л.Г. Тугашова: формальный анализ, проведение исследования, разработка методологии, написание черновика рукописи, написание рукописи – рецензирование и редактирование.

А.В. Затонский: формальный анализ, написание черновика рукописи, написание рукописи – рецензирование и редактирование.

Конфликт интересов: **авторы заявляют об отсутствии конфликта интересов.**

Авторы прочитали и одобрили окончательный вариант рукописи.

Received / **Поступила в редакцию** 16.02.2026
Reviewed / Поступила после рецензирования 13.03.2026
Accepted / **Принята к публикации** 23.03.2026

INFORMATION TECHNOLOGY, COMPUTER SCIENCE AND MANAGEMENT
ИНФОРМАТИКА, ВЫЧИСЛИТЕЛЬНАЯ ТЕХНИКА И УПРАВЛЕНИЕ

UDC 681.51:004.81:536.2
https://doi.org/10.23947/2687-1653-2026-26-2-2661

Original Empirical Research

Hardware Implementation of Fuzzy Logic Based on Thermal Memory Elements for Fault-Tolerant Control in Mechanical Engineering

EDN: PHGHYE

Olga V. Volodina[1], **Arkadiy A. Skvortsov**[1] ✉, **Margarita R. Rybakova**[1], **Marina V. Koryachko**[1,2]

[1] Moscow Polytechnic University, Moscow, Russian Federation
[2] Russian Technological University — MIREA, Moscow, Russian Federation
✉ skvortsovaa2009@yandex.ru

Abstract

Introduction. The automation of high-temperature processes (for example, laser welding) requires fault-tolerant real-time control systems. Traditional microprocessors exhibit critical software latencies, while promising in-memory computing platforms (MRAM, RRAM) are subject to thermal instability and state drift in hot zones. There is a significant scientific gap in the development of controllers capable of utilizing heat transfer physics as a computational medium, thereby converting thermal interference into a useful logic signal. This study is aimed at the computer modeling of heat flows in thermal memory elements (TME) to justify the hardware implementation of fuzzy logic inference. The research addresses the tasks of the topological formation of AND/OR logic gates and the analysis of the impact of dielectric insulation on the weight parameter adjustment.

Materials and Methods. The investigation of thermal processes in memory cells (a 2–5 μm aluminum film on a silicon substrate) was conducted by the finite element method in the Transient Thermal module of ANSYS Workbench. The cells were fabricated via vacuum electron-beam evaporation: aluminum tracks 75 μm wide and 4 mm long were formed on the silicon substrate. The structures were subjected to rectangular current pulses with a current density amplitude of $(2–2.5) \cdot 10^{10}$ A/m^2 and a duration of 1–2 ms; the local heating of the structures reached up to 30°C. To implement AND and OR logic gates, the interelement distances were topologically varied to 0.1 mm and 0.5 mm, respectively. Furthermore, SiO_2 dielectric pockets with a depth of 30 μm were introduced into the design for directional heat flow control.

Results. Based on the developed computer models in ANSYS Workbench, a comprehensive study of non-stationary thermal fields in TME structures was conducted. It is proven that the integration of SiO_2 dielectric insulation effectively controls the direction and power of the heat flow, eliminating parasitic energy dissipation. The modeling physically substantiates the feasibility of hardware formation of a fuzzy inference rule base directly within the crystal topology. It is established that varying the interelement distances is the key factor in logic setting: a distance of 0.1 mm between the input and output elements provides the realization of the OR logic operation, whereas a 0.5 mm distance corresponds to the AND operation.

Discussion. The data obtained confirm that thermal field superposition enables delay-free fuzzy logic operations. The logic gate models developed exhibit response times (1–2 ms) that are an order of magnitude lower than those of standard PLC (20–50 ms). In contrast to phase-change memory (PCM), the proposed method demonstrates robustness against external temperature noise through the algorithmic correction of logic thresholds. The primary limitation of this study is the thermal inertia of the silicon substrate, which accounts for a 5–7% discrepancy between the ANSYS simulation results and in-situ experiments.

Conclusion. The findings validate the feasibility of hardware-based topological design for a fuzzy inference rule base and the practical implementation of in-memory computing. This opens up promising prospects for integrating peripheral artificial intelligence (Edge AI) directly into the hot zones of industrial equipment.

Keywords: thermal memory, fuzzy logic, hardware fuzzy inference, fuzzification, in-memory computing, silicon structures

Acknowledgments. The authors would like to thank Professor S.G. Kalenkov, Dr.Sci. (Physics-Mathematics), and Professor A.N. Beskopylny, Dr.Sci. (Engineering), for stimulating discussions. We also appreciate the Journal editorial team and the reviewer for their professional assessment and valuable recommendations for improving the article.

Funding Information. This research was supported by the Russian Science Foundation, grant No. 25-79-10123.

For Citation. Volodina OV, Skvortsov AA, Rybakova MR, Koryachko MV. Hardware Implementation of Fuzzy Logic Based on Thermal Memory Elements for Fault-Tolerant Control in Mechanical Engineering. *Advanced Engineering Research (Rostov-on-Don).* 2026;26(2):2661. https://doi.org/10.23947/2687-1653-2026-26-2-2661

Оригинальное эмпирическое исследование

Аппаратная реализация нечеткой логики на базе элементов тепловой памяти для отказоустойчивого управления в машиностроении

О.В. Володина[1], А.А. Скворцов[1]✉, М.Р. Рыбакова[1], М.В. Корячко[1,2]

[1] Московский политехнический университет, г. Москва, Российская Федерация

[2] Российский технологический университет — МИРЭА, г. Москва, Российская Федерация

✉ skvortsovaa2009@yandex.ru

Аннотация

Введение. Автоматизация высокотемпературных процессов (например, лазерной сварки) требует отказоустойчивых систем управления в реальном времени. Традиционные микропроцессоры имеют критические программные задержки, а перспективные платформы вычислений в памяти (MRAM, RRAM) подвержены термической нестабильности и дрейфу состояний в горячих зонах. Существует научный пробел в знаниях о разработке контроллеров, использующих физику теплопереноса в качестве вычислительной среды, превращая тепловую помеху в логический сигнал. Цель данной работы — компьютерное моделирование тепловых потоков в элементах тепловой памяти (ЭТП) для обоснования аппаратной реализации нечеткого вывода. В исследовании решаются задачи топологического формирования вентилей AND/OR и анализа влияния диэлектрической изоляции на настройку весовых параметров.

Материалы и методы. Исследование тепловых процессов в ячейках памяти (алюминиевая плёнка, 2–5 мкм, на кремниевой подложке) были проведены методом конечных элементов в модуле Transient Thermal платформы ANSYS Workbench. Ячейки изготовлены методом вакуумного электронно-лучевого испарения: алюминиевые дорожки шириной 75 мкм и длиной 4 мм формировались на подложке кремния. Воздействие осуществлялось прямоугольными токовыми импульсами с амплитудой тока $(2–2{,}5) \cdot 10^{10}$ А/м^2 и длительностью 1–2 мс, локальный нагрев структур доходил до 30 °C. Для реализации логических вентилей AND и OR менялись межэлементные расстояния — 0,1 и 0,5 мм соответственно — топологическим способом. Для направленного управления тепловыми потоками в конструкцию были введены диэлектрические карманы из SiO_2 глубиной 30 мкм.

Результаты исследования. На основе разработанных компьютерных моделей в среде ANSYS Workbench проведено комплексное исследование нестационарных тепловых полей в структурах ЭТП. Доказано, что внедрение диэлектрической изоляции из SiO_2 позволяет эффективно управлять направлением и мощностью теплового потока, исключая паразитное рассеивание энергии. В ходе моделирования физически обоснована возможность аппаратного формирования базы правил нечеткого вывода непосредственно в топологии кристалла. Установлено, что варьирование межэлементных расстояний является ключевым фактором настройки логики: дистанция в 0,1 мм между входными и выходным элементами обеспечивает реализацию логической операции OR, а дистанция 0,5 мм — операции AND.

Обсуждение. Полученные данные подтверждают, что использование пространственного наложения тепловых полей позволяет реализовать нечеткие операции без программных задержек. Время реакции разработанных моделей логических вентилей (1–2 мс) на порядок превосходит показатели стандартных программируемых логических контроллеров (ПЛК) — 20–50 мс. В отличие от памяти на фазовых переходах предложенный метод демонстрирует

устойчивость к внешним температурным помехам за счет алгоритмической коррекции логических порогов. Основным ограничением работы является тепловая инерционность кремниевой подложки, которая обуславливает расхождение между результатами моделирования в ANSYS и натурными экспериментами на уровне 5–7 %.

Заключение. Полученные результаты подтверждают возможность аппаратного задания топологии базы правил нечеткого вывода и реализацию вычислений в памяти (in-memory computing). Это открывает перспективы для внедрения периферийного искусственного интеллекта (Edge AI) непосредственно в горячие зоны промышленного оборудования.

Ключевые слова: тепловая память, нечеткая логика, аппаратный логический вывод, фаззификация, вычисления в памяти, кремниевые структуры

Благодарности. Авторы выражают признательность доктору физико-математических наук, профессору Каленкову С.Г. и доктору технических наук, профессору Бескопыльному А.Н. за стимулирующие дискуссии. Также благодарим редакционную команду журнала и рецензента за компетентную экспертизу и ценные рекомендации по улучшению статьи.

Финансирование. Исследование выполнено в рамках гранта Российского научного фонда РНФ № 25-79-10123.

Для цитирования. Володина О.В., Скворцов А.А., Рыбакова М.Р., Корячко М.В. Аппаратная реализация нечеткой логики на базе элементов тепловой памяти для отказоустойчивого управления в машиностроении. *Advanced Engineering Research (Rostov-on-Don).* 2026;26(2):2661. https://doi.org/10.23947/2687-1653-2026-26-2-2661

Introduction. The current stage of development of global mechanical engineering, which is characterized by the transition to the concepts of Industry 4.0 and 5.0, places high demands on the reliability of automation systems [1]. Technological processes, such as high-precision casting, laser and electron beam welding, as well as multistage heat treatment, operate under the impact of extreme factors: high-intensity electromagnetic fields, vibration loads, and ultra-high temperature gradients. Under extreme temperature conditions and electromagnetic interference, traditional von Neumann microprocessor architecture exhibits a critical reduction in efficiency [2, 3]. Up to 80% of the PLC computational time and energy is consumed by data transmission over vulnerable buses, causing response delays of 20–50 ms. Standard microprocessors require cumbersome protection and shielding systems against electromagnetic interference. Moreover, the implementation of intelligent control algorithms, in particular fuzzy logic, in software is associated with critical delays that arise due to the multiple conversion of signals in the “analog-to-digital converter (ADC) — processor — digital-to-analog converter (DAC)” chain and the sequential execution of the microcontroller software code. High-speed production system control algorithms must operate without latency [4], necessitating the use of parallel hardware processors where logical inference is independent of the CPU clock rate. The transition to alternative in-memory computing (IMC) platforms will enable signal processing directly in the physical environment (in situ).

One of the possible directions for implementing the IMC algorithm is the creation of multi-valued logic circuits [5], which provides the implementation of fuzzy logic in circuit design through changing the physical properties of the material, such as resistance or thermal conductivity. The most studied thermal method for implementing IMC is phase-transition memory (pulse code modulation, PCM) [6], whose operating algorithm is based on encoding information through a change in the aggregate state of chalcogenide glass as a result of an increase in temperature under heating. But it must be taken into account that the use of PCM in hot shops (for example, in the laser welding zone) faces the problem of spontaneous phase switching due to the high external thermal background, which makes them unsuitable for emergency protection systems.

Memristor structures (RRAM) [7], which are characterized by similar problems, are also considered as basic elements of hardware fuzzy logic of the second type. Memristor crossbars are subject to thermal drift of resistive states, which results in the accumulation of errors in the weight coefficients of fuzzy inference. A logical continuation of this approach is the field of thermotronics [8] (phononics [9]). Experiments have been conducted that demonstrate the operation of nanoscale thermal logic gates (NOT, AND, OR) with power consumption on the order of femtojoule [10]. The study of wave-based thermoplastic logic gates built using thermally tunable metamaterials has led to the conclusion that it is possible to create highly complex, combinable circuits embedded directly into the structural material [11]. However, these solutions are purely laboratory-scale: they operate at the nanoscale and require high-quality insulation from macroscopic thermal noise.

Thus, there is a clear gap in current scientific knowledge: existing solid-state solutions (PCM, RRAM) are sensitive to external thermal interference, and nanophononic devices are not scalable for industrial environments. A solution to this problem could be the development of macroscopic thermal memory elements (MTME) that utilize the superposition of thermal fluxes for computation, converting harmful equipment overheating into a useful signal.

Unlike classical electronics, thermal memory uses the dynamic heating range [12] as an analog value. The dynamic change in TME temperature directly reflects the membership functions of fuzzy sets. Thus, the thermal memory element does not simply become a storage device, but turns into an active computing environment that implements fuzzy logic algorithms of the second type.

Unlike classical algorithms, Type-2 Fuzzy Logic operates on membership functions that are themselves fuzzy sets. The degree of membership here is not a specific number, but a range (interval). Fuzzy logic algorithms can directly process linguistic variables and perform an intuitive decision-making process similar to that of humans [13], which allows them to be used in fault-tolerant control systems (FTCS) [14].

The objective of this work is to develop a method for hardware implementation of fuzzy inference based on thermal memory structures. The proposed method will combine the advantages of thermal stability, system noise immunity, and intelligent data processing to solve the problem of creating next-generation fault-tolerant control systems for modern mechanical engineering.

Materials and Methods. The thermal memory elements discussed in this paper are metal film-on-silicon substrate structures. Unlike standard digital memory cells, these elements store information in a thermal state. As an active computing medium, they integrate storage, processing, and fuzzy logic in a single cell, exhibiting strong sensitivity to input energy. Current pulses serve as input signals: heat distribution from local heating implements AND/OR operations. This enables the creation of transistor-free neuromorphic networks for response recognition with energy efficiency of up to 10^{-15} J/operation.

For this reason, the authors used structures consisting of metallization tracks deposited on a silicon wafer through electron beam evaporation (Fig. 1) as the thermal memory cell. A 450-μm-thick silicon wafer with a resistivity of 30 Ω·cm served as the substrate. Aluminum films with a thickness of h = 3–5 μm served as the conductive layer. The metallization track width was b = 75 μm, and its length was l = 4 mm. Probes (1–12) were used to record oscillograms during the passage of current pulses [12]. Single current pulses were generated using an original setup. The duration of a rectangular current pulse did not exceed τ = 1 ms, and the amplitude $j = 8 \cdot 10^{10}$ A/m^2. The ohmic resistance of the structure was in the range R = 0.3–0.5 Ω.

Preliminary studies have shown that this system operates well up to a temperature of T = 550 °C. Further increases in thermal loads lead to the onset of degradation processes. These processes are associated with contact melting at the Al–Si interface (T_e = 577 °C) and electrodiffusion processes, resulting in irreversible changes in the structure of the metal track [15].

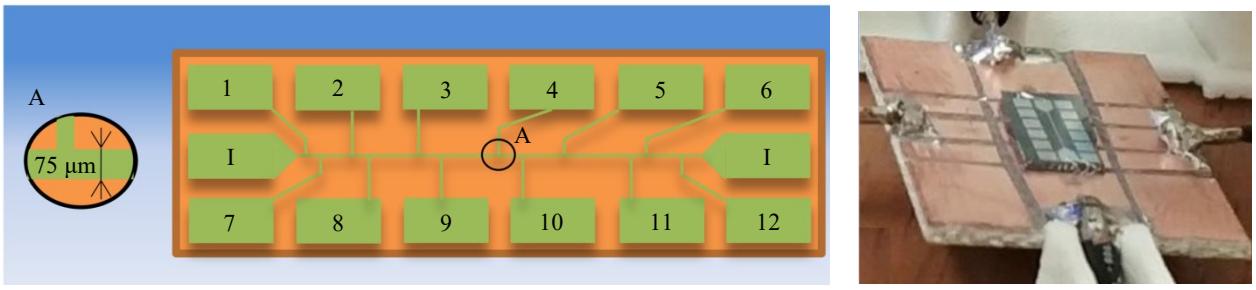

a) *b)*

Fig. 1. Hardware implementation of a thermal memory cell:
a — schematic representation; *b* — experimental electrophysical setup

To conduct a computational experiment and evaluate the spatial distribution of thermal fields, the finite element method in the Transient Thermal module of the ANSYS Workbench platform was used. The numerical solution through constructing a thermal model based on the finite element method in the ANSYS engineering analysis system has proven to be an effective approach for calculating the temperature fields of various mechanical engineering objects [16].

The three-dimensional geometric model (Fig. 2) included a 2 mm thick single-crystal silicon substrate with conductive aluminum tracks (4 mm long, 75 μm wide, 3 μm thick) located on its surface, serving as TME. To specifically control the heat flow and eliminate mutual influence of the input elements, dielectric heat-insulating pockets made of silicon dioxide (SiO_2) 30 μm deep and 1 μm thick were integrated into the structure.

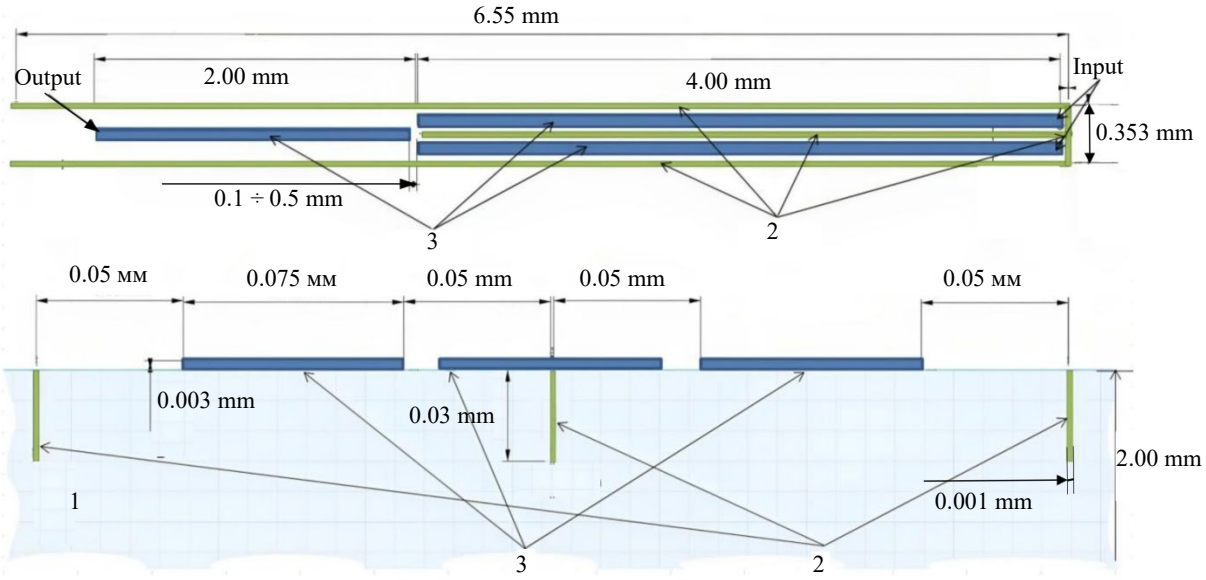

Fig. 2. Logic gate structure geometry: 1 — silicon wafer;
2 — insulating dielectric layers; 3 — metal tracks

When setting up the solver, the following thermodynamic properties of materials were specified:
1. Silicon (Si): density — 2330 kg/m³, thermal conductivity — 148 W/(m·°C), specific heat — 712 J/(kg·°C).
2. Silicon dioxide (SiO_2): density — 2220 kg/m³, thermal conductivity — 1.5 W/m·°C), specific heat — 745 J/(kg·°C).
3. Aluminum (Al): density — 2689 kg/m³, thermal conductivity — 237.5 W/m·°C), specific heat — 951 J/(kg·°C).
The computational unstructured mesh was generated in the built-in ANSYS Meshing module (Fig. 3).

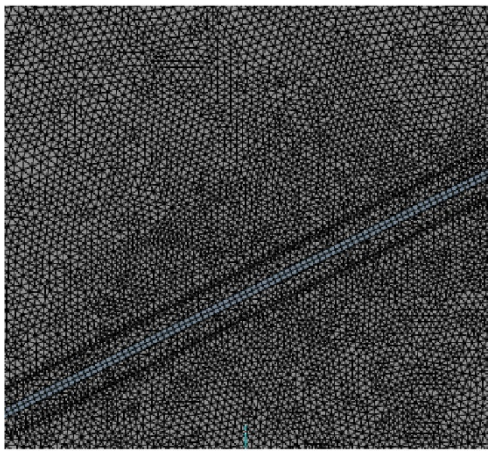

Fig. 3. Image of the constructed mesh on a model of a silicon wafer with a thermal memory element
in a 100 μm wide dielectric pocket

Convective heat exchange with the environment was specified as the boundary conditions on the free surfaces of the silicon wafer, with a heat transfer coefficient of 5 W/(m²·°C). Thermal exposure was modeled by specifying the heat dissipation power distributed over the volume of the aluminum tracks. The logic of the gate operation was verified through evaluating the temperature at the output TME with varying thermal clearance distances (from 0.1 to 0.5 mm).

To use this physical structure as a fuzzy logic calculator, a direct connection must be established between the thermophysical processes and the mathematical apparatus of fuzzy sets. To establish a hardware correspondence between a specific numerical value of the input variable (signal from the temperature sensor) and the value of the membership function of the corresponding term of the input linguistic variable (terms “logic 0”, “logic 1”, “critical overheating”), a procedure for finding the values of the membership functions of fuzzy sets (terms) based on clear initial data was carried out — the fuzzification process.

Fuzzification and Input Weight Generation. In the developed TME architecture, input electrical pulses from sensors are converted into local thermal fields directly within the aluminum track — silicon substrate structure. The key parameter at this stage is the input signal weight. While in classical software algorithms, the weight is defined by an abstract numerical coefficient, in the proposed hardware implementation, it has a specific physical meaning, characterizing the

intermediate state of the system between logical 0 and 1. The weight is determined by the amount of thermal energy released (heat flow power), which depends on the amplitude of the current pulse ($2 \cdot 10^{10} < I_м < 2.5 \cdot 10^{10}$ A/m^2) and its duration (1–2 ms). The higher the values of these electrical parameters, the more intense the local Joule heating of the element. A physical increase in the temperature of the TME is equivalent to a mathematical increase in the degree of membership of the input variable to the fuzzy term "logic 1". Thus, the temperature dynamics T(t) of the TME acts as an analog carrier of information about membership in a fuzzy set.

Thus, once the membership degrees of several inputs are established, the system must perform fuzzy inference to generate the hardware output according to a rule base. Unlike microprocessors, where logical inference requires resource-intensive mathematical calculations, in the TME matrix, this procedure is implemented at the hardware level by adding heat fluxes in the volume of the silicon substrate. To level out the uncontrolled mutual influence of thermal memory elements and to set strict inference rules (formation of the rule base topology), dielectric pockets made of silicon oxide (SiO_2) are used (Fig. 2).

Dielectric pockets act as thermal barriers, strictly directing heat flows to the weight (output) element of the matrix for performing intersection or union operations.

Hardware Implementation of AND Intersection and OR Union Operations. To create fault-tolerant control systems implementing hardware fuzzy logic directly within the structure of a memory device, the authors investigated mechanisms for controlling the spatial distribution of thermal fields. Using SolidWorks software, 3D models were constructed demonstrating the topological hardware implementation of AND and OR logic operations based on thermal memory elements (TME).

OR Operation (MAX / Union). This is implemented with a minimum distance between elements (0.1 mm) (Figs. 4, 5). The thermal power of even one heated input under conditions of localized heat flow pockets is sufficient to switch the output element to the "logic 1" state (heating by ≈ 2 °C), which corresponds to the recording of a critical event on any of the channels.

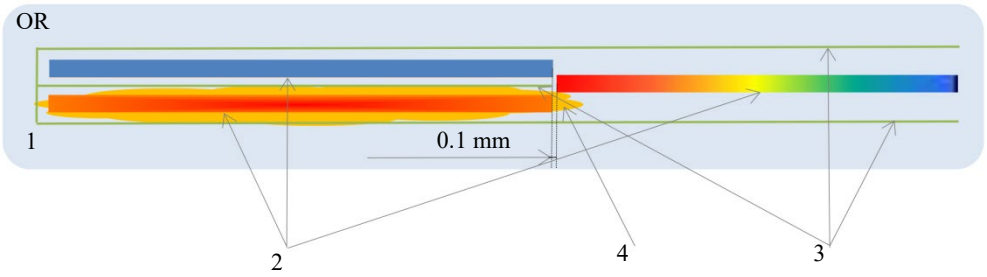

Fig. 4. OR gate hardware implementation (input–output distance: 0.1 mm): 1 — Si wafer; 2 — metal tracks; 3 — dielectric insulation; 4 — heat flow direction

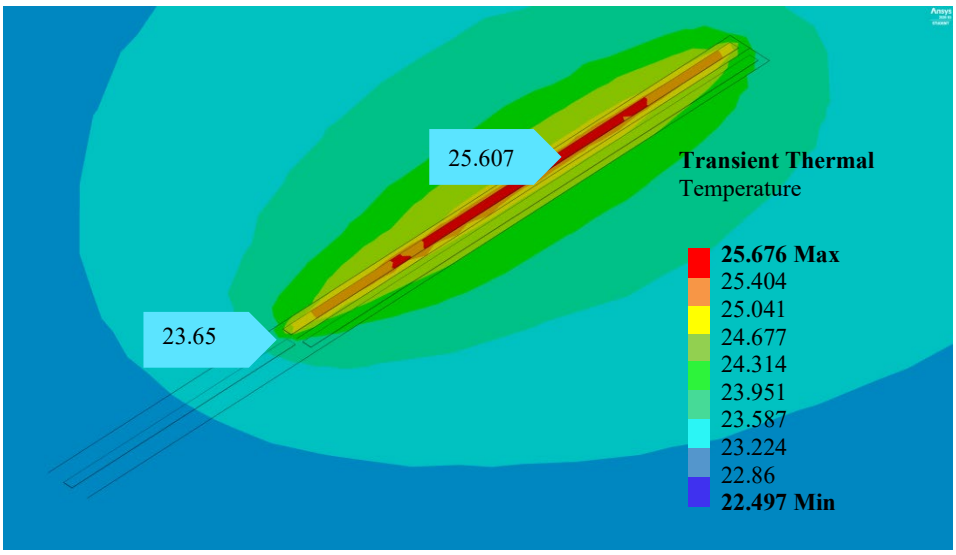

Fig. 5. Simulation model of OR logic gate: temperature field at a distance of 0.1 mm between input and output TME (heating of one input element)

AND (MIN / Intersection) Operation. This is implemented through increasing the distance to 0.5 mm (Figs. 6, 7). In this case, the output element reaches the response threshold only when both inputs are heated simultaneously, which physically emulates the intersection of conditions (e.g., "high temperature" and "long exposure time").

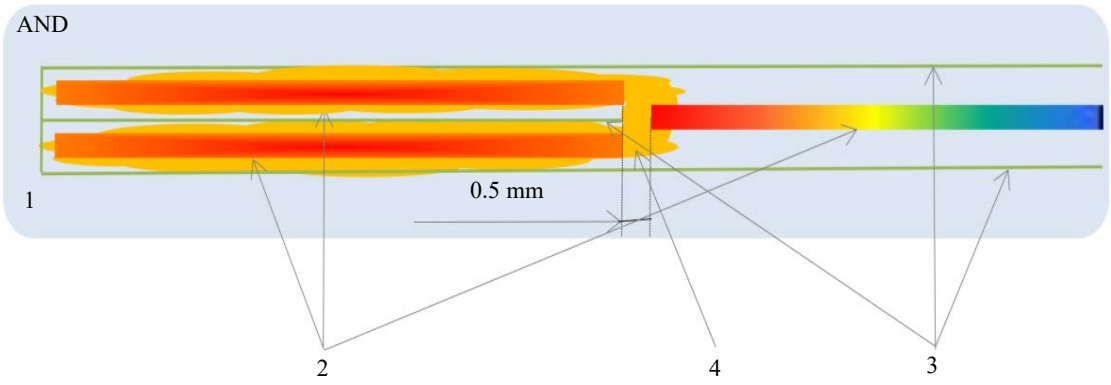

Fig. 6. Hardware implementation of AND operation, distance between input and output elements is 0.5 mm: 1 — silicon wafer; 2 — metal tracks; 3 — insulating dielectric layers; 4 — heat flow direction

Simulation modeling of the operation of logic gates was performed on the ANSYS Workbench platform (Figs. 5, 7) using the Transient Thermal module for non-stationary thermal calculations.

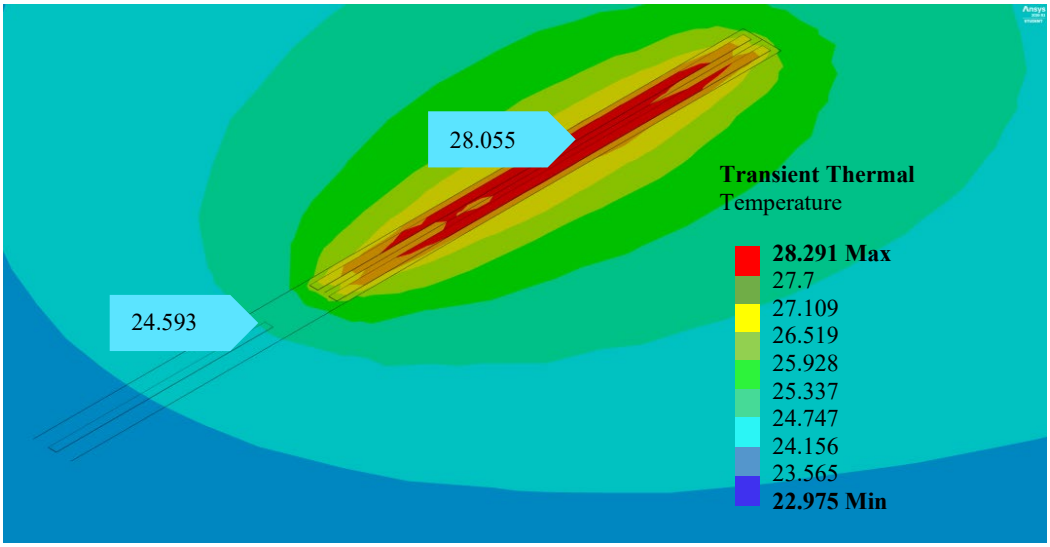

Fig. 7. Simulation model of AND logic gate: temperature field at a distance of 0.5 mm between input and output TME (simultaneous heating of two input elements)

The simulation results (Figs. 5, 7) fully confirmed the efficiency of using thermal insulation (SiO_2) and the selected geometric distances for adjusting the weight parameters of the hardware fuzzy inference.

Research Results. In the course of the study, the concept of hardware implementation of fuzzy logical inference based on thermal memory elements (TME) was theoretically substantiated. It has been established that the use of a planar metallization system on a silicon substrate allows bypassing the hardware limitations of the classical von Neumann architecture through transferring the fuzzification and defuzzification processes directly into the physical environment of the semiconductor.

Computer simulation results in ANSYS Workbench have confirmed that the proposed spatial organization of thermal field superposition within the material enables successful implementation of basic fuzzy logic operations. It is found that the ability to define the fuzzy rule base topology enables precise spatial arrangement of the TME matrix and the use of insulating dielectric pockets made of silicon oxide (SiO_2). Optimal linear dimensions between the input TME and the output weight TME are specified: a distance of 0.1 mm between elements guarantees the execution of the combination operation (logic OR), and an increase in the thermal gap to 0.5 mm establishes rules for the intersection operation (logic AND), switching the output element only under combined thermal effect.

The simulation results prove that the hardware implementation of fuzzy logic based on the electronic control platform allows overcoming the limitations of standard microprocessor systems in the tasks of automating fast-moving processes.

The response time of the developed logic gate models is 1–2 ms, compared to the typical 20–50 ms processing cycle for fuzzy algorithms in standard PLC. The use of macroscopic heat transfer as a useful signal distinguishes the proposed TME from PCM (phase-change memory) technologies, which are subject to spontaneous switching under external thermal conditions. Unlike memristor structures (RRAM), TME are more resistant to temperature drift in hot zones due to the use of a unique floating-zero algorithm.

Discussion. The results of the study have practical significance in the fault-tolerant process control (PC) for automated laser (or electron beam) welding of thin-walled structures. This PC is characterized by high-speed thermophysical reactions (millisecond range) and the presence of electromagnetic interference from power inverters, making the use of conventional microprocessors for fuzzy control impossible without special protection techniques.

A severe violation of this PC is the formation of weld defects (burn-through, evaporation of alloying elements, or critical thermal stresses). To prevent defects, it is required to simultaneously monitor two parameters: the temperature of the welding pool (determined by a non-contact pyrometer) and the time it is maintained at this temperature (or laser pump current).

Fault-tolerant control of this PC can be built on the basis of a hardware implementation of a logic AND gate, which is a three-element structure of thermal memory: two input TME (input A is the temperature factor, input B is the time or power factor) and one output (weight) element that generates a command for correction or emergency shutdown of the process (Fig. 8).

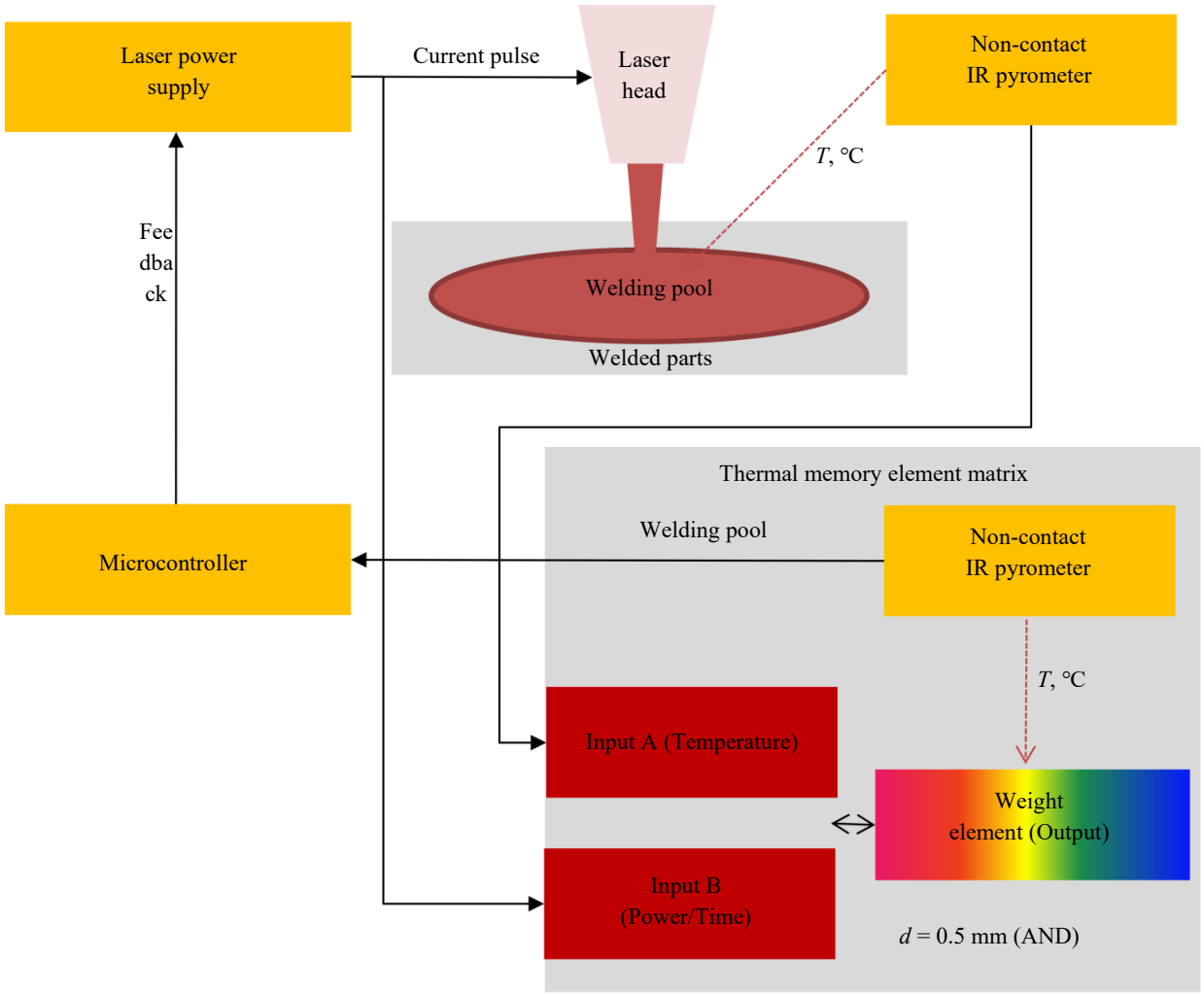

Fig. 8. Schematic diagram for integrating fault-tolerant computer based on TME into laser welding process

The high response rate is due to the fact that logical inference takes place directly in the physical medium, without intermediate analog-to-digital conversion. The implemented AND gate (based on a three-element structure) physically sums the laser power and welding pool temperature factors, allowing the system thermal state to be interpreted as a linguistic variable.

Integrating an active computing environment into a laser welding PC solve the following problems:

– prevent irreversible process failures (weld microstructure degradation, thermal drift, or burn-through);

– adjust energy supply within 1–2 ms;

– TME matrix enables the implementation of an Edge Computing paradigm directly in the hot zone of the process. This relieves the load on industrial data networks and eliminates latency in critical decision-making.

Hardware implementation of fuzzy logic on TME solves the problems of high-temperature diagnostics in hot workshops (for example, foundries), where standard semiconductor controllers inevitably fail or are forcibly turned off by built-in overheating protection systems [17].

The basic limitation of the TME operation is the thermal inertia of the silicon substrate, which causes a discrepancy between the results of ANSYS simulations and field experiments at a level of 5–7%. It should also be noted that the proposed method is focused on high-speed threshold logic (protection against defects) and does not replace high-precision numerical control systems.

Conclusion. A hardware implementation method for fuzzy inference using thermal memory elements (TME) in industrial automation systems is proposed and validated in the study.

1. A method for organizing information storage and a floating-zero algorithm have been developed, providing adaptive correction of logic thresholds. This allows for the stabilization of logic cell operation under non-stationary temperature conditions typical of industrial environments.

2. The feasibility of topological formation of a fuzzy inference rule base was validated through simulation. It was found that varying the interelement distance in a silicon structure (0.1 mm for the OR operation, and 0.5 mm for the AND operation) allowed logical operations to be emulated directly through the distribution of thermal fields.

3. The efficiency of using TME as peripheral computing links in extreme impact zones is substantiated. It is shown that the use of the proposed structures reduces the system response time to a thermal event to 1–2 ms, which is sufficient to prevent burn-throughs and defects during laser welding.

Prospects for further research suggest the following. Based on the successful hardware implementation of basic logic gates (AND/OR), further research should be pursued in the following areas.

1. Scaling the computing architecture: moving from single logic gates to topological synthesis of multidimensional TME matrices. This will enable hardware implementation of complex fuzzy inference rule bases operating with three or more input linguistic variables for multicriteria process control. According to modern research, multicriteria optimization, taking into account conflicting criteria (for example, finding the optimal temperature), is in demand for improving product quality and the efficiency of complex chemical reactions. Hardware implementation will allow such multicriteria calculations to be transferred directly to the physical environment of the equipment.

2. Optimizing system performance: since simulations have revealed a 5–7% error due to the thermal inertia of the silicon substrate, a promising area is exploring alternative dielectric materials and topologies (for example, localized substrate thinning). This will minimize parasitic heat dissipation and reduce controller response time to the submillisecond range.

3. Hardware-in-the-Loop (HIL) simulation: testing in which a physical prototype of a fault-tolerant computer based on an electronic process platform will be integrated into the control loop of a digital twin of real process equipment. This will enable the robustness of the proposed architecture (Edge AI) to be assessed under conditions of real-world high-frequency electromagnetic interference generated by power welding inverters.

References

1. Praveen Kumar Reddy Maddikunta, Quoc Viet Pham, Prabadevi B, N Deepa, Kapal Dev, Thippa Reddy Gadekallu, et al. Industry 5.0: A Survey on Enabling Technologies and Potential Applications. *Journal of Industrial Information Integration*. 2022;26:100257. https://doi.org/10.1016/j.jii.2021.100257

2. Hao Wang, Bin Sun, Shuzhi Sam Ge, Jie Su, Ming Liang Jin. On Non-Von Neumann Flexible Neuromorphic Vision Sensors. *npj Flex Electron.* 2024;8:28. https://doi.org/10.1038/s41528-024-00313-3

3. Zhou Wenjun, Zhu Chuan, Ma Jianmin. Single-Layer Folded RNN for Time Series Prediction and Classification under a Non-Von Neumann Architecture. *Digital Signal Processing*. 2024;147:104415. https://doi.org/10.1016/j.dsp.2024.104415

4. Nada AA, Bayoumi MA. Development of Embedded Fuzzy Control Using Reconfigurable FPGA Technology. *Automatika.* 2024;65(2):609–626. https://doi.org/10.1080/00051144.2024.2313904

5. Jiayang Wang, Yuzhe Lin, Chenhao Hu, Shiqi Zhou, Shenyu Gu, Mengjie Yang, et al. A Kind of Optoelectronic Memristor Model and Its Applications in Multi-Valued Logic. *Electronics (MDPI)*. 2023;12(3):646. https://doi.org/10.3390/electronics12030646

6. Sebastian A, Le Gallo M, Khaddam-Aljameh R, Eleftheriou E. Memory Devices and Applications for In-Memory Computing. *Nature Nanotechnology*. 2020;15:529–544. https://doi.org/10.1038/s41565-020-0655-z

7. Haghzad Klidbary S, Javadian M, Omidi R, Hasanzadeh RPR. Memristor Crossbar-Based Hardware Implementation of Type-2 Fuzzy Membership Function and On-Chip Learning. *International Journal of Engineering*, 2021;34(9):2180–2188. https://doi.org/10.5829/ije.2021.34.09c.15

8. Ben-Abdallah Ph, Biehs S-A. Thermotronics: Towards Nanocircuits to Manage Radiative Heat Flux. *Zeitschrift fur Naturforschung A*. 2016;72(2):151–162 https://doi.org/10.1515/zna-2016-0358

9. Lei Wang, Baowen Li. Thermal Memory: A Storage of Phononic Information. *Physical Review Letters.* 2008;101:267203. https://doi.org/10.1103/PhysRevLett.101.267203

10. Hui Wang, Noordzij N, Mikhailov M, Steinhauer S, Descamps Th, Oksenberg E, et al. Attojoule Superconducting Thermal Logic and Memories. *Nano Letters.* 2025;25(11):4401–4407. https://doi.org/10.1021/acs.nanolett.4c06545

11. Fort E, Mousa M, Nouh M. Thermoelastic Wave-Based Logic for Mechanically Cognitive Materials. *arXiv:2511.00647* 2025. https://doi.org/10.48550/arXiv.2511.00647

12. Skvortsov AA, Pshonkin DE, Volodina OV, Nikolaev VK. Metallization System as a Part of Thermal Memory. *Heliyon.* 2023;9(5): e15797. https://doi.org/10.1016/j.heliyon.2023.e15797

13. Haziqah B, Idris A. Temperature Control in a Shower Using Fuzzy Logic. *Proceedings of Science and Mathematics*. 2024;24:56–64.

14. Riaz U, Amin AA, Tayyeb M. Design of active fault-tolerant control system for Air-fuel ratio control of internal combustion engines using fuzzy logic controller. *Science Progress*. 2022;105(2):1–29. https://doi.org/10.1177/00368504221101962

15. Kulchin YuN, Skvortsov AA, Nikolaev VK, Volodina OV. Development of Thermal Memory Cells on Silicon Using the Floating Zero Algorithm. *Scientific Reports*. 2025;15:5184. https://doi.org/10.1038/s41598-025-89566-0

16. Alexandrova AA, Koledin SN. Optimal Temperature Calculation for Multicriteria Optimization of the Hydrogenation of Polycyclic Aromatic Hydrocarbons by NSGA-II Method. *Advanced Engineering Research (Rostov-on-Don).* 2024; 24(1):109–118. https://doi.org/10.23947/2687-1653-2024-24-1-109-118

17. Vasiliev A. LED Luminaires for Hot Shops. *Electrical Engineering Market Magazine.* 2025;(2):62–65. (In Russ.)

About the Authors:

Olga V. Volodina, Senior Lecturer of the Department of Dynamics, Strength of Machines and Resistance of Materials, Moscow Polytechnic University (38, Bolshaya Semyonovskaya Str., Moscow, 107023, Russian Federation), SPIN-code, ORCID, ScopusID, ResearcherID, moosbeere_O@mail.ru

Arkadiy A. Skvortsov, Dr.Sci. (Phys.-Math.), Head of the Department of Dynamics, Strength of Machines and Resistance of Materials, Moscow Polytechnic University (38, Bolshaya Semyonovskaya Str., Moscow, 107023, Russian Federation), SPIN-code, ORCID, ScopusID, ResearcherID, ResearchGate, skvortsovaa2009@yandex.ru

Margarita R. Rybakova, Senior Lecturer of the Department of Dynamics, Strength of Machines and Resistance of Materials, Moscow Polytechnic University (38, Bolshaya Semyonovskaya Str., Moscow, 107023, Russian Federation), SPIN-code, ScopusID, sopr_kaf@mospolytech.ru

Marina V. Koryachko, Cand.Sci. (Phys.-Math.), Associate Professor of the Department of Higher Mathematics-3, Russian Technological University — MIREA (78, Vernadsky Ave., Moscow, 119454, Russian Federation), SPIN-code, ORCID, ScopusID, ResearcherID, ResearchGate, m.v.koryachko@gmail.com

Claimed Contributorship:

OV Volodina: conceptualization, methodology, software, investigation, “floating zero” algorithm development, writing – original draft preparation, visualization.

AA Skvortsov: supervision, conceptualization, methodology, validation.

MR Rybakova: formal analysis, investigation.

MV Koryachko: formal analysis, validation.

Conflict of Interest Statement: **the authors declare no conflict of interest.**

All authors have read and approved the final version of manuscript.

Об авторах:

Ольга Вячеславовна Володина, старший преподаватель кафедры «Динамика, прочность машин и сопротивление материалов» Московского политехнического университета (107023, Российская Федерация, г. Москва, ул. Большая Семёновская, 38), SPIN-код, ORCID, ScopusID, ResearcherID, moosbeere_O@mail.ru

Аркадий Алексеевич Скворцов, доктор физико-математических наук, заведующий кафедрой «Динамика, прочность машин и сопротивление материалов» Московского политехнического университета (107023, Российская Федерация, г. Москва, ул. Большая Семёновская, 38), SPIN-код, ORCID, ScopusID, ResearcherID, ResearchGate, skvortsovaa2009@yandex.ru

Маргарита Рушановна Рыбакова, доцент кафедры «Динамика, прочность машин и сопротивление материалов» Московского политехнического университета (107023, Российская Федерация, г. Москва, ул. Большая Семёновская, 38), SPIN-код, ScopusID, sopr_kaf@mospolytech.ru

Марина Валерьевна Корячко, кандидат физико-математических наук, доцент кафедры «Высшая математика-3» МИРЭА — РТУ (119454, Российская Федерация, г. Москва, пр. Вернадского, 78), SPIN-код, ORCID, ScopusID, ResearcherID, ResearchGate, m.v.koryachko@gmail.com

Заявленный вклад авторов:

О.В. Володина: концептуализация, методология, программное обеспечение, проведение исследования, разработка алгоритма плавающего нуля, написание черновика рукописи, визуализация.

А.А. Скворцов: научное руководство, концептуализация, методология, валидация результатов.

М.Р. Рыбакова: формальный анализ, проведение исследования.

М.В. Корячко: формальный анализ, валидация результатов.

Конфликт интересов: **авторы заявляют об отсутствии конфликта интересов.**

Все авторы прочитали и одобрили окончательный вариант рукописи.

Received / **Поступила в редакцию** 10.03.2026
Reviewed / Поступила после рецензирования 17.04.2026
Accepted / **Принята к публикации** 07.05.2026

INFORMATION TECHNOLOGY, COMPUTER SCIENCE AND MANAGEMENT
ИНФОРМАТИКА, ВЫЧИСЛИТЕЛЬНАЯ ТЕХНИКА И УПРАВЛЕНИЕ

UDC 621.395.4
https://doi.org/10.23947/2687-1653-2026-26-2-2221

Original Theoretical Research

Analytical Model of the Buffer Memory of an OpenFlow Switch in a Software-Defined Network (SDN)

Gennady V. Slyusarev, Valery P. Mochalov, Dar'ya V. Gosteva ✉
North-Caucasus Federal University, Stavropol, Russian Federation
✉ DVGus@yandex.ru

EDN: MPFRRV

Abstract

Introduction. Reliable identification of the probabilistic and temporal features of switching nodes is required for assessing the quantitative characteristics of software-defined networks. Widely used queuing theory (QT) methods only approximately specify and model the processes in an OpenFlow switch and its buffer memory. This results in understated and unrealistic performance estimates for the designed network equipment, causing switch buffer overloading and packet loss. A different modeling approach can solve this problem. The objective of this paper is to develop and study an analytical model for the buffer memory of an OpenFlow switch in an SDN using advanced techniques.

Materials and Methods. The discrete Laplace-Stieltjes transform was used. Statistical characteristics of packet flows and the throughput of communication channels for a given packet loss probability were taken into account. The OpenFlow switch buffer memory model was based on the mathematical apparatus of the QT. It was constructed under the assumption of recurrence of input data flows with batch arrivals. The model was based on schematic representations of the switch structure, its record set, and a graph description of the transmission of network packets leaving the switch. We started with schematic representations of the switch structure, its record set, and a graph description of the transmission of network packets exiting the switch. Two model assumptions were taken as acceptable:

– arbitrary distribution of the relationship between the volume of data flows and their service time;

– discreteness of the distribution of the information flow structure.

Results. The developed model integrated the probability of packet flow loss, their statistical characteristics, the throughput of computing devices, and the multiphase service procedure. When testing the model performance, we assumed that the switch load increased from 0.1 to 0.9, and the loss probability — from 10^{-3} to 10^{-6}. For these metrics, we determined how the switch load affected the buffer memory size and latency. In the first case, the minimum value (memory capacity) was 0.201, the maximum — 10564. In the second, they were 0 and 470 ms, respectively. For simulation modeling, the minimum time was 0 ms, the maximum — 2300 ms. The simulation and analytical modeling indicators were close at loads below 50% and increased several times at loads above 50%. The indicators increased sharply with loads up to 70%, and then increased exponentially.

Discussion. At low network loads, queues did not overflow, packets were not lost, and linear dependences were maintained. At medium and high loads, packet flow processing was described by nonlinear dependences. The results of analytical and simulation modeling diverged due to the explosive nature of self-similar network traffic and its approximate description by the Pareto distribution. Switch load determined the feasibility of the proposed approach. The model is suitable for designing elements of software-defined networks to analyze their resilience under various information impacts.

Conclusion. The proposed SDN analytical model determined the values and variances of the switch buffer memory size, as well as the memory capacity for constructing address flow tables. The solution performance was tested with switch loads ranging from 0.1 to 0.9. It is planned to create a model that takes into account request flows from both the external network and the server.

Keywords: improving queueing theory methods, OpenFlow buffer memory analytical model, network packet loss, switch simulation modeling

Acknowledgements. The authors would like to thank the Editorial board and the reviewers for their attentive attitude to the article and for the specified comments that improved its quality.

For Citation. Slyusarev GV, Mochalov VP, Gosteva DV. Analytical Model of the Buffer Memory of an OpenFlow Switch in a Software-Defined Network (SDN). *Advanced Engineering Research (Rostov-on-Don).* 2026;26(2):2221. https://doi.org/10.23947/2687-1653-2026-26-2-2221

Оригинальное теоретическое исследование

Аналитическая модель буферной памяти OpenFlow коммутатора программно управляемой сети SDN

Г.В. Слюсарев, В.П. Мочалов, Д.В. Гостева ✉

Северо-Кавказский федеральный университет, г. Ставрополь, Российская Федерация

✉ DVGus@yandex.ru

Аннотация

Введение. Достоверное выявление вероятностно-временных особенностей узлов коммутации необходимо для оценки количественных характеристик программно конфигурируемых сетей. Широко используемые методы теории массового обслуживания (ТМО) лишь приближенно определяют и моделируют процессы в коммутаторе OpenFlow и его буферной памяти. Это ведет к получению заниженных, не реалистичных характеристик проектируемых сетевых устройств, перегрузке буферной памяти коммутаторов и потере сетевых пакетов. Проблему может решить иной подход к моделированию. Цель представленной работы — создание и исследование аналитической модели буферной памяти OpenFlow коммутатора программно управляемой сети SDN с использованием усовершенствованных методов ТМО.

Материалы и методы. Задействовали аппарат дискретного преобразования Лапласа-Стилтьеса. Учитывались статистические характеристики потоков пакетов и пропускная способность каналов связи при заданной вероятности потерь пакетов. Модель буферной памяти коммутатора OpenFlow базируется на математическом аппарате ТМО. Его строили в предположении рекуррентности входных потоков данных с групповым поступлением. Исходили из схематически представленных структур коммутатора, набора его записей и графового описания передачи выходящих из коммутатора сетевых пакетов. Приняли как допустимые два ограничения модели:

– произвольное распределение зависимости между объемом потоков данных и временем их обслуживания;

– дискретность распределения структуры информационных потоков.

Результаты исследования. Созданная модель интегрирует вероятность потери потоков пакетов, их статистические характеристики, пропускную способность вычислительных устройств и процедуру многофазного обслуживания. При проверке работоспособности модели приняли, что загрузка коммутатора увеличивается от 0,1 до 0,9, а вероятность потери — от 10^{-3} до 10^{-6}. Для этих показателей выяснили, как от загрузки коммутатора зависят объем буферной памяти и время ожидания. В первом случае минимальное значение (объем памяти) — 0,201, максимальное — 10564. Во втором — 0 и 470 мс соответственно. Для имитационного моделирования минимум по времени — 0 мс, максимум — 2300 мс. Показатели имитационного и аналитического моделирования близки при загрузке менее 50 % и увеличиваются в несколько раз при загрузке более 50 %. Показатели резко возрастают с загрузкой до 70 %, а затем кратно увеличиваются.

Обсуждение. При невысокой сетевой загрузке очереди не переполняются, пакеты не теряются, сохраняются линейные зависимости. При средней и высокой загрузке обработка потоков пакетов описывается нелинейными зависимостями. Результаты аналитического и имитационного моделирования расходятся из-за взрывообразного характера самоподобного сетевого трафика и его приближенного описания распределением Парето. Загруженность коммутатора определяет целесообразность применения предложенного подхода. Модель подойдет при проектировании элементов программно конфигурируемых сетей для анализа их устойчивости при различных информационных воздействиях.

Заключение. Предложенная аналитическая модель SDN определяет значения и дисперсии объема буферной памяти коммутатора, а также объемы памяти для построения таблиц потоков адресации. Работоспособность решения проверили при загрузке коммутатора от 0,1 до 0,9. Планируется создать модель, учитывающую потоки заявок как из внешней сети, так и от сервера.

Ключевые слова: совершенствование методов теории массового обслуживания, аналитическая модель буферной памяти OpenFlow, потеря сетевых пакетов, имитационное моделирование коммутатора

Благодарности. Авторы выражают благодарность редакции, академическому редактору и рецензентам за внимательное отношение к статье и замечания, которые позволили повысить ее качество.

Для цитирования. Слюсарев Г.В., Мочалов В.П., Гостева Д.В. Аналитическая модель буферной памяти OpenFlow коммутатора программно управляемой сети SDN. *Advanced Engineering Research* (*Rostov-on-Don*). 2026;26(2):2221. https://doi.org/10.23947/2687-1653-2026-26-2-2221

Introduction. Programmable SDN networks and the OpenFlow network device management protocol were created to improve automation of modern computer network management and support the specified quality of cloud services, that is, for tasks solved by dynamically redistributing network resources between users. One of the core elements of software-defined networks is the OpenFlow flow switch, and its most important component is the buffer memory. Using an internal software pipeline, the switch distributes and balances loads between network links. This provides the flexibility of centralized network resource management.

Quantitative performance evaluation of networks involves identifying the probabilistic and temporal characteristics of switching nodes. This is done by widely used queuing theory (QT) methods, which only approximately define and model processes in an OpenFlow switch and its buffer memory. This results in underestimated, unrealistic performance of the designed network devices, overloading the switch buffer memory, and loss of network packets. To address this challenge, a different modeling approach is proposed. This work aims to develop and evaluate an analytical model for OpenFlow switch buffer memory in SDN using advanced queueing theory approaches. For this, the discrete Laplace-Stieltjes transform (DLT) is used, taking into account the statistical characteristics of packet flows and the throughput of communication channels for a given packet loss probability. A similar mathematical model based on the classical QT is described in [1], but it does not eliminate the problems that arise due to the approximate description of network processes.

Scientific literature offers design solutions for improving data network elements, demonstrating the importance and relevance of the scientific and technical problem being solved. OpenFlow models for switches in software-defined networks (SDN) are the subject of works by Raghav S.S., Baskakov A.E., Volkov A.S., Filippov I.A., Nikishin K.I., Gurin E.I., Tikhonenko O.M., Gorbunov A.V., Lebedev A.V., Samouylov K.E.., Shalimov I.A., and others. In [2], a fairly comprehensive review of network solutions based primarily on classical QT is given. Finite-capacity systems with a recurrent input flow, a Markovian service process, and infinite-capacity buffers are studied. The modeling methods are based on replacing recurrent arrival flows with simpler ones. The dependence of the volume of requests on the service time is assumed to be given or neglected. The probability of packet loss is supposed to be negligible. Such models often assume packet loss when the buffer is fully occupied, but this assumption is not always accurate. They also assume an unlimited total memory capacity and a well-defined relationship between message volume and service time. Most publications lack finite expressions for analyzing switch service quality, taking into account the specifics of buffer memory allocation, loss indicators, and load. In these cases, the authors use numerical methods from off-the-shelf software packages.

The scientific novelty of this research lies in the improvement of classical queuing theory methods, which support the analysis of systems with arbitrarily distributed arrival and service requests. The practical significance of the results is confirmed by two factors. First, an analytical model of the buffer memory of an OpenFlow switch in an SDN network is created, allowing for a sufficiently accurate analysis. Second, it opens the possibility of selecting alternative design options at the design stage. The efficiency of the proposed model is assessed under simulation. The resulting performance metrics provide evaluating the efficiency of an OpenFlow switch in an SDN network.

Materials and Methods. The incoming SDN network packet flow enters an OpenFlow switch, which extracts metadata, checks it against entries in address tables, and determines the forwarding direction. The network operating system of the SDN controller distributes the packets into flows configured by the OpenFlow classifier. The OpenFlow switch integrates multiple flow tables managed by the central controller through instructions and packet forwarding. The SDN controller periodically updates its records of the network structure, load, resources used, and reserves. Accordingly, it establishes forwarding rules for all incoming flows, sequentially distributes them to the switch OpenFlow output ports, sets new action parameters, and performs distribution or transmission back into the network. This utilizes the switch software pipeline, which consists of sequential flow tables.

Packets not identified in the flow tables are sent to another switch port or forwarded to the controller for field modification. The SDN controller generates switch output ports, address tables, and data flow classifiers [3].

Much attention is paid to issues of network device management, and ready-made design solutions are available. Despite this, new, efficient methods and protocols for network load management are being developed, and network management protocols are constantly being refined. The short period of operational experience with SDN networks and the lack of systematic testing results for switching equipment on the OpenFlow platform necessitate further research using analytical and simulation models.

Thus, the switch structural diagram can be represented as a queueing system (QS) with limited memory. Its input receives a flow of packets with arbitrary distributions of the number and volume of requests. The operating mode of such a system will be stationary if the average number of requests arriving per unit of time does not exceed the maximum possible service rate. One of the most challenging tasks is determining the mean values and variances of the switch total buffer memory capacity, as well as the memory capacity for constructing flow tables [4]. Assume that there are no packet flow queues at the input of a high-performance central control server. In this case, the switch operation in steady-state mode can be described by the apparatus of queuing systems with Laplace-Stieltjes transforms. Data distribution and processing using a software pipeline is modeled as a multiphase random process [5].

The advanced QT method used in this paper allows for the creation of models of numerous real systems, including switching ones. It can be reasonably assumed that such systems have stationary characteristics, and that the parameters of the input packet flow do not affect the order and time of its processing. We also assume that each flow is characterized by a random number of packets, that is, its volume takes only positive discrete values, and this, with a high degree of probability, reflects the real situation.

A switch forwarding pipeline consists of one or more address tables connected in series. Input network traffic, described by an arbitrary distribution law, enters the conveyor and is sequentially processed by k address tables.

It is assumed that the query processing time for each table is random and exponential. The sum of the times of all processing stages forms the final service time distribution (the Erlang k distribution). It is known that a k-order Erlang flow with parameters (μ, r) can be represented as the sum of r random flows with parameters μ_i, and the characteristics of the system under consideration can be obtained from the characteristics of its constituent elements [6]. Then, the stationary probabilities $p(i_1,\ldots, i_r)$ of the system under consideration:

$$p\left(i_1,\ldots,i_r\right)=\prod_{k=1}^{r}\lim_{t\to\infty}p\left\{i_k\left(t\right)=i_k\right\}.$$

The structure of the switch record set is shown in Figure 1.

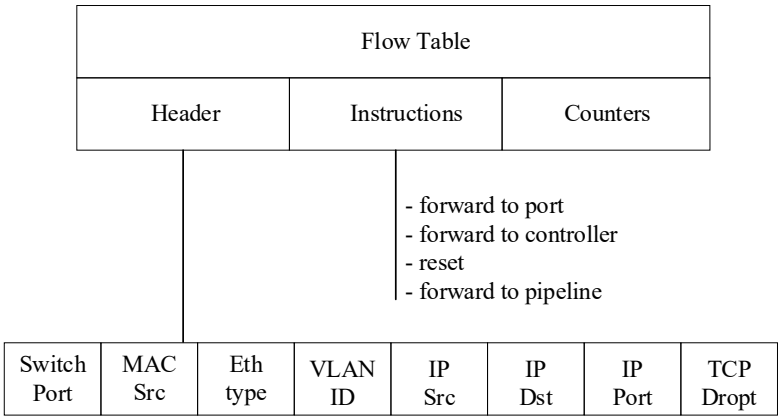

Fig. 1. Switch entry set structure

A simplified structure of an OpenFlow switch is shown in Figure 2.

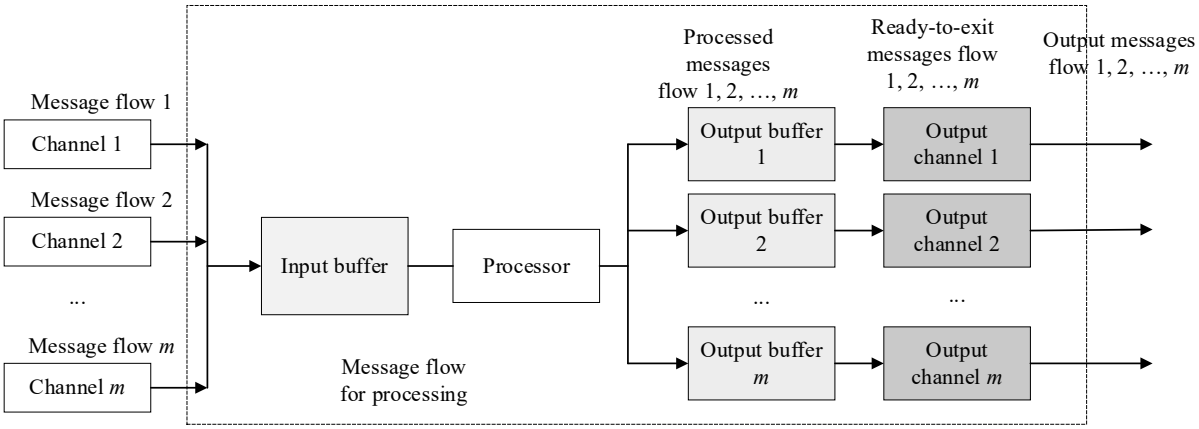

Fig. 2. OpenFlow switch structure

The time intervals between packets are random. The input flow is Markovian, but its service time does not obey an exponential distribution, that is, the analyzed processing of input flows contains a Markovian component. Therefore, this system can be studied using the mathematical apparatus of semi-Markovian processes [7], and the distribution function of the time intervals of the process in state *i* will be an arbitrarily distributed random variable [8]. The intervals between the end of service and the next arrival of service requests are subject to the same distribution. We also assume that random packet flows, determined by the Erlang distribution function, arrive via *m* channels with intensities $a_i\left(i=\overline{1,m}\right)$, $\lambda=\sum_{i=1}^{m}a_i$.

For *M*/*G*/1/*n* system, the Laplace-Stieltjes transform of the distribution function of the volume of the serviced packet *R*(*x*):

$$l_i(s)=1-\frac{a_i}{g_i}\left[\frac{1}{f}-\frac{f}{(s+f)^2}\right].$$

Here, $g_i > 0$ — packet reception delay time on the *i*-th channel, *f* — distribution parameter, *s* — complex parameter of the Laplace-Stieltjes transform. In this expression, it functions as a multiplier in the exponent and allows finding the moments of the distribution of a random variable of any degree.

Mean value and variance:

$$l_{1i}=\frac{2a_i}{g_i f^2}=\frac{2\rho_i}{f}, l_{2i}=\frac{2a_i}{g_i f^3}=\frac{6\rho_i}{f^2},$$

where ρ_i — input channel loading, $\left(l_{2i}-l_{1i}^2\right)=\frac{2\rho_i}{f^2}(3-2\rho_i)$.

Then the volume of packet flow is DLT:

$$\delta(s)=\prod_{i=1}^{m}\left\{1-\frac{a_i}{g_i}\left[\frac{1}{f}+\frac{f}{(s+f)^2}\right]\right\}.$$

Mean values and variance:

$$\delta_1=\frac{2}{f}\sum_{i=1}^{m}\rho_i,\ \left(\delta_2-\delta_1^2\right)=\frac{2}{f^2}\sum_{i=1}^{m}\rho_i(3-2\rho_i).$$

We consider that the probability of packet flow loss [9]:

$$\rho_{\Pi}=1-R(V),$$

where $R(V)=\int_o^V D(V-x)dL(x)$, $L(x)=1-e^{-fx}$ — distribution function (DF) of the packet flow volume; $D(x)=p(\delta<x)$ — DF of the total volume of packet flow δ.

DF moments *R*(*x*):

$$r_1=\delta_1+\varphi_1,\ r_2=\varphi_2+2\varphi_1\delta_1+\delta_2,$$

where $\varphi_1=1/f$ — mean packet flow volume; δ_1, δ_2 — moments of the total volume of packet flow.

Finding the explicit form of the DF *D*(*x*) does not seem possible. In [10], it is shown that when performing calculations, this function can be approximated quite accurately by the expression:

$$D(V)=p_0+(1-p_0)\frac{\gamma(p,gx)}{\Gamma(p)}.$$

Here, $\gamma(p,gx)=\int_0^{gx}t^{p-1}e^{-t}dt$ — incomplete gamma function; p_0 — probability of no service requests; $\Gamma(p)=\gamma(p,\infty)$ — gamma function; *p* and *g* — parameters determined from the condition of equality of the corresponding moments of the switch memory volume:

$$p=\frac{r_1^2}{r_2-r_1^2},\ g=\frac{r_1}{r_2-r_1^2}.$$

The numerical values of the DF *D*(*x*) are obtained through simulation modeling by standard numerical methods, which allow the solution to be reduced to a finite number of arithmetic operations. The results of the simulation modeling are virtually identical to the results of the analytical modeling described in this article, demonstrating the validity of the developed model.

When forming network flows, the following actions are performed [11].

1. Identification of the traffic packet flow.
2. Packet-to-flow classification for the flow being formed.
3. Formation of network packet flows or transmission of an unidentified packet to the management controller.

The function of allocating the service time for the input packet flow $B(t) = p + (1 - p)(1 - e^{pt})$, and its DLT [12]:

$$\beta(q) = p + \frac{(1-p)p}{p+g} = \frac{p(1+q)}{p+g}.$$

Mean service time:

$$\beta_1 = -\beta'(0) = \frac{1-p}{p}.$$

If the system load $\rho = a\beta_1 = a(1-p)/p$, then the DLT service waiting time:

$$W(q) = \frac{(1-\rho)(p+q)}{p+q-a(1-p)} = \frac{(1-p)(p+q)}{q+p(1-\rho)}.$$

Then the mean value of the waiting time is: $W_1 = -W'(0) = \dfrac{p}{p(1-\rho)}$.

The image has the form of rational fraction $(A_n(p))/(B_n(p))$. $P_1, P_2, \ldots, P_n$ — roots of multiplicity $r_1, r_2, \ldots, r_n$, where $r_1 + r_2 + \cdots + r_n = m$ и $B_m(p) = \beta_0 (p - P)_1^{r_1} (p - P_2)^{r_2} \ldots (p - P_n)^{r_n}$ .This means that the original can be found from formula [13]:

$$f(t) = \sum Res\left[\frac{A_n(p)e^{pt}}{B_m(p)}\right].$$

For simple roots of the denominator $P_1, P_2, \ldots, P_n$:

$$f(t) = \sum \frac{A_n(P_k)}{B_m(P_k)} e^p k^t.$$

The inversion of the DLT function $W(q)$ is determined by the relation:

$$W(t) = \sum Res\left[\frac{(1-\rho)(\rho+q)}{q(q+p(1-\rho))}e^{qt}\right].$$

The distribution function of random variable V has the form:

$$V(t) = p\{V < t\} = \int_0^t W(t-u)dU = 1 - e^{-(1-\rho)\mu t}.$$

For the case $p\{W > 0\} = 1 - W(0) = \dfrac{(n\rho)^n p_0}{n!(1-\rho)}$, mean value of stationary waiting time:

$$W_1 = EW = \int_0^\infty dW(t) = \frac{n^{n-2}\rho^n p_0}{\mu(1-\rho)^2(n-1)!}.$$

Mean value of stationary service time:

$$V_1 = EV = \int_0^\infty t dV(t) = \beta_1 + T_1 = \frac{1}{\mu} + \frac{n^{n-2}\rho^n p_0}{\mu(1-\rho)^2(n-1)!}.$$

These random variables are approximated by the DF $Z(x) = p_0 + (1-p_0)\dfrac{\gamma(p,gx)}{\Gamma(p)}$. Here, $\gamma(p,gx) = \int_0^{gx} t^{p-1}e^{-t}dt$, $\Gamma(p) = \gamma(p,\infty)$, p_0 — stationary probability of no requests:

$$p = \frac{\delta_1^2}{(1-p_0)\delta_2 - \delta_1^2}, \quad g = \frac{(1-p_0)\delta_1}{(1-p_0)\delta_2 - \delta_1^2}.$$

Obviously, the phases of transmission of network packets leaving the switch can be described by the graph (Fig. 3) [14].

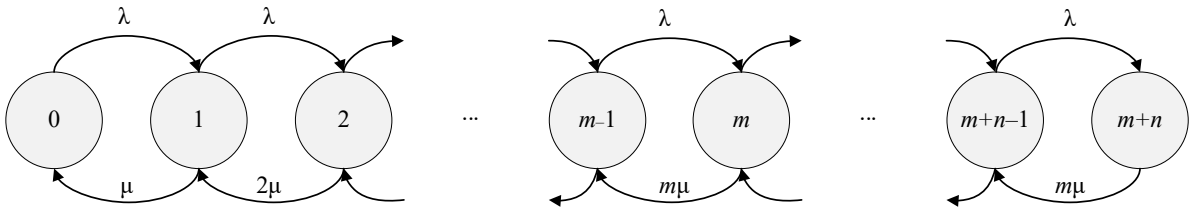

Fig. 3. QS state and transition graph *M*/*M*/*m*/*n*

From [15], the probability of system *M*/*M*/*m*/*n* being in the state p_k is known:

$$p_k = \frac{\frac{\rho^k}{k!}}{\sum_{k=0}^{m} \frac{\rho^k}{k!} + \frac{\rho^{m+1}}{mm!} - \frac{1-\left(\frac{\rho}{m}\right)^n}{1-\frac{\rho}{m}}}, \; 0 \le k \le m.$$

Here, ρ = λ/μ — load.

Accordingly, the probability of the state p_{m+s} is:

$$p_{m+s} = \frac{\frac{\rho^m}{m!}\left(\frac{\rho}{m}\right)^s}{\sum_{k=0}^{m} \frac{\rho^k}{k!} + \frac{\rho^{m+1}}{mm!} - \frac{1-\left(\frac{\rho}{m}\right)^n}{1-\frac{\rho}{m}}}, \; 0 \le \rho \le n.$$

Then the intensity of the output flow is: $y = \lambda - \lambda p_{m+n} = \lambda \sum_{i=0}^{m+n-1} p_i$.

$$p_0 = \frac{\rho}{\sum_{k=0}^{m} \frac{\rho^k}{k!} + \frac{\rho^{m+1}}{mm!} - \frac{1-\left(\frac{\rho}{m}\right)^n}{1-\frac{\rho}{m}}}.$$

$$p_{m+n} = \frac{\frac{\rho^m}{m!}\left(\frac{\rho}{m}\right)^n}{\sum_{k=0}^{m} \frac{\rho^k}{k!} + \frac{\rho^{m+1}}{mm!} - \frac{1-\left(\frac{\rho}{m}\right)^n}{1-\frac{\rho}{m}}} = \frac{\frac{\rho^m}{m!}\left(\frac{\rho}{m}\right)^n}{\rho} p_0.$$

According to [16], taking into account lost packets, the output flow intensity:

$$y = \lambda\left(1 - p_{m+n}\right) = \lambda\left(1 - \frac{\frac{\rho^m}{m!}\left(\frac{\rho}{m}\right)^n}{\rho} p_0\right) = \lambda \frac{\rho - \frac{\rho^m}{m!}\left(\frac{\rho}{m}\right)^n}{\rho} p_0.$$

Time spent by packets in the system:

$$V = \frac{N}{m\mu\left(1-p_0\right)} = \frac{\sum_{k=0}^{m+n} k p_k}{m\mu\left(1-p_0\right)}.$$

Waiting time for packets in the queue:

$$W = \frac{N_0}{m\mu\left(1-p_0\right)} = \frac{\sum_{k=m+1}^{m+n} \left(k-m\right) p_k}{m\mu\left(1-p_0\right)}.$$

Service time:

$$T_{\text{об}} = V - W = \frac{\sum_{k=0}^{m+n} kp_k}{m\mu(1-p_0)} - \frac{\sum_{k=m+1}^{m+n}(k-m)p_k}{m\mu(1-p_0)} = \frac{1}{m\mu} + \frac{(m-1)\sum_{k=m}^{m+n} p_k + \sum_{k=2}^{m-1}(k-1)p_k}{m\mu(1-p_0)}.$$

The presented expressions allow deriving the basic characteristics of an OpenFlow switch. In this case, packet flow processing and management, as well as interaction with the central network controller are taken into account. Buffer memory is considered a shared, dynamically allocated resource and is determined by constraints on the percentage of lost packets for a given loss probability. Acceptable model constraints:

– arbitrary distribution of the relationship between the volume of data flows and their service time;

– assumed discreteness of the distribution of the structure of information flows.

Research Results. Thus, as part of this study, a model of an OpenFlow switch is developed to calculate and evaluate its buffer memory. Using the mathematical apparatus of semi-Markovian processes and Laplace-Stieltjes transforms, the following parameters are defined:

– packet flow loss probability;

– their statistical characteristics;

– computing device throughput.

Packet flow processing consists of multiple independent sequential phases, and the service time across them is exponentially distributed. Therefore, the proposed model is based on a multiphase servicing procedure, in which the service time is determined by the *n*-th order Erlang distribution, and the moments of the distribution functions are found using the Laplace-Stieltjes transform.

Tables 1 and 2 show the results of analytical modeling of the switch buffer memory volume and the dependence of the mean service waiting time on the load. In this case, it increases from 0.1 to 0.9. Switch memory capacity is measured by the number of mean input packet flows.

Table 1

Dependence of Buffer Memory Size on Switch Load

Probability of loss, p_n	Loading switch buffer memory, ρ								
	0.1	0.2	0.3	0.4	0.5	0.6	0.7	0.8	0.9
10^{-3}	0.201	0.307	0.412	0.478	0.617	37.05	69.07	94.36	178.87
10^{-4}	0.403	0.481	0.521	0.680	2.15	4.31	21.05	232.7	831.3
10^{-5}	0.762	0.790	0.840	0.932	3.76	7.83	16.07	476.5	983.2
10^{-6}	0.937	0.951	1.511	1.79	5.07	16.08	87.13	748.1	10564

Table 2

Dependence of Mean Waiting Time on Switch Load, ms

Probability of loss, p_n	Loading switch buffer memory, ρ								
	0.1	0.2	0.3	0.4	0.5	0.6	0.7	0.8	0.9
10^{-4}	0.00	0.00	0.00	0.02	0.07	0.17	30	120	470
10^{-4}	0.00*	0.00*	0.01*	0.04*	0.12*	0.53*	90*	510*	2300*

Note: * Results of switch simulation are marked.

The simulation results were obtained using self-similar network traffic described by a Pareto distribution with a parameter of 1.5. If the system load is less than 50%, the simulation-based characteristics for the *P*/*G*/1 system deviate slightly from the mean values obtained in the analytical modeling. At loads exceeding 50%, the values increase several-fold. The indicators increase sharply as the switch load reaches 70% and increase exponentially if this level is exceeded.

Discussion. The results of this scientific work were obtained under the condition that the distribution function of the intensity of the packet flow was independent of the phase that processed them, as well as the constant nature of the volume of the packet flow. Only in this case the result of the Laplace–Stieltjes transformation was valid for the memory size of the switch.

The main drawback of the results is that the obtained estimates are only reliable at the level of partial distributions. The OpenFlow network switch model is built on the assumption of using shared dynamically allocated buffer memory, and the considered phases of request flow processing are assumed to be independent. Therefore, the results of the study can only be used if the time is equal to:

– input of a packet flow into the switch memory;

– its output to the communication channel.

Such conditions should be considered acceptable, taking into account the capabilities of modern data processing and transmission tools.

The simulation results presented in Tables 1 and 2 are obtained taking into account the specified loss characteristics and current network load. At low loads, queues do not overflow, packets are not lost, and linear dependences are maintained. At moderate, and specifically high loads, network packet flow processing is described by nonlinear dependences. The discrepancy between the analytical and simulation results is due to the explosive nature of self-similar network traffic and the rather approximate nature of its description by the Pareto distribution.

Obviously, the feasibility of using the proposed model is determined by the current switch load. This model can be used in the design of network elements of software-defined networks to analyze their resilience to various information impacts.

The results of the presented research for a load of up to 50% are practically identical to the results obtained within the framework of classical methods of queuing theory [5]. Critical losses of input packet flows start at a switch load of 50%. A further increase in load is not considered; therefore, neither the behavior nor the stability of the system under higher loads are assessed.

The performance level of the proposed model corresponds to the known results of simulation modeling using self-similar network traffic described by the Pareto distribution.

Conclusion

1. An analytical model of the OpenFlow buffer memory of a software-defined network (SDN) switch was developed to determine:

– mean values and variance of the switch total buffer memory;

– memory volumes for constructing address flow tables.

2. Analytical expressions were obtained to determine the following characteristics of the quality of service of a software-defined network switch:

– output packet flow rate, taking into account losses;

– packet sojourn time in the system;

– packet waiting time in the queue;

– service time;

– dependence of the buffer memory size and the average service waiting time on the load.

3. The model performance was confirmed by a comparison of the results of analytical and simulation modeling when the switch load varied from 0.1 to 0.9.

4. The model allows testing SDN networks without using physical equipment to justify switch parameters taking into account its environment.

It is expected that the next article, devoted to the development of a model for the functioning of an SDN switch, will take into account the flow of requests both from the external network and from the management controller (server).

References

1. Samouylov KE, Shalimov IA, Buzhin IG, Mironov YuB. Model of Functioning of Telecommunication Equipment for Software-Configurated Networks. *Modern Information Technologies and IT-Education*. 2018;14(1):13–26. https://doi.org/10.25559/SITITO.14.201801.013-026

2. Ivanova D, Adou Y, Markova E, Gaidamaka Yu, Samouylov K. Mathematical Framework for Mixed Reservation- and Priority-Based Traffic Coexistence in 5G NR Systems. *Mathematics.* 2023;11(4):1046. https://doi.org/10.3390/math11041046

3. Baskakov AE, Volkov AS. Resources Managing Algorithm for Transport Software-Defined Communication Network *Trudy MAI*. 2020;(115). https://doi.org/10.34759/trd-2020-115-06

4. Stepanov MS, Stepanov SN, Kanischeva MG, Kroshin FS. Analysis of Procedures to Ensure the Required QoS Indicators in Multiservice Access Nodes. In: *Proceedings of the XXVI International Conference. on "Distributed Computer and Communication Networks: Control, Computation, Communications (DCCN)"*. Moscow: V.A. Trapeznikov Institute of Control Sciences, Russian Academy of Sciences; 2023. Iss. 1. P. 47–55. https://doi.org/10.25728/dccn.2023.007

5. Mochalov VP, Linets GI, Bratchenko NY, Govorova SV. An Analytical Model of a Corporate Software-Controlled Network Switch. *Scalable Computing: Practice and Experience*. 2020;21(2):337–346. https://doi.org/10.12694/scpe.v21i2.1698

6. Malakhov SV, Yakupov DO, Osipova AA, Kopylova DA, Zelenina EA. The Use of a Queuing System to Study the Characteristics of the Communication Channel in IoT Networks. *Vestnik NSU. Series: Information Technologies*. 2024;22(1):49–61. https://doi.org/10.25205/1818-7900-2024-22-1-49-61

7. Tikhonenko OM. Generalized Erlang Problem for Service Systems with Finite Total Capacity. *Communication Network Theory*. 2005;41:243–253. https://doi.org/10.1007/s11122-005-0029-z

8. Antonova PV. Principles of Developing a Limited-Queue Mass Service System on the .NET Platform. *Software Systems and Computational Methods*. 2023;(2):15–28. https://doi.org/10.7256/2454-0714.2023.2.43403

9. Voronova AG. Typification of Projects for the Transition to Cloud Services. *Advanced Engineering Research* (*Rostov-on-Don*). 2024;24(3):274–282. https://doi.org/10.23947/2687-1653-2024-24-3-274-282

10. Gorbunova AV, Lebedev AB. On Estimating the Characteristics of a Fork-Join Queueing System with Poisson Input and Exponential Service Times. *Advances in Systems Science and Applications*. 2023;23(2):99–114. https://doi.org/10.25728/assa.2023.23.2.1351

11. Mochalov VP, Bratchenko NYu, Moiseenko VA, Gosteva DV. *A Simulation Model of Algorithms for the Operation of Nodes of Future Communication Networks*. Certificate of Software State Registration No. 2019618220, 2019. (In Russ.) URL: https://new.fips.ru/registers-docview/fips_servlet?DB=EVM&DocNumber=2019618220&-TypeFile=html (accessed: 09.06.2026.)

12. Topilin IV, Han M, Feofilova AA, Beskopylny NA. Comparative Analysis of Neural Network and Machine Learning Models for Short-Term Traffic Flow Prediction on Shenzhen Expressway. *Advanced Engineering Research* (*Rostov-on-Don*). 2025;25(4):350–362. https://doi.org/10.23947/2687-1653-2025-25-4-2215

13. Gorbunova AV. On the Features of Service Speed Control in Fork-Join Systems with Pareto Distribution of Service Time. *Proceedings of Voronezh State University. Series: Systems Analysis and Information Technologies*. 2025;(4):53–62. https://doi.org/10.17308/sait/1995-5499/2024/4/53-62

14. Dudin SA, Dudin AN, Dudina OS, Chakravarthy SR. Analysis of a Tandem Queuing System with Blocking and Group Service in the Second Node. *International Journal of Systems Science: Operations and Logistics*. 2023;10(1):2235270. https://doi.org/10.1080/23302674.2023.2235270

15. Samoylenko VV. Concept of a Multilevel Network Infrastructure for Monitoring Agricultural Facilities Based on Wireless Sensor Networks. *Advanced Engineering Research* (*Rostov-on-Don*). 2025;25(4):371–382. https://doi.org/10.23947/2687-1653-2025-25-4-2238

16. Gorbunova AV, Lebedev AV. On the Features of Service Rate Control in Fork-Join Queueing System. *Automation and Remote Control*. 2024;12:70–88. https://doi.org/10.31857/S0005231024120048

About the Authors:

Gennady V. Slyusarev, Dr.Sci. (Eng.), Leading Researcher of the Department of Science, Professor of the Department of Civil Engineering and Prototyping, Institute of Advanced Engineering, North-Caucasus Federal University (2, Kulakov Pr., Stavropol, 355029, Russian Federation), SPIN-code, ORCID, ScopusID, ResearchGate, gsliusarev@ncfu.ru

Valery P. Mochalov, Dr.Sci. (Eng.), Professor of the Department of Digital, Robotic Systems and Electronics, Institute of Advanced Engineering, North-Caucasus Federal University (2, Kulakov Pr., Stavropol, 355029, Russian Federation), SPIN-code, ORCID, ScopusID, ResearcherID, ResearchGate, mochalov.valery2015@yandex.ru

Dar'ya V. Gosteva, programmer, North-Caucasus Federal University (2, Kulakov Pr., Stavropol, 355029, Russian Federation), SPIN-code, ORCID, ScopusID, ResearcherID, ResearchGate, DVGus@yandex.ru

***Claimed Contributorship*:**
GV Slyusarev: conceptualization.
VP Mochalov: project administration, writing – review & editing.
DV Gosteva: software.

***Conflict of Interest Statement:* the authors declare no conflict of interest.**

All authors have read and approved the final manuscript.

Об авторах:

Слюсарев Геннадий Васильевич, доктор технических наук, ведущий научный сотрудник департамента науки, профессор департамента «Строительная инженерия и прототипирование» института перспективной инженерии Северо-Кавказского федерального университета (355029, Российская Федерация, г. Ставрополь, пр. Кулакова, 2), SPIN-код, ORCID, ScopusID, ResearchGate, gsliusarev@ncfu.ru

Мочалов Валерий Петрович, доктор технических наук, профессор департамента «Цифровые, робототехнические системы и электроника» института перспективной инженерии Северо-Кавказского федерального университета (355029, Российская Федерация, г. Ставрополь, пр. Кулакова, 2), SPIN-код, ORCID, ScopusID, ResearcherID, ResearchGate, mochalov.valery2015@yandex.ru

Гостева Дарья Валерьевна, программист, Северо-Кавказский федеральный университет (355029, Российская Федерация, г. Ставрополь, проспект Кулакова, 2), SPIN-код, ORCID, ScopusID, ResearcherID, ResearchGate, DVGus@yandex.ru

Заявленный вклад авторов:

Г.В. Слюсарев: разработка концепции.

В.П. Мочалов: административное руководство исследовательским проектом, написание рукописи – внесение замечаний и исправлений.

Д.В. Гостева: разработка программного обеспечения.

Конфликт интересов: **авторы заявляют об отсутствии конфликта интересов.**

Все авторы прочитали и одобрили окончательный вариант рукописи.

Received / Поступила в редакцию 26.02.2026
Reviewed / Поступила после рецензирования 01.04.2026
Accepted / Принята к публикации 17.05.2026

MACHINE BUILDING AND MACHINE SCIENCE
МАШИНОСТРОЕНИЕ И МАШИНОВЕДЕНИЕ

UDC 669.1:66.04
https://doi.org/10.23947/2687-1653-2026-26-2-2170

Original Empirical Research

Elimination of Distortion during Strengthening Heat Treatment of Small Rod Products

Viktor N. Pustovoit, Yuri V. Dolgachev ✉
Don State Technical University, Rostov-on-Don, Russian Federation
✉ ydolgachev@donstu.ru

EDN: HZFVXR

Abstract

Introduction. Rod-shaped products, such as various needles, axles, pins, shafts, studs, plungers, etc., are in high demand in modern industry. In production of small long products, distortion of their shapes due to the action of internal stresses caused by uneven heating, cooling, deformation or phase transformations of the metal, is a pressing issue. Known methods for eliminating warping involve additional mechanical straightening (often manual), which increases labor intensity and product costs while reducing product performance. To avoid this phenomenon, the use of magnetic field heat treatment (MFHT) technology is proposed. This technology facilitates the initiation of stress-induced martensite within the superplastic temperature range of austenite, along with the simultaneous constraint of the rod product along the magnetic flux. Therefore, the objective of the present study is to explore the feasibility of reducing distortion in rod-shaped products by applying a magnetic field during heat treatment. It is proposed to test the capabilities of MFHT technology on machine needles, where the warping criterion is the magnitude of residual deformation, and the key property indicators are hardness and fatigue limit. The study involves testing needles during both serial and experimental processing, including between different process steps.

Materials and Methods. Machine needles made of U10A steel (GOST 1435-99) with diameters of 0.65 mm, 0.75 mm, 1.10 mm and 1.20 mm were studied. Standard processing modes and MFHT processing on a special installation were used. The radial runout value was measured. The fine structure was studied using TEM and X-ray diffractometry. The operational characteristics were assessed by fatigue tests with determination of the fatigue limit.

Results. The data on the distribution of radial runouts and deviation angles of the needle tip after conventional quenching and low tempering, as well as after MFHT and low tempering were obtained. The operational characteristics (fatigue limit) of needles with different warping after standard treatment and after MFHT were estimated. Changes in the parameters of the fine structure of martensite after quenching in a magnetic field were studied. The dispersion of the martensite structure (packet and twinned morphology) after conventional quenching and MFHT was analyzed. Data on the change in hardness along the length of the needle after various treatment modes were presented.

Discussion. Experimental data obtained demonstrate the feasibility of eliminating warping in small rod-shaped components using the MFHT hardening technology. Hardening in a magnetic field involves a kind of internal straightening and constraining of the long axis of the product in a vertical position along the magnetic flux lines.

Conclusion. Experimental evidence demonstrates that the hardening technology involving heat treatment in a magnetic field (MFHT), which relies on steel quenching under a magnetic field, can additionally eliminate radial runout in rod-shaped products. The internal straightening process, which is achieved using a specified MFHT processing scheme, eliminates the need for conventional machining, which reduces performance characteristics.

Keywords: small rod products, needles, tool steel, warping, magnetic field hardening, radial runout

Acknowledgements. The authors would like to thank the editorial board of the Journal for their valuable comments on the content of the article, the staff of the Department of Materials Science and Technology of Metals, DSTU, Professor Yu.M. Dombrovsky and Head of the Department M.S. Egorov for their help in obtaining and discussing the research results.

For Citation. Pustovoit VN, Dolgachev YuV. Elimination of Distortion during Strengthening Heat Treatment of Small Rod Products. *Advanced Engineering Research* (*Rostov-on-Don*). 2026;26(2):2170. https://doi.org/10.23947/2687-1653-2026-26-2-2170

Оригинальное эмпирическое исследование

Устранение короблений при упрочняющей термической обработке мелких стержневых изделий

В.Н. Пустовойт, Ю.В. Долгачев ✉

Донской государственный технический университет, г. Ростов-на-Дону, Российская Федерация

✉ ydolgachev@donstu.ru

Аннотация

Введение. Стержневые изделия, например всевозможные иглы, оси, штифты, валы, шпильки, плунжеры и др., широко востребованы в современной промышленности. В технологическом процессе производства мелких длинномерных изделий существует проблема искажения их форм вследствие действия внутренних напряжений, вызванных неравномерным нагревом, охлаждением, деформацией или фазовыми превращениями металла. Известные способы устранения коробления предполагают дополнительную механическую правку (зачастую ручным способом), что увеличивает трудоёмкость производства и себестоимость продукции, при этом снижаются эксплуатационные характеристики изделий. Чтобы избежать этого явления, предлагается использовать особенности технологии термической обработки в магнитном поле (ТОМП), которые обуславливают возможность зарождения мартенсита напряжения в температурном интервале сверхпластичности аустенита и одновременного заневоливания стержневого изделия вдоль магнитного потока. Таким образом, целью настоящей работы является исследование возможности уменьшения коробления продукции стержневой формы с помощью воздействия магнитным полем при термической обработке.

Возможности технологии ТОМП предлагается апробировать на машинных иглах, в качестве критерия коробления которых выступает величина остаточной деформации, а основными показателями свойств являются твёрдость и предел выносливости. Исследование игл проведено в процессе серийной и экспериментальной технологии обработки, в том числе между различными операциями технологического процесса.

Материалы и методы. Изучались машинные иглы из стали У10А диаметром 0,65, 0,75, 1,10 и 1,20 мм. Применялись стандартные режимы обработки и обработка ТОМП на специальной установке. Измерялась величина радиального биения. Исследовалась тонкая структура с помощью ПЭМ и рентгеновской дифрактометрии. Эксплуатационные характеристики оценивались усталостными испытаниями с определением предела выносливости.

Результаты исследования. Получены данные о распределении радиальных биений и углов отклонения острия игл после обычной закалки и низкого отпуска, а также после ТОМП и низкого отпуска. Дана оценка эксплуатационным характеристикам (пределу выносливости) игл с различным короблением после стандартной обработки и после ТОМП. Представлены изменения параметров тонкой структуры мартенсита после закалки в магнитном поле, анализ дисперсности структуры мартенсита (пакетной и двойниковой морфологии) после обычной закалки и ТОМП. Показаны изменения твердости по длине иглы после различных режимов обработки.

Обсуждение. Результаты проведенных экспериментов свидетельствуют о возможности устранения коробления мелких стержневых деталей при использовании упрочняющей технологии ТОМП. Закалка в магнитном поле сопровождается своеобразной внутренней правкой и заневоливанием длинной оси изделия в вертикальном положении вдоль линий магнитного потока.

Заключение. Опытным путем получены свидетельства того, что упрочняющая технология ТОМП, основанная на закалке стали в магнитном поле, позволяет дополнительно устранять радиальные биения изделий стержневой формы. В процессе внутренней рихтовки, которая реализуется особой схемой обработки ТОМП, исключается необходимость обычной мехобработки, снижающей эксплуатационные характеристики изделия.

Ключевые слова: мелкие стержневые изделия, иглы, инструментальная сталь, коробление, закалка в магнитном поле, радиальные биения

Благодарности. Авторы благодарят редакцию журнала за ценные замечания по содержанию статьи, сотрудников кафедры «Материаловедение и технологии металлов» ДГТУ, профессора Ю.М. Домбровского и заведующего кафедрой М.С. Егорова за помощь в получении и обсуждении результатов исследования.

Для цитирования. Пустовойт В.Н., Долгачев Ю.В. Устранение короблений при упрочняющей термической обработке мелких стержневых изделий. *Advanced Engineering Research* (*Rostov-on-Don*). 2026;26(2):2170. https://doi.org/10.23947/2687-1653-2026-26-2-2170

Introduction. In modern industry, various rod-shaped products with (length(L))/(diameter$D$)) > 10 ratio are in high demand. These include all kinds of needles (sewing, industrial, medical), axles, pins, shafts, studs, plungers, etc. Heat treatment of such products, used to form the required properties of the finished product, is associated with severe warping [1, 2]. This problem is solved through subsequent straightening and alignment operations [3, 4]. However, this approach has its drawbacks. Firstly, such procedures are quite labor-intensive, as they are often performed manually, which increases the cost of production (≥50% of the original cost [5, 6]). Secondly, they can have a negative impact on the product performance properties, reducing its service life [7, 8].

To solve the problem identified, it is proposed to use the features of heat treatment technology in a magnetic field [9]. Under the impact of a magnetic field, stress-induced martensite can nucleate [10], which makes it possible to straighten the internal structure of the product through acting in a state of superplasticity [11, 12] and simultaneously forcing the processed rod along the magnetic field vector. The effect of MFHT (hardening efficiency of 8÷12 %) is comparable in character to that of high-temperature thermomechanical treatment (HTMT) (19÷24 %) [13, 14], in that both methods simultaneously improve resistance to plastic deformation and brittle fracture. It is known that when using MFHT, the optimal combination of properties is formed by quenching in a magnetic field with tempering without a field [9].

The capabilities of the MFHT technology are proposed to be tested on machine needles, where the warping criterion is the magnitude of residual deformation (radial runouts), and the key property indicators are hardness and fatigue limit. The needles are expected to be studied under serial and experimental processing, including between different process steps.

The objective of this work is to study the possibility of reducing the warping of rod-shaped products by exposing them to a magnetic field during heat treatment.

Materials and Methods. The study utilized products from the Artinsk Mechanical Plant: 100 machine needles (GOST 22249-82) of varying diameters (0.65, 0.75, 1.10, and 1.20 mm) for each mode. The needles were made of U10A steel needle wire (GOST 1435-99). The chemical composition of this wire is listed in Table 1.

Table 1

Chemical Composition of Wire for Making Needles

Batch number	Diameter, mm	C, %	Mn, %	Si, %	S, %	P, %
367	1.90	0.98	0.20	0.18	0.014	0.020
598	1.64	1.01	0.26	0.29	0.015	0.023
1239	2.04	1.01	0.27	0.28	0.013	0.016
471	2.04	1.03	0.27	0.29	0.016	0.021

These products undergo numerous technological processing stages during the manufacturing process, due to their design features. The following main operations can be distinguished: mechanical processing, heat treatment, and finishing operations (chrome plating). After all the shaping operations, the needles undergo heat treatment, retaining their original granular pearlite structure. The standard heat treatment regime involves partial quenching and low tempering. Quenching was performed in heated oil (~60°C). After quenching, the hardness should be 59÷63 HRC. Tempering was performed in oil baths at 200÷225°C for 30 minutes. The hardness of the shank after tempering was 53÷59 HRC, and the hardness of the butt was at least 23 HRC.

The MFHT was conducted on the laboratory setup described in [15]. The key feature of the setup is that the needle is heated and held vertically at the top of the furnace by a magnetic field generated by a solenoid. When the needle temperature reaches ~745°C, it loses its magnetic properties and falls vertically, simultaneously heating to 780°C in the furnace, into the quenching tank. A magnetic field is applied here, which promotes the intensive formation of martensite and vertical forcing of the product. This is followed by tempering without a magnetic field. As shown in [9], applying a magnetic field during tempering of hypereutectoid steels is inadvisable, as it inhibits the decomposition of the solid solution.

To study the fine structure, UEMV-100K (universal electron microscope) was used for direct transmission of the foil, and DRON-0.5 X-ray (multifunctional X-ray diffractometer) with a FeKa tube.

The degree of warping was assessed through measuring the radial runout using “EC METAM PB-22” (metallographic aggregate microscope of the unified METAM series with an upper stage location) and “Micromed MC-2-Zoom вар.2CR” (stereoscopic microscope) with an Eakins digital eyepiece attachment and an object micrometer.

Hardness measurements were performed using the Rockwell and Vickers standardized techniques on TK-2M and ITBRV-187.5-M hardness testers, respectively.

Transverse bending fatigue tests were conducted with a pulsating load generated by an asynchronous electric motor. The fatigue limit was determined using V.S. Ivanova's method [16].

To process the array of data obtained, the MS Excel statistical functions package was used; histograms, diagrams and graphs were also created in this environment.

Research Results. Standard processing forms the structure of the needles, which determines the following properties: fatigue limit $\sigma_{-1} = 480$ MPa, residual deformation $\Delta l_{ост.} \approx 0.15$ mm (for a needle with a diameter of Ø 1.20 mm). The smaller the diameter of the needles, the lower the value of residual deformation after heat treatment; for example, for a diameter of Ø 0.75 mm, it decreases to $\Delta l_{ост.} = 0.07 \div 0.08$ mm.

An important operational parameter of the needle is the radial runout (l) of the rod axis relative to the butt axis. Radial runouts [17, 18] arise from internal stresses caused by uneven plastic deformation under machining and temperature distribution during heat treatment operations. Radial runouts are eliminated at various stages of the manufacturing process (reducing, milling, punching, sharpening, grinding, heat treatment, galvanizing, polishing, etc.) through a series of correct operations. Therefore, to produce high-quality products and reduce labor costs, it is necessary to eliminate factors causing radial runouts in the manufacturing process.

The distribution of needle radial runout values (l) and angles (φ) of tip deviation from the vertical axis after standard machining are shown in Figures 1 and 2.

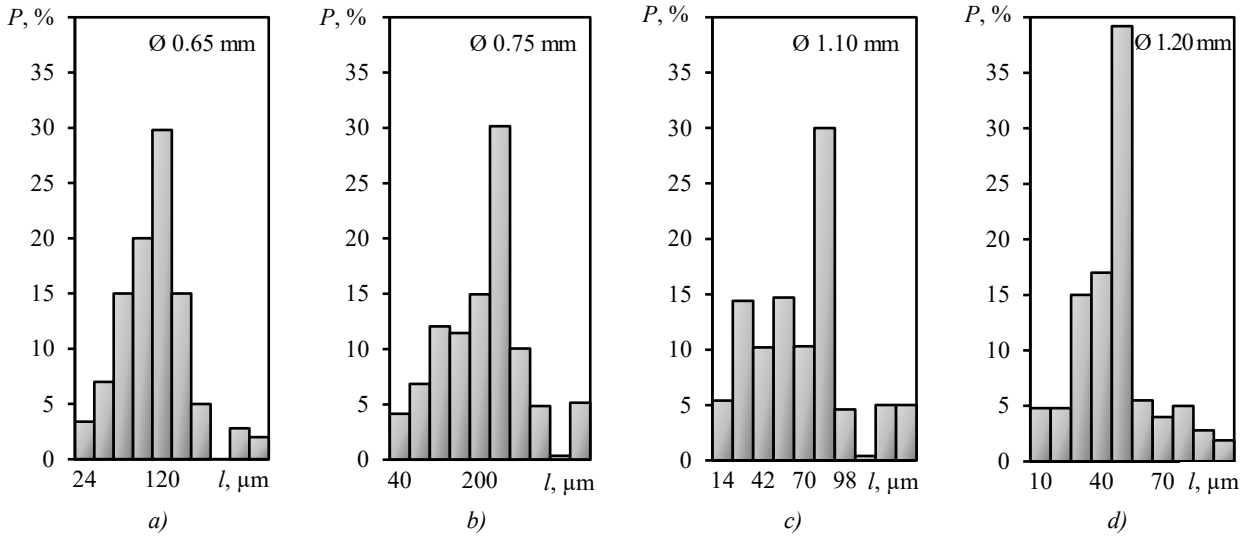

Fig. 1. Distribution of radial runouts (l) of needles of different diameters after hardening:
a — Ø 0.65 mm; *b* — Ø 0.75 mm; *c* — Ø 1.10 mm; *d* — Ø 1.20 mm

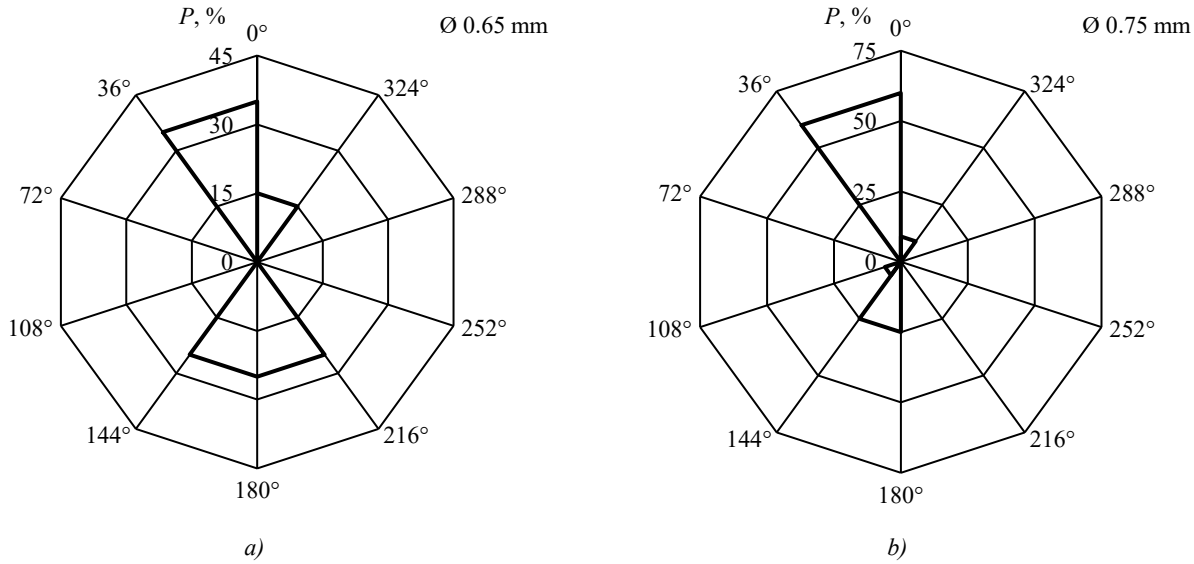

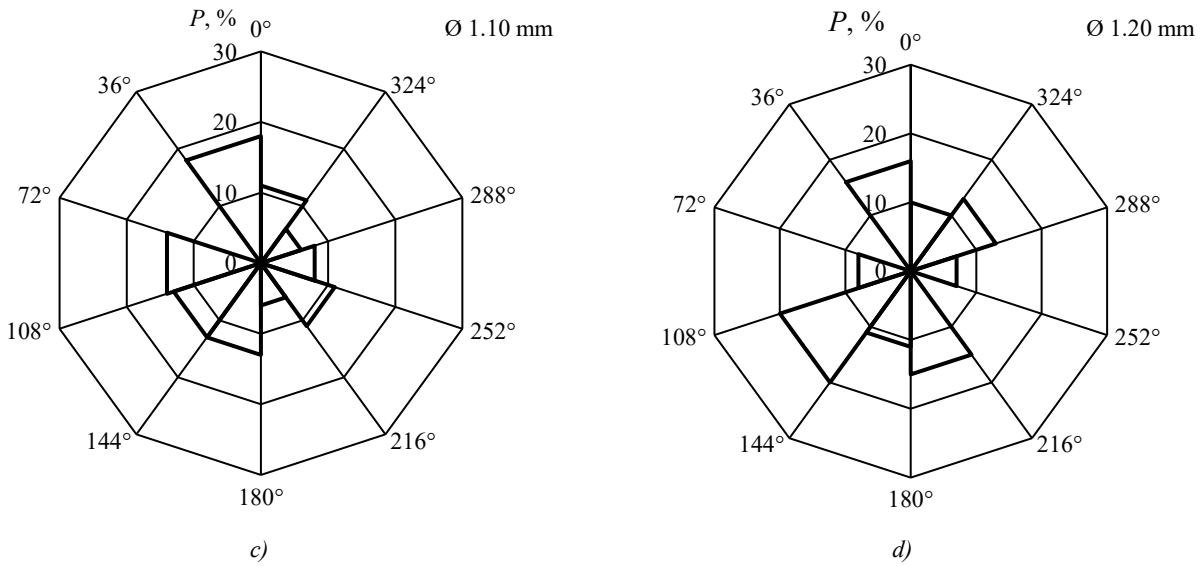

Fig. 2. Distribution of angles (φ) of deviation of tip of needles of different diameters from vertical axis (reference point is milled groove) after hardening: *a* — Ø 0.65 mm; *b* — Ø 0.75 mm; *c* — Ø 1.10 mm; *d* — Ø 1.20 mm

After hardening of Ø 0.65 mm diameter products, the range of dispersion values was similar to the results obtained after machining. They amounted to ~0.3 mm, while the technical specifications required $l_0 \leq 0.1$ mm for finished products. Half of the 100 processed needles had an excess of this parameter. A tendency for deviation (φ) of the shank either towards the milled groove (45%) or in the opposite direction (40%), can be noted. This behavior is attributed to the preferential orientation of internal stresses induced by machining operations (both preliminary and finishing). Quenching does not eliminate all of these stresses, and they accumulate with thermal stresses and ultimately result in the observed warping.

A similar pattern was observed for Ø 0,75 mm: 60% of the shanks deviated toward φ = 0°, while 25% deviated toward φ = 180°. Warping exceeding the permissible limit for this diameter ($l_0 \leq 0.15$ mm), was found in 65% samples, maximum value of l=0.4 mm. Hardening of larger diameter products (Ø 1.10 mm, Ø 1.20 mm) resulted in maximum warping (l = 0.14 and 0.10 mm, respectively), satisfying the requirements of the technical specifications ($l_0 \leq 0.15$ mm), and the distribution of the tip deflection angles (φ) was equally probable.

Tempering narrowed the range of maximum warping values l (Fig. 3) by the following values: Ø 0.75 mm — 0.04 mm; Ø 1.10 mm — 0.02 mm. For products of smaller diameters, a twofold increase in the proportion of products meeting technical specifications was observed. For Ø 1.10 mm (Fig. 4), equally probable distribution φ, was characteristic, while for Ø 0.75 mm, it had a preferential direction: 30 % —φ ≈ 0°, 50 % — φ ≈ 180°.

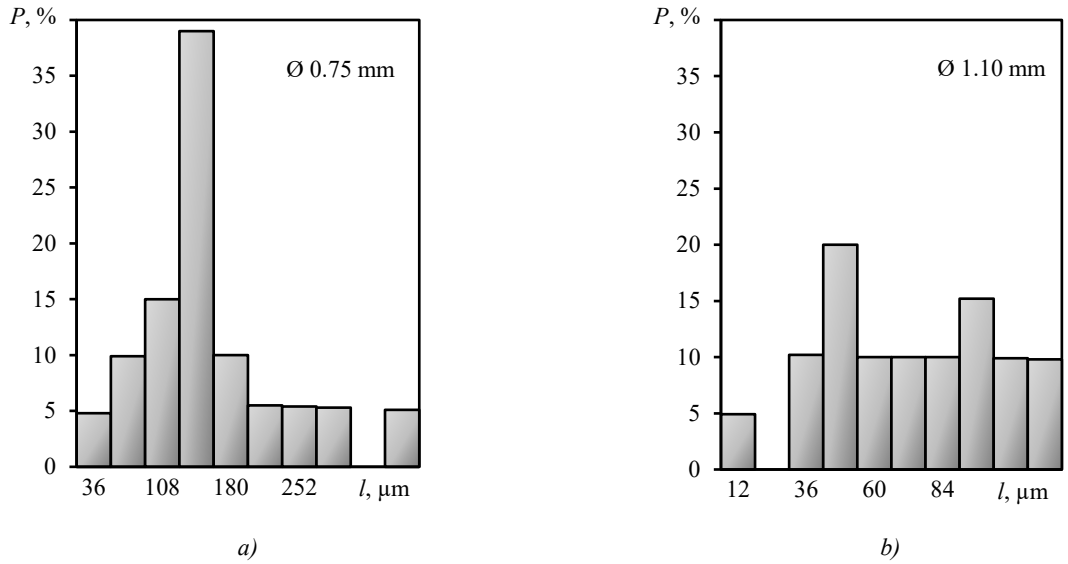

Fig. 3. Distribution of warping value (l) after low tempering: *a* — Ø 0.75 mm; *b* — Ø 1.10 mm

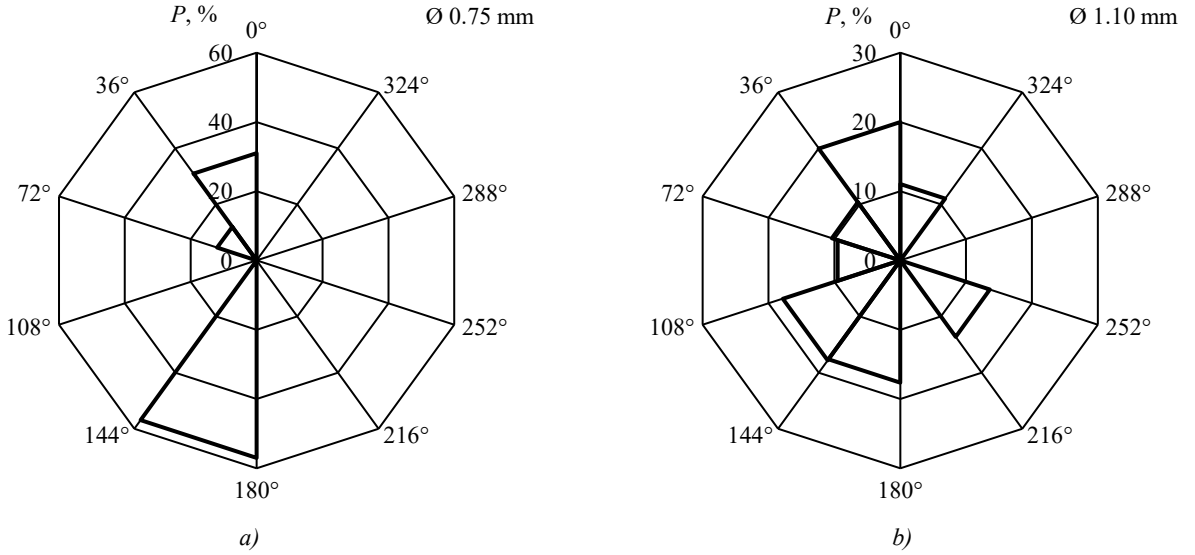

Fig. 4. Distribution of angles (φ) of deviation of tip of needles of different diameters from vertical axis (reference point is milled groove) after tempering: *a* — Ø 0.75 mm; *b* — Ø 1.10 mm

The conducted studies of products with different levels of warping established that the best performance characteristics (σ_{-1}, $l_{ост.}$) were shown by products which, during manufacturing, either exhibited no warping after heat treatment or only minimal warping, and consequently were not subjected to straightening operations (Table 2).

Table 2

Performance Characteristics of Ø 0.65 mm Diameter Products with Varying Warping

l, μm	$l_{ост.}$, mm	σ_{-1}, MPa
0–20	0.02–0.08	460–480
0–20 (after alignment)	0.16–0.24	420–440
80–100	0.32–0.36	400–420
180–200	0.34–0.40	370–410

Morphology studies [9, 10] revealed no qualitative difference between the stress-induced cooling martensite obtained under quenching in a magnetic field and after conventional quenching. X-ray structural studies showed that the effect of the magnetic field was reduced mainly to an increase in the volume fraction of $V_ч$ ч-martensite (by 10% when quenched from 1000°C) and a decrease in the tetragonality of α-martensite (Fig. 5).

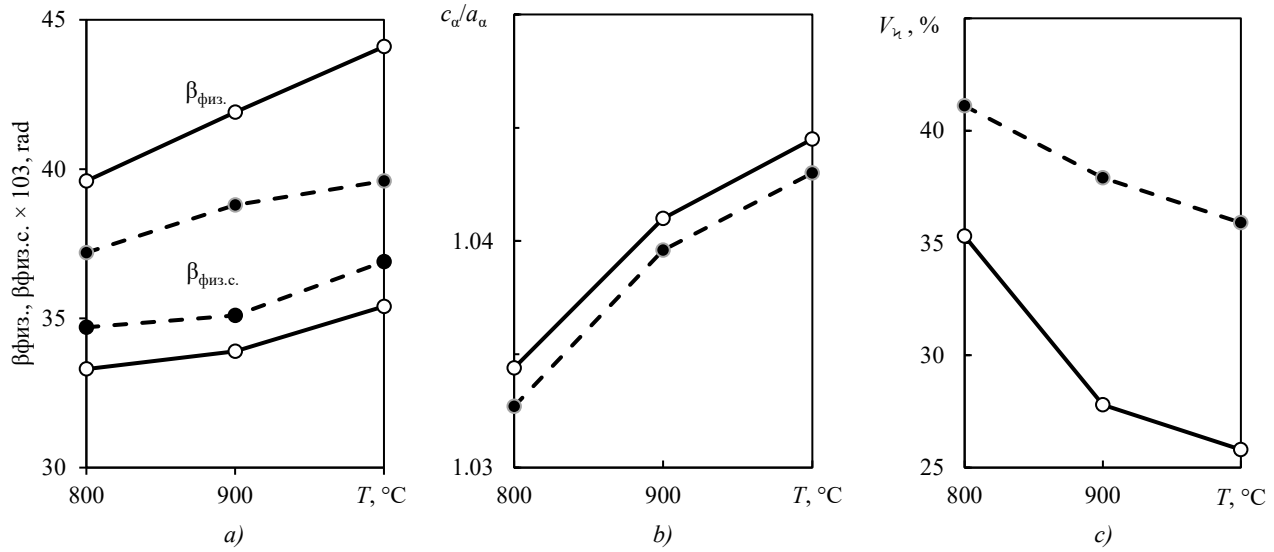

Fig. 5. Results of X-ray structural studies on martensite parameters in U10 steel (solid line — conventional quenching, dashed line — quenching in field H = 1.2 MA/m): *a* — change in physical profile of diffraction lines; *b* — tetragonality parameter of α- martensite; *c* — volume fraction of ч- martensite

When quenching in a magnetic field, compared to conventional quenching, a consistent broadening of the martensite singlet $\beta_{физ.с.}$ was observed due to a greater number of crystal structure disturbances. Under the impact of the field, the degree of two-phase decomposition increased, as clearly indicated by the narrowing physical profile of the martensite X-ray diffraction line multiplet $\beta_{физ.}$

Metal foil transmission studies showed that the resulting martensite had a mixed morphology (lath+twinned crystals) under all processing conditions. It was established that the high defect density during field quenching was explained by the increased dispersion of the martensitic reaction products. The results of the statistical evaluation of fine structure elements are shown in Figure 6. The effect of the magnetic field is manifested in the refinement of lath martensite (reduction in the number of large packets), more uniform packet sizes, a tendency toward reduced lath thickness within packets, and an increase in the proportion of lath martensite itself (by 12 ± 4 %). The morphological changes are due to the boundary between different martensite types shifting toward regions of higher carbon concentration. These changes are attributed to the explosive kinetics of multiple martensite nucleation: cooling-induced nuclei in the martensite start temperature region, and stress-induced nuclei in the superplasticity region of the martensitic transformation (slightly above $M_н$). Furthermore, the field enhances the role of deformation slip in α-phase nucleation.

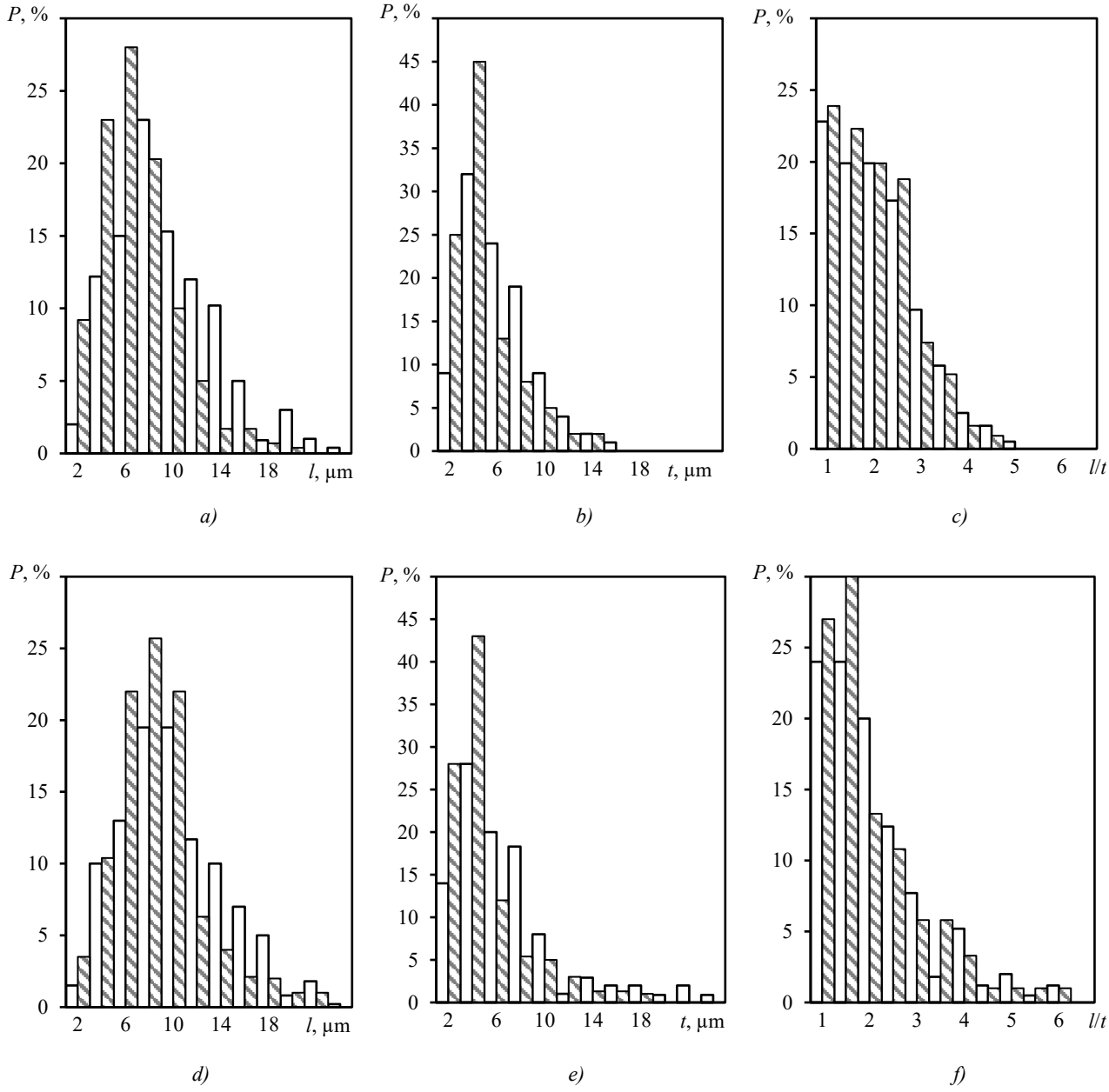

Fig. 6. Distribution of length (l), width (t) and formfactor (l/t) of martensite in U10A steel after conventional quenching (white columns) and quenching in magnetic field of 1.6 MA/m (hatched columns) for: *a*, *b*, *c* — martensite packets; *d*, *e*, *f* — twinned martensite crystals

Figure 6 shows that processing in a magnetic field refines the regions containing twinned martensite crystals, while their formfactor remains unchanged. The increased dispersity is also linked to the catalytic effect of the magnetic field on the multiple and widespread nucleation of martensite. The formation of lath martensite (formed at higher temperatures [19, 20]) is intensified, which causes the phenomenon of cold hardening of γ–phase.

Hardness values were consistently higher after magnetic field assisted processing than after processing without a field (Fig. 7). These results are attributed to a reduction in martensite crystal dimensions, lower volume fractions of austenite $A_{ост.}$ and non martensitic phases, as well as dispersion hardening (during quenching, intermediate carbide precipitates directly [21, 22]). The exception is the hardness in the butt region, which drops under magnetic quenching due to intensified self-tempering [23, 24] in the larger section of the component.

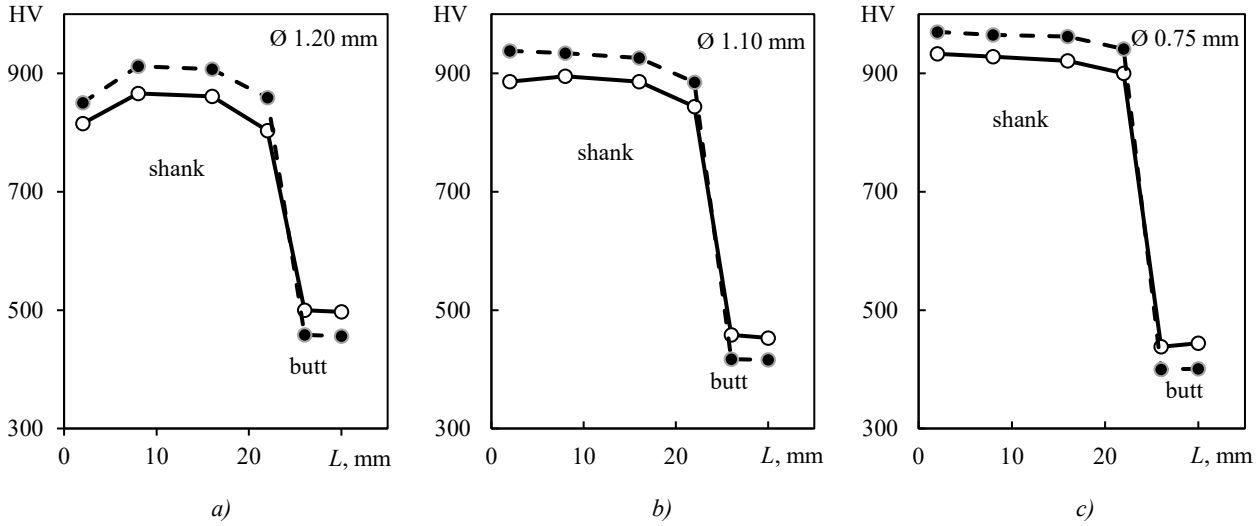

Fig. 7. Results of measuring needle hardness by Vickers method (normal hardening — solid line; hardening in magnetic field H = 0.8 MA/m — dashed line): *a* — ∅ 1.20 mm; *b* — ∅ 1.10 mm; *c* — ∅ 0.75 mm

Examination of the l value of products after magnetic field assisted heat treatment showed no warping beyond the technical specifications ($l < l_0$), with the angular distribution φ being uniform across all diameters. Representative data for the ∅ 0.65 mm diameter — which exhibited the most severe warping under standard processing — are presented in Figure 8. All needles displayed warping $l < l_0/2$ (l_0 = 0.1 mm), and two thirds also met the stricter condition $l < l_0/4$. Post quenching and tempering hardness values remained largely unchanged, whilst with a slight decrease (Fig. 8, b).

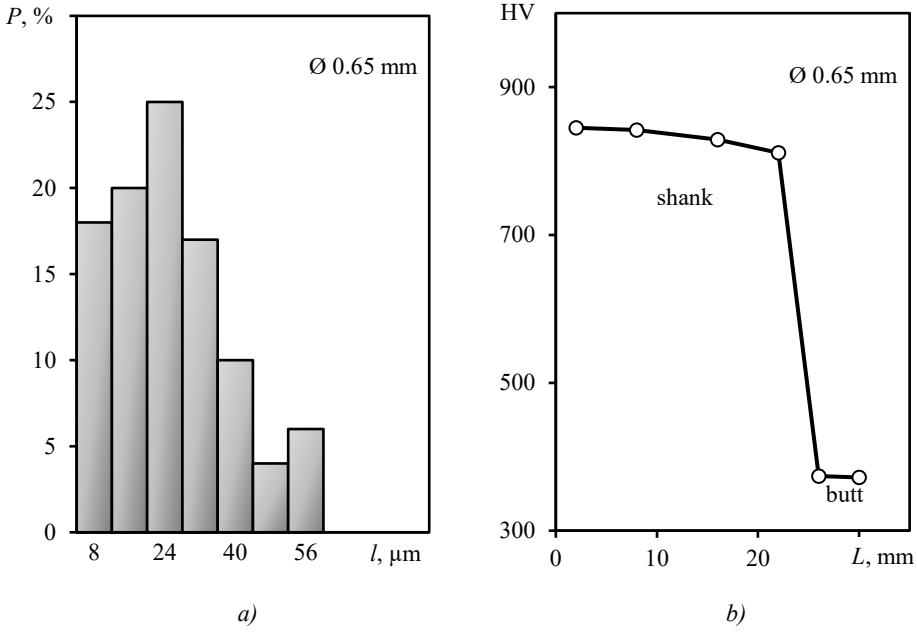

Fig. 8. Distribution of values for the product after MFHT and tempering:
a — warping value; *b* — hardness

In the MFHT treatment mode, no intermediate straightening operations were performed. Thus, the substantial reduction in radial runout arose solely from internal mechanisms during MFHT. The key factors were superplasticity [25] occurring in steel just above the martensite start temperature, and the direct constraint of the needle along the vertical axis by the magnetic flux — an effect governed by the design of the proposed setup [15] for individual MFHT processing of parts with ratio $L/D > 10$.

Since intermediate straightening operations were excluded in MFHT, the fatigue limit of the products was impacted. The studied values σ_{-1} (Fig. 9) measured for needles with a radial runout $l \approx 25$ μm were higher across all diameters compared to those obtained after standard processing.

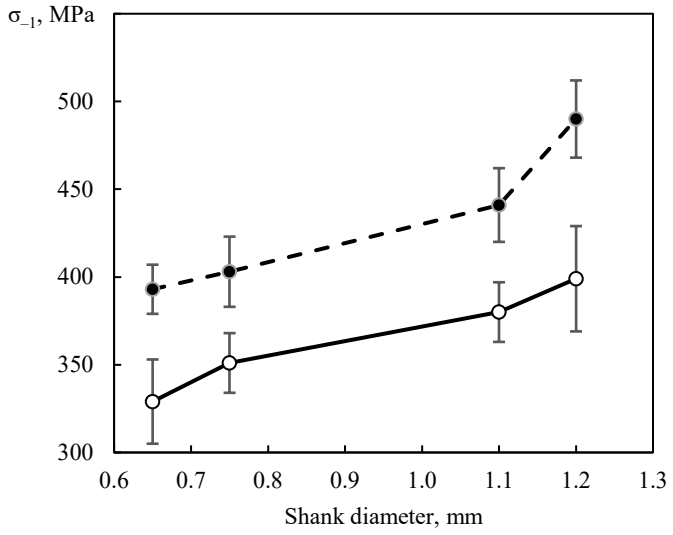

Fig. 9. Fatigue limit of products with $l \approx 25$ μm: standard processing with straightening operations (solid line); MFHT (dashed line)

Discussion. The data presented in Figures 1 and 2 reveal a clear correlation between needle shank bending and its stiffness. Larger-diameter needles exhibit higher shank stiffness relative to the butt, which corresponds to reduced warping susceptibility (primarily caused by groove milling). After machining, large-diameter needles showed $l \leq l_0$ values — that is, they remained within acceptable tolerances — while the angular distribution φ deviations was uniform across all directions.

After quenching, smaller-size products exhibited preferential deviation along the milled groove (in either direction). This type of warping results from an oriented internal stress state in the component originating from machining and the subsequent straightening operation. Since heating does not eliminate these stresses, they combine with quenching deformations and ultimately cause the tip to deviate at a specific angle.

The tempering processes (Figs. 3–4) slightly reduce values l across all diameters, though for small diameters, these values remain outside the acceptable range, and the prevailing distribution by φ is preserved.

Table 2 shows that machining induces a change in the stress state of the component that leads to a substantial degradation in its performance properties. Thus, eliminating warping (and, consequently, the need for straightening) can improve the performance properties of the products [26]. Deformation-free quenching is made possible through a form of internal straightening (Figs. 5, 6) due to the generation of stress-induced martensite crystals (under the impact of a magnetic field in the superplastic range) and the oriented hardening of needles along the magnetic flux lines.

The statistical data presented in Figure 6 demonstrate refinement of the martensitic phase (both lath and twinned morphologies), the overall packet structure, and separate crystals when quenching is performed in a magnetic field. The dispersion, respectively, increases the specific surface area of the boundary and subboundary — dislocation barriers for plastic deformation are created. Peak stresses are reduced and more homogeneously distributed when regions of dislocation pile-up are fragmented and martensite packets are dispersed more uniformly. Consequently, magnetic field quenching produces a martensitic microstructure that offers greater potential for both strength and ductility, resulting in superior overall properties following MFHT treatment.

From the results of the study on the effect of low tempering (Figs. 3, 4, 8), it can be concluded that while it reduces the level of hardening stresses, it does not completely eradicate radial runouts.

The research results of the fatigue limit (Fig. 9) showed its increase during processing in a magnetic field, in comparison with the serial mode, which involved mechanical processing to eliminate warping.

Conclusion. It has been established that mechanical straightening operations used to eliminate warping create a stress pattern that reduces significantly the performance characteristics of products (fatigue limit can drop to 370 MPa, residual deformation can reach 0.40 mm).

Experimental evidence has shown that the MFHT hardening technology, based on quenching steel in a magnetic field, eliminates radial runouts in rod-shaped products ($L/D > 10$). The internal straightening process, implemented through a specified MFHT processing scheme, eliminates the need for conventional machining, which reduces the product performance characteristics.

This is accomplished, firstly, through the direct vertical constraint of the needle during processing by the magnetic flux vector, and secondly, via the effect of the magnetic field on the quenching processes themselves (increasing martensite dispersion). Compared to the standard mode, an increase in the fatigue limit of an average of ~82 MPa was observed, while warping values (with a twofold safety margin) did not exceed the technical requirements (0.10 mm).

References

1. Pustovoit VN, Dolgachev YuV. Formation of Residual Stress Diagram after Quenching in a Magnetic Field. *Safety of Technogenic and Natural Systems.* 2024;(4):54–61. https://doi.org/10.23947/2541-9129-2024-8-4-54-61

2. Samuel A, Prabhu KN. Residual Stress and Distortion during Quench Hardening of Steels: A Review. *Journal of Materials Engineering and Performance*. 2022;31:5161–5188. https://doi.org/10.1007/s11665-022-06667-x

3. Schlegel J. Finishing. In book: *The World of Steel*. Wiesbaden: Springer; 2023. P. 357–368. https://doi.org/10.1007/978-3-658-39733-3_9

4. Rajan TV, Sharma CP, Sharma A. *Heat Treatment: Principles and Techniques*, 3rd ed. Delhi: PHI Learning Pvt. Ltd.; 2023. 376 p. https://books.google.ru/books?id=zuraEAAAQBAJ&hl=ru&lr= (accessed: 01.04.2026).

5. Coca-Gonzalez M, Jimenez-Martinez M. Warpage: Causes, Manufacturing Processes and Future Challenges: A Review. *Proceedings of the Institution of Mechanical Engineers, Part L: Journal of Materials: Design and Applications*. 2025;239(6):1201–1217. https://journals.sagepub.com/doi/full/10.1177/14644207241285399 (accessed: 01.04.2026).

6. Iskakova D, Kasenov A, Magellan D, Zoltan K. Analysis of Methods of Hardening and Restoration of Worn Parts. *Studia Universitatis Babeş-Bolyai Engineering*. 2024;69(1):137–148. https://doi.org/10.24193/subbeng.2024.1.14

7. Babich VE, Bagrets DA, Belotserkovsky MA, Vegera II, Goltseva MV, Gromyko GF, et al. *Topical Problems of Strength*. Monograph. In 2 vol. Vol 2. Vitebsk: Vitebsk State Technological University; 2018. 512 p. (In Russ).

8. Andreev IG, Shakirov AR. Obtaining a Finegrained Structure by Applying Annealing and Normalization. *Sovremennye materialy, tekhnika i tekhnologii.* 2023;47(2):22–24. (In Russ).

9. Pustovoit VN, Dolgachev YuV. *Magnetic Heterogeneity of Austenite and Transformations in Steels.* Monograph. Rostov-on-Don: Don State Technical University; 2021. 198 p. (In Russ).

10. Dolgachev YuV, Pustovoit VN, Vernigorov YuM. Stress Martensite Nucleation in a State of Premartensitic Lattice Instability. *Advanced Engineering Research (Rostov-on-Don).* 2024;24(1):58–65. https://doi.org/10.23947/2687-1653-2024-24-1-58-65

11. Huda Z. Plasticity and Superplasticity – Theory and Applications. In book: *Mechanical Behavior of Materials. Mechanical Engineering*. Cham: Springer; 2022. P. 165–188. https://doi.org/10.1007/978-3-030-84927-6_9

12. Gvozdev AE. *Deformation, Structuring and Destruction of High-Speed Steels under Superplasticity Conditions*. Monograph. Tula: Tula State University; 2021. 487 p. (In Russ).

13. Bernstein ML. *Thermomechanical Treatment of Metals and Alloys*. In 2 vol. Moscow: Metallurgiya; 1968. 574 p. (In Russ).

14. Guo Yuan, Zhenlei Li, Jian Kang. *New Generation TMCP Technology for Hot Strip*. Singapore: Springer; 2024. 482 p. https://doi.org/10.1007/978-981-97-5257-7

15. Pustovoit VN, Dolgachev YuV. Distortion-Free Heat Treatment of Thin Rods in Magnetic Field. *Materials Performance and Characterization*. 2018;7(6):20170159. https://doi.org/10.1520/MPC20170159

16. Ivanova VS. *Destruction of Metals*. Moscow: Metallurgiya; 1979. 168 p. https://search.rsl.ru/ru/record/01007811077 (In Russ.)

17. Roberts WL. *Cold Rolling of Steel*. New York: Routledge; 2017. 808 p. https://doi.org/10.1201/9781315139661

18. Kharitonov BA, Taranin IV. *Cold Wire Rolling: History and Development Trends*. Monograph. Magnitogorsk: Nosov Magnitogorsk State Technical University; 2018. 124 p. (In Russ).

19. Morsdorf L, Jeannin O, Barbier D, Mitsuhara M, Raabe D, Tasan CC. Multiple Mechanisms of Lath Martensite Plasticity. *Acta Materialia.* 2016;121:202–214. https://doi.org/10.1016/j.actamat.2016.09.006

20. Galindo-Nava EI, Rivera-Díaz-del-Castillo PEJ. A Model for the Microstructure Behaviour and Strength Evolution in Lath Martensite. *Acta Materialia.* 2015;98:81–93. https://doi.org/10.1016/j.actamat.2015.07.018

21. Bhadeshia HKDH. *Theory of Transformations in Steels.* Boca Raton, FL: CRC Press; 2021. 604 p. https://doi.org/10.1201/9781003056782

22. Mikhailov MS, Riabov VV. The Study of Carbide Formation in Middle-Carbon High-Strength Steels. *Novosti materialovedeniya. Nauka i tekhnika.* 2016;1(19):1.

23. Sackl S, Clemens H, Primig S. Investigation of the Self Tempering Effect of Martensite by Means of Atom Probe Tomography. *Practical Metallography.* 2022;52(7):374–383. https://www.degruyter.com/document/doi/10.3139/147.110343/html (accessed: 01.04.2026).

24. Silveira ACF, Fechte-Heinen R, Epp J. Microstructure Evolution during Laser-Directed Energy Deposition of Tool Steel by in situ Synchrotron X-ray Diffraction. *Additive Manufacturing.* 2023;63:103408. https://doi.org/10.1016/j.addma.2023.103408

25. Padmanabhan KA, Balasivanandha Prabu S, Mulyukov RR, Nazarov A, Imayev RM, Ghosh Chowdhury S. *Superplasticity. Common Basis for a Near-Ubiquitous Phenomenon*. Berlin, Heidelberg: Springer; 2018. 526 p. https://link.springer.com/book/10.1007/978-3-642-31957-0

26. Rybak AT, Teplyakova SV, Olshevskaya AV, Prutskov AS. A Method for Monitoring the Reliability of Technical Systems by Identifying the Entropy of the Causes of their Failures. *Advanced Engineering Research (Rostov-on-Don).* 2025;25(2):112–119. https://doi.org/10.23947/2687-1653-2025-25-2-112-119

About the Authors:

Viktor N. Pustovoit, Dr.Sci. (Eng.), Professor of the Department of Materials Science and Technology of Metals, Don State Technical University (1, Gagarin Sq., Rostov-on-Don, 344000, Russian Federation), SPIN-code, ORCID, ResearchGate, ResearcherID, pustovoyt45@gmail.com

Yuri V. Dolgachev, Dr.Sci. (Eng.), Associate Professor of the Department of Materials Science and Technology of Metals, Don State Technical University (1, Gagarin Sq., Rostov-on-Don, 344000, Russian Federation), SPIN-code, ORCID, ResearchGate, ResearcherID, ydolgachev@donstu.ru

Claimed Contributorship:

VN Pustovoit: supervision, conceptualization, methodology, project administration, resources, writing – original draft preparation.

YuV Dolgachev: investigation, formal analysis, validation, visualization, writing – review & editing.

***Conflict of Interest Statement*: the authors declare no conflict of interest.**

All authors have read and approved the final version of manuscript.

Об авторах:

Виктор Николаевич Пустовойт, доктор технических наук, профессор кафедры «Материаловедение и технологии металлов» Донского государственного технического университета (344003, Российская Федерация, г. Ростов-на-Дону, пл. Гагарина, 1), SPIN-код, ORCID, ResearchGate, ResearcherID, pustovoyt45@gmail.com

Юрий Вячиславович Долгачев, доктор технических наук, доцент, профессор кафедры «Материаловедение и технологии металлов» Донского государственного технического университета (344003, Российская Федерация, г. Ростов-на-Дону, пл. Гагарина, 1), SPIN-код, ORCID, ResearchGate, ResearcherID, ydolgachev@donstu.ru

Заявленный вклад авторов:

В.Н. Пустовойт: научное руководство, разработка концепции, методологии, административное руководство исследовательским проектом, предоставление ресурсов, написание черновика рукописи.

Ю.В. Долгачев: проведение исследования, формальный анализ, валидация результатов, визуализация, написание рукописи — устранение замечаний, внесение исправлений.

Конфликт интересов: **авторы заявляют об отсутствии конфликта интересов.**

Все авторы прочитали и одобрили окончательный вариант рукописи.

Received / **Поступила в редакцию** 02.03.2026
Reviewed / Поступила после рецензирования 30.03.2026
Accepted / **Принята к публикации** 08.04.2026

MACHINE BUILDING AND MACHINE SCIENCE
МАШИНОСТРОЕНИЕ И МАШИНОВЕДЕНИЕ

UDC 621.914.3
https://doi.org/10.23947/2687-1653-2026-26-2-2662

Original Empirical Research

Experimental and Curvature-Based Analysis for Accuracy Optimization in 3-Axis CNC Milling of Concave Parabolic Freeform Surfaces

EDN: NRNBJD

Ngoc Tuyen Bui[1], **Nguyen Tho Van**[2] ✉

[1] Hanoi University of Science and Technology, Hanoi, Vietnam
[2] Haiphong University, Haiphong, Vietnam
✉ thonv@dhhp.edu.vn

Abstract

Introduction. Concave parabolic freeform surfaces are integral to high-performance optical reflectors and precision mechanical components, where stringent geometric accuracy is paramount to functional efficiency. Despite their widespread application, achieving high surface fidelity in 3-axis CNC milling remains a significant technical challenge. This difficulty arises from the intricate, non-linear interactions between cutting tool geometry, machining parameters, and the varying local curvature of the surface. While conventional research often focuses on global parameter optimization, there exists a notable scientific gap in understanding how localized curvature gradients dictate error distribution during the material removal process. This study addresses this gap by establishing a curvature-aware analytical framework aimed at identifying the fundamental drivers of machining inaccuracies in parabolic geometries.

Materials and Methods. The research methodology integrates theoretical modeling with rigorous experimental validation. Initially, a mathematical model based on principal deviation theory was formulated to characterize the geometric deviations inherent in the 3-axis milling process. This analytical foundation allowed for the mapping of theoretical errors against surface differential geometry. Subsequently, an experimental investigation was executed using a Taguchi L_9 orthogonal array design to systematically evaluate the influence of three primary machining factors: tool diameter, feed rate, and step-over. Concave parabolic samples were machined and measured using high-precision metrology equipment. The resulting data were processed via Analysis of Variance (ANOVA) and Signal-to-Noise (S/N) ratio analysis to quantify the individual and interactive statistical contributions of each parameter to the total machining error.

Results. The findings demonstrate that tool diameter and step-over are the predominant factors, accounting for the majority of the variance in machining accuracy, whereas the influence of feed rate is found to be statistically marginal within the tested range. Crucially, the results have revealed that machining errors are not uniformly distributed but are highly correlated with the local principal curvatures of the parabolic profile. MATLAB simulations further corroborated these findings, showing that the maximum deviation occurs in regions of high curvature where the tool-surface engagement geometry is most constrained. These specific results provide a quantitative map of how tool geometry interacts with parabolic concavity to produce predictable error patterns.

Discussion. This research provides a novel interpretation of machining errors through the lens of surface differential geometry, successfully bridging the gap between theoretical surface modeling and practical CNC manufacturing. The findings demonstrate that “one-size-fits-all” toolpath strategy is inherently insufficient for concave freeform geometries due to localized geometric complexities. Instead, this study validates that the implementation of an adaptive step-over strategy, dynamically adjusted based on local curvature values, significantly enhances surface forming accuracy. The core scientific novelty lies in the proposed integration of curvature-based compensation directly into the toolpath planning phase, allowing for proactive error mitigation rather than reactive adjustments.

Conclusion. In conclusion, the proposed approach offers a robust and scalable solution for improving the precision of complex freeform components in real-world industrial environments. By adopting this methodology, high-precision manufacturing processes can potentially reduce post-processing requirements and overall production costs. While this study focuses on static and geometric accuracy, future research will extend this model to incorporate the assessment of dynamic processing errors. This expansion will provide a more comprehensive framework for accuracy optimization in multi-axis CNC machining of complex surface.

Keywords: freeform surface with concave parabolic structure, tool diameter, feed rate, step-over, surface curvature, geometric deviation, Taguchi method

Acknowledgments. The authors would like to appriciate the Technical Practice Center for providing the test samples and equipment used in the experimental process. In addition, we would like to thank the Editorial Board of the Journal and the anonymous reviewers for their insightful professional evaluations and valuable recommendations, which significantly contributed to the improvement and enhancement of the quality of this article.

For Citation. Ngoc Tuyen Bui, Nguyen Tho Van. Experimental and Curvature-Based Analysis for Accuracy Optimization in 3-Axis CNC Milling of Concave Parabolic Freeform Surfaces. *Advanced Engineering Research* (*Rostov-on-Don*). 2026;26(2):2662. https://doi.org/10.23947/2687-1653-2026-26-2-2662

Оригинальное эмпирическое исследование

Экспериментальный анализ и подход на основе кривизны для оптимизации точности при 3-осевом фрезеровании с ЧПУ вогнутых параболических поверхностей произвольной формы

Нгок Туен Буй[1], **Нгуен Тхо Ван**[2] ✉

[1] Ханойский университет науки и технологий, Ханой, Вьетнам

[2] Хайфонский университет, Хайфон, Вьетнам

✉ thonv@dhhp.edu.vn

Аннотация

Введение. Вогнутые параболические поверхности свободной формы играют ключевую роль в высокоэффективных оптических отражателях и прецизионных механических узлах, где жесткие требования к геометрической точности определяют функциональную эффективность изделий. Несмотря на широкое распространение таких поверхностей, обеспечение высокого качества их обработки на 3-осевых фрезерных станках с ЧПУ остается существенной технической проблемой. Данная сложность обусловлена комплексными нелинейными взаимодействиями между геометрией режущего инструмента, параметрами обработки и изменяющейся локальной кривизной поверхности. В то время как традиционные исследования обычно сосредоточены на глобальной оптимизации параметров, существует заметный научный пробел в понимании того, как локальные градиенты кривизны определяют распределение погрешностей в процессе съема материала. Настоящее исследование устраняет этот пробел, предлагая аналитическую основу, учитывающую кривизну и направленную на выявление фундаментальных факторов погрешностей обработки параболических геометрий.

Материалы и методы. Методология исследования сочетает теоретическое моделирование со строгой экспериментальной проверкой. На первом этапе на основе теории главных отклонений была разработана математическая модель, характеризующая геометрические отклонения, свойственные процессу 3-осевой фрезеровки. Данная аналитическая база обеспечила возможность отображения теоретических погрешностей относительно дифференциальной геометрии поверхности. Затем было проведено экспериментальное исследование с применением ортогонального плана Taguchi L_9 для систематической оценки влияния трех основных технологических факторов: диаметра инструмента, подачи и поперечного смещения. Были изготовлены образцы вогнутых параболических поверхностей, которые затем подверглись измерениям на высокоточном метрологическом оборудовании. Обработка полученных данных выполнялась методами дисперсионного анализа (ANOVA) и анализа отношения сигнал/шум (S/N ratio), что позволило количественно оценить индивидуальный и интерактивный статистический вклад каждого из рассматриваемых параметров в суммарную погрешность обработки.

Результаты исследований. Полученные результаты показали, что диаметр инструмента и поперечный шаг являются доминирующими факторами, на долю которых приходится основная часть дисперсии точности обработки, в то время как влияние скорости подачи в пределах исследуемого диапазона оказалось статистически незначительным. Важно отметить, что погрешности обработки распределены не равномерно, а существенно коррелируют с локальной главной кривизной параболического профиля. Моделирование в MATLAB дополнительно подтвердило эти выводы, показав, что максимальное отклонение происходит в областях с высокой кривизной, где геометрия взаимодействия инструмента с поверхностью наиболее ограничена. Данные результаты обеспечивают количественное отображение того, как взаимодействие геометрии инструмента с параболической вогнутостью приводит к образованию предсказуемых закономерностей распределения погрешностей.

Обсуждение. Настоящее исследование предлагает новую интерпретацию погрешностей механической обработки сквозь призму дифференциальной геометрии поверхности, успешно преодолевая разрыв между теоретическим моделированием поверхности и практическим фрезерованием на станках с ЧПУ. Результаты показывают, что универсальная стратегия построения траектории инструмента («один размер для всех») является принципиально недостаточной для вогнутых свободных поверхностей из-за присущих им локальных геометрических сложностей. Данная работа подтверждает, что применение адаптивной стратегии изменения поперечного шага, динамически подстраиваемого в зависимости от локальных значений кривизны, существенно повышает точность формообразования поверхности. Ключевая научная новизна состоит в предложенной интеграции компенсации, основанной на кривизне, непосредственно на этапе планирования траектории движения инструмента, что позволяет упреждающе минимизировать погрешности вместо того, чтобы исправлять их постфактум.

Заключение. В заключение следует отметить, что предлагаемый подход представляет собой надежное и масштабируемое решение для повышения точности изготовления сложных компонентов произвольной формы в реальных промышленных условиях. Внедрение данной методологии в высокоточные производственные процессы позволит потенциально сократить объем последующей обработки и снизить общие производственные издержки. Несмотря на то, что настоящее исследование сосредоточено на статической и геометрической точности, в будущем предполагается расширить данную модель за счет включения оценки динамических погрешностей обработки. Это расширение создаст более комплексную основу для оптимизации точности при многокоординатной фрезерной обработке сложных поверхностей на станках с ЧПУ.

Ключевые слова: поверхность произвольной формы с вогнутой параболической структурой, диаметр инструмента, скорость подачи, поперечный шаг, кривизна поверхности, геометрическое отклонение, метод Тагучи

Благодарности. Авторы выражают искреннюю признательность Техническому практическому центру за предоставление образцов для испытаний и оборудования, использованного в экспериментальной работе. Авторы также благодарят редакционную коллегию журнала и анонимных рецензентов за их глубокие профессиональные заключения и ценные замечания, которые внесли существенный вклад в доработку и повышение качества настоящей статьи.

Для цитирования. Нгок Туен Буй, Нгуен Тхо Ван. Экспериментальный анализ и подход на основе кривизны для оптимизации точности при 3-осевом фрезеровании с ЧПУ вогнутых параболических поверхностей произвольной формы. *Advanced Engineering Research* (*Rostov-on-Don*). 2026;26(2):2662. https://doi.org/10.23947/2687-1653-2026-26-2-2662

Introduction. Freeform surfaces are increasingly employed in advanced engineering applications such as precision molds, optical components, and aerodynamic structures due to their superior functional and aesthetic performance. Among various local geometrical features, concave parabolic structures are widely utilized in components such as parabolic reflectors and antenna devices, where geometric accuracy directly affects functional efficiency. In particular, the machining of such surfaces using 3-axis CNC milling remains a challenging task due to the complex interaction between tool geometry, surface curvature, and toolpath strategy.

In the context of ball-end milling, surface generation errors are strongly influenced by geometric factors such as tool radius, feed rate, and step-over, as well as by the local curvature of the machined surface. Previous studies have extensively investigated the influence of machining parameters on freeform surface quality. Recently, significant contributions from the Russian metalworking school have addressed both the experimental characterisation and the predictive modelling of geometric accuracy in the milling of complex-shape parts. In [1], the authors developed an experimental methodology and a mathematical model for controlling the geometric accuracy indicators of die impressions in ball-end milling, with the resulting model employed to adjust the toolpath. In related study [2], empirical models were established linking spherical end-mill life to geometric accuracy and surface roughness, using these models to define both tool-replacement schedules and criteria for surface analysis. Furthermore, paper [3] explored the influence of tool orientation angles on surface roughness when processing complex-profile surfaces, highlighting the critical role of tool-surface contact geometry in determining final quality.

Specifically, the effects of toolpath strategies were evaluated in [4], while the impact of feed rate was analyzed in [5]. The role of step-over in determining geometric deviation was established in [6]. Other studies applied experimental design approaches, such as the Taguchi method combined with analysis of variance (ANOVA), to determine optimal machining conditions for minimizing surface errors [7]. These approaches have demonstrated that toolpath strategy is often a primary

factor affecting machining accuracy [8]. In addition, the significant contribution of step-over to surface forming quality has been confirmed through statistical analysis [9]. Furthermore, some researchers focus on comparing toolpath strategies in various CAM systems [10] or proposing solutions to determine scallop heights from CNC part programs [11]. Strategies to reduce the variation of the effective tool diameter have also been proposed to ensure uniform machining accuracy [12].

However, most existing studies focus on general freeform surfaces or specific geometries such as impellers [13]. Other research has targeted specific profiles like saddle surfaces [14] or the optimization of geometric characteristics for specialized cycloidal profiles [15]. Meanwhile, the machining characteristics of concave parabolic structures have received limited attention. More importantly, the relationship between machining parameters and surface accuracy is often analyzed from a purely experimental perspective, without explicitly considering the role of surface curvature in governing geometric deviations. As a result, the underlying mechanisms that explain why certain parameters dominate the machining accuracy remain insufficiently clarified.

To address these limitations, this study focuses on the machining of freeform surfaces with concave parabolic structures, characterized by a first principal curvature of zero and a second principal curvature with a variable negative value. Based on the theory of principal deviations and surface geometry [16], an experimental model is developed to investigate the influence of key machining parameters, including tool diameter, feed rate, and step-over, on surface forming accuracy in 3-axis CNC milling. A systematic experimental design based on the Taguchi orthogonal array is employed, and the results are analyzed using ANOVA to quantify the contribution of each parameter [17].

The objective of this study is to evaluate the influence of surface curvature, tool radius, step-over, and feedrate on the geometric error of a concave parabolic surface structure during 3-axis CNC milling. Theoretical error models and MATLAB simulations aim to assess the distribution of feedrate error, step-over error, and total error on the surface for parallel toolpaths in two principal curvature directions. From this, the appropriate toolpath direction is determined, and an adaptive toolpath solution based on the developed theoretical model is proposed. Experimental models are used to evaluate the extent to which tool radius, step-over, and feedrate affect the shaping accuracy. In addition to conventional experimental analysis, this work emphasizes the geometric interpretation of machining errors by linking them to curvature-related factors, thereby providing deeper insight into the interaction between tool geometry and surface characteristics. The findings of this study contribute to a better understanding of parameter sensitivity in machining concave parabolic surfaces and provide a basis for improving toolpath planning and machining efficiency in practical applications.

Materials and Methods. The investigated surface is generated by sweeping a parabolic curve along a straight line, resulting in a parabolic cylindrical surface. The parametric representation of the surface is defined as:

$$\mathbf{P}(u,v) = \left(x(u), \left|y(v), \right|z(u)\right) = \left(60u - 30, \left|70v, \right|240u^2 - 240u + 60\right). \quad (1)$$

$$0 \le u, v \le 1.$$

This construction implies that the surface exhibits curvature only along the parametric direction u, while remaining geometrically linear along the direction v.

A sample experimental model with the concave parabolic freeform surface $\mathbf{P}(u,v)$ was constructed using NX12 as shown in Figure 1.

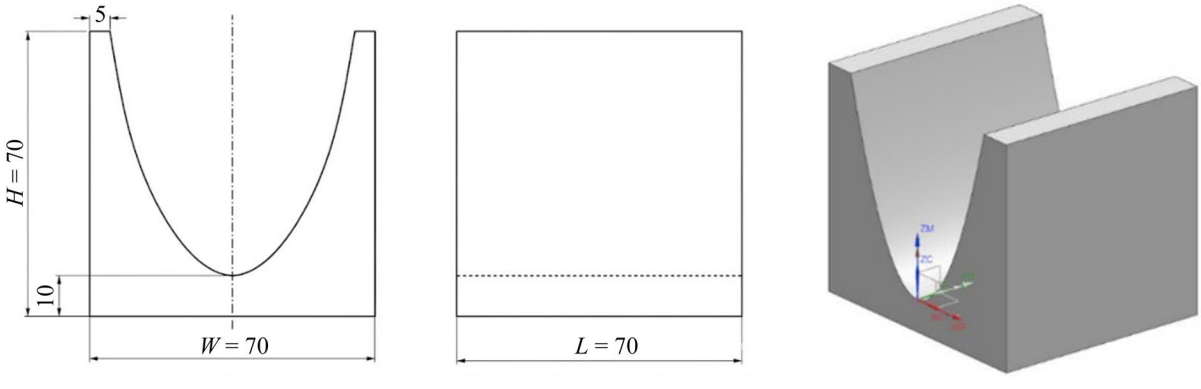

a) *b)*

Fig. 1. Drawing of the experimental sample *a* — 2D drawing; *b* — 3D model

The first-order partial derivatives are expressed as:

$$\mathbf{P}_u = \left(60, |0, |480u - 240\right), \mathbf{P}_v = \left(0, |70, |0\right). \tag{2}$$

The second-order derivatives are:

$$\mathbf{P}_{uu} = \left(0, |0, |480\right), \mathbf{P}_{vv} = \left(0, |0, |0\right).$$

Along the *v*-direction (generator direction), the first principal curvature is:

$$k_1 = 0.$$

Along the *u*-direction (profile curve direction), the second principal curvature is:

$$k_2 = \frac{z''(u)}{\left[1 + \left(z'(u)\right)^2\right]^{3/2}} = \frac{480}{\left[1 + \left(480u - 240\right)^2\right]^{3/2}}. \tag{3}$$

The sign of the curvature depends on the surface orientation; for concave configurations, it is considered negative. Importantly, k_2 varies continuously along the parameter *u*, reflecting the non-uniform curvature distribution of the parabolic profile.

The Gaussian curvature is given by:

$$K = k_1 \cdot k_2 = 0. \tag{3}$$

This confirms that the surface is a developable surface, characterized by zero Gaussian curvature.

The mean curvature is:

$$H = \frac{1}{2}\left(k_1 + k_2\right) = \frac{k_2}{2}, \tag{4}$$

which varies along the surface due to the dependence of k_2 on *u*.

Surface curvature characteristics significantly influence the geometric accuracy in CNC milling, leading to critical implications for overall machining precision.

Since $k_1 = 0$, there is no curvature-induced deviation along the toolpath direction when it is aligned with the generator direction.

The varying curvature $k_2(u)$ leads to non-uniform tool-surface contact conditions, which significantly influence geometric deviations.

Regions with higher curvature (smaller radius) are more sensitive to tool diameter and step-over, resulting in larger scallop height and form error.

Therefore, the geometric deviation in ball-end milling can be interpreted as a curvature-dependent phenomenon, where the second principal curvature plays a dominant role.

The optimization of machining accuracy is achieved through a comprehensive analysis of toolpath strategies and curvature-based modeling. Two representative toolpath strategies are investigated for machining the concave parabolic cylindrical surface. In Case A, the feed direction is aligned with the zero-curvature direction ($k_1 = 0$), while the step-over is applied along the parabolic profile. In Case B, the feed direction follows the parabolic profile, and the step-over is aligned with the zero-curvature direction.

In ball-end milling of freeform surfaces, the geometric deviation is strongly influenced by the local curvature of the machined surface. For the considered parabolic cylindrical surface, the curvature is anisotropic, with one principal curvature equal to zero and the other varying along the surface.

Let the second principal curvature be:

$$k(u) = k_2(u), R(u) = \frac{1}{|k(u)|}, \tag{5}$$

where $R(u)$ is the local radius of curvature.

The total geometric deviation in ball-end milling can be approximated as the sum of two components:

$$h_\Sigma(u) = h_f + h_s,$$

where h_f, h_s are feed-direction deviation and step-over (scallop) deviation in turn.

The geometric deviations can be approximated using a second-order Taylor expansion of the surface profile [18]. This approach leads to the classical relation h ≈ s2/(8R), which is widely documented in manufacturing theory [19].

The effective curvature radius $R_{eff}(u)$ is defined by combining the curvature of the machined surface and the ball-end tool. Based on curvature superposition, the effective radius can be expressed as:

$$\frac{1}{R_{eff}(u)} = \frac{1}{R(u)} + \frac{1}{R_T}, \tag{6}$$

which leads to:

$$R_{eff}(u) = \frac{R(u)R_T}{R(u)+R_T}. \tag{7}$$

where $R(u)$ and R_T are curvature radius of the machined surface and the ball-end tool, in turn.

Due to the anisotropic curvature characteristics of the surface, the geometric deviation exhibits distinct behaviors in the feed rate and step-over directions.

For Case A, the feed-direction error h_f^A remains constant along the toolpath because the curvature in this direction is zero, leading to an effective radius equal to the tool radius. Feed-direction deviation

$$h_f^A \approx \frac{f_z^2}{8R_{eff,f}^A}, \tag{8}$$

where the effective radius is:

$$R_{eff,f}^A = R_T.$$

The dominant geometric error in finishing is the step-over deviation (scallop height) $h_s^A(u)$ caused by the step-over S.

$$h_s^A(u) = \frac{S^2}{8R_{eff,s}^A(u)}, \tag{9}$$

where the effective radius is:

$$R_{eff,s}^A(u) = \frac{R(u)R_T}{R(u)+R_T}.$$

Total curvature dependent deviation h_A in Case A is:

$$h_A = \frac{f_z^2}{8R_T} + \frac{S^2}{8R_{eff,s}^A(u)}. \tag{10}$$

For Case B, the situation is reversed. The step-over error remains constant, while the feed-direction error varies significantly with the local curvature. As the curvature reaches its maximum near the vertex of the parabola, the effective radius decreases, resulting in a sharp increase in feed-direction error. This leads to a non-uniform error distribution, with pronounced peaks in regions of high curvature.

The feed-direction deviation $h_f^B(u)$ depends on the feed per tooth f_z, tool radius R_T, and curvature radius $R(u)$:

$$h_f^B(u) \approx \frac{f_z^2}{8R_{eff,f}^B(u)}, \tag{11}$$

where the effective radius is:

$$R_{eff,f}^B(u) = \frac{R(u)R_T}{R(u)+R_T}.$$

The step-over deviation h_s^B, caused by the step-over S in this case can be approximated as:

$$h_s^B \approx \frac{S^2}{8R_{eff,s}^B}, \tag{12}$$

where the effective radius is:

$$R_{eff,s}^B = R_T.$$

Total curvature-dependent deviation in case B is

$$h_B = \frac{f_z^2}{8R_{eff,f}^B(u)} + \frac{S^2}{8R_T}. \tag{13}$$

Regarding the curvature-based optimization model for machining accuracy, the total error $h_\Sigma(u)$ must satisfy the following constraint to meet the precision requirements:

$$h_\Sigma(u) \le [h], \tag{14}$$

where $[h]$ is maximum allowable geometric deviation.

Substituting deviation h_A into this inequality, we get:

$$\frac{f_z^2}{8R_T} + \frac{S(u)^2}{8R_{eff,s}^A(u)} \le [h]. \tag{15}$$

Solving for $S(u)$, the curvature-based adaptive step-over is obtained as:

$$S(u) = \sqrt{8R_{eff,s}^A(u)\left([h]\frac{f_z^2}{8R_T}\right)}. \tag{16}$$

For the experimental study, the experimental setup was established to validate the proposed model.

Machine tool: CNC milling machine DX-6080 from WANTAI (Taiwan) with some basic technical characteristics as follows: machine table size of 600 x 800 (mm); main spindle motor power of 5.5 kw, spindle speed of 600–18000 rev/min; max feed rate of 6000 mm/min; repeatable positioning accuracy of 0.005 mm.

Cutting tool: from the formula for determining curvature k_2 above, the smallest radius of curvature of the surface is determined as Rp_{min} = 7.5 mm. Therefore, to avoid undercutting, the ball end mills used in this study are chosen as Φ6, Φ10, Φ14 from G.T. cutting tools (Taiwan) with number of teeth Z = 2.

Workpiece: L × W × H =70 × 70 × 70 (mm), aluminum alloy A6061

CAM software: NX12

Equipment for measurement: 3D Scanner SIMSCAN from SCANTECH (HANGZHOU) CO., LTD, with accuracy up to 0.020 mm, scanning rate up to 2020000 measurements/sec, resolution up to 0.025 mm, scanning area up to 410 mm × 400 mm.

Experiment plan: the workpieces are rough machined and semi-finished to form a cylindrical surface with a finish allowance of 0.1 mm.

The experimental finishing process was performed with zigzag parallel cutting strategy (Case A) according to the experimental plan designed based on the Taguchi $OA_9(3^3)$ orthogonal array with 3 factors: Step-over (S), Feed rate (F) and Tool diameter (D). The factors and experimental levels are presented in Table 1.

Table 1.

Factors and Levels

Factors	Levels		
	1	2	3
Step-over S (mm)	0.1	0.4	0.7
Feed rate F (mm/min)/f_z (mm/tooth)	100/(0.025)	500/(0.125)	900/(0.225)
Tool diameter D (mm)	6	10	14

The remaining technological conditions are unchanged for all 9 samples: velocity of spindle n = 2000 rpm, depth of cut of 0.1 mm, flushing with cutting fluid. The output indicators of this experimental planning are the machining accuracy assessed by the geometric error of the surface of the machined sample compared to the surface of the designed sample.

The finished machined samples (Figure 4) were digitized using a SIMSCAN handheld 3D scanner. These 9 point cloud data files were used for sequential registration with the design CAD model surface to determine the geometric errors of the samples using Geomagic Quality 2003. Geomagic Quality performed iterative rigid-body registration between the measured point cloud and the nominal CAD surface by minimizing the least-squares distance between corresponding geometric entities, following the ICP framework. The criterion for evaluating geometric errors was the average deviation determined by the formula: average deviation = (max dev – min dev)/2.

Results and Discussion. Based on the above analysis, a machining error simulation program was written in MATLAB with input parameters tool radius $R_T = 7$ mm, feed rate $f_z = 0.2$ mm/tooth, step over $S = 0.1$ mm. The program results for machining errors for the two cases A and B are shown in Figure 2. Comparison of the total machining error shows that both strategies produce errors that vary along the surface. However, Case A consistently yields lower error values than Case B across the entire parameter domain. More importantly, the error distribution in Case A is smoother and more stable, whereas case B exhibits strong sensitivity to curvature variations. This difference is critical from a manufacturing perspective, as large variations in feed-direction error are directly associated with surface waviness and form deviation.

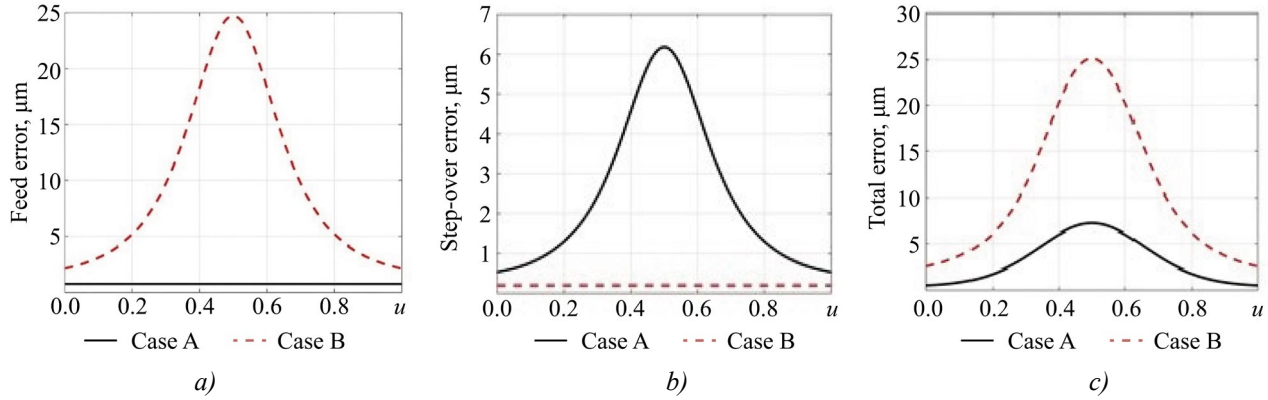

Fig. 2. Errors simulation for two Cases

a — Feed error; *b* — Step-over error; *c* —Total error

The results indicate that the feed-direction error plays a dominant role in determining the overall form accuracy. Although the total error magnitude may appear comparable under certain parameter combinations, the redistribution of error components significantly affects the final surface quality. By aligning the feed direction with the minimum-curvature direction, Case A effectively decouples the most critical error component from curvature variations, thereby improving machining stability and accuracy. Therefore, the toolpath strategy in Case A is better than the toolpath strategy in Case B.

From a practical standpoint, this finding supports the strategy commonly adopted in advanced CAM systems such as Siemens NX and PowerMill, where toolpaths are preferentially oriented along directions of minimal curvature. Therefore, for the machining of parabolic cylindrical surfaces, the optimal strategy is to align the feed direction with the zero-curvature direction and to control the step-over according to the local curvature.

Figure 3 shows the result of running the program with input data $R_T = 7$ mm, $f_z = 0.02$ mm/tooth, allowable error $[h] = 0.02$mm. With the step-over that adapts according to the surface curvature as in the diagram, the geometric surface error will remain unchanged at 0.02 mm. Currently, commercial CAM systems like Siemens NX and PowerMill also have adaptive step-over in an indirect and heuristic way, but not explicitly formulated as here.

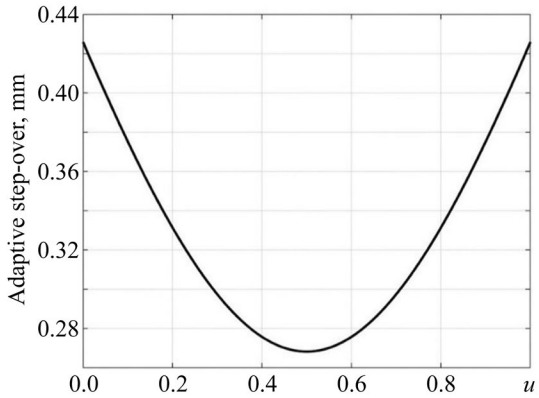

Fig. 3. Adaptive step-over simulation for Case A

Regarding the experimental results and discussion, the machined samples are presented in Figure 4, the measured geometric errors for Sample 2 are illustrated in Figure 5, while the comprehensive error data are summarized in Table 2.

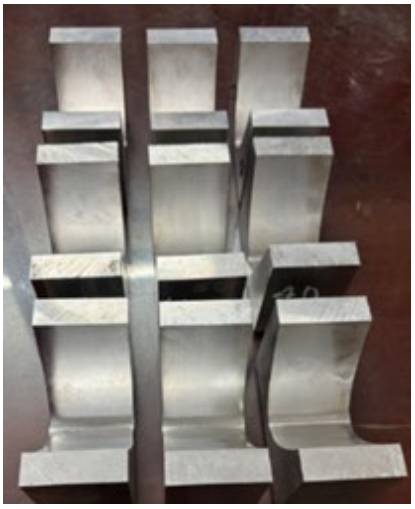

Fig. 4. Nine experimental samples

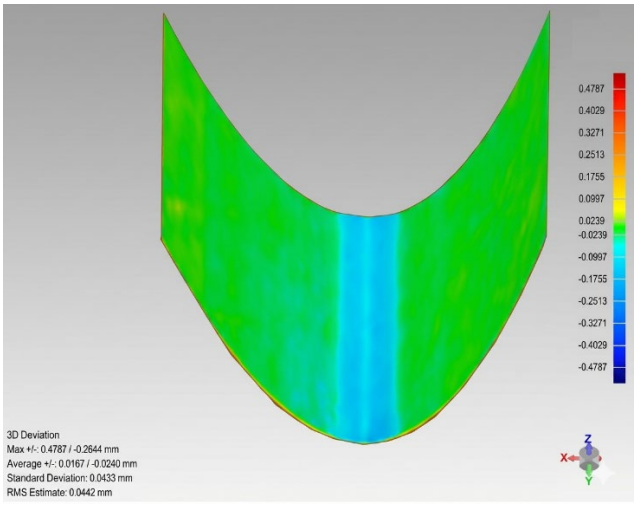

Fig. 5. Geometrical error of sample 2

In the analysis and assessment of machining accuracy, the performance is evaluated based on specific machining error criteria. The smaller the machining error, the higher the machining accuracy. According to the choice of output as small as possible (smaller is better), the S/N ratio for each experiment is determined (Table 2).

Table 2

Experimental Results Obtained from the Orthogonal Array Taguchi $OA_9(3^3)$

N^0	S (mm)	F (mm/min)	D	Geometric Deviation (μm)			$(S/N)_\Delta$
				Upper	Lower	Average Δ	
1	0.1	100	6	18.9	35.3	**27.1**	–14.3297
2	0.1	500	10	16.7	24	**20.35**	–13.0856
3	0.1	900	14	20.4	18	**19.2**	–12.833
4	0.4	100	10	16.8	28.7	**22.75**	–13.5698
5	0.4	500	14	16.6	22.1	**19.35**	–12.8668
6	0.4	900	6	18.2	39.2	**28.7**	–14.5788
7	0.7	100	14	15.5	34	**24.75**	–13.9358
8	0.7	500	6	22.6	45.8	**34.2**	–15.3403
9	0.7	900	10	25.7	38.2	**31.95**	–15.0447

The average S/N ratio for each factor at levels 1, 2 and 3 can be calculated by averaging the S/N ratios of the corresponding experiments. The influence of each factor on the machined surface geometric error is determined using Minitab as shown in Figure 6. A large S/N ratio indicates that the machined surface has small geometric errors. Analysis of variance (Table 3) shows that the coefficients of determination are quite high (98.92% and 95.68%), confirming that the model fits the data well.

Table 3

Analysis of Variance (ANOVA) for $(S/N)_\Delta$
Model Summary R-Sq = 98.92%, R-Sq(adj) = 95.68%

Source	DF	Seq SS	Adj SS	Adj MS	F	P
S	2	12.4878	12.4878	6.2439	41.36	0.024
F	2	0.9044	0.9044	0.4522	2.99	0.250
D	2	14.2398	14.2398	7.1199	47.16	0.021
Residual Error	2	0.3020	0.3020	0.1510		
Total	8	27.9339				

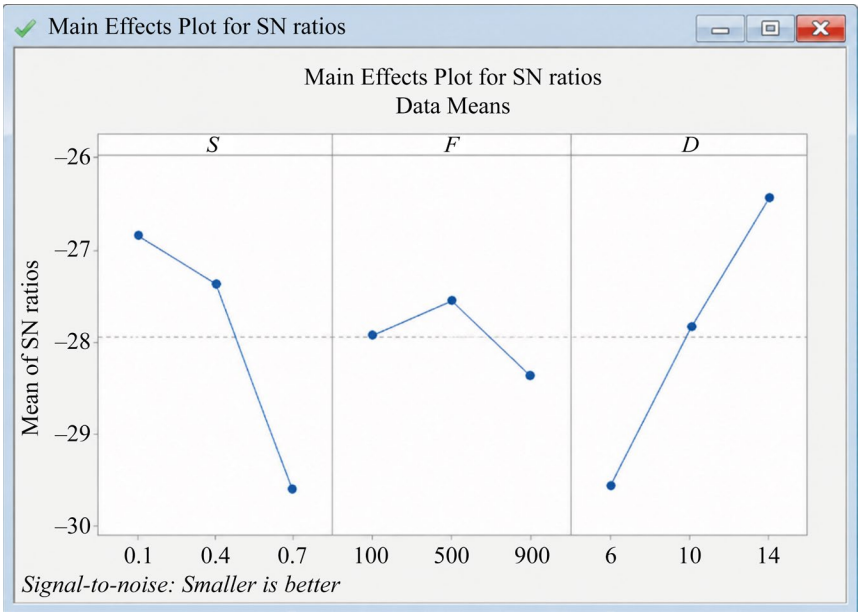

Fig. 6. Main effects plot for (S/N)Δ ratios

Through the data in this table, the influence of each factor on machining accuracy can also be determined. Diameter of Tool (*D*) has the largest influence (51%), followed by the influence of Step-over (44.7%). The influence of Feed rate is the smallest (3%) (Table 4).

Table 4

Influence of Factors on the Machining Accuracy

N^0	Factor	Contribution %
1	Step-over (*S*)	44.7
2	Feed rate (*F*)	3
3	Diameter of Tool (*D*)	51
4	Errors	1.3

From here, it can be seen that the conformity of a generating tool and the machined surface has a significant influence on shaping accuracy. With the S/N value as large as possible, we can choose the optimal parameter set $S_1F_2D_3$. The optimal parameters to have the best geometrical accuracy of the machined surface are step-over of 0.1 mm, feed rate of 500 mm/min, and the tool diameter of 14 mm.

The predicted average deviation in this case would be:

$$\Delta_{min} = \overline{\Delta}(S_1) + \overline{\Delta}(F_2) + \overline{\Delta}(D_3) - 2\frac{\sum \Delta_i}{9} = 22.22 + 24.63 + 21.1 - 2 \cdot 228.35 / 9 \approx 17.2 \text{ (μm)}. \quad (17)$$

Conclusion. This study investigated the influence of machining parameters on the forming accuracy of concave parabolic freeform surfaces in 3-axis CNC milling. In contrast to conventional experimental approaches, a curvature-based analytical framework was introduced to interpret machining errors from a geometric perspective.

The results confirm that the considered surface exhibits anisotropic curvature characteristics, where one principal curvature is zero and the other varies continuously along the surface. This geometric property leads to non-uniform tool–surface interaction conditions, which significantly affect machining accuracy. Experimental analysis based on the Taguchi method and ANOVA indicates that step-over and tool diameter are the dominant factors influencing geometric deviation, while feed rate has a comparatively smaller effect.

To provide a theoretical explanation for these observations, a curvature-based optimization model was developed. The model relates machining errors to local curvature through an effective radius formulation, demonstrating that both feed-direction deviation and scallop height are inversely proportional to the curvature radius. Based on this relationship, a curvature-adaptive step-over strategy was proposed to maintain a constant allowable error across the surface.

The comparison between constant and curvature-adaptive step-over strategies shows that the adaptive approach significantly reduces error variation and improves overall surface accuracy. This finding highlights the importance of incorporating geometric characteristics into machining parameter selection, rather than relying solely on empirical optimization methods.

Although the direct implementation of continuous curvature-adaptive step-over is not supported by standard CNC controllers, the proposed model provides a theoretical foundation for constant scallop height toolpath generation available in modern CAM systems. Therefore, the results of this study have practical relevance for improving machining efficiency and accuracy in industrial applications.

Future work will focus on extending the proposed approach to more complex freeform surfaces with non-zero Gaussian curvature, as well as integrating curvature-based optimization into automated toolpath generation and intelligent machining systems.

References

1. Safarov DT, Glinina GF, Kasyanov SV. Improving the Accuracy of Die Impression Milling for Large-Size Forgings of Heavy-Duty Vehicle Parts. *Russian Engineering Research*. 2024;44(8):1128–1136. https://doi.org/10.3103/S1068798X24701880

2. Safarov DT, Glinina GF, Kondrashov AG. Geometric Accuracy of Die Engraving: Experimental Data and Modeling. *Russian Engineering Research*. 2023;43(11):1400–1407. https://doi.org/10.3103/S1068798X23110266

3. Gimadeev MR, Nikitenko AV, Berkun VO. Influence of the Sphero-Cylindrical Tool Orientation Angles on Roughness under Processing Complex-Profile Surfaces. *Advanced Engineering Research (Rostov-on-Don).* 2023;23(3):231–240. https://doi.org/10.23947/2687-1653-2023-23-3-231-240

4. Mali RA, Gupta TVK, Ramkumar J. A Comprehensive Review of Free-Form Surface Milling – Advances over a Decade. *Journal of Manufacturing Processes*. 2021;62:132–167. https://doi.org/10.1016/j.jmapro.2020.12.014

5. Marin F, Souza AF, Gaspar HS, Calleja-Ochoa A, López de Lacalle LN. Topography Simulation of Free-Form Surface Ball-End Milling through Partial Discretization of Linearised Toolpaths. *Engineering Science and Technology, an International Journal*. 2024;55:101757. https://doi.org/10.1016/j.jestch.2024.101757

6. Beňo J, Tomáš M, Ižol P, Varga J. Analysis of the Free Form Surface Milling Based on a Fragmentation Approach. *Journal of Production Engineering*. 2015;18(1):31–34.

7. Varga J, Tóth T, Kaščák L, Spišák E. The Effect of the Machining Strategy on the Surface Accuracy When Milling with a Ball End Cutting Tool of the Aluminum Alloy AlCu4Mg. *Applied Sciences*. 2022;12(20):10638. https://doi.org/10.3390/app122010638

8. Grešová Z, Ižol P, Vrabel M, Kaščák L, Brindza J, Demko M. Influence of Ball-End Milling Strategy on the Accuracy and Roughness of Free Form Surfaces. *Applied Sciences*. 2022;12(9):4421. https://doi.org/10.3390/app12094421

9. Cica D, Zeljkovic M, Sredanovic B, Tesic S. Optimization of Machining Parameters with Minimum Surface Roughness for Three-Axis Milling of Sculptured Parts. *Journal of Production Engineering*. 2017;20(2):75–78. https://doi.org/10.24867/JPE-2017-02-034

10. Ižol P, Vrabel M, Maňková I. Comparison of Milling Strategies in Case of Free Form Surface Milling. *Materials Science Forum*. 2016;862:18–25. https://doi.org/10.4028/www.scientific.net/MSF.862.18

11. Mgherony A, Mikó B. Tool Path Planning of Ball-End Milling of Free-Form Surfaces as a Search Algorithm. *Acta Technica Jaurinensis*. 2024;17(2):75–83. https://doi.org/10.14513/actatechjaur.00736

12. Kukreja A, Pande SS. Estimation of Scallop Height in Freeform Surface Machining. *The International Journal of Advanced Manufacturing Technology*. 2019;103:167–181. https://doi.org/10.1007/s00170-019-04269-x

13. Ngoc Tuyen Bui, Duc Luong Ngo. An Experimental Study of 3 Axes CNC Milling for a Blade of the Axial Flow Pump Impeller. In: *Proc. Int. Conf. on Material, Machines and Methods for Sustainable Development*. Cham: Springer; 2021. P. 330–336. https://doi.org/10.1007/978-3-030-99666-6_11

14. Van Quy Hoang, Bui Ngoc Tuyen. Effect of Feed Rate, Tool Path and Step over on Geometric Accuracy of Freeform Surfaces When 3 Axis CNC Milling. *Applied Mechanics and Materials*. 2019;889:107–114. https://doi.org/10.4028/www.scientific.net/AMM.889.10

15. Kireyev SO, Lebedev AR, Korchagina MV. Optimization of Geometric Characteristics of Cycloidal Profiles of Gerotor Hydraulic Machines. *Advanced Engineering Research (Rostov-on-Don).* 2023;23(3):269–282. https://doi.org/10.23947/2687-1653-2023-23-3-269-282

16. Radzevich SP. *Kinematic Geometry of Surface Machining*. Boca Raton, FL: CRC Press; 2007. 536 p.

17. Roy RK. *A Primer on the Taguchi Method*, 2nd ed. Southfield, MI: SME; 2010. 300 p.

18. Stephenson DA, Agapiou JS. *Metal Cutting Theory and Practice*, 3rd ed. Boca Raton, FL: CRC Press; 2016. 956 p.

19. Kalpakjian S, Schmid SR. *Manufacturing Engineering and Technology*, 7th ed. Singapore: Pearson; 2020. 407 p.

About the Authors:

Ngoc Tuyen Bui, Dr.Sci. (Eng.), Associate Professor, Head of the Division of Material Machining and Industrial Tools, School of Mechanical Engineering, Hanoi University of Science and Technology (01, Dai Co Viet Str., Hanoi city, 11626, Vietnam), ORCID, ScopusID, ResearcherID, ResearchGate, tuyen.buingoc@hust.edu.vn

Nguyen Tho Van, Dr.Sci. (Eng.), Faculty of Technology and Engineering, Haiphong University (171, Phan Dang Luu Str., Haiphong city, 04617, Vietnam), ORCID, ResearcherID, ResearchGate, thonv@dhhp.edu.vn

Claimed Contributorship:

Ngoc Tuyen Bui: conceptualization, methodology, data curation, formal analysis, writing – original draft preparation.
Nguyen Tho Van: investigation, visualization, writing – original draft preparation, writing – review & editing.

Conflict of Interest Statement: **the authors declare no conflict of interest.**

All authors have read and approved the final version of manuscript.

Об авторах:

Нгок Туен Буй, доктор технических наук, доцент, начальник отдела механической обработки материалов и промышленного инструмента инженерной школы машиностроения Ханойского университета науки и технологий (01, ул. Дай Ко Вьет, Ханой, 11626, Вьетнам), ORCID, ScopusID, ResearcherID, ResearchGate, tuyen.buingoc@hust.edu.vn

Нгуен Тхо Ван, доктор технических наук, факультет технологий и инженерии Хайфонского университета (171, ул. Фан Данг Луу, Хайфон, 04617, Вьетнам), ORCID, ResearcherID, ResearchGate, thonv@dhhp.edu.vn

Заявленный вклад авторов:

Нгок Туен Буй: разработка концепции, разработка методологии, курирование данных, формальный анализ, написание черновика рукописи.
Нгуен Тхо Ван: проведение исследования, визуализация, написание черновика рукописи, написание рукописи – рецензирование и редактирование.

Конфликт интересов: **авторы заявляют об отсутствии конфликта интересов.**

Все авторы прочитали и одобрили окончательный вариант рукописи.

Received / Поступила в редакцию 16.03.2026
Reviewed / Поступила после рецензирования 29.04.2026
Accepted / Принята к публикации 20.05.2026

MACHINE BUILDING AND MACHINE SCIENCE
МАШИНОСТРОЕНИЕ И МАШИНОВЕДЕНИЕ

UDC 621.791
https://doi.org/10.23947/2687-1653-2026-26-2-2288

Original Empirical Research

Quantitative Evaluation of Fusion Zone Curvature Correlation with Electrode Positioning in Shielded Gas Split-Arc Surfacing

Iakov P. Skoblikov ✉, **Sergey B. Sapozhkov**
Saint Petersburg State Marine Technical University, Saint Petersburg, Russian Federation
✉ iakov98sp@gmail.com

EDN: KDYBZG

Abstract

Introduction. Improving the efficiency of arc surfacing with a consumable electrode is one of the key vectors in the development of modern manufacturing. Split-arc gas-shielded welding with a consumable electrode is of particular interest. The electrode arrangement in this welding process affects the fusion zone, namely its shape and curvature. The shape of the penetration zone significantly affects the property gradient and the operational reliability of the coating. The effect of the electrode arrangement on the curvature of the penetration front remains quantitatively unassessed. The objective of this study is to quantitatively evaluate and determine the correlation of the curvature of the penetration shape depending on the relative arrangement of the electrodes.

Materials and Methods. The effect of electrode positioning on the penetration shape was studied by building up six layers and subsequently analyzing the fusion shape in the base metal. The selected influencing parameters were the interelectrode distance (z) and the electrode inclination angle (α). The surfacing process was performed in an Ar/CO_2 shielding gas atmosphere in a ratio of 98/2%. To make the fusion zone visible, the transverse cross-sections of the layers were subjected to etching. The fusion zone boundaries were digitized. A 6th-degree polynomial was used to determine the functions describing the penetration shape. The obtained functions were differentiated to analyze the fusion shape. The first-order derivative was used to determine the number of extremes. To assess the curvature of the penetration shape, the average value of the absolute second derivative was calculated over the range of values within the layer width. Correlation was established using Pearson's method.

Results. As a result of the conducted experiment, a quantitative assessment of the curvature of the penetration shape depending on the relative arrangement of the electrodes was performed. Functions describing the penetration shapes were determined. The curvature of the obtained shapes and the number of extremes were calculated. Correlation coefficients between the interelectrode distance, the electrode inclination angle, the penetration curvature, and the number of extremes were determined. It was found that the curvature of the penetration shape and the number of extremes weakly depend on the interelectrode distance. The electrode inclination angle determines the penetration curvature to a greater extent. A damping effect of the heat flux of the electric arc by the volume of the weld pool was identified at an interelectrode distance of 15 mm.

Discussion. In each experiment, the base metal fusion zone displayed a saddle-shaped geometry. Increasing the electrode included angle resulted in a shallower penetration shape, attributed to an alteration in the vector of electromagnetic forces that govern plasma streams and molten metal droplet transfer. The damping effect occurred because reducing the interelectrode distance enlarged the weld pool. A layer of molten metal, possessing high heat capacity but low thermal conductivity, separated the electric arc from the base metal, thus damping the heat flux from the arc.

Conclusion. The conducted study made it possible to quantitatively assess the effect of the electrode arrangement on the curvature of the penetration shape, as well as to determine the degree of influence of the interelectrode distance and the electrode inclination angle on the curvature of the penetration shape. The interelectrode distance was found to have a weak effect on both the fusion shape curvature and the number of extremes. The correlation coefficients for these parameters were –0.22 and 0.43. The effect of the electrode inclination angle on both the fusion shape curvature and the number of extremes was considered substantial. The correlation coefficients for these parameters were –0.65 and –0.71. As the angle of inclination of the electrodes relative to the vertical increased, the curvature of the penetration shape decreased.

Keywords: split-arc surfacing, GMAW, multiwire surfacing, mutual arrangement of electrodes, fusion zone

Acknowledgements. The authors would like to thank the Editorial board of the journal and the reviewers for their professional analysis of the article and valuable recommendations for its improvement.

For Citation. Skoblikov IP, Sapozhkov SB. Quantitative Evaluation of Fusion Zone Curvature Correlation with Electrode Positioning in Shielded Gas Split-Arc Surfacing. *Advanced Engineering Research (Rostov-on-Don).* 2026;26(2):2288. https://doi.org/10.23947/2687-1653-2026-26-2-2288

Оригинальное эмпирическое исследование

Количественная оценка кривизны формы проплавления в зависимости от взаиморасположения электродов при наплавке расщепленной дугой в среде защитного газа

Я.П. Скобликов ✉, **С.Б. Сапожков**

Санкт-Петербургский государственный морской технический университет, г. Санкт-Петербург, Российская Федерация

✉ iakov98sp@gmail.com

Аннотация

Введение. Повышение эффективности дуговой наплавки плавящимся электродом является одним из ключевых направлений развития современного производства. Особый интерес представляет наплавка расщеплённым плавящимся электродом в среде защитного газа. Взаиморасположение электродов для данного способа наплавки сказывается на зоне проплавления, а именно на ее форме и кривизне. Форма проплавления влияет на градиент свойств и эксплуатационную надёжность покрытия. Влияние взаиморасположения электродов на кривизну фронта проплавления остаётся количественно не оценённым. Целью настоящего исследования являются определение корреляции кривизны формы проплавления в зависимости от взаиморасположения электродов и ее количественная оценка.

Материалы и методы. Исследование влияния взаиморасположения электродов на форму проплавления проводилось путем наплавки шести слоёв и последующего анализа формы проплавления основного металла. В качестве влияющих факторов были выбраны расстояние между электродами (z) и угол их наклона (α). Процесс наплавки осуществлялся в среде защитного газа Ar/CO_2 в соотношении 98/2 %. Для выявления зоны проплавления поперечные сечения слоев были протравлены. Границы зон проплавления оцифрованы. Для определения функций, описывающих форму проплавления, использовался полином степени 6. Для анализа формы проплавления выполнялось дифференцирование полученных функций. Дифференциал первого порядка использовался для определения количества экстремумов. Для оценки кривизны формы проплавления использовался метод расчета среднего значения модуля второй производной для значений, лежащих в пределах ширины слоя. Установление корреляции выполнялось по методике Пирсона.

Результаты исследования. В ходе проведённого эксперимента дана количественная оценка кривизны формы проплавления в зависимости от взаиморасположения электродов. Определены функции, описывающие профили проплавления. Вычислены кривизна полученных профилей и количество экстремумов. Установлены коэффициенты корреляции между межэлектродным расстоянием, углом наклона электродов, кривизной проплавления и количеством экстремумов. Сделан вывод о том, что кривизна формы проплавления и количество экстремумов слабо зависят от межэлектродного расстояния. Угол наклона электродов в большей степени определяет кривизну проплавления. Выявлен эффект демпфирования теплового потока электрической дуги объемом сварочной ванны при межэлектродном расстоянии в 15 мм.

Обсуждение. Зона проплавления основного металла для каждого опыта имеет седловатую форму. Увеличение угла развала электродов приводит к формированию более пологой формы проплавления из-за изменения вектора действия электромагнитных сил, влияющих на потоки плазмы и капли расплавленного металла. Возникновение демпфирующего эффекта объясняется тем, что при сближении электродов объём сварочной ванны увеличивается. Между электрической дугой и основным металлом возникает прослойка жидкого металла с высокой теплоемкостью и низкой теплопроводностью, за счет этого происходит демпфирование тепла от электрической дуги.

Заключение. Проведённое исследование позволило количественно оценить влияние взаиморасположения электродов на кривизну формы проплавления, а также определить степень влияния межэлектродного расстояния и угла наклона электродов на кривизну формы проплавления. Установлено слабое влияние межэлектродного расстояния на кривизну формы проплавления и количество экстремумов. Коэффициенты корреляции для данных параметров равны –0,22 и 0,43. Влияние угла наклона электродов на кривизну формы проплавления и количество экстремумов оценивается как существенное. Коэффициенты корреляции для данных параметров равны –0,65 и –0,71. С увеличением угла наклона электродов относительно вертикали кривизна формы проплавления уменьшается.

Ключевые слова: наплавка расщепленной дугой, GMAW, многопроволочная наплавка, взаимное расположение электродов, зона проплавления

Благодарности. Авторы выражают благодарность редакционной коллегии журнала и рецензенту за профессиональный анализ статьи и рекомендации для ее корректировки.

Для цитирования. Скобликов Я.П., Сапожков С.Б. Количественная оценка кривизны формы проплавления в зависимости от взаиморасположения электродов при наплавке расщепленной дугой в среде защитного газа. *Advanced Engineering Research (Rostov-on-Don).* 2026;26(2):2288 https://doi.org/10.23947/2687-1653-2026-26-2-2288

Introduction. In the current era of industrial development and additive manufacturing, improving the productivity of manufacturing processes is key to competitiveness, as it reduces cycle times and lowers product costs. These processes include the application of metal coatings using gas-shielded metal arc welding (GMAW) [1]. It is known that boosting the deposition rate of this welding process through higher wire feed speeds results in increased arc energy. This, in turn, causes deeper penetration into the base metal, along with spatter, undercutting, and the expulsion of alloying elements.

An alternative strategy for enhancing the deposition rate of this welding process exists. Instead of raising the wire feed speed, this approach increases the number of wires delivered to the weld pool. Paper [2] reports the outcomes of investigations into this method. One conclusion is that adding more wires to the welding system yields an exponential productivity gain, owing to more efficient utilization of the arc thermal energy.

Split-electrode surfacing is a multiwire surfacing method developed on the basis of the aforementioned approach. The essence of this method is that not one, but several filler wires are fed through the current lead. The current lead is connected to a single current source [3]. Surfacing by this method is used to solve problems related to the application of anticorrosion and wear-resistant coatings or the repair of components.

When depositing anticorrosion coatings, minimal base metal penetration with a uniform fusion line is required. This penetration characteristic provides a minimum content of the base metal in the deposited layer. In [4], the influence of the type of current on the shape of penetration during surfacing with a split electrode under a flux layer is studied. The effect of the distance between the electrodes on the shape of penetration is indirectly presented. The study notes that when surfacing with an interelectrode distance of 10–12 mm, a saddle-shaped penetration is formed. However, this penetration shape is acceptable for anticorrosion surfacing, provided no fusion defect exists at the saddle top, and the base metal content stays within 15–25%. The study does not assess the curvature of the penetration shape or establish a correlation between it and the relative position of the electrodes.

The authors of article [5] note that when applying wear-resistant coatings, the use of a curved penetration shape provides more reliable adhesion of the layers to the base metal, in contrast to a flat penetration shape. In [6], devoted to a comprehensive study of penetration shapes in various arc surfacing methods, it is emphasized that the curvature of the penetration shape determines the nature of the transition of the deposited metal to the base metal, which affects the stress concentration in the deposited metal, determines the gradient of mixing of the base metal in the deposited metal, and affects the properties of the deposited metal.

The authors [7] successfully applied the double-wire surfacing method to additive manufacturing. This makes the method attractive for repairs and additive manufacturing, where layer-to-layer metal transfer behavior is crucial. Thus, it can be concluded that, when solving problems related to the application of functional coatings, one of the quality parameters is the morphology of the base metal penetration zone.

The impact of the relative positioning of the electrodes on the penetration shape is due to changes in the electromagnetic forces in the arc gap and the characteristics of heat and mass transfer. In exploring this topic, the authors analyzed a number of studies devoted to the processes occurring in the arc gap during surfacing by this method. In [8], the forces acting on the droplet and molten metal under surfacing with a consumable electrode with a pulsed power supply were determined, and in [9], the change in these forces within two adjacent electrodes was described. It was established that when the electrodes were located close together, the droplet of molten metal and the plasma flow were affected by the Lorentz force directed into the interelectrode space. This force changes the droplet trajectory and lowers arc pressure. Paper [10] describes the process of modeling the heat distribution in an electric arc arising on a split electrode, and it is found that the heat distribution in a split arc depends on the distance between electrodes and the current strength. At certain values of current strength and interelectrode distance, the thermal field in the electric arc takes on a single-peak or double-peak structure. This heat flux distribution is an important factor that determine the shape of the penetration.

In [11], two key parameters of electrode positioning that affect the weld penetration shape are identified. These parameters are the electrode angle relative to the vertical and the distance between the electrodes. Thus, it is found that when selecting the optimal welding mode, it is required to determine not only the current strength but also the electrode positioning. This conclusion is consistent with the conclusion reached by the authors of article [10]. In [12], it has been found that the inclination angle of the working head affects the deposited layer morphology in forehand surfacing. The optimal inclination angle was found to be in the range of 10 to 30°. With this head position, it was possible to obtain layers 25 mm wide with a base metal content of 30–33%. The distance between the electrodes was 6 mm. Inconel 625 wire was used as the electrodes. Surfacing was performed under a flux layer.

From the analysis of the literature on this subject, it may be concluded that investigating the fusion shape in split-arc gas-shielded welding is of high relevance for applying functional coatings, repairing parts, and additive manufacturing. The relative positioning of the electrodes during surfacing by this method significantly affects the forces acting in the arc gap and the heat and mass transfer of the electrode metal. The change in the penetration shape depending on the distance between the electrodes and the angle of inclination of the electrodes for such a surfacing process has not been fully studied. The identified knowledge gap is the absence of quantitative data relating penetration shape to electrode spacing and inclination angle with respect to the vertical plane. Therefore, the objective of this study is to quantify and determine the correlation between penetration shape curvature and electrode relative positioning. To achieve this goal, the following tasks must be addressed:

1. Determine the number of extremes and the function curvature describing the weld penetration shape for each experiment.

2. Determine the correlation values of the interelectrode distance with the weld penetration shape curvature and the number of extremes, as well as the correlation values of the electrode inclination angle with the weld penetration shape curvature and the number of extremes.

Materials and Methods. To assess the curvature of the penetration shape depending on the electrode positioning, flat layers were deposited with different distances between the electrodes and the angle between them. The working tool was moved using a Fanuc 120iD robot (Japan). The electric arc was powered from a pulsed power supply EWM Titan XQ500 (Germany). The surfacing head consisted of two burners mounted on an adjustable bracket. The substrates used were St3 (GOST 380- 2005) steel plates, measuring 150x70x20 mm. Surfacing was performed in GMAW-Pulse mode using Sv-08G2S (GOST 2246-70) wire with a diameter of 1.2 mm. The chemical composition of the wire is presented in Table 1. A mixture of Ar (98%) and CO_2 (2%) was used as a shielding gas. This gas mixture, compared to mixtures with a higher CO_2 content, has a reduced oxidizing capacity, resulting in fewer nonmetallic inclusions under surfacing. To visualize the macrostructure of the deposited layer, samples were electrolytically etched in a sodium chloride (NaCl) solution with a concentration of 200 g/L. Before etching, the samples were polished. Etching was performed at a current density of 7–10 A/dm². A 12Kh18N10T (GOST 5632-2014) steel rod with a swab attached to the end served as the cathode. Etching was performed through rubbing the sample until the structure was revealed. This etching method was selected as one of the available methods at the time of the study. Penetration shape measurements were performed using Digimizer software (version 6.5.1).

Table 1

Chemical Composition of Wire Sv-08G2S (GOST 2246-70) (wt.%)

C	Si	Mn	P	S	Ni	Cr	Cu
0.05–0.11	0.70–0.95	1.80–1.90	≤0.030	≤0.025	≤0.025	≤0.020	≤0.025

The distance between the electrodes (z) and their angle of inclination (α) relative to the vertical plane were selected as independent factors determining the relative positioning of the torches. During the experiment, surfacing was performed with a uniform overhang (SO) of 20 mm. Figure 1 shows the electrode arrangement under surfacing and the parameters studied.

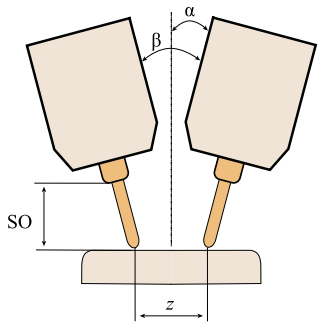

Fig. 1. Layout diagram [11]

The layers were deposited at a wire feed speed (WFS) of 6.5 m/min for a single torch. Since two torches were used during the deposition process, the total wire feed speed was 13 m/min. The working tool moved at a constant linear speed (TS) of 4 mm/s. During the deposition process, current (I) and voltage (U) were recorded using the ammeter and voltmeter integrated into the power source. During the experiments, identical substrates were used to maintain a similar thermal pattern. Before depositing the layer, the substrates were cleaned to a metallic luster and preheated to a temperature (MPT) of 150 °C. Preheating was performed with a gas torch to simulate actual process conditions under which production work is carried out. Temperature monitoring was performed with a HIKMICRO B20 thermal imager (China). The shielding gas flow rate for each torch was 15 l/min. The total gas flow rate was 30 l/min. Table 2 shows the deposition mode.

Table 2

Surfacing Mode

WFS, m/min	I, A	U, B	TS, mm/s	MPT,°C	SO, mm	Gas, l/min
13	420	25	4	150	20	30

The experimental design included six runs with different z (1Cr, 18, 21 mm) and α (5°, 10°) parameters. Samples for analysis were collected from a section comprising 3/4 of the deposited layer length. The experimental design is presented in Table 3. Figure 2 shows a photograph of a sample with its dissection line.

Table 3

Experimental Design

Run	z, mm	α, °
1	15	5
2	18	5
3	21	5
4	15	10
5	18	10
6	21	10

Fig. 2. Appearance of the sample

To assess the influence of the relative positioning of the electrodes on the penetration shape, its boundaries were determined in the Digimizer program. Figure 3 shows a photograph of macrosections with the boundaries outlined.

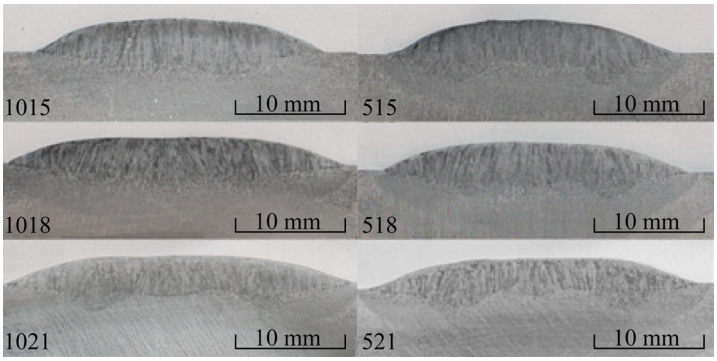

Fig. 3. Photo of macrosections with outlined boundaries [5]

Since during split-arc surfacing two heat sources are located symmetrically relative to the motion vector, the shape of the penetration is conditionally symmetrical. To assess the penetration shape, it was decided to mirror and superimpose the measured values on each other relative to the layer axis, and invert the values along the Y axis. Figure 4 shows this technique. As a result of the operation performed, it was possible to present the data as points in the XY, where X — the width of penetration from the layer axis, and Y — the depth of penetration. Moreover, the Y axis is the axis of the deposited layer.

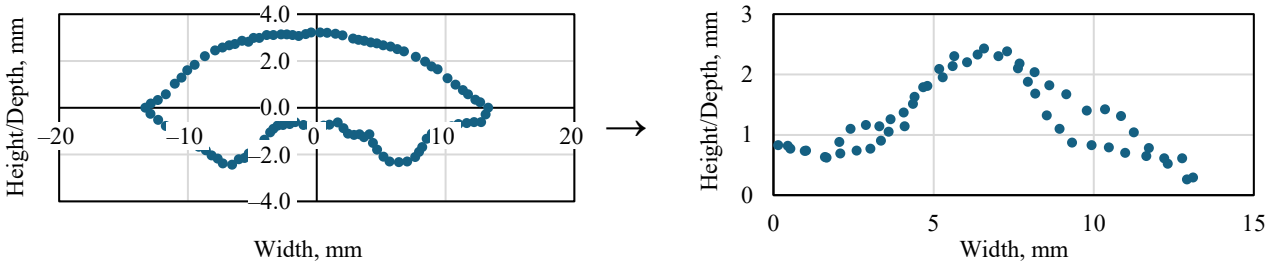

Fig. 4. Data processing

To assess the curvature of the penetration shape based on the measured data, the regression function of each profile was determined. A sixth-degree polynomial was used to describe all curves. The first derivative of the equations describing the form of penetration was used to determine the number of extremes. The second derivative was used to quantify curvature. The curvature of the penetration shape for each experiment was calculated as the average value of the modulus of the second derivative for points lying within the layer width. The correlation between the curvature of the penetration shape and the extremes depending on the distance between the electrodes and the angle of their inclination was calculated by the Pearson method.

Research Results. Regression equations describing the shape of the penetration were determined. The coefficient of determination was greater than 0.9. The equations are presented in Table 4.

Table 4

Regression Equations

No.	X^6	X^5	X^4	X^3	X^2	X^1	Const	R^2
515	–0.000075	0.002839	–0.0385	0.216	–0.41	0.15	0.83	0.91
1015	–0.000003	–0.000049	0.0039	–0.050	0.17	0.16	0.75	0.90
518	–0.000070	0.002942	–0.0449	0.296	–0.77	0.46	1.87	0.93
1018	–0.000013	0.000466	–0.0058	0.027	–0.04	–0.02	2.08	0.92
521	–0.000035	0.001672	–0.0292	0.222	–0.67	0.60	1.02	0.92
1021	–0.000052	0.002405	–0.0413	0.315	–0.99	1.00	0.65	0.92

Figure 5 shows graphs illustrating the shape of the penetration and the pattern of its change depending on the angle of inclination of the electrodes at the same distance between them. Figure 6 shows graphs describing the shape of the penetration and the pattern of its change depending on the distance between the electrodes for experiments with a fixed angle of inclination.

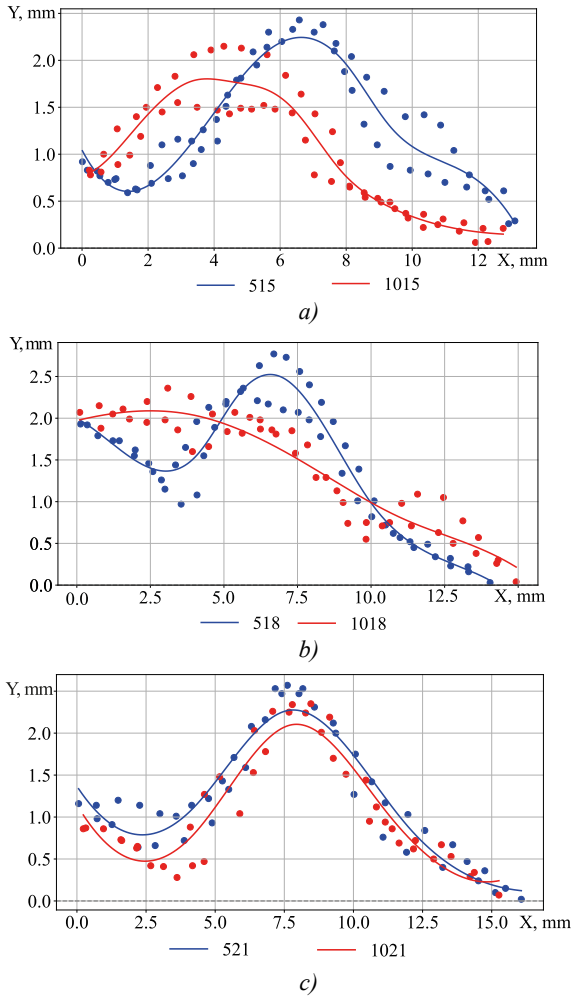

Fig. 5. Penetration shape and behavior for an angle of 5 and 10°:
a — for *z* = 15 mm; *b* — for *z* = 18 mm; *c* — for *z* = 21 mm

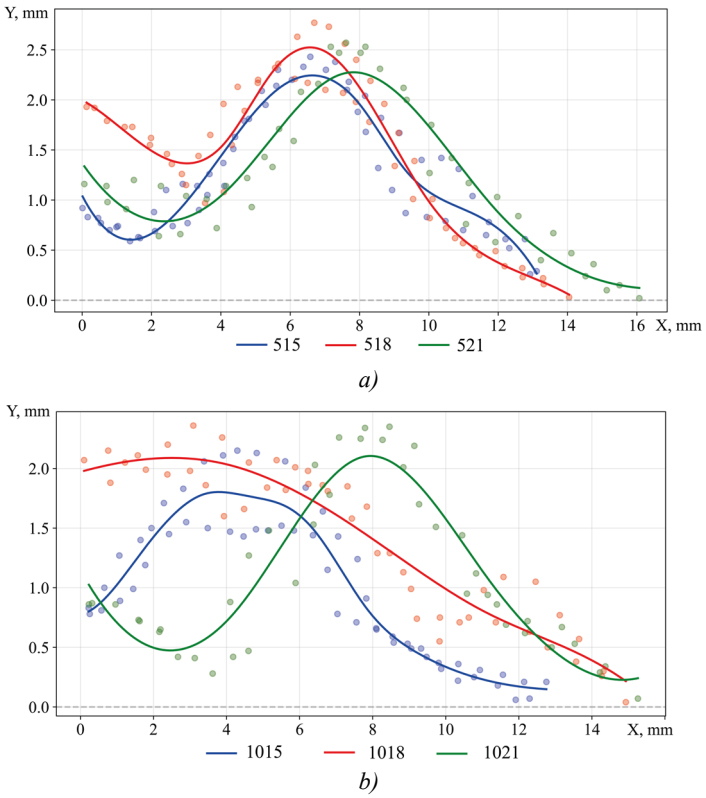

Fig. 6. Penetration shape and behavior at *Z* = 15, 18, 21 mm:
a — angle of inclination of electrodes 5°; *b* — angle of inclination of electrodes 10°

It can be seen from the graphs that all experiments exhibit a curved, saddle shape of penetration. Depending on the electrode arrangement, the penetration profiles display either one or two extremes.

Graphs illustrating how the curvature of the penetration shape varies with electrode positioning are shown in Figure 7. The digits 1 and 2 denote the number of extremes present on the penetration shape curve.

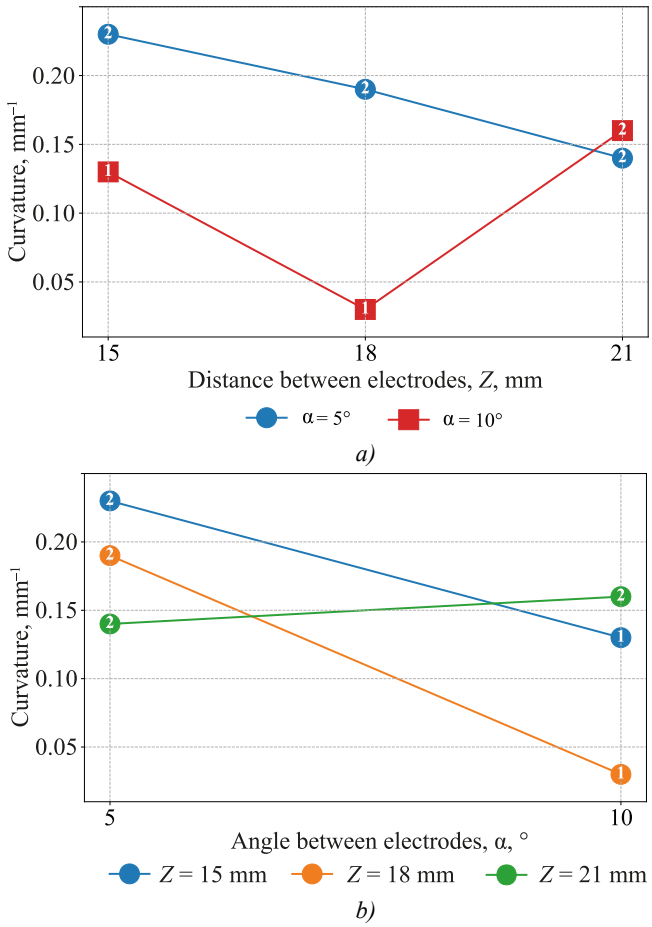

Fig. 7. Graphs of the dependence of the curvature of the fusion zone: *a* — on the distance between the electrodes; *b* — on the angle between the electrodesα°

For experiments with an interelectrode distance of 21 mm, the curvature of the penetration shape lies in the region of 0.15 mm^{-1}. The fusion zone has two extremes. For experiments with a distance between electrodes of 18 and 15 mm, the amount of curvature of the penetration shape depends on the angle of inclination of the electrodes. At an inclination angle of 10°, the penetration shape has a curvature of 0.03 mm^{-1} and 0.14 mm^{-1}, respectively. The number of extremes is equal to one. As the angle decreases to 5°, the curvature increases to 0.19 mm^{-1} and 0.24 mm^{-1}, respectively. The number of extremes becomes equal to two.

Table 5 shows the matrix obtained during the evaluation of the correlation value of the curvature of the penetration shape and the number of extremes depending on the distance between the electrodes and their angle of inclination.

Table 5

Correlation Matrix

	Z	α	Curvature	Extremes
Z	1	–0.08	–0.22	0.43
α	–0.08	1	–0.65	–0.71
Curvature	–0.22	–0.65	1	0.36
Extremes	0.43	–0.71	0.36	1

The correlation coefficient of the distance between the electrodes with the curvature of the penetration shape is –0.22, and with the number of extremes — 0.43. The correlation coefficient of the slope angle with the curvature of the penetration shape is –0.65, and with the number of extremes — –0.71.

Discussion. The penetration shape of the base metal is characterized by the presence of an axial zone (P1) and a primary zone (P2) of penetration. The primary zone of penetration is formed directly under the action of the heat source. The formation of the axial zone of penetration is caused by the superposition of thermal fields from each heat source and the thermal effect of plasma flows rushing into the area between the electrodes [13]. Figure 8 shows a schematic representation of the fusion zone during split-arc surfacing.

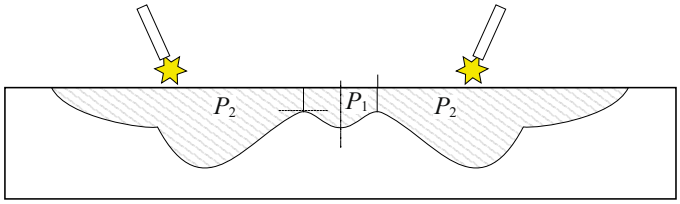

Fig. 8. Schematic representation of the fusion zone during surfacing with a split electrode

The analysis of the penetration shape curvature shows that at an interelectrode distance of 21 mm, it is independent of the electrode inclination angle. When surfacing with this electrode positioning, the electric arcs behave as independent heat sources. This is evidenced by the similar penetration shape, a shape curvature value of approximately 0.15 mm^{-1}, and an equal number of extremes. As the interelectrode distance decreases to 18 or 15 mm, the penetration shape curvature becomes dependent on the electrode inclination angle. With increasing electrode inclination, penetration becomes flatter. This is evidenced by a decrease in penetration shape curvature and the number of extremes. For tests with an 18 mm electrode spacing, penetration curvature decreases by 84%, while for tests with a 15 mm electrode spacing, it decreases by 42%.

According to the results of the correlation assessment, the relationship between the interelectrode distance (z) and the curvature of the penetration shape is weak (Pearson's coefficient $r = –0.22$), and the relationship between the interelectrode distance and the number of extremes is moderate ($r = –0.43$ The correlation between the electrode inclination angle (α) and the curvature of the penetration shape is determined as moderate, close to strong ($r = –0.65$), while the correlation of the inclination angle with the number of extrema is estimated as strong ($r = –0.71$).

The change in the curvature of the penetration shape depending on the relative positioning of the electrodes is associated with a change in the vector of forces acting on the droplet in the arc. The forces acting on the droplet during GMAW surfacing were analyzed in [14]. When the droplet detaches, it is acted upon by gravity, electromagnetic force, and the force caused by the plasma flows. During split-electrode welding, the interaction of electromagnetic fields from adjacent arcs generates a Lorentz force that deflects the arc column and droplet toward the weld axis [15]. As a result, the molten metal droplets fall not directly under the electrode, but with a shift toward the weld axis. This is confirmed by the results of high-speed video recording of the tandem welding process, presented in [16]. This shift results in the formation of a shallower penetration shape.

Notably, the minimum penetration curvature, equal to 0.03 mm^{-1}, occurs at an interelectrode distance of 18 mm and an inclination angle of 10° to the vertical. As the electrodes approach 15 mm, the penetration shape becomes steeper, despite the closer heat sources and the increased radial component of the electromagnetic force.

A comparison of the experimental results shows that when surfacing with the parameter $z = 15$ mm, the width of the deposited layer is smaller. However, due to the equal volume of molten electrode material, the thickness (or height) of this layer is greater. Figure 9 shows a graph of the dependence of the height and width of the deposited layer on the location of the electrodes [11].

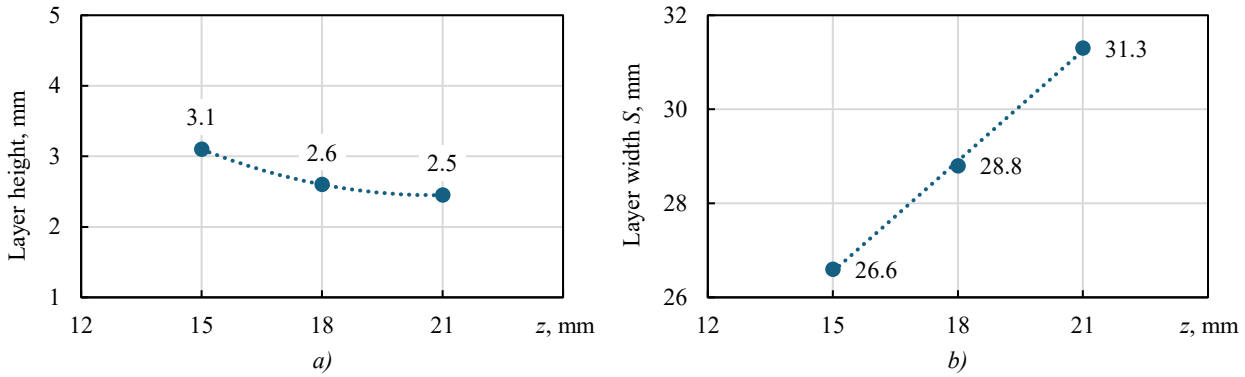

Fig. 9. Layer dimensions depending on the electrode arrangement:
a — layer height; *b* — layer width [11]

Therefore, it can be concluded that surfacing with a smaller interelectrode distance results in a thicker weld pool. A layer of liquid metal with high heat capacity and low thermal conductivity is formed between the electric arc and the base metal. This dampens the heat flow and reduces temperature fluctuations in the weld pool. This effect is described in [17].

Practically, these results clarify the effects of electrode arrangement and can guide the selection of welding conditions for other filler materials. For the application of anticorrosion coatings, it is recommended to use a welding mode with an electrode inclination angle of 10° and a spacing of 15–18 mm. This relative position of the electrodes allows for a fusion zone with less curvature. This provides a uniform distribution of chemical elements in the deposited layer. For repair welding, it is recommended to select an electrode positioning with an inclination angle of 5° and an interelectrode distance of 15 mm. In this case, the weld penetration shape has the greatest curvature, resulting in a stronger bond between the weld and the base metal compared to a weld with a flat penetration shape [6].

The results of this study indicate that the distance between electrodes has only a weak effect on both the penetration shape curvature and the number of extremes. The correlation coefficient for these parameters is –0.22 and 0.43. The effect of the electrode inclination angle relative to the vertical on the weld penetration shape curvature and the number of extremes is estimated to be significant. The correlation coefficient for these parameters is –0.65 and –0.71. As the electrode inclination angle increases relative to the vertical, the weld penetration shape curvature decreases.

Surfacing with an 18 mm interelectrode distance and a 5° decrease in electrode inclination angle resulted in an 84% reduction in penetration curvature. For tests with a 15 mm interelectrode distance, the reduction was 42%.

It is determined that the curvature of the penetration shape depends on the thickness of the weld pool, which is explained by the damping of the thermal flow by the layer of molten metal.

Conclusion. This paper assessed the effect of the relative electrode positioning on the penetration shape curvature under gas-shielded welding with a split electrode. Regression functions describing the penetration shape for each of the six experiments were determined, the number of extremes was established, and the curvature of each penetration curve was calculated. Correlation coefficients for the parameters studied were estimated.

It was shown that for all electrode configurations considered, the penetration shape was curved and saddle-shaped. It was found that at an interelectrode distance of $z = 21$ mm, the penetration shape curvature was independent of the electrode inclination angle and was approximately 0.15 mm^{-1}, and the arcs behaved as independent heat sources. As the distance decreased to $z = 18$ mm and $z = 15$ mm, the penetration shape curvature became significantly dependent on the electrode inclination angle α. As the angle increased, the penetration shape became flatter, indicating increased electromagnetic interaction between the arcs and a shift in electrode metal droplets toward the weld axis.

The results of the correlation analysis show that the relationship between the interelectrode distance z and the curvature of the weld penetration shape is weak ($r = -0.22$), while the electrode inclination angle α exhibits a moderate, close to strong correlation with the curvature of the weld penetration shape ($r = -0.65$) and a strong correlation with the number of extremes ($r = -0.71$). Thus, the electrode inclination angle is a more significant control parameter of the weld penetration shape than the interelectrode distance.

The results obtained are applicable only to the conditions of the study conducted. When using other brands of filler wire, the quantitative indicators will differ, but the physical mechanisms determining the effect of the relative positioning of the electrodes on the penetration pattern remain unchanged.

The practical value of this study is that the data obtained enable a reasonable approach to the selection of electrode arrangement for functional coating deposition, when the shape and curvature of the penetration directly determine the content of the base metal in the deposited layer and the stress concentration characteristics.

Promising future work includes modeling heat and mass transfer in split-arc surfacing for various electrode arrangements and developing a finite element heat source model for this process.

References

1. Rui Xiang, Jiankang Huang, Xiaoquan Yu, Huayu Zhao, Ding Fan. A Review of Double-Electrode GMAW: Approaches, Developments and Variants. *Journal of Manufacturing Processes.* 2025;133:1160–1182. https://doi.org/10.1016/j.jmapro.2024.12.017

2. Tušek J. Mathematical Modelling of Melting Rate in Arc Welding with a Triple-Wire Electrode. *Journal of Materials Processing Technology.* 2004;146(3):415–423. https://doi.org/10.1016/j.jmatprotec.2003.12.006

3. Elsukov SK, Sokolov GN, Zorin IV, Fastov SA, Polunin IA. Investigation of the Arc Process of a Split Electrode in a Gas Metal Arc Welding. *Izvestia VSTU.* 2020;237(2):62–66. https://doi.org/10.35211/1990-5297-2020-2-237-62-66

4. Elsukov SK, Fastov SA, Zorin IV, Lysak VI, Nesin DS. Application of Modulated AC Current for Two-Electrode Submerged Arc Cladding. *Izvestia VSTU*. 2023;281(10):53–59. https://doi.org/10.35211/1990-5297-2023-10-281-53-59

5. Ivanov VP, Lavrova EV. Controlling Penetration Zone Formation in Arc Surfacing. *Automatic Welding*. 2016;(8):6–11. https://doi.org/10.15407/as2016.08.01

6. Ryabtsev IA, Kuskov YuM, Perepletchikov EF, Babinets AA. *Surfacing. Control of Penetration of the Base Metal and Formation of Deposited Layers*. Kiev: Interservis; 2021. 392 p. (In Russ).

7. Filomeno Martina, Jialuo Ding, Stewart Williams, Armando Caballero, Gonçalo Pardal, Luisa Quintino. Tandem Metal Inert Gas Process for High Productivity Wire Arc Additive Manufacturing in Stainless Steel. *Additive Manufacturing*. 2019;25:545–550. https://doi.org/10.1016/j.addma.2018.11.022

8. Junling Hu, Hailung Tsai. Heat and Mass Transfer in Gas Metal Arc Welding. Part I: The Arc. *International Journal of Heat and Mass Transfer*. 2007;50(5-6):833–846. https://doi.org/10.1016/j.ijheatmasstransfer.2006.08.025

9. Kaiyuan Wu, Peimin Xie, Zhao Liu, Min Zeng, Zhuoyong Liang. Investigation of Double Arc Interaction Mechanism and Quantitative Analysis of Double Arc Offset in High-Power Double-Wire DP-GMAW. *Journal of Manufacturing Processes*. 2020;49:423–437. https://doi.org/10.1016/j.jmapro.2019.10.022

10. Ding Xueping, Li Huan, Wei Huiliang. Numerical Analysis of Arc Plasma Behavior in Double-Wire GMAW. *Vacuum*. 2016;124:46–54. https://doi.org/10.1016/j.vacuum.2015.11.006

11. Skoblikov IP, Efimov EI, Murzin VV. Study of Effect of Electrode Arrangement on Layer Geometry and Fusion Zone Morphology under Twin-Arc Surfacing. *Advanced Engineering Research (Rostov-on-Don).* 2025;25(3):208–220. https://doi.org/10.23947/2687-1653-2025-25-3-208-220

12. Zorin IV, Elsukov SK, Sokolov GN, Dubtsov YuN, Lysak VI, Kharlamov VO. Investigation of the Alloy Inconel 625 Deposition Process by a Split Electrode. *Welding Production*. 2018;11:9–15.

13. Xiaoli Wang, Yangsen Liu, Qi Zhang. Numerical Analysis Arc Behavior in Single-Power Double-Wire Single-Arc Gas Metal Arc Welding. *Results in Engineering*. 2025;26:105538. https://doi.org/10.1016/j.rineng.2025.105538

14. Xiaochao Zhang, Hongming Gao, Zhiwei Li. Forces Analysis of Droplets and Accurate Control of Metal Transfer in GMAW by Utilizing Droplet Resonance. *Journal of Manufacturing Processes.* 2021;70:121–131. https://doi.org/10.1016/j.jmapro.2021.08.028

15. Kaiyuan Wu, Qianrun Chen, Zitao Liu. Effect of Phase Shift on Arc Interference and Weld Bead Formation in Aluminum Alloy Tandem GMAW with a Median Pulsed Waveform. *The International Journal of Advanced Manufacturing Technology*. 2022;120(12):8013–8030. https://doi.org/10.1007/s00170-022-09200-5

16. Kaiyuan Wu, Haoran Yang, Jing Lin, Yonghua Sh, Min Zeng, Xiaobin Hong. Novel Double-Wire GMAW Arc Length Control Method Based on PID with Derivative on Measurement. *Journal of Manufacturing Processes*. 2025;150:827–842. https://doi.org/10.1016/j.jmapro.2025.06.060

17. Kaiyuan Wu, Shuxiang Liang, Jiaqi Li, Liemin Liao, Hao Huang, Xiaobin Hong. Metal Transfer Behavior in Aluminum Alloy Multi-Phase Double-Wire High-Frequency Pulsed GMAW. *Vacuum.* 2026;246:115020. https://doi.org/10.1016/j.vacuum.2025.115020

About the Authors:

Iakov P. Skoblikov, Postgraduate student of the Department of Welding of Ship Structures, Saint Petersburg State Marine Technical University (3, Lotsmanskaya Str., Saint Petersburg, 190121, Russian Federation), SPIN-code, ORCID, ScopusID, ResearchGate, iakov98sp@gmail.com

Sergey B. Sapozhkov, Dr.Sci. (Eng.), Professor of the Department of Welding of Ship Structures, Saint Petersburg State Marine Technical University (3, Lotsmanskaya Str., Saint Petersburg, 190121, Russian Federation), SPIN-code, ORCID, ScopusID, wh13@bk.ru

Claimed Contributorship:

IP Skoblikov: conceptualization, investigation, methodology, visualization.

SB Sapozhkov: writing – review & editing.

Conflict of Interest Statement: **the authors declare no conflict of interest.**

All authors have read and approved the final manuscript.

Об авторах:

Яков Павлович Скобликов, аспирант кафедры «Сварка судовых конструкций» Санкт-Петербургского государственного морского технического университета (190121, Российская Федерация, г. Санкт-Петербург, ул. Лоцманская, 3), SPIN-код, ORCID, ScopusID, ResearchGate, iakov98sp@gmail.com

Сергей Борисович Сапожков, доктор технических наук, профессор кафедры «Сварка судовых конструкций» Санкт-Петербургского морского технического университета (190121, Российская Федерация, г. Санкт-Петербург, ул. Лоцманская, 3), SPIN-код, ORCID, ScopusID, wh13@bk.ru

Заявленный вклад авторов:

Я.П. Скобликов: разработка концепции, проведение исследования, разработка методологии, визуализация.

С.Б Сапожков: написание рукописи – внесение замечаний и исправлений.

Конфликт интересов: **авторы заявляют об отсутствии конфликта интересов.**

Все авторы прочитали и одобрили окончательный вариант рукописи.

Received / Поступила в редакцию 06.03.2026
Reviewed / Поступила после рецензирования 01.04.2026
Accepted / Принята к публикации 08.04.2026